micromachines

Special Issue Reprint

Photonic and Optoelectronic Devices and Systems, 4th Edition

Edited by
Muhammad Ali Butt

mdpi.com/journal/micromachines

MDPI

Photonic and Optoelectronic Devices and Systems, 4th Edition

Photonic and Optoelectronic Devices and Systems, 4th Edition

Guest Editor

Muhammad Ali Butt

MDPI

Basel • Beijing • Wuhan • Barcelona • Belgrade • Novi Sad • Cluj • Manchester

Guest Editor
Muhammad Ali Butt
Institute of Microelectronics
and Optoelectronics
Warsaw University of
Technology
Warsaw
Poland

Editorial Office
MDPI AG
Grosspeteranlage 5
4052 Basel, Switzerland

This is a reprint of the Special Issue, published open access by the journal *Micromachines* (ISSN 2072-666X), freely accessible at: https://www.mdpi.com/journal/micromachines/special_issues/006OXR2O38.

For citation purposes, cite each article independently as indicated on the article page online and as indicated below:

Lastname, A.A.; Lastname, B.B. Article Title. *Journal Name* **Year**, *Volume Number*, Page Range.

ISBN 978-3-7258-8747-7 (Hbk)
ISBN 978-3-7258-8748-4 (PDF)
https://doi.org/10.3390/books978-3-7258-8748-4

© 2026 by the authors. Articles in this reprint are Open Access and distributed under the Creative Commons Attribution (CC BY) license. The reprint as a whole is distributed by MDPI under the terms and conditions of the Creative Commons Attribution-NonCommercial-NoDerivs (CC BY-NC-ND) license (https://creativecommons.org/licenses/by-nc-nd/4.0/).

Contents

About the Editor . . . . . **vii**

Preface . . . . . **ix**

Muhammad A. Butt
Photonic and Optoelectronic Devices and Systems, 4th Edition
Reprinted from: *Micromachines* **2026**, *17*, 671, https://doi.org/10.3390/mi17060671 . . . . . **1**

Bobin Seo and Sung-Min Park
An Energy-Efficient LiDAR Receiver Using Time-to-Voltage Converter and SAR ADC in 180 nm CMOS
Reprinted from: *Micromachines* **2026**, *17*, 622, https://doi.org/10.3390/mi17050622 . . . . . **5**

Siyi Zhang, Shuhan Zhang, Qian Fan, Xianfeng Ni and Xing Gu
Wafer-Level Transfer of GaN-on-Si Light-Emitting Devices via SiO_2–SiO_2 Direct Bonding: Strain Evolution and Optoelectronic Performance
Reprinted from: *Micromachines* **2026**, *17*, 607, https://doi.org/10.3390/mi17050607 . . . . . **24**

Dewang Guo, Yun You, Zhimin Liu and Jie Xu
All-Optical Terahertz Dual-Band Logic Gates Based on Unidirectional Modes
Reprinted from: *Micromachines* **2026**, *17*, 509, https://doi.org/10.3390/mi17050509 . . . . . **39**

Sang-Uk Byun, Su-Been Lee, Seo-Young Kim, Yu-Lim Seok, Gun Park and Dae-Gyu Moon
Polydimethylsiloxane-Based Quantum Dot Color Conversion Layers for QD-OLED Applications
Reprinted from: *Micromachines* **2026**, *17*, 505, https://doi.org/10.3390/mi17050505 . . . . . **51**

Juan Zhang, Qilu Huang, Yingxin Xu, Chaocheng Yang and Tingdi Liao
Design and Ultra-Precision Fabrication of Freeform Fresnel Lenses for Generating Rectangular Dark Hollow Beams
Reprinted from: *Micromachines* **2026**, *17*, 448, https://doi.org/10.3390/mi17040448 . . . . . **62**

Vera La Ferrara, Marco Martino, Antonio Marino, Giovanni Landi, Silvano Del Gobbo, Nicola Lisi, et al.
Triple-Cation Perovskite Photoanodes for Solar Water Splitting: From Photovoltaic-Assisted to Immersed Photoelectrochemical Operation
Reprinted from: *Micromachines* **2026**, *17*, 431, https://doi.org/10.3390/mi17040431 . . . . . **73**

Hongfei Wang and Zheng Li
A Novel Spiral Si Drift Detector with a Constant Cathode Gap and Arbitrary Cathode Pitch Profiles
Reprinted from: *Micromachines* **2026**, *17*, 354, https://doi.org/10.3390/mi17030354 . . . . . **92**

Yingsong Zheng, Longfeng Lv, Yuxiao Zou, Bo Cheng, Hanxiao Shao, Guofeng Song and Kunpeng Zhai
High-Extinction-Ratio Chiral Mid-Wave Infrared Photodetector Using Trapezoidal Si Pillars
Reprinted from: *Micromachines* **2026**, *17*, 181, https://doi.org/10.3390/mi17020181 . . . . . **110**

Huan Wang, Weicheng Tang, Mengru Li and Xiaoli Mao
PN Tandem Solar Cells Based on Combination of Dye-Sensitized TiO_2 Photoanode and Perovskite-Sensitized NiO Photocathode
Reprinted from: *Micromachines* **2026**, *17*, 99, https://doi.org/10.3390/mi17010099 . . . . . **120**

Saveli Shaul Smolanski and Dror Malka
O-Band 4 × 1 Combiner Based on Silicon MMI Cascaded Tree Configuration
Reprinted from: *Micromachines* **2026**, *17*, 31, https://doi.org/10.3390/mi17010031 . . . . . **130**

Muhammad A. Butt
Plasmonics Meets Metasurfaces: A Vision for Next Generation Planar Optical Systems
Reprinted from: *Micromachines* **2026**, *17*, 119, https://doi.org/10.3390/mi17010119 . . . . . **143**

About the Editor

Muhammad Ali Butt

Muhammad Ali Butt is an Assistant Professor at the Institute of Microelectronics and Optoelectronics, Warsaw University of Technology, Poland. His research focuses on integrated photonics, silicon photonics, optical waveguides, photonic integrated circuits, optical biosensors, plasmonics, and nanophotonic devices for sensing and communication applications. He is currently leading several national and international research projects on photonic integrated technologies, including Horizon Europe and National Science Center initiatives related to label-free biosensing and advanced photonic platforms. Dr. Butt has authored more than 240 peer-reviewed journal articles and numerous conference publications in the fields of photonics and optoelectronics. His work has received broad international recognition through collaborations with leading research institutions and contributions to the development of compact, high-performance photonic devices. He serves as a reviewer for numerous high-impact scientific journals and as a Guest Editor for several international Special Issues dedicated to photonics and sensing technologies. His current research interests include microring resonators, integrated optical biosensors, subwavelength photonic structures, photonic device optimization, and emerging photonic technologies for biomedical diagnostics, environmental monitoring, and next-generation optical systems.

Preface

Photonics and optoelectronics continue to transform modern science and engineering by enabling advanced technologies for communications, sensing, healthcare, environmental monitoring, computing, and quantum information processing. Continuous progress in materials, device design, fabrication processes, and system integration has accelerated the development of compact, efficient, and high-performance photonic platforms capable of addressing both fundamental scientific challenges and practical industrial applications.

This Reprint brings together a collection of peer-reviewed articles that reflect recent advances in photonic and optoelectronic devices and systems. The contributions encompass theoretical investigations, numerical modeling, device optimization, fabrication technologies, and experimental demonstrations across a broad range of topics, including integrated photonics, optical waveguides, resonators, photonic sensors, plasmonics, metamaterials, photonic crystals, semiconductor light sources, nonlinear photonics, and emerging quantum and artificial intelligence-enabled photonic technologies. Collectively, these studies illustrate the multidisciplinary nature of the field and highlight innovative approaches for improving device performance, functionality, and integration.

The primary aim of this Reprint is to provide researchers, engineers, and graduate students with an up-to-date overview of current developments while promoting the exchange of ideas across different disciplines within photonics and optoelectronics. It is intended to serve as a valuable reference for both established researchers and newcomers seeking insight into recent scientific progress and future research opportunities.

I would like to express my sincere appreciation to all authors for their valuable contributions and to the reviewers for their careful evaluations and constructive comments, which have helped maintain the high scientific quality of this Reprint. I also thank the editorial staff of *Micromachines* for their continuous support throughout the publication process. I hope this Reprint will contribute to further advances in photonic and optoelectronic technologies and inspire future research in this rapidly evolving field.

Muhammad Ali Butt
Guest Editor

micromachines

Editorial

Photonic and Optoelectronic Devices and Systems, 4th Edition

Muhammad A. Butt

Institute of Microelectronics and Optoelectronics, Warsaw University of Technology, Koszykowa 75, 00-662 Warsaw, Poland; ali.butt@pw.edu.pl

The rapid development of photonic and optoelectronic technologies continues to shape progress across integrated photonics, optical sensing, energy harvesting, imaging, communication systems, and semiconductor-enabled optical devices [1–4]. As modern applications increasingly demand compactness, higher functionality, and improved efficiency, advances in materials, device engineering, and fabrication technologies are steadily transforming the capabilities of optical systems [5–8]. This 4th edition of the Special Issue Photonic and Optoelectronic Devices and Systems brings together eleven contributions that collectively highlight recent progress across several important areas of photonics and optoelectronics. The Issue includes one review article and ten original research papers covering silicon photonics, metasurfaces, radiation detectors, photovoltaics, photoelectrochemical systems, optical logic, beam shaping, display technologies, LiDAR systems, and wafer level optoelectronic integration. Together, these studies reflect the increasingly interdisciplinary nature of photonics research and demonstrate how innovations in materials, device physics, and system integration continue to drive the field forward [9].

The review article by the guest editor Dr. Butt presents a broad and timely overview of the growing convergence between plasmonics and metasurfaces for next generation planar optical systems [Contribution 1]. The review discusses how the strong field confinement enabled by plasmonic structures can complement the versatile wavefront control offered by metasurfaces within compact and multifunctional optical platforms. Important developments in modulators, detectors, nanolasers, metalenses, beam steering devices, and programmable optical surfaces are critically examined alongside key challenges associated with optical losses, thermal effects, fabrication scalability, and material selection. By bringing together recent developments across plasmonic, metasurface, and hybrid architectures, this work provides a useful perspective on how planar optical systems may continue to evolve for applications in sensing, imaging, communication, and optical information processing.

The ten original research articles in this Issue address a diverse range of topics spanning integrated photonics, photodetection, energy conversion, optical computing, and display technologies. The study by Smolanski and Malka investigates a compact O band 4×1 optical power combiner based on a cascaded multimode interference tree configuration implemented on a silicon on insulator platform [Contribution 2]. Designed to operate around 1310 nm, the proposed device employs low loss S bends and adiabatic tapers to achieve efficient coherent power combining while maintaining compactness and fabrication tolerance. Thermal analysis further demonstrates stable operation over a broad temperature range, making the design attractive for O band photonic transmitters and integrated photonic systems requiring efficient power scaling.

In the area of solar energy harvesting, Wang et al. report a novel PN tandem solar cell based on the combination of a dye sensitized TiO_2 photoanode and a perovskite sensitized NiO photocathode [Contribution 3]. The work addresses an important limitation of tandem

dye sensitized solar cells, namely the poor performance of p-type sensitizers, by introducing a hybrid sensitization approach capable of simultaneously improving open circuit voltage and short circuit current density. Through optimization of the photoelectrode thickness and device structure, the authors demonstrate enhanced power conversion efficiency, offering useful insights into future strategies for improving tandem photovoltaic systems.

Infrared polarization sensitive photodetection is explored in the contribution by Zheng et al., who propose a compact chiral mid wave infrared photodetector based on trapezoidal silicon pillars [Contribution 4]. By carefully engineering geometric asymmetry through displacement and tilt angle manipulation, the proposed metasurface enables significantly different responses to left and right circularly polarized light, leading to a high extinction ratio. The compatibility of the design with semiconductor fabrication processes further highlights its practical relevance for integrated infrared sensing, quantum communication, and compact polarization selective photonic systems.

Radiation detection technologies are further advanced in the work by Wang and Li, who propose a novel spiral silicon drift detector featuring a constant cathode gap and arbitrary cathode pitch profiles [Contribution 5]. Unlike conventional concentric ring detector geometries, the proposed design enables improved control of electric field distribution while reducing surface leakage current. Theoretical modeling, together with three dimensional TCAD simulations, reveal smooth electric potential profiles, uniform drift channels, and highly symmetric charge transport. This study provides an important contribution toward the development of high performance detectors for applications in X ray spectroscopy, particle physics, and radiation monitoring.

Freeform optical beam shaping is examined in the contribution by Zhang et al., who present the design and ultra precision fabrication of freeform Fresnel lenses for generating rectangular dark hollow beams [Contribution 6]. By dividing the lens into multiple fan-shaped sectors capable of independently redirecting light toward prescribed spatial locations, the authors successfully demonstrate the generation of square hollow beam profiles. Experimental measurements show strong agreement with simulations, validating the feasibility of the proposed design. The work highlights the practical value of combining freeform optics with Fresnel structures for compact beam shaping applications in optical manipulation, communications, and laser systems.

La Ferrara et al. contribute an interesting study on triple cation perovskite photoanodes for solar water splitting, comparing photovoltaic assisted and immersed photoelectrochemical operating modes [Contribution 7]. By integrating encapsulated mixed halide perovskite solar cells with catalytic nickel foils, the authors demonstrate efficient solar driven water splitting under alkaline conditions while addressing the long standing stability challenges associated with perovskite materials. Particularly noteworthy is the strong performance observed in the immersed configuration, emphasizing the importance of device architecture in maximizing photovoltage utilization and charge transfer efficiency. This work represents a promising step toward scalable and efficient photoelectrochemical systems for hydrogen generation.

All optical information processing in the terahertz regime is explored in the work of Guo et al., who propose dual band all optical logic gates based on unidirectional electromagnetic modes [Contribution 8]. Using a Y-shaped structure capable of supporting robust one way signal propagation, the authors demonstrate several logic operations including AND, OR, NOT, and XNOR functions across different frequency bands. Importantly, the proposed architecture enables simultaneous processing of multiple signals without cross talk, highlighting its potential for future high throughput optical computing and integrated photonic logic systems.

https://doi.org/10.3390/mi17060671

Seo and Park present an energy efficient LiDAR receiver based on a time-to-voltage converter combined with a successive approximation register analog to digital converter [Contribution 9]. Instead of relying on conventional time to digital conversion schemes, the proposed architecture converts time intervals into voltage signals before digitization, significantly reducing circuit complexity and power consumption. Fabricated in a CMOS platform, the receiver demonstrates compactness and low energy consumption while maintaining sufficient temporal resolution for short range LiDAR applications. The proposed approach provides a practical route toward compact sensing systems for autonomous technologies and environmental monitoring.

Display technologies are represented by the contribution of Byun et al., who investigate polydimethylsiloxane-based quantum dot color conversion layers for QD OLED applications [Contribution 10]. By embedding quantum dots within a thermally curable PDMS matrix, the authors successfully suppress blue light leakage while improving overall color conversion efficiency compared with conventional quantum dot only layers. Through systematic optimization of quantum dot concentration and layer thickness, the study demonstrates the benefits of PDMS as a stable and optically transparent host material for future high quality display technologies.

Finally, Zhang et al. report a wafer level transfer process for GaN on Si light-emitting devices based on SiO_2-to-SiO_2 direct bonding [Contribution 11]. The proposed strategy combines hybrid planarization with direct bonding to enable efficient transfer of large area wafers while reducing optical losses associated with silicon absorption. Detailed investigations of strain relaxation and optoelectronic performance reveal notable improvements in light output together with important insights into thermal and stress related behavior during substrate transfer. This work offers a practical pathway for advancing high performance GaN based optoelectronic devices and Micro LED technologies.

These eleven contributions collectively provide a timely perspective on several important directions currently shaping photonic and optoelectronic research. A noticeable theme across the Issue is the increasing emphasis on compact and multifunctional optical systems, whether through integrated silicon photonics, metasurface-enabled photodetection, freeform beam shaping, wafer level integration, or energy efficient sensing and computation. At the same time, advances in renewable energy devices, radiation detection, and display technologies illustrate how innovations in materials and device engineering continue to expand the practical reach of photonic technologies. This Special Issue highlights not only the diversity of modern photonics research but also the growing convergence between optical physics, semiconductor technologies, materials engineering, and system level design. We hope that the studies presented here will stimulate further developments and encourage continued efforts toward compact, efficient, and application driven photonic and optoelectronic systems.

Funding: This research received no external funding.

Acknowledgments: The Guest Editor acknowledges the support of all the authors in the completion of this Special Issue.

Conflicts of Interest: The author declares no conflicts of interest.

List of Contributions:

1. Butt, M.A. Plasmonics Meets Metasurfaces: A Vision for Next Generation Planar Optical Systems. *Micromachines* **2026**, *17*, 119. https://doi.org/10.3390/mi17010119.
2. Smolanski, S.S.; Malka, D. O-Band 4 × 1 Combiner Based on Silicon MMI Cascaded Tree Configuration. *Micromachines* **2026**, *17*, 31. https://doi.org/10.3390/mi17010031.

https://doi.org/10.3390/mi17060671

3. Wang, H.; Tang, W.; Li, M.; Mao, X. PN Tandem Solar Cells Based on Combination of Dye-Sensitized TiO_2 Photoanode and Perovskite-Sensitized NiO Photocathode. *Micromachines* **2026**, *17*, 99. https://doi.org/10.3390/mi17010099.
4. Zheng, Y.; Lv, L.; Zou, Y.; Cheng, B.; Shao, H.; Song, G.; Zhai, K. High-Extinction-Ratio Chiral Mid-Wave Infrared Photodetector Using Trapezoidal Si Pillars. *Micromachines* **2026**, *17*, 181.
5. Wang, H.; Li, Z. A Novel Spiral Si Drift Detector with a Constant Cathode Gap and Arbitrary Cathode Pitch Profiles. *Micromachines* **2026**, *17*, 354. https://doi.org/10.3390/mi17030354.
6. Zhang, J.; Huang, Q.; Xu, Y.; Yang, C.; Liao, T. Design and Ultra-Precision Fabrication of Freeform Fresnel Lenses for Generating Rectangular Dark Hollow Beams. *Micromachines* **2026**, *17*, 448. https://doi.org/10.3390/mi17040448.
7. La Ferrara, V.; Martino, M.; Marino, A.; Landi, G.; Del Gobbo, S.; Lisi, N.; Viscardi, R.; Giaconia, A.; Monteleone, G. Triple-Cation Perovskite Photoanodes for Solar Water Splitting: From Photovoltaic-Assisted to Immersed Photoelectrochemical Operation. *Micromachines* **2026**, *17*, 431. https://doi.org/10.3390/mi17040431.
8. Guo, D.; You, Y.; Liu, Z.; Xu, J. All-Optical Terahertz Dual-Band Logic Gates Based on Unidirectional Modes. *Micromachines* **2026**, *17*, 509. https://doi.org/10.3390/mi17050509.
9. Seo, B.; Park, S.-M. An Energy-Efficient LiDAR Receiver Using Time-to-Voltage Converter and SAR ADC in 180 nm CMOS. *Micromachines* **2026**, *17*, 622. https://doi.org/10.3390/mi17050622.
10. Byun, S.-U.; Lee, S.-B.; Kim, S.-Y.; Seok, Y.-L.; Park, G.; Moon, D.-G. Polydimethylsiloxane-Based Quantum Dot Color Conversion Layers for QD-OLED Applications. *Micromachines* **2026**, *17*, 505. https://doi.org/10.3390/mi17050505.
11. Zhang, S.; Zhang, S.; Fan, Q.; Ni, X.; Gu, X. Wafer-Level Transfer of GaN-on-Si Light-Emitting Devices via SiO_2–SiO_2 Direct Bonding: Strain Evolution and Optoelectronic Performance. *Micromachines* **2026**, *17*, 607. https://doi.org/10.3390/mi17050607.

References

1. Butt, M.A.; Janaszek, B.; Piramidowicz, R. Lighting the Way Forward: The Bright Future of Photonic Integrated Circuits. *Sens. Int.* **2025**, *6*, 100326. [CrossRef]
2. Alberti, S.; Datta, A.; Jágerská, J. Integrated Nanophotonic Waveguide-Based Devices for IR and Raman Gas Spectroscopy. *Sensors* **2021**, *21*, 7224. [CrossRef] [PubMed]
3. Astratov, V.N. Roadmap on Label-Free Super-Resolution Imaging. *Laser Photonics Rev.* **2023**, *17*, 2200029. [CrossRef] [PubMed]
4. Du, H.; Lu, J.; Zhang, W.; Yang, G.; Zhang, W.; Xu, Z.; Wang, H.; Dai, K.; Gao, L. Advancements and Future Prospects of Energy Harvesting Technology in Power Systems. *Micromachines* **2025**, *16*, 964. [CrossRef] [PubMed]
5. Mukhtar, S.; Arbabi, A.; Viegas, J. Compact Spectral Imaging: A Review of Miniaturized and Integrated Systems. *Laser Photonics Rev.* **2025**, *19*, e01042. [CrossRef]
6. Bogdanov, S.; Shalaginov, M.Y.; Boltasseva, A.; Shalaev, V.M. Material Platforms for Integrated Quantum Photonics. *Opt. Mater. Express OME* **2017**, *7*, 111–132. [CrossRef]
7. Prosa, M.; Bolognesi, M.; Fornasari, L.; Grasso, G.; Lopez-Sanchez, L.; Marabelli, F.; Toffanin, S. Nanostructured Organic/Hybrid Materials and Components in Miniaturized Optical and Chemical Sensors. *Nanomaterials* **2020**, *10*, 480. [CrossRef] [PubMed]
8. Bhatia, Y.; Zheng, L.; Steinbach, L.; Günther, A.; Schneider, A.; Roth, B. Low-Cost Scalable Fabrication of Functionalized Optical Waveguide Arrays for Gas Sensing Application. *Int. J. Adv. Manuf. Technol.* **2025**, *138*, 617–633. [CrossRef]
9. Kazanskiy, N.L.; Nesterenko, D.V.; Khonina, S.N. Surface and Interface Engineering in Integrated Photonic Sensors: Performance Trade-Offs, Stability, and Benchmarking. *Micromachines* **2026**, *17*, 522. [CrossRef] [PubMed]

Disclaimer/Publisher's Note: The statements, opinions and data contained in all publications are solely those of the individual author(s) and contributor(s) and not of MDPI and/or the editor(s). MDPI and/or the editor(s) disclaim responsibility for any injury to people or property resulting from any ideas, methods, instructions or products referred to in the content.

micromachines

MDPI

Article

An Energy-Efficient LiDAR Receiver Using Time-to-Voltage Converter and SAR ADC in 180 nm CMOS

Bobin Seo and Sung-Min Park *

Division of Electronic & Semiconductor Engineering, Ewha Womans University, Seoul 03760, Republic of Korea; qhqls28@ewha.ac.kr
* Correspondence: smpark@ewha.ac.kr

Abstract

This paper proposes an energy-efficient LiDAR receiver topology based on a time-to-voltage converter (TVC) followed by a 5-bit SAR ADC. By converting the time-interval between START and STOP signals into the voltage domain, the proposed topology avoids the complexity of conventional TDC-based designs and enables the use of a moderate-speed, energy-efficient SAR ADC. The proposed TVC in the proposed LiDAR receiver consists of an on-chip avalanche photodiode (APD), a CMOS transimpedance-limiting amplifier (CTLA), a time-gating circuit, a ramp generator, and a peak-and-hold (PDH) block. Thereafter, the converted voltages are digitized by a VCM-based single-ended SAR ADC with a binary-weighted CDAC, a strong-arm latch comparator, and custom digital logic. A reset generator is also incorporated to coordinate the sampling, comparison, and settling phases. The proposed LiDAR receiver is implemented in a 180 nm CMOS process, where the TVC occupies an area of 171 μm × 98.8 μm, while the TVC-SAR receiver occupies 417 μm × 356 μm, respectively. The proposed LiDAR receiver consumes 13 mW from a single 1.8 V supply, in which the SAR ADC consumes 3.68 mW only. The TVC-SAR receiver resolves the time-intervals ranging from 7 ns to 32.1 ns with a resolution of 0.81 ns. Hence, the proposed topology provides an energy-efficient solution along with its reduced circuit complexity and chip implementation for short-range LiDAR applications.

Keywords: TIA; time-to-voltage converter; LiDAR; SAR ADC; CMOS

1. Introduction

Light detection and ranging (LiDAR) technology has become increasingly important in a wide range of applications, including transportation and autonomous systems, environmental and geospatial monitoring, satellite-based atmospheric observation, and healthcare monitoring such as activity recognition and fall detection [1–6]. These applications require highly accurate, fast, low-power, and cost-effective sensing solutions, rendering LiDAR sensors an essential component in modern electronic systems. As the adoption of LiDAR continues to expand, there has been a growing demand for compact and energy-efficient circuit implementations that can maintain reliable performance under strict power and size constraints.

In time-of-flight (ToF) LiDAR sensor systems, CMOS implementation often requires substantial downstream digital processing for timing extraction and digitization [7]. In some conventional architectures, these functions are performed using either on-chip or off-chip processing units. To address this issue, time-to-digital converters (TDCs) have been widely adopted in recent LiDAR systems [8–10]. However, TDC-based implementations

usually involve considerable design complexity, and moreover their timing accuracy can be sensitive to mismatch, process-voltage-temperature (PVT) variations, metastability, and layout/routing parasitic components [11,12].

To alleviate these limitations, this paper proposes a topology in which a successive-approximation-register analog-digital-converter (SAR ADC) is placed after a time-to-voltage converter (TVC). The SAR ADC is an attractive choice because of its simple architecture and high energy-efficiency, particularly in low-to-medium-speed applications because the TVC first converts the time-interval between START and STOP signals into a voltage-domain quantity.

Figure 1 shows the block diagram of the proposed LiDAR receiver, where the SAR ADC is connected to the output of the TVC so that the time-intervals can be directly translated into digital codes.

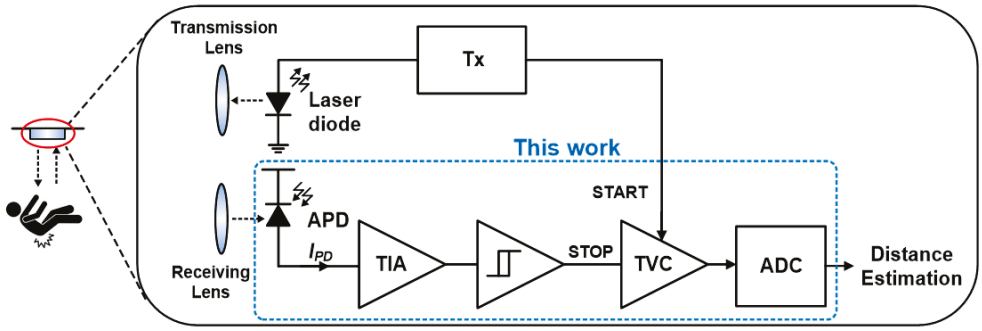


Figure 1. Block diagram of the proposed LiDAR sensor.

Figure 2 shows the block diagram of the proposed TVC circuit, which consists of an on-chip avalanche photodiode (APD), a CMOS transimpedance-limiting amplifier (CTLA), a Schmitt trigger, a time-gating circuit called rising edge detector (RED), an enable-controlled ramp generator (i.e., an integrator circuit), and a peak-and-hold (PDH) block. Therefore, the TVC converts the time-intervals between the START signals transmitted from the transmitter (Tx) and the STOP signals reflected from the targets into the corresponding voltages, hence enabling the voltage-domain time-encoding for ToF LiDAR sensor applications [13]. Thereafter, a common-mode voltage (VCM)-based SAR ADC is employed as a back-end digitizer.

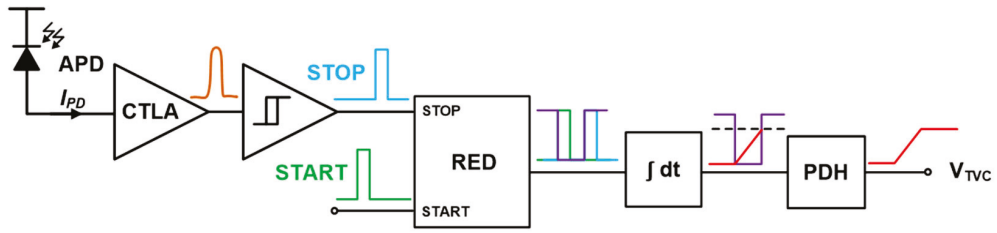


Figure 2. Block diagram of the TVC circuit.

This paper is organized as follows. Section 2 discusses the circuit operations and, Section 3 presents the post-layout simulation results, and the conclusion is followed in Section 4.

2. Circuit Description

2.1. Front-End Detection

In this work, on-chip APDs are implemented based on a P^+/N-Well/Deep N-Well (P^+/NW/DNW) structure where avalanche multiplication is initiated at the P^+/NW junction. The central P^+ contacts are tied to the TIA input, suppressing slow substrate diffusion currents while maintaining high responsivity and wide bandwidth. Shallow-trench-

https://doi.org/10.3390/mi17050622

isolation (STI) formed deeper than the junction serves as a guard ring, thus reducing electric field crowding and preventing premature breakdown at the cost of slightly worse responsivity. The DNW enhances the NIR sensitivity by blocking hole diffusion into the P-substrate via a built-in potential barrier. For optical access, salicide blocking is applied to the P^+ source/drain regions, while P^+ contacts remain silicided for low resistance. Minimizing the contact area is also necessary to preserve responsivity [14,15].

Figure 3 shows the internal cross-section of the proposed P^+/NW/DNW APD. For improved optical and electrical performance, salicide blocking is applied to the P^+ source/drain regions to enable efficient light absorption, while the P+ contacts remain silicided to reduce series resistance. The active area diameter is designed to be 40 μm to enhance responsivity, and an octagonal layout is adopted to mitigate edge breakdown. The device achieves a responsivity of 4.16 A/W at a reverse bias of 10.5 V and a photodetection bandwidth of 1.7 GHz at 10.25 V.

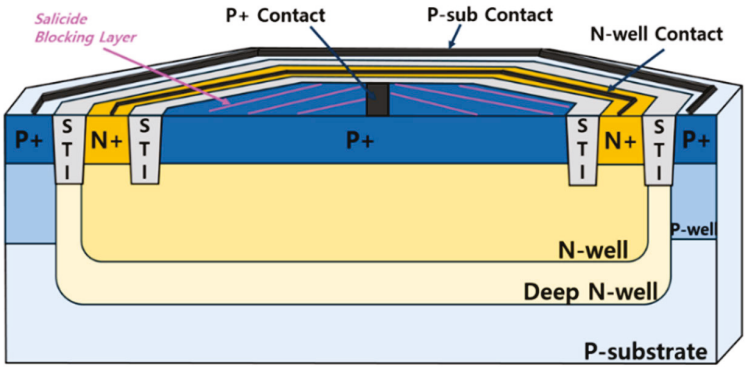


Figure 3. Internal cross-section of the P^+/NW/DNW APD [14,15].

Figure 4 illustrates the schematic diagram of the CMOS transimpedance-limiting amplifier (CTLA) employed as the front-end amplifier. The CTLA adopts a dual-feedback topology composed of a main inverter-based TIA and an additional active feedback path. An NMOS switch is inserted in the feedback loop so that the auxiliary feedback is activated only when the input photocurrent exceeds a certain threshold [16,17]. Under small-signal input conditions, the circuit operates as a conventional TIA to maintain linear amplification, while for large input currents the active feedback path drives the output into saturation, thus performing a limiting function. This approach suppresses pulse distortion and extends the input dynamic range without requiring a multi-stage limiting amplifier. The CTLA exhibits a transimpedance gain of 69.8 dBΩ and a bandwidth of 2.78 GHz, while consuming 6.76 mW. The input-referred noise spectral density is 14.9 pA/$\sqrt{\text{Hz}}$, and the input dynamic range is 40 dB (10 μA_{pp} to 1 mA_{pp}).

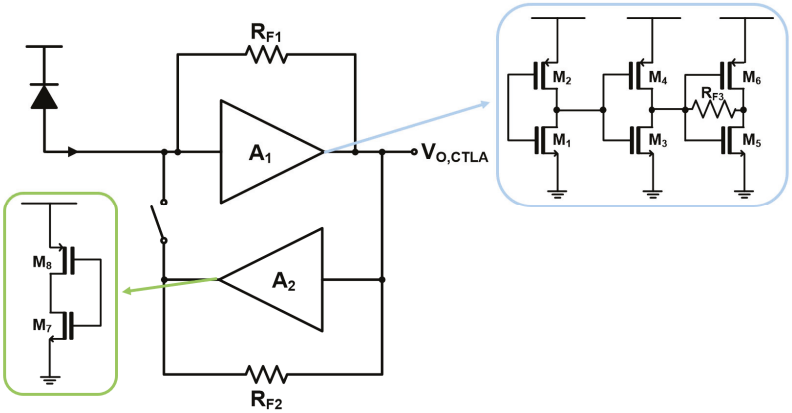


Figure 4. Schematic diagram of the CTLA [16,17].

https://doi.org/10.3390/mi17050622

Figure 5 shows the schematic diagram of the Schmitt trigger that is employed in the proposed TVC to convert the analog output of the CTLA into a digital signal. Compared to a conventional latch-based design, the suggested Schmitt trigger can be realized using a smaller number of CMOS transistors, enabling a more compact and power-efficient design. In this work, the circuit uses only six CMOS transistors.

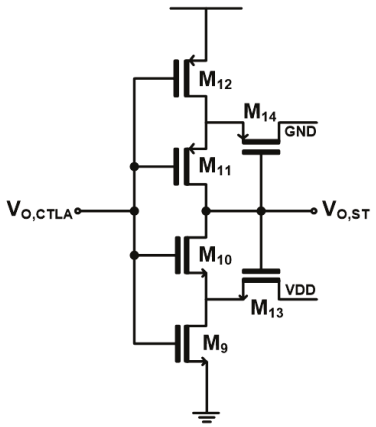


Figure 5. Schematic diagram of the Schmitt trigger.

Due to its inherent hysteresis characteristics, the Schmitt trigger improves noise immunity and prevents false switching caused by small fluctuations in the TIA output. This effectively allows reliable signal detection over a wider input range, which can be interpreted as an improvement in the usable dynamic range of the TIA output. Although the Schmitt trigger consumes 1.02 mW, which is not particularly low for a simple six-transistor implementation, it provides a simpler and more power-efficient solution when compared to conventional approaches in time-based conversion systems that rely on more complex latch or comparator structures for analog-to-digital pulse generation.

2.2. Time-to-Voltage Converter

Figure 6 illustrates the schematic diagram of the time-gating circuit, where START and STOP signals pass through inverter stages to introduce a slight delay, thereby generating narrow pulse signals based on edge-detection principles. Unlike a conventional rising-edge detector that only indicates the occurrence of a signal transition, the proposed circuit utilizes both START and STOP signals to capture the time-interval between them.

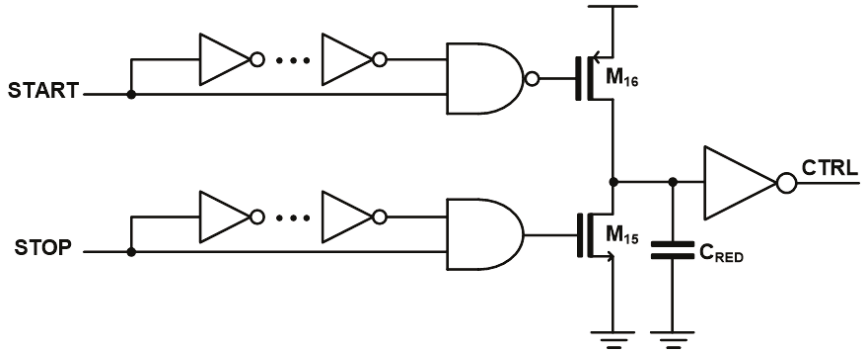


Figure 6. Schematic diagram of the time-gating circuit.

In this implementation, the STOP signal corresponds to $V_{O,ST}$, while the START signal is externally applied from the Tx. These signals drive the gates of the PMOS and NMOS transistors, which selectively connect the capacitor node to VDD or GND. Consequently, the capacitor is charged during the time-interval between START and STOP, effectively

https://doi.org/10.3390/mi17050622

converting the time-difference into a voltage level. The inverted voltage across the capacitor is then used as the CTRL signal.

Figure 7 shows the schematic of the proposed ramp generator that operates as a time-gated integrator rather than a conventional continuous-time ramp generator. It consists of a voltage-to-current conversion stage (op-amp, a resistor, and M_{17}), a current mirror (M_{19}–M_{20}), a load capacitor (C_{RG}) and a reset switch (M_{18}). The op-amp regulates the source node of M_{17} such that a current proportional to the input voltage is continuously generated through M_{17}. This current is mirrored by M_{19}–M_{20} and serves as the charging current for the load capacitor (C_{RG}). The CTRL signal generated from the time-gating circuit defines the integration window and operates as an active-low enable signal.

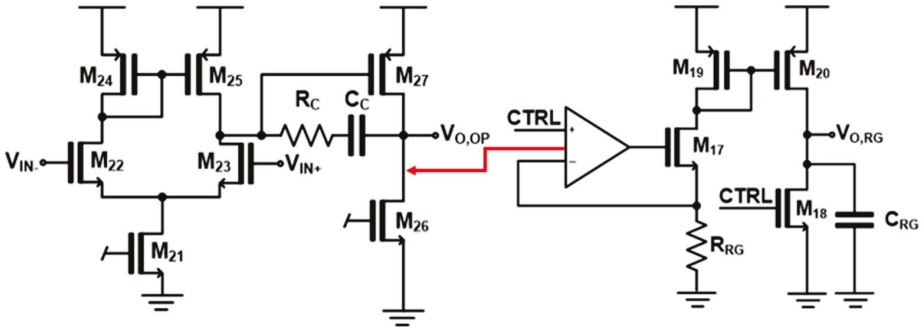


Figure 7. Schematic diagram of the time-gated ramp generator circuit.

When CTRL is high, M_{18} is turned-on, thus forcing the output node to ground and resetting the capacitor. In this phase, the mirrored current is diverted through M_{18}, and no integration occurs.

When CTRL transitions to low (i.e., during the time-interval between START and STOP signals), M_{18} is turned-off and the mirrored current from M_{20} is injected into the capacitor. In consequence, the capacitor is actively charged during this interval, generating a voltage ramp proportional to the input time difference. Therefore, the proposed circuit can generate ramp signals only within the defined time-interval, hence enabling accurate time-to-voltage conversion for the subsequent SAR ADC.

Figure 8 shows the peak detect-and-hold (PDH) circuit where the input of the PDH (V_{IN}) is connected to $V_{O,RG}$, so that the circuit detects and holds the peak voltage stored on the capacitor. The reset signal (RST) discharges the stored voltage on the capacitor and is externally applied after two cycles of the SAR ADC to ensure stable operations. This configuration enables accurate sampling of the peak value and maintains it for subsequent processing by the ADC, thereby preventing signal loss due to rapid signal variations.

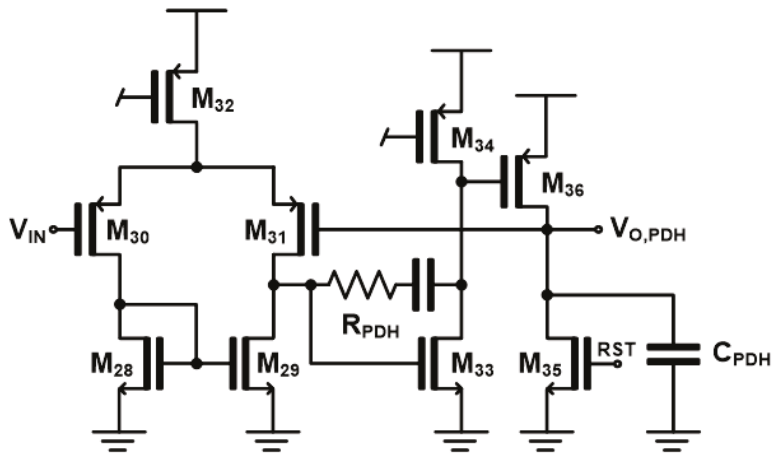


Figure 8. Schematic diagram of the peak-detect and hold (PDH) circuit.

https://doi.org/10.3390/mi17050622

Figure 9 illustrates the block diagram of the proposed TVC-SAR receiver. As aforementioned, START signals from the Tx are applied directly to the TVC whereas STOP pulses reflected from targets enter the TVC after being processed through the analog front-end circuit including the on-chip APD and the CTLA. The TVC converts the time-intervals between the START and STOP signals into analog voltages. Then, the generated voltages are transferred to the SAR ADC through a sample-and-hold (S/H) circuit followed by a VCM-based single-ended SAR ADC.

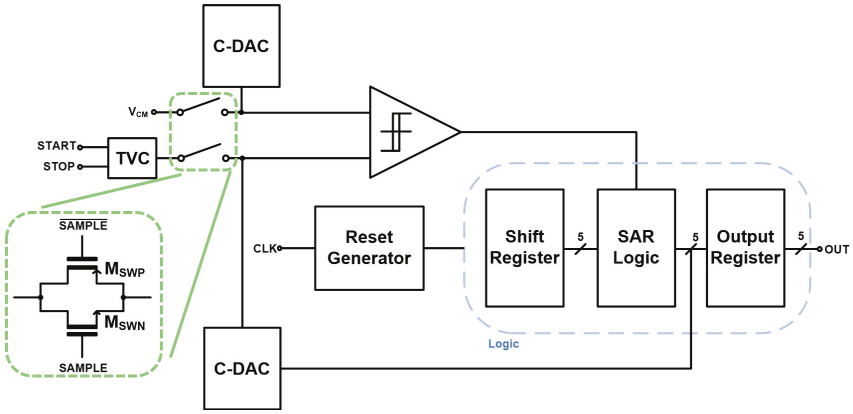
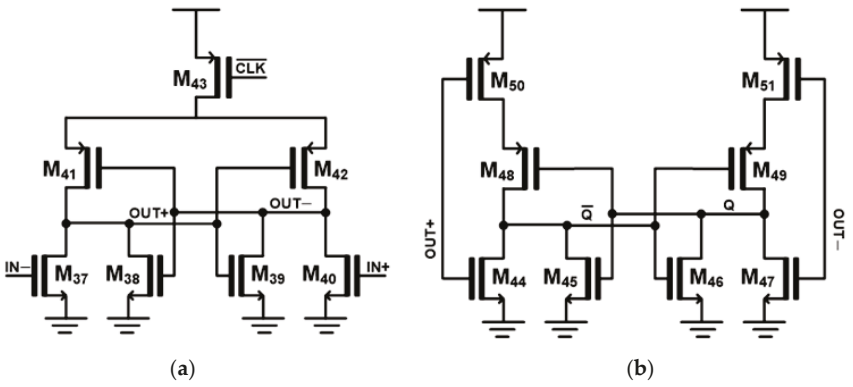


Figure 9. Block diagrams of the proposed TVC-SAR receiver.

The SAR ADC consists of an S/H circuit that samples both IN+ and IN− inputs (which correspond to the comparator's differential inputs), a capacitive digital-to-analog converter (C-DAC), a strong-arm latch comparator, a reset generator, and digital logic. To maintain sampling consistency, the VCM is sampled by using a C-DAC. The S/H circuit is implemented using a transmission-gate (TG) based sampling structure, and is controlled by the 'Sample' and 'Sample_B' signals generated from the logic block of the SAR ADC.

2.3. Strong-Arm Comparator and SR Latch

Figure 10a depicts the schematic diagram of the strong-arm comparator. Whenever IN+ is greater than IN−, the transistor M_{40} is turned on. Therefore, a low signal is delivered to both M_{38} and M_{41}, turning M_{38} off and M_{41} on. In consequence, the output node (OUT+) is pulled up to V_{DD}, producing a strong logic high signal. To the contrary, the opposite output node (OUT-) is discharged toward ground, generating a strong logic low signal. These regenerative operations rapidly amplify the small input difference and enable fast decision-making. In addition, the clock signal (CLK) is applied to the transistor M_{15}, which acts as a tail switch. The comparator operates only when the clock signal is high, thereby reducing static power consumption and improving overall power efficiency.



(**a**) (**b**)

Figure 10. Schematic diagrams of (**a**) strong-arm comparator and (**b**) SR latch.

https://doi.org/10.3390/mi17050622

Figure 10b shows the schematic diagram of the SR latch. By placing the SR latch after the strong-arm comparator, the comparison result is stored and maintained until the next clock cycle, ensuring stable digital output for subsequent logic processing. The SR latch is implemented by using NOR gates constructed at the MOSFET level, which improves the circuit uniformity and allows more consistent device matching when compared to gate-level implementations. Furthermore, the SR latch prevents the output glitches and provides a reliable digital interface between the analog comparator and the following digital logic.

In this work, the strong-arm latch is driven by $\overline{CLK}$, i.e., the inverted clock signal, instead of the main clock used in the preceding logic blocks. By operating on the complementary clock phase, the latch functions at a different timing from the logic that generates signals synchronized with the main clock signal. This timing separation provides additional settling time for the comparator outputs and helps to prevent potential timing errors, thereby ensuring more reliable and accurate comparison results.

2.4. C-DAC

As aforementioned, a V_{CM}-based single-ended SAR ADC architecture is employed in the proposed TVC-SAR receiver. For proper V_{CM}-based operations, the negative input (IN−) node is connected to the common-mode voltage (V_{CM}), while the positive input (IN+) node is connected to V_{in} that is the output of the preceding TVC. The IN-node in this C-DAC is solely connected for symmetry and therefore does not affect the switching operations, comparator decision, or conversion, hence serving only to sample and hold the common-mode voltage (V_{CM}).

Figure 11 shows the schematic diagram of the C-DAC. Here, the unit capacitance (C) has a minimum value of 35.6 fF. During the sampling phase, the top plate of the C-DAC is connected to V_{in} while the bottom plate is tied to V_{CM}, thus allowing the input signal (V_{in}) to be stored. Then, the input signal is sampled at the top plate of the C-DAC through the connected sample-and-hold (S/H) circuit. According to the bit decision generated by the SAR logic, the bottom plate of the C-DAC is switched to either V_{REFP} or V_{REFN}.

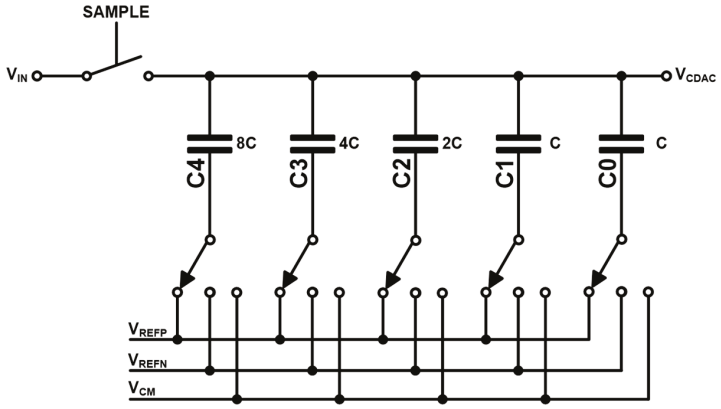


Figure 11. Schematic diagram of the C-DAC circuit.

After the sampling phase, the SAR conversion process begins. Starting from the most significant bit (MSB), the comparator sequentially performs bit-by-bit comparisons. The resulting C-DAC voltage (V_{CDAC}) is compared with the input signal (V_{in}) through the comparator to determine each bit. The total capacitance of the C-DAC array is designed to be 16C that corresponds to the binary-weighted capacitor structure, i.e., (8C + 4C + 2C + C + C). In the MSB decision step, the C-DAC output is adjusted by $\pm(V_{REFP} - V_{REFN})/2$, depending on the switching result. In the subsequent steps, the voltage change becomes $\pm(V_{REFP} - V_{REFN})/4$, $\pm(V_{REFP} - V_{REFN})/8$, and so on for the lower bits. It is noted that the value of V_{CM} is defined as the mid-point between V_{REFP} and V_{REFN}.

https://doi.org/10.3390/mi17050622

Figure 12 depicts the switching control circuit for the C-DAC. Through this switching block, each capacitor is connected to V_{CM} during the sampling phase, allowing the input signal to be properly stored. During the conversion phase, based on the bit-decision result, the capacitor is switched to V_{REFP} when the decision becomes '1' and to V_{REFN} when the decision becomes '0'. These switching operations enable the C-DAC to generate the corresponding reference voltage levels for each bit, hence facilitating the accurate successive approximation during the conversion process.

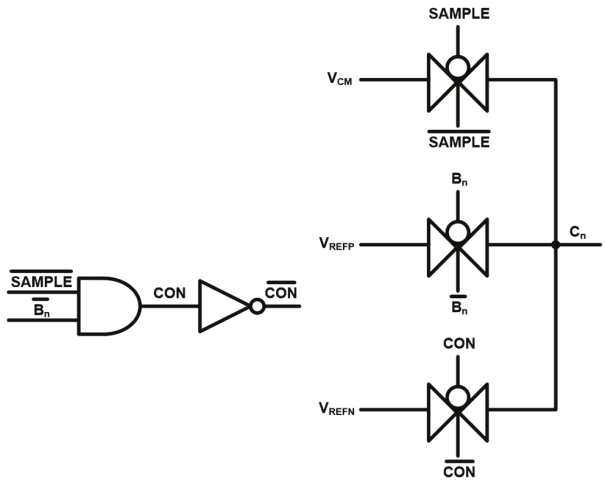


Figure 12. Schematic diagram of the switching control circuit of C-DAC.

Figure 13 illustrates the principal operations of the C-DAC for the upper 2-bit example. During the sampling phase, V_{in} is sampled onto the capacitors. Afterward, the input signal is disconnected, and the comparator determines the polarity between V_{IN+} and V_{IN-}. Based on the decision, the capacitor is switched from V_{CM} to either V_{REFP} or V_{REFN}, resulting in a step change of $\pm(V_{REFP} - V_{REFN})/2$ in the C-DAC output for the MSB decision. In the subsequent bit cycle, the C-DAC output is further adjusted by $\pm(V_{REFP} - V_{REFN})/4$.

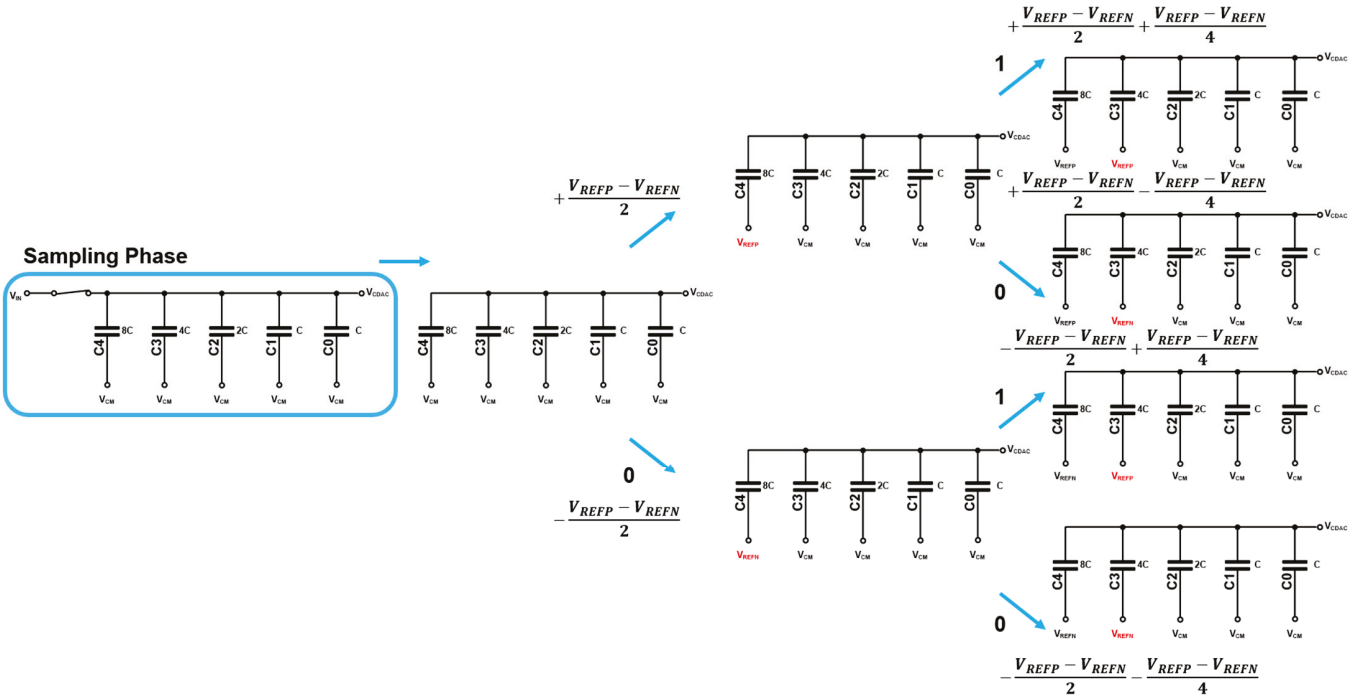


Figure 13. Schematic diagram of the C-DAC operations during SAR conversion.

https://doi.org/10.3390/mi17050622

2.5. Digital Logic and Reset Generator

Figure 14 depicts the block diagram of the reset generator circuit that consists of a D flip-flop (DFF) and logic gates. It can count eight clock cycles and generate a reset signal at the 9th cycle. In the proposed SAR ADC architecture, the sampling phase occupies two clock cycles, followed by five comparison cycles. Thereafter, one additional clock cycle is allocated for settling before the end-of-conversion (EOC) signal is generated. At every 9th rising edge of the clock, the reset signal is generated, returning the SAR ADC to the sampling phase. Although the proposed converter is a 5-bit SAR ADC, the reset signal is generated every eight clock cycles rather than six cycles in order to allocate additional timing for the end-of-conversion (EOC) signal generation and the SAMPLE state control. The generated reset signal is distributed to the digital logic block, where it initializes the internal registers and coordinates the timing of the SAMPLE and EOC signals.

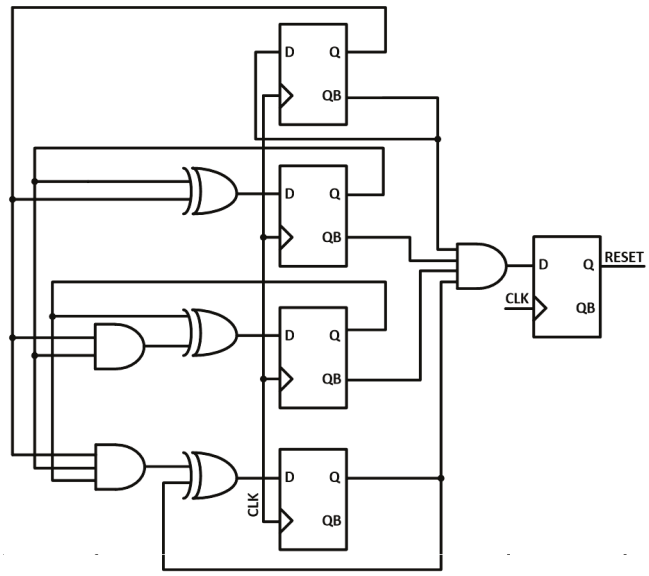


Figure 14. Schematic diagram of the reset generator.

Figure 15 shows the block diagram of the digital logic, consisting of a shift register and several DFFs that perform the bit-decision operation of the SAR algorithm. To ensure sufficient sampling and settling time before the sampled signal is transferred from the sample-and-hold (S/H) circuit to the C-DAC, the SAMPLE signal occupies twice the duration of a single bit-comparison state. Consequently, the sampling operation lasts for two clock cycles, followed by five clock cycles dedicated to the bit-by-bit comparison process. After the final comparison, an additional clock cycle is consumed to allow for redundancy in the bit decision and sufficient settling time. Although this results in more than five clock cycles being used for the conversion, the removal of redundancy improves the overall accuracy. Moreover, since the target ADC is not designed for high-speed operations, the additional clock cycle does not significantly degrade performance.

During the conversion phase, the SAR logic receives the comparator output and determines the switching direction of the C-DAC. Depending on whether the comparator output is logic '1' or '0', the corresponding capacitor is connected to either V_{REFP} or V_{REFN}, respectively. In addition, the set input of each DFF is controlled by the output of the shift register so that the decision-making process is activated only for the corresponding bit position, while the other stages remain inactive. This mechanism enables the sequential bit evaluation and the proper propagation of the SAR decision through the register chain.

https://doi.org/10.3390/mi17050622

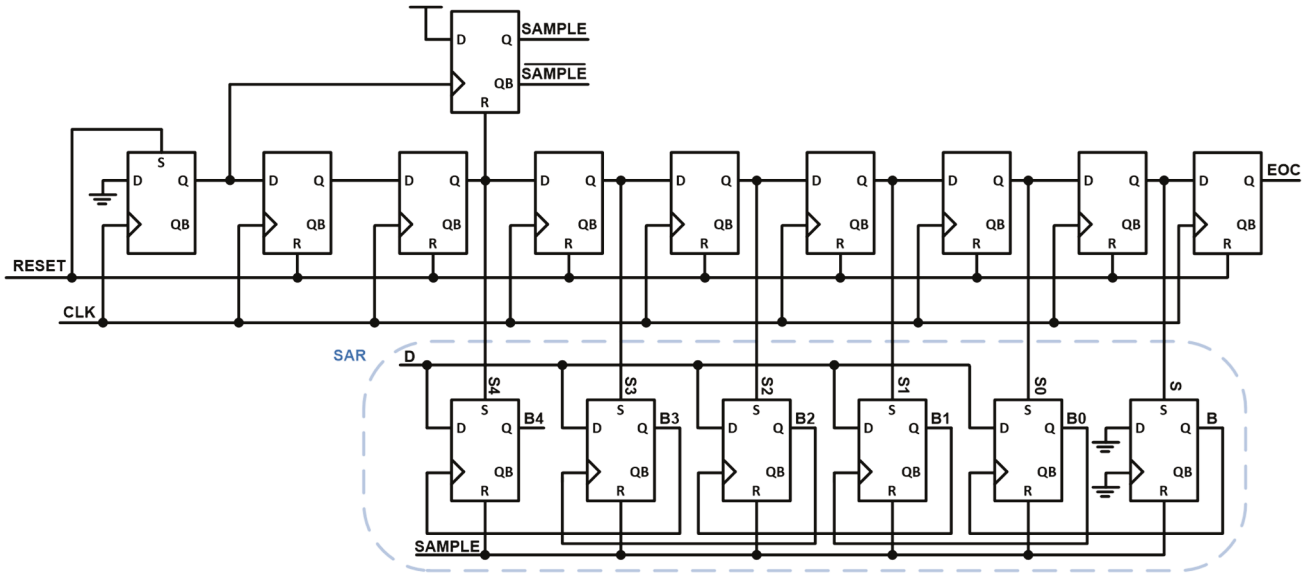


Figure 15. Block diagram of the digital logic.

3. Layout and Simulation Results

Figure 16 illustrates the layout of the proposed TVC-SAR receiver, in which the TVC block integrated with two on-chip P^+/NW/DNW APDs occupies an area of 171 µm × 98.8 µm, while the overall TVC-SAR receiver layout occupies an area of 417 µm × 356 µm, respectively. It should be noted that a dummy APD is added not only to enhance the responsivity of the on-chip APD, but also to improve the symmetry of the analog front-end circuitry. Also, it is clearly seen that the layout of the proposed TVC-SAR receiver includes a TVC followed by a 5-bit SAR ADC. Post-layout simulations were carried out for the TVC-SAR receiver by using the model parameters based on a standard 180 nm CMOS technology. The DC simulation results indicate that the proposed TVC-SAR receiver consumes 13 mW from a single 1.8 V supply voltage, in which the SAR ADC only consumes 3.68 mW.

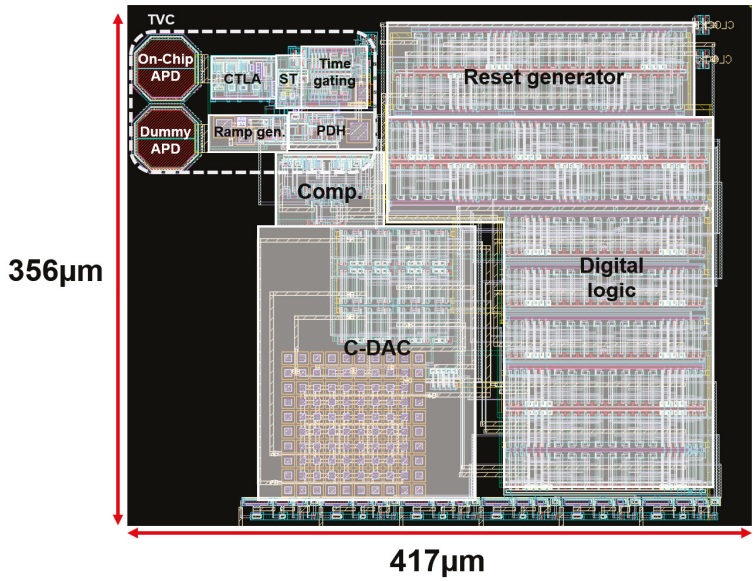


Figure 16. Layout of the proposed TVC-SAR receiver.

Figure 17 compares the simulated pulse response of the CTLA alone with that of the CTLA plus Schmitt trigger for various input currents. As observed from the results, the Schmitt trigger starts to recognize the input signals from ~14 μA_{pp}. This corresponds

https://doi.org/10.3390/mi17050622

to a time-interval of 32.9 ns, which translates to a distance of 4.93 m. In the case of the CTLA alone, the output pulse begins to exhibit distortion starting from around 1 mA_{pp}. However, with the addition of the Schmitt trigger, the distorted pulses are effectively restored, maintaining a stable pulse shape up to ~2.8 mA_{pp}, confirming enhancement in the effective dynamic range. At 2.8 mA_{pp}, the corresponding time-interval is 2.32 ns, which translates to a distance of 0.35 m.

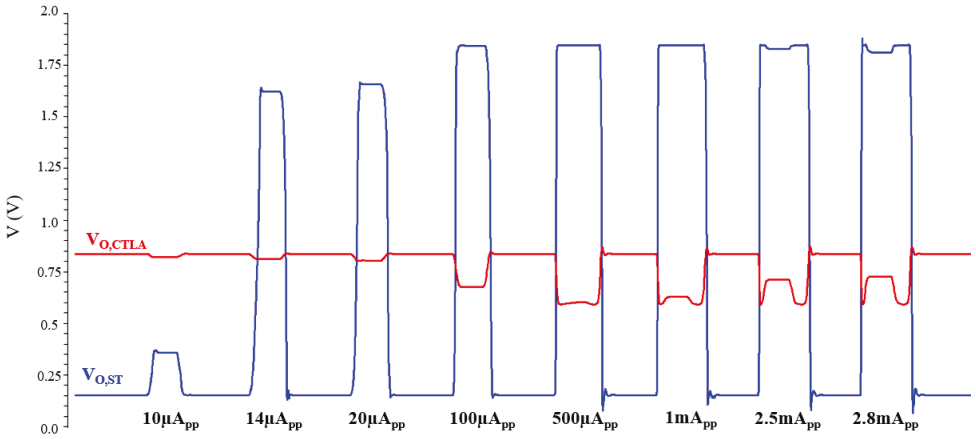


Figure 17. Pulse response comparison of the CTLA alone with the CTLA plus Schmitt trigger for various input currents.

Figure 18 presents the simulated AC responses of the CTLA alone and the CTLA + Schmitt trigger, respectively. The inclusion of the Schmitt trigger increases the effective transition gain up to 81.3 dBΩ. While the Schmitt trigger is inherently non-linear, this AC response characterizes its small-signal behavior during switching, thus confirming that the system maintains a high bandwidth of 2.2 GHz for high-speed pulse restoration.

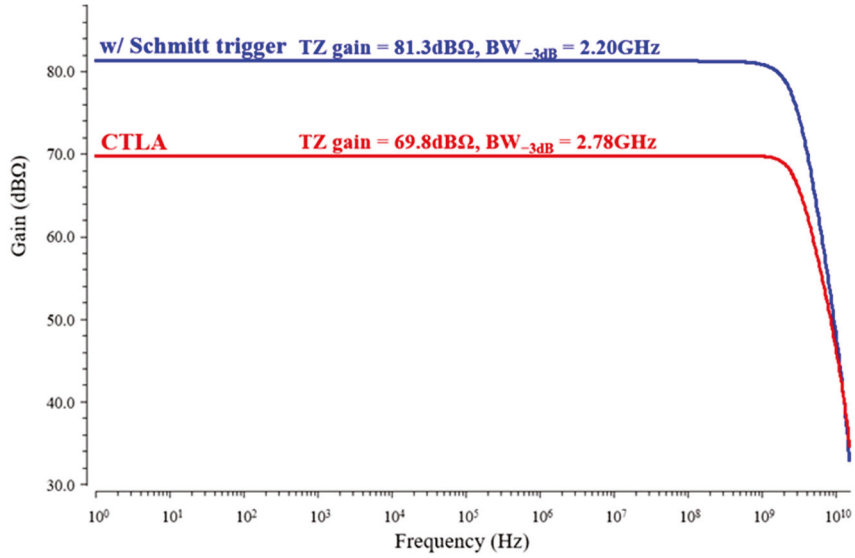


Figure 18. AC response comparison of the CTLA alone and the CTLA plus Schmitt trigger.

Figure 19 shows the simulation results of the proposed time-to-voltage converter (TVC) with Δt = 7 ns. The START and STOP signals are detected at their rising edges to generate the CTRL signal, which remains low only during the interval Δt and stays high otherwise. This CTRL signal drives the ramp generator-based integrator, enabling charging exclusively during Δt. The resulting $V_{O,RG}$ is then processed by the peak-detect-and-hold (PDH) circuit, effectively converting the input time interval into a proportional voltage.

https://doi.org/10.3390/mi17050622

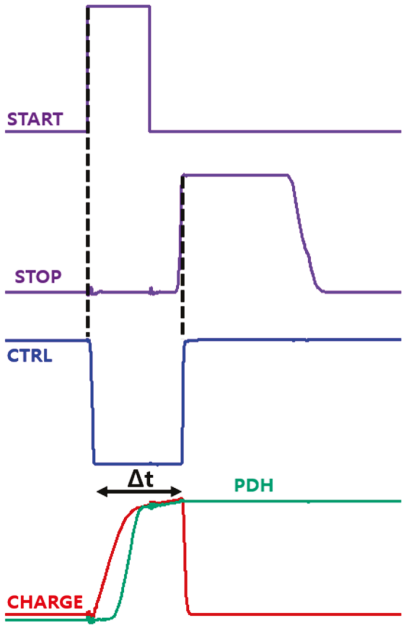


Figure 19. Simulation results of the proposed TVC for Δt = 7 ns.

Figure 20a depicts the transfer characteristic from the input time-interval (Δt) to the TVC output voltage, along with its best-fit linear approximation. While the overall trend follows a linear relationship, noticeable deviation is observed particularly in the lower time region due to the intrinsic nonlinear behavior of the TVC.

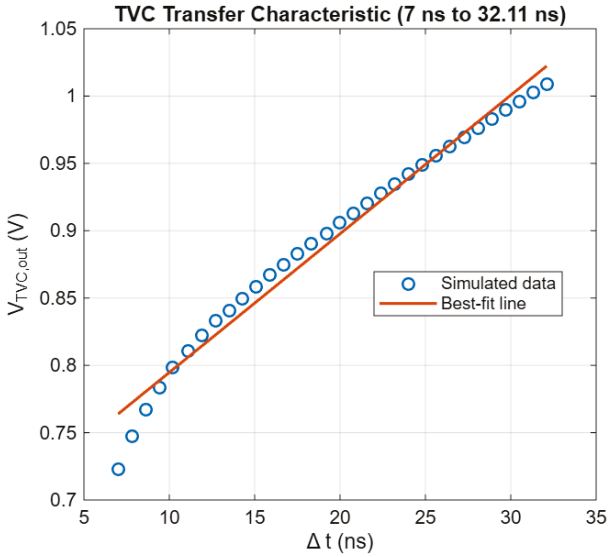
Figure 20b reveals the corresponding integral nonlinearity (INL), calculated with respect to the best-fit line and normalized by the 5-bit equivalent LSB. Over the evaluated range, the INL is simulated to be +1.276/−4.557 LSB, resulting in a peak-to-peak INL of 5.833 LSB. The relatively large INL mainly originates from the nonlinear voltage-time characteristic in the initial charging region.

To further evaluate the local linearity, the differential nonlinearity (DNL) was extracted based on the variation in the instantaneous slope relative to the ideal slope obtained from linear fitting.

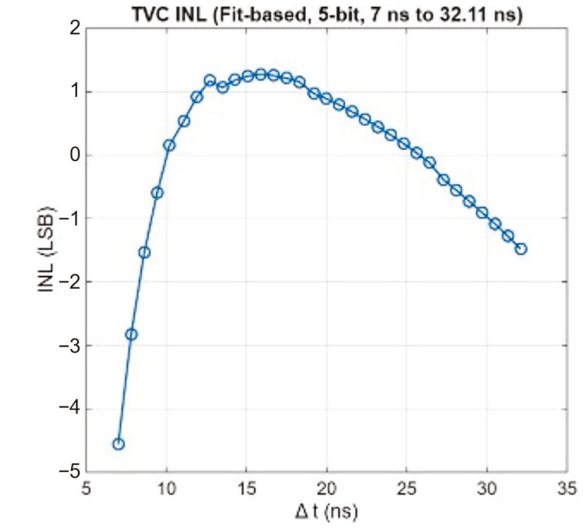
Figure 20c shows the simulated results of DNL, where the DNL ranges from −0.264 to +1.860 LSB, with a peak-to-peak value of 2.124 LSB. Despite the non-ideal linearity reflected in the INL, the TVC maintains a monotonic transfer characteristic across the entire operating range, without any missing codes. This is also supported by the bounded DNL behavior, indicating that the local step variation remains controlled. Therefore, although the absolute linearity is limited, the proposed TVC is still suitable for applications where monotonicity and consistent time resolution are more critical than strict linearity.

Figure 21 presents the simulated phase operations of the proposed SAR ADC. The operation consists of a 2-clock-cycle sampling phase, followed by 5 comparison cycles. Afterward, one clock cycle is allocated for settling, during which the EOC signal is generated. This sequence repeats periodically. In the proposed implementation, the SAR ADC operates with a fixed synchronous timing scheme without an explicit asynchronous start-of-conversion (SOC) signal, while the PDH circuit holds the converted voltage before the SAR conversion phase begins.

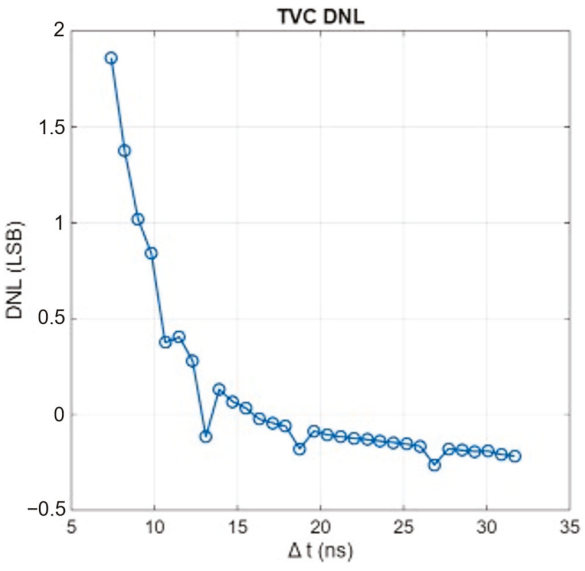
https://doi.org/10.3390/mi17050622



(**a**)



(**b**)



(**c**)

Figure 20. Simulation (**a**) transfer characteristic vs. best-fit line, (**b**) INL, and (**c**) DNL results of the proposed TVC.

https://doi.org/10.3390/mi17050622

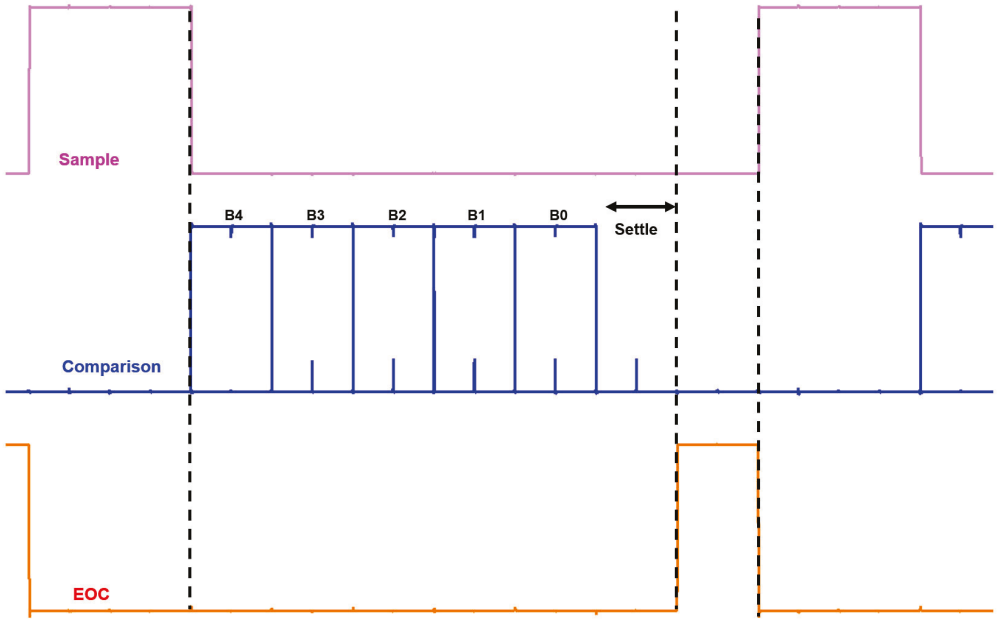


Figure 21. Simulated timing diagrams of the proposed SAR ADC operation phases.

Figure 22 shows the simulated C-DAC output (V_{CDAC}) for different time intervals. The results correspond to Δt = 8.62 ns, 16.72 ns, 17.53 ns, and 27.25 ns. The first sample (blue and red) on the left presents the results for 16.72 ns and 17.53 ns. It demonstrates that the SAR ADC can clearly distinguish even a small time-difference of 0.81 ns that corresponds to the LSB resolution. This LSB resolution of 0.81 ns corresponds to the detection range of 12.2 centimeters in distance. Therefore, it is noted that the proposed sensor system has a minimum detectable range of 1.05 m and a maximum detectable range of 4.82 m. The second sample (purple and green) on the right figure shows the results for 8.62 ns and 27.25 ns, where different switching behaviors of the C-DAC can be observed depending on the input time-interval.

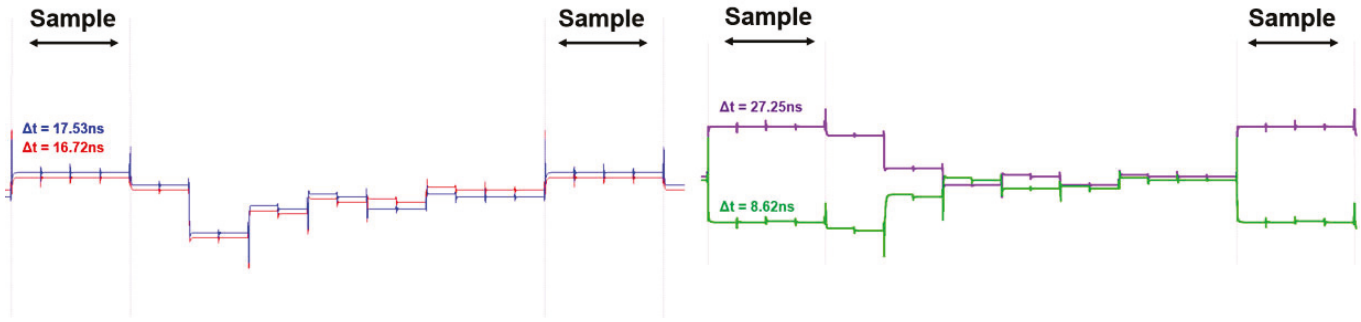


Figure 22. Simulated V_{CDAC} for different time intervals, respectively.

Figure 23 shows the timing-diagrams of the C-DAC switching control circuit. The signals include B_n (generated by the SAR logic based on bit decisions), which switches the capacitor to V_{REFP}, CON (that is connected to V_{REFN}), and SAMPLE (that is connected to V_{CM}). These timing-diagrams confirm that the capacitor switching occurs without overlap, thus ensuring proper and reliable C-DAC operations.

https://doi.org/10.3390/mi17050622

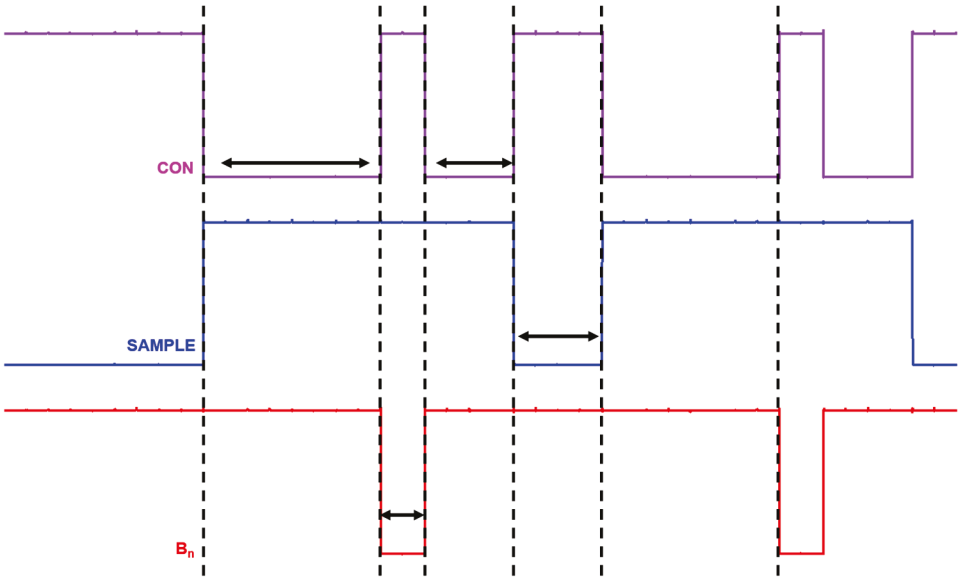


Figure 23. Timing diagrams of the C-DAC switching control signals.

Figure 24 presents an example of the full 5-bit digital output for Δt = 18.34 ns. It can be observed that the final output is determined and becomes valid simultaneously with the assertion of the end-of-conversion (EOC) signal. In addition, all output bits (P_n) exhibit clearly distinguishable logic low and high levels, indicating stable and accurate digital conversion.

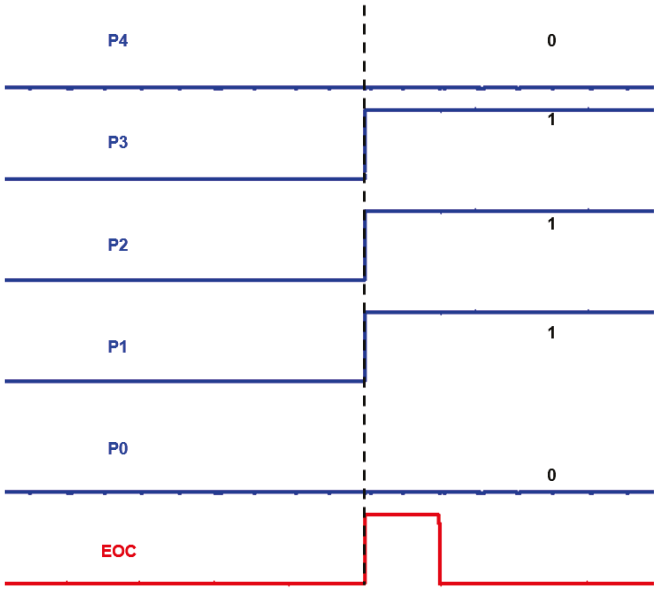


Figure 24. 5-bit SAR ADC output waveforms at Δt = 18.34 ns.

Figure 25 shows the FFT spectra of the standalone SAR ADC only and the proposed TVC + SAR system. The FFT spectra were normalized with respect to the fundamental tone at 40.148 kHz, where the fundamental tone was set to 0 dB. Figure 25a shows the FFT spectrum of the standalone SAR ADC, where the measured SINAD and ENOB were 26.67 dB and 4.14 bits, respectively. Figure 25b shows the FFT spectrum of the complete TVC + SAR ADC system under the same sampling condition, in which the measured SINAD and ENOB were 20.57 dB and 3.12 bits, respectively. Compared to the standalone SAR ADC, the proposed TVC + SAR ADC system exhibits increased distortion due to the nonlinearity and timing conversion error introduced by the TVC stage.

https://doi.org/10.3390/mi17050622

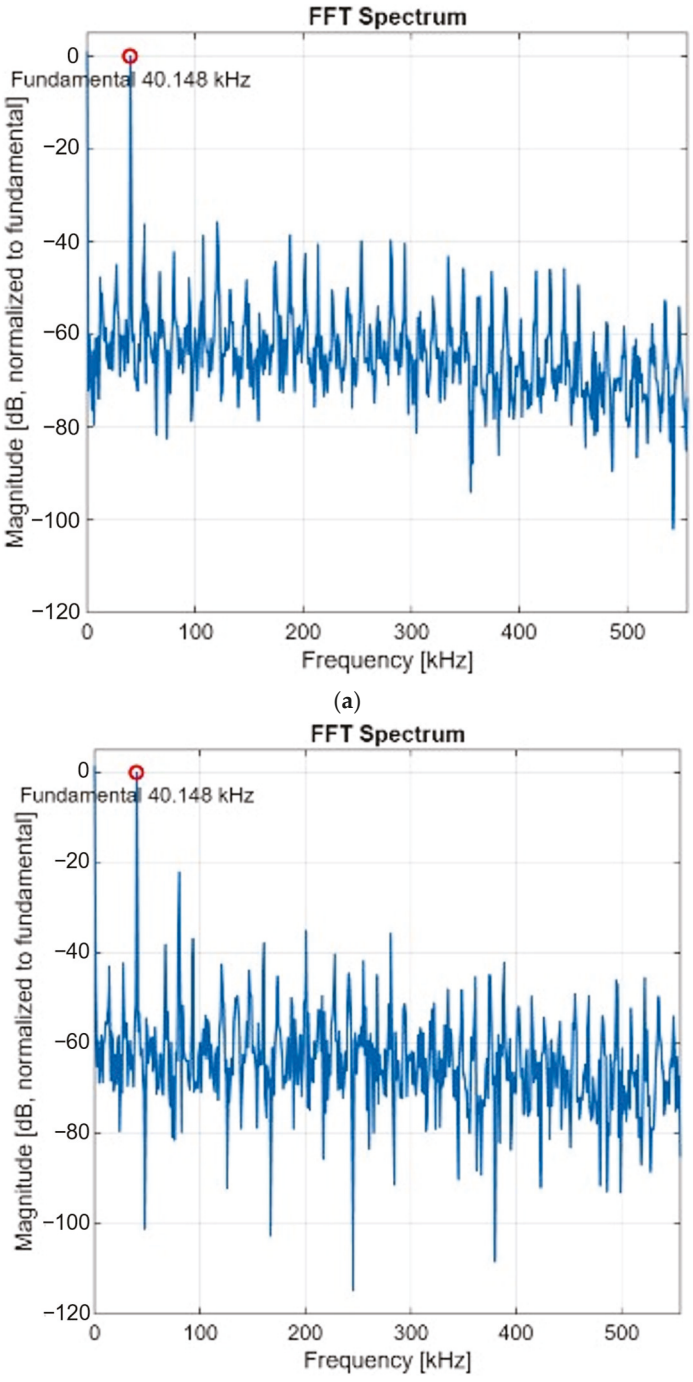


Figure 25. FFT spectra of (**a**) the standalone SAR ADC only, and (**b**) the complete TVC + SAR ADC system.

Table 1 summarizes the prior time-of-flight (ToF) sensing systems together with the proposed work. Since the prior arts target various LiDAR applications and adopt different architectures such as ADC- and TDC-based implementations, the comparison is primarily intended to provide system-level architectural overview rather than strict specification-to-specification benchmark comparison. Nonetheless, Table 1 highlights the differences in backend conversion strategy, implementation complexity, power consumption, and scalability relevant to LiDAR receiver designs.

https://doi.org/10.3390/mi17050622

Table 1. Performance comparison of the proposed TVC-SAR with the previously reported ToF systems.

Parameters	[18]	[19]	[20]	[21]	This Work
Architecture	AFE + TDC	TDC	TDC	ADC + TDC	TVC + SAR ADC
Target	Wide-DR	High precision	Multichannel	Long-range	Short-range
Time Conv.	Zero-crossing	Direct time	Sampling	VTC + TDC	TVC
Technology (nm)	350	350	180	65	180
Supply Voltage (V)	3.3	3.3	3.3	1.2/1.8	1.8
Resolution (ps)	~100	~10	~180	6.25	810
Power dissipation (mW)	155	~150	45 (per channel)	12.44	13.0
Core area (mm^2)	N/A	10 (Whole IC)	2.52	0.06	0.148
Complexity	Very high	High	High	High	Low
Digitization	TDC	TDC	SSA-TDC	ADC/TDC	SAR ADC

Ref. [18] employed pulse-shaping with zero-crossing detection to achieve a wide dynamic range (~1:50,000). However, the proposed work significantly reduces analog front-end complexity by eliminating the need for LC resonators and nonlinear feedback TIAs, while maintaining a scalable architecture.

Ref. [19] achieved high timing accuracy using a multi-channel TDC with additional time-domain parameters for walk error compensation. Meanwhile, the proposed architecture avoids complex TDC calibration and multi-parameter extraction, resulting in lower implementation complexity and improved energy efficiency.

Ref. [20] adopted a hybrid sampling-based readout (SSA-TDC) to capture waveform information, whereas the proposed design eliminates the need for high-speed sampling arrays and memory, thereby reducing hardware overhead and simplifying the signal processing chain.

Ref. [21] utilized a multiplexed ADC/TDC structure to improve integration efficiency. However, the proposed work further simplifies the architecture by directly converting time information into the voltage domain, avoiding duplicated conversion paths and synchronization issues.

Overall, the proposed TVC–SAR ADC-based LiDAR receiver achieves a more favorable tradeoff among circuit complexity, power consumption, and scalability by removing the need for high-speed TDCs and complex hybrid architectures, while still enabling efficient time-interval digitization.

4. Conclusions

We have proposed a low-power LiDAR receiver topology based on a time-to-voltage converter (TVC) followed by a 5-bit SAR ADC, implemented in a 180 nm CMOS process. By translating the time-intervals into the voltage domain, the proposed topology eliminates the need for a complex TDC-based architecture and enables a simpler and more energy-efficient back-end conversion. The proposed topology integrates on-chip APDs, a CTLA, a time-gating circuit, a ramp generator, a PDH, and a V_{CM}-based SAR ADC with a binary-weighted C-DAC and strong-arm comparator. In addition, dedicated digital logic and a reset generator were exploited to ensure the proper timing coordination and reliable operations. With its reduced architectural complexity, compact implementation, and low power consumption, the proposed TVC-SAR receiver topology provides an energy-efficient solution for time-interval detection and is well suited for low-power and area-constrained LiDAR sensor applications.

https://doi.org/10.3390/mi17050622

Author Contributions: Conceptualization, S.-M.P.; methodology, B.S. and S.-M.P.; software, B.S.; validation, B.S.; formal analysis, B.S. and S.-M.P.; investigation, S.-M.P.; writing—original draft preparation, B.S. and S.-M.P.; writing—review and editing, S.-M.P.; visualization, B.S.; supervision, S.-M.P.; project administration, S.-M.P.; funding acquisition, S.-M.P. All authors have read and agreed to the published version of the manuscript.

Funding: This work was supported by the IITP (Institute of Information & Communications Technology Planning & Evaluation)-ITRC (Information Technology Research Center) grant funded by the Korean government (Ministry of Science and ICT) (IITP-2026-RS-2020-II201847). This research was supported by Global—Learning & Academic research institution for Master's·PhD students, and Postdocs (G-LAMP) Program of the National Research Foundation of Korea (NRF) grant funded by the Ministry of Education (No. RS-2025-25442252).

Institutional Review Board Statement: Not applicable.

Informed Consent Statement: Not applicable.

Data Availability Statement: The data supporting this study's findings are available from the corresponding author upon reasonable request.

Acknowledgments: The EDA tool was supported by the IC Design Education Center (IDEC), Republic of Korea.

Conflicts of Interest: The authors declare no conflicts of interest.

References

1. Gargoum, S.; El-Basyouny, K. Automated Extraction of Road Features Using LiDAR Data: A Review of LiDAR Applications in Transportation. In *Proceedings of the 2017 4th International Conference on Transportation Information and Safety (ICTIS)*; IEEE: Banff, AB, Canada, 2017; pp. 563–574.
2. Cherif, B.; Ghazzai, H.; Alsharoa, A.; Besbes, H.; Massoud, Y. Aerial LiDAR-Based 3D Object Detection and Tracking for Traffic Monitoring. In *Proceedings of the 2023 IEEE International Symposium on Circuits and Systems (ISCAS)*; IEEE: Monterey, CA, USA, 2023.
3. Deems, J.S.; Painter, T.H.; Finnegan, D.C. LiDAR Measurement of Snow Depth: A Review. *J. Glaciol.* **2013**, *59*, 467–479. [CrossRef]
4. Paschou, P.; Marinou, E.; de Kloe, J.; Donovan, D.P.; Van Zadelhoff, G.J.; Voudouri, K.A.; Amiridis, V. Sensitivity Study Using ATLID Lidar Simulator and Upcoming Plans for the EarthCare Validation. In *Proceedings of the IGARSS 2024–2024 IEEE International Geoscience and Remote Sensing Symposium*; IEEE: Athens, Greece, 2024; pp. 1144–1146.
5. Azuma, K.; Akiyama, K.; Shinkuma, R.; Trovato, G.; Nihei, K.; Iwai, T. Estimation of Spatial Features in 3-D Sensor Network Using Multiple LiDARs for Indoor Monitoring. *IEEE Sens. J.* **2023**, *23*, 7850–7865. [CrossRef]
6. Masson, P.; Wallace, B.; Green, J.; Goubran, R. Comparison of Spatial Coverage of LiDAR Systems for In-Home Activity of Daily Living Applications. In *Proceedings of the 2023 IEEE Sensors Applications Symposium (SAS)*; IEEE: Ottawa, ON, Canada, 2023; pp. 1–6.
7. Zhang, T.; Sha, Y.; Zhang, K.; Guo, J.; Huang, R.; Qi, X.; Hu, W. Broadband Very Long Wavelength Infrared Focal Plane Array Based on Phosphorus-Doped Silicon Blocked Impurity Band. *Appl. Phys. Lett.* **2025**, *127*, 021102. [CrossRef]
8. Hu, J.; Liu, B.; Ma, R.; Liu, M.; Zhu, Z. A 32×32-Pixel Flash LiDAR Sensor with Noise Filtering for High-Background Noise Applications. *IEEE Trans. Circuits Syst. I Regul. Pap.* **2022**, *69*, 645–656. [CrossRef]
9. Manuzzato, E.; Tontini, A.; Seljak, A.; Perenzoni, M. A 64×64-Pixel Flash LiDAR SPAD Imager with Distributed Pixel-to-Pixel Correlation for Background Rejection, Tunable Automatic Pixel Sensitivity and First-Last Event Detection Strategies for Space Applications. In *Proceedings of the IEEE International Solid-State Circuits Conference (ISSCC) 2022*; IEEE: San Francisco, CA, USA, 2022; pp. 96–98.
10. Arvani, F.; Carusone, T.C. A Reconfigurable 5-Channel Ring-Oscillator-Based TDC for Direct Time-of-Flight 3D Imaging. *IEEE Trans. Circuits Syst. II Exp. Briefs* **2022**, *69*, 2408–2412. [CrossRef]
11. Tancock, S.; Arabul, E.; Dahnoun, N. A Review of New Time-to-Digital Conversion Techniques. *IEEE Trans. Instrum. Meas.* **2019**, *68*, 3406–3417. [CrossRef]
12. Ma, J.; Zhuo, S.; Qiu, L.; Gao, Y.; Wu, Y.; Zhong, M.; Chiang, P.Y. A Review of ToF-Based LiDAR. *J. Semicond.* **2024**, *45*, 101201. [CrossRef]
13. Choi, S.; Chon, Y.; Park, S.M. A Low-Power Optoelectronic Receiver IC for Short-Range LiDAR Sensors in 180 nm CMOS. *Micromachines* **2024**, *15*, 1066. [CrossRef] [PubMed]
14. Joo, J.E.; Lee, M.J.; Park, S.M. A CMOS Optoelectronic Receiver IC with an On-Chip Avalanche Photodiode for Home-Monitoring LiDAR Sensors. *Sensors* **2021**, *21*, 4364. [CrossRef]

https://doi.org/10.3390/mi17050622

15. Lee, M.J.; Choi, W.Y. Effects of Parasitic Resistance on the Performance of Silicon Avalanche Photodetectors in Standard CMOS Technology. *IEEE Electron Device Lett.* **2015**, *37*, 60–63. [CrossRef]
16. Park, S.; Lee, S.; Seo, B.; Choi, Y.; Song, Y.; Chon, Y.; Park, S.M. A CMOS Inverter-Based Active Feedback Transimpedance Amplifier. *Photonics* **2024**, *11*, 617. [CrossRef]
17. Park, S.; Lee, S.; Seo, B.; Jung, D.; Choi, S.; Park, S.M. A Low-Noise CMOS Transimpedance-Limiting Amplifier for Dynamic Range Extension. *Micromachines* **2025**, *16*, 153. [CrossRef] [PubMed]
18. Baharmast, A.; Kurtti, S.; Kostamovaara, J. A Wide Dynamic Range Laser Radar Receiver Based on Input Pulse-Shaping Techniques. *IEEE Trans. Circuits Syst. I Reg. Pap.* **2020**, *67*, 2566–2577. [CrossRef]
19. Kurtti, S.; Jansson, J.P.; Kostamovaara, J. A CMOS Receiver–TDC Chip Set for Accurate Pulsed TOF Laser Ranging. *IEEE Trans. Instrum. Meas.* **2020**, *69*, 2208–2217. [CrossRef]
20. Ye, M.; Zheng, X.; Li, Y.; Zhao, Y. A Low-Complexity Hybrid Readout Circuit for LiDAR Receiver. *IEEE Trans. Very Large Scale Integr. VLSI Syst.* **2020**, *28*, 828–832. [CrossRef]
21. Liu, M.; Liu, H.; Li, X.; Zhu, Z. A 60-m Range 6.16-mW Laser-Power Linear-Mode LiDAR System With Multiplex ADC/TDC in 65-nm CMOS. *IEEE Trans. Circuits Syst. I Reg. Pap.* **2020**, *67*, 753–764. [CrossRef]

Disclaimer/Publisher's Note: The statements, opinions and data contained in all publications are solely those of the individual author(s) and contributor(s) and not of MDPI and/or the editor(s). MDPI and/or the editor(s) disclaim responsibility for any injury to people or property resulting from any ideas, methods, instructions or products referred to in the content.

https://doi.org/10.3390/mi17050622

micromachines

MDPI

Article

Wafer-Level Transfer of GaN-on-Si Light-Emitting Devices via SiO_2–SiO_2 Direct Bonding: Strain Evolution and Optoelectronic Performance

Siyi Zhang, Shuhan Zhang, Qian Fan, Xianfeng Ni and Xing Gu *

Institute of Next Generation Semiconductor Materials, Southeast University, Suzhou 215123, China; 220234936@seu.edu.cn (S.Z.); shuhanzhang@seu.edu.cn (S.Z.); 103200035@seu.edu.cn (Q.F.); 103200036@seu.edu.cn (X.N.)
* Correspondence: xinggu@seu.edu.cn

Abstract

GaN-on-Si light-emitting devices have been widely studied in the field of opto-electronics, while their optical performance and characterization accessibility are severely limited by the strong visible light absorption of the native silicon substrate. Conventional substrate transfer technologies often suffer from inherent thermal, optical, or mechanical bottlenecks. In this study, we developed a robust wafer-level substrate transfer strategy for 8-inch green GaN-on-Si light-emitting device wafers, utilizing a hybrid planarization process combined with SiO_2–SiO_2 direct bonding. The hybrid planarization precisely eliminated the 900 nm macroscopic steps, achieving sub-nanometer surface roughness for high-yield wafer bonding. We systematically investigated the physical evolution during substrate removal. Results indicate that the removal of the thick native silicon and high-stress buffer layers effectively released the additional in-plane biaxial compressive stress within the multiple quantum wells (MQWs), thereby mitigating the quantum-confined Stark effect (QCSE). Benefiting from the elimination of the light-absorbing silicon substrate and the incorporation of a built-in back-surface reflector (BSR), the transferred devices achieved a remarkable 1.9-fold enhancement in relative optical performance, albeit with an inherent trade-off of increased reverse leakage current while preserving basic diode functionality. Furthermore, optothermal dynamic analysis at high injection levels suggests a potential localized thermal bottleneck at the thick SiO_2 bonding interface, where a hypothesized heat-induced spectral red shift may counteract the carrier-screening blue shift. This work provides a feasible wafer-level substrate transfer process for GaN-on-Si devices and offers systematic experimental insights into stress relaxation and optothermal behaviors during the substrate transfer process.

Keywords: GaN-on-Si; Micro-LEDs; SiO_2–SiO_2 direct bonding; substrate transfer

1. Introduction

Micro-light-emitting diodes (Micro-LEDs) have been widely investigated for advanced optoelectronic applications, owing to their outstanding advantages in brightness, contrast, response speed, and long-term stability under harsh environments [1–4]. For the fabrication of high-brightness blue and green light-emitting devices, the InGaN/GaN material system is the most mature and mainstream choice. Regarding the epitaxial growth substrate, compared to traditional sapphire substrates with inherent limitations in thermal conductivity and electrical insulation, silicon (Si) substrates have been widely recognized as a promising

platform for GaN-based optoelectronic devices. This is primarily attributed to their mature large-scale wafer manufacturing processes, low material cost, excellent thermal conductivity, and inherent compatibility with complementary metal-oxide-semiconductor (CMOS) manufacturing lines [5,6].

Despite the above advantages of GaN-on-Si technology, the narrow bandgap of silicon renders it a strong absorption medium for visible light. Consequently, a large portion of photons emitted downward from the active region is absorbed by the native silicon substrate, leading to a drastic reduction in light extraction efficiency (LEE) of the devices [7]. Furthermore, the opacity of the silicon substrate completely blocks the backside optical access, making it difficult to perform accurate optoelectronic characterization and failure analysis of the device arrays from the backside. Therefore, to address the above issues, substrate lift-off and transfer technologies are required, which refer to detaching the as-grown GaN epitaxial layers from the native silicon substrate and transferring them onto a target carrier substrate [8].

Among the various substrate transfer technologies explored to date, micro-transfer printing or adhesive bonding based on organic polymers has been widely adopted due to its broad process window and high tolerance for surface topography [9–11]. However, when used as the bonding medium, these organic polymer layers have inherently poor thermal conductivity, which will introduce a large thermal resistance at the bonding interface and lead to accelerated device degradation under high-current or high-frequency driving conditions. More critically, the significant refractive index mismatch between organic materials, high-index GaN, and the carrier substrate will trigger total internal reflection (TIR) at the interface, which further reduces the light extraction efficiency [12–14].

Recently, flip-chip bonding (FCB) has been widely studied for the assembly of Micro-LED arrays, which achieves electrical and mechanical interconnection between the device and the driver substrate via metallic micro-bumps (e.g., Indium and Tin) [15–17]. While FCB shows good feasibility for small-scale array assembly, it faces several inherent bottlenecks when applied to large-area wafer-level transfer. First, the transfer yield of flip-chip processes is difficult to meet the requirements of high-pixel-density device arrays. Second, the large mismatch in the coefficient of thermal expansion (CTE) between silicon and GaN will easily cause micro-bump cracking and interfacial failure during the high-temperature bonding process [18,19]. Most crucially, in conventional flip-chip architectures, the silicon substrate is often retained, which means the aforementioned issues of light absorption and characterization obstruction remain unresolved.

In contrast, SiO_2–SiO_2 wafer-level direct bonding presents distinct advantages. By eliminating the need for any intermediate adhesive layers, this technology not only ensures superior mechanical reliability but also mitigates optical discontinuities and air gaps at the interface. This establishes a continuous and optimized optical medium channel for the efficient extraction of photons at the micro and nanoscales [20–22]. However, SiO_2–SiO_2 direct bonding imposes stringent requirements on surface morphology, where achieving void-free bonding across an entire wafer is predicated on maintaining a sub-nanometer surface roughness [23,24].

Direct wafer bonding has been explored in GaN-based materials and device platforms. Ryu et al. demonstrated the transfer of AlGaN/GaN epilayers grown on Si(111) onto Si(100) wafers by direct wafer bonding, followed by selective dry etching to fabricate thin-body N-face GaN-on-insulator wafers for HEMT applications [25]. Dragoi et al. reported GaN-engineered substrates based on SiO_2-assisted plasma-activated bonding and oxide-free covalent bonding, highlighting the flexibility of wafer bonding for integrating GaN with different target substrates [26]. In addition, the electrical characteristics of SiO_2/GaN interfaces have been shown to be strongly affected by Ga–OH-related interfacial states,

https://doi.org/10.3390/mi17050607

emphasizing the importance of interface chemistry in GaN/oxide systems [27]. However, these studies mainly focused on transistor-oriented N-face GaN transfer, engineered GaN substrates, or electrically active SiO_2/GaN interfaces. Wafer-level transfer of fully processed GaN-on-Si light-emitting devices, especially after the formation of mesa structures and thick metal electrodes, remains less explored.

Different from the transfer of bare epitaxial layers or transistor-oriented GaN structures, the wafers used in this work had already undergone front-side LED fabrication. The mesa etching and Ni/Al/Ti p-metal deposition introduced macroscopic steps of approximately 900 nm. To overcome the severe geometric undulations introduced by the front-end fabrication process, this study developed a hybrid planarization strategy and successfully achieved wafer-level bonding and substrate transfer of 8-inch GaN-on-Si green light-emitting device wafers. To systematically explore the fundamental physical evolution during the transfer process, devices with a mesa diameter of 200 μm were adopted as representative test vehicles in this study. Although their size exceeds the definition of conventional Micro-LEDs, they were fabricated with the full front-end process flow of Micro-LEDs, and provide a robust and representative platform to clearly analyze the complex stress, electrical, and optothermal dynamic behaviors during the bonding and transfer process without the interference of size effects.

This work conducted multidimensional analyses on the evolution of the mechanical, optical, and electrical properties of the devices before and after transfer. The study first revealed the stress evolution law during the substrate thinning process, confirming that the removal of the massive bulk silicon and high-stress buffer layer caused severe fluctuations in macroscopic wafer warpage while realizing the steady relaxation of the additional in-plane compressive stress in the active region, which effectively mitigates the quantum-confined Stark effect (QCSE). The impact of substrate removal and thermal annealing on the electrical characteristics of the devices was also evaluated, confirming that the core p-n junction rectification characteristics remained robust despite an inevitable increase in process-induced leakage current. More importantly, the luminescence test results verified the significant optical benefits brought by substrate transfer: by eliminating the strongly light-absorbing native silicon substrate and introducing a built-in metal Back-Surface Reflector (BSR), a 1.9-fold increase in luminous intensity was achieved at low injection currents. These detailed optoelectromechanical analyses provide solid process verification and experimental reference for the substrate transfer of GaN-on-Si optoelectronic devices.

2. Materials and Methods

The 8-inch green GaN-on-Si (111) epitaxial wafers used in this study were grown via metal–organic chemical vapor deposition (MOCVD) by Suzhou Hanhua Semiconductors Ltd. (Suzhou, China). As illustrated in Figure 1, the epitaxial structure primarily consists of the following: an AlN/AlGaN strain-control buffer layer to mitigate the mismatch in lattice constants and thermal expansion coefficients, a high-crystalline-quality unintentionally doped GaN (u-GaN) layer, a Si-doped n-GaN contact layer (approximately 1 μm thick), an InGaN/GaN-based strain-release underlayer, an InGaN/GaN multiple quantum well (MQW) active light-emitting region with a peak emission wavelength centered around 520 nm, and a Mg-doped p-GaN hole injection layer.

Figure 2 illustrates the overall fabrication process flow. To verify the wafer-level, ultra-high-yield bonding and non-destructive substrate lift-off, front-side fabrication processes for Micro-LEDs were performed on the epitaxial wafers. As shown in Figure 2a, a 100 nm thick indium tin oxide (ITO) layer was first deposited onto the p-GaN surface, followed by rapid thermal annealing (RTA) at 600 °C for 5 min to form a high-quality ohmic contact. Subsequently, as depicted in Figure 2b, circular mesa structures with a diameter of

https://doi.org/10.3390/mi17050607

200 μm were defined via photolithography and a Cl_2-based inductively coupled plasma (ICP) etching process. Following this, a Ni/Al/Ti composite multilayer metal stack with thicknesses of 100 nm/400 nm/20 nm was sequentially deposited onto the ITO surface of the mesas via electron beam evaporation, as shown in Figure 2c. This metal layer serves not only as the p-contact interconnection electrode but also acts as a BSR in the final transferred device architecture. The real morphology corresponding to the processing stage shown in Figure 2c is provided in Figure A1a,b. Figure A1a shows the optical microscope image of the fabricated circular LED mesa structure after Ni/Al/Ti p-metal deposition, and Figure A1b presents a representative optical photograph of the 8-inch wafer.

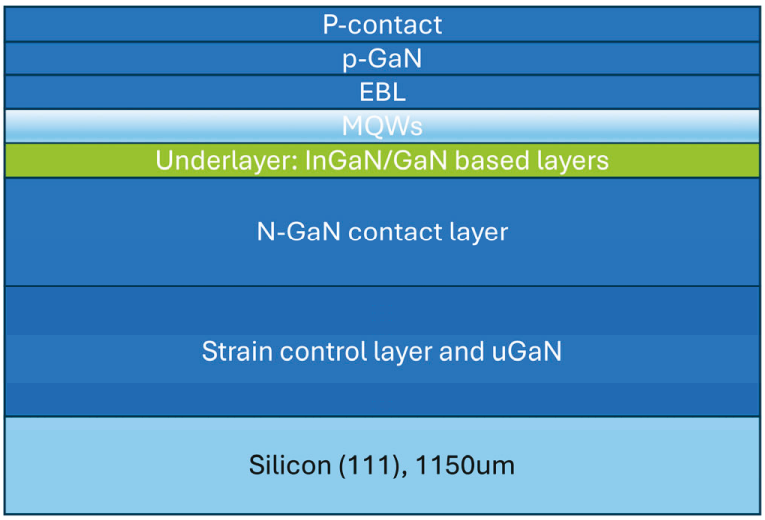


Figure 1. Schematic diagram of the epitaxial structure for green Micro-LEDs.

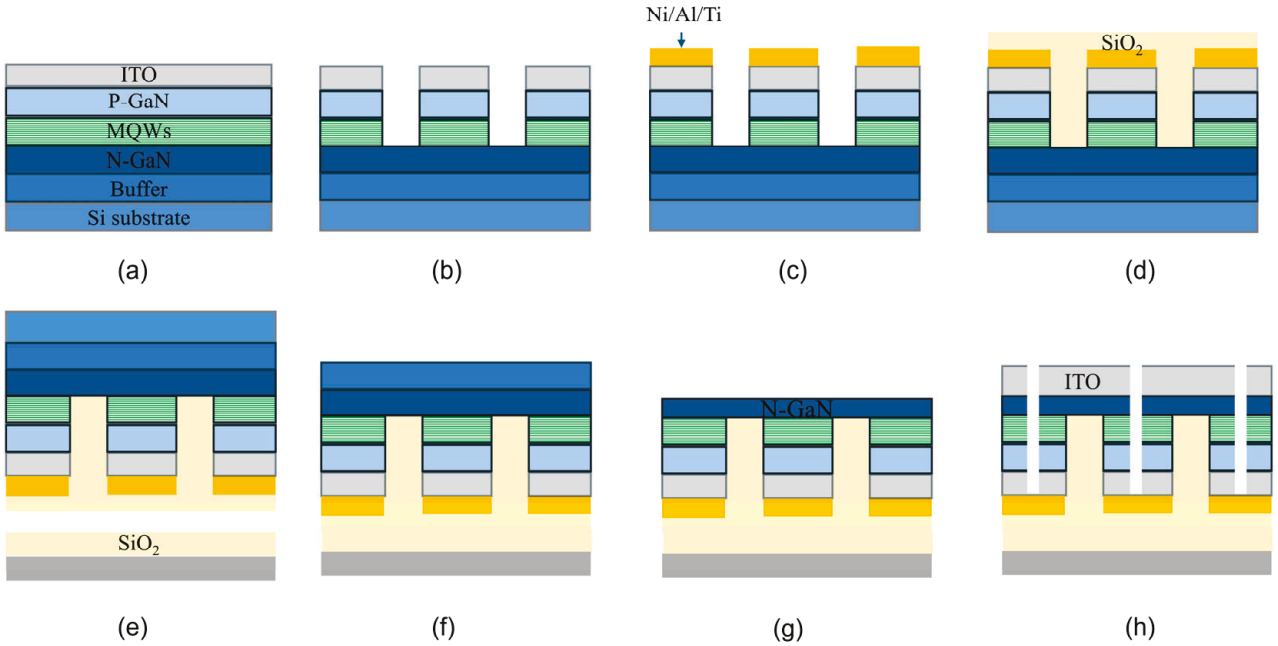


Figure 2. Schematic of the fabrication process: (**a**) deposition and thermal annealing of the 100 nm-thick ITO transparent conductive layer; (**b**) mesa etching to define the light-emitting area; (**c**) deposition of the p-metal (Ni/Al/Ti) on the mesa; (**d**) deposition of a 1.5 μm SiO_2 layer covering the entire structure, followed by planarization via CMP; (**e**) wafer-level direct bonding to a silicon carrier wafer with a 300 nm SiO_2 layer; (**f**) complete removal of the native silicon substrate; (**g**) thinning of the N-face nitride materials to remove the buffer layers and expose the n-GaN; (**h**) deposition of N-face ITO and fabrication of through-vias.

https://doi.org/10.3390/mi17050607

The aforementioned etching and the introduction of the thick multilayer metal electrodes resulted in macroscopic steps of up to 900 nm. To eliminate these steps and prepare a high-quality interface for bonding, a hybrid planarization strategy combining selective etching and multiple rounds of chemical–mechanical polishing (CMP) was employed in this study. As shown in Figure 2d, an approximately 1.5 μm thick SiO_2 layer was deposited over the entire device wafer surface using plasma-enhanced chemical vapor deposition (PECVD). Due to the high conformality of the PECVD process, the underlying 900 nm macroscopic steps were faithfully replicated on the oxide surface, resulting in significant topographic undulations. Subsequently, precise overlay lithography and dry etching were utilized to selectively remove these protruding oxide features. Finally, the wafer surface underwent multiple CMP treatments to achieve a sub-nanometer smooth surface (Ra < 0.21 nm) suitable for direct bonding.

Following planarization, the wafers were ready for bonding. An 8-inch silicon wafer with a 300 nm oxide layer grown on its surface was selected as the receptor carrier wafer. Both the planarized Micro-LED wafer and the silicon carrier wafer were subjected to an optimized N_2/O_2 mixed plasma activation treatment at room temperature to achieve a highly hydroxylated surface. Subsequently, a high-precision alignment system was used to accurately align and pre-bond the two wafers in a vacuum environment, as illustrated in Figure 2e. The pre-bonded wafer pair was then placed in a vacuum annealing furnace and annealed at a constant temperature of 300 °C for 3 h to form a dense SiO_2–SiO_2 covalent bond network.

After bonding, a combined thinning process was performed on the native thick silicon substrate. First, back-grinding was used to rapidly and completely remove most of the bulk native silicon, as shown in Figure 2f. Subsequently, highly selective deep ICP etching was utilized to completely clear the residual silicon and the underlying high-stress buffer layers, achieving precise thinning of the n-GaN face and completing the non-destructive, wafer-level transfer of the epitaxial layers, as illustrated in Figure 2g. After removing the native substrate, exposing the N-face, and completing the thinning process, a 200 nm thick ITO transparent conductive layer was grown on the n-GaN surface, as shown in Figure 2h. To facilitate optoelectronic characterization, probe-access vias with a diameter of 80 μm were defined using photolithography and ICP etching, providing localized access to the buried p-metal electrodes. The optical morphology of the fabricated mesa and the detailed cross-sectional schematic of the probing configuration are provided in Figure A1c,d of Appendix A. During the electroluminescence (EL) measurements, a microprobe station (with a typical probe tip diameter of 10–20 μm) was employed to establish the electrical interconnection: one probe was precisely positioned through the via to contact the underlying p-electrode, while the complementary probe was biased against the n-face ITO transparent conductive layer, thereby completing a robust vertical current injection path. The current density and integrated optical intensity were normalized to the active LED mesa area, which excluded the vias.

3. Results and Discussion

3.1. Hybrid Planarization and Wafer-Level Transfer

Achieving high-precision, high-yield wafer-level direct bonding is critically dependent on achieving sub-nanometer surface roughness and the complete elimination of macroscopic topographic fluctuations. As previously described, the mesa etching and the deposition of thick multilayer p-metal electrodes inevitably introduced a severe macroscopic step height of approximately 900 nm on the wafer surface. To overcome this significant geometric obstacle, a hybrid planarization strategy was systematically developed, and its evolution was closely monitored in this study.

https://doi.org/10.3390/mi17050607

Figure 3a displays the surface profile evolution recorded by a step profiler at key stages of the planarization process. In the initial state, a distinct step height of 900 nm is observed above the Micro-LED mesa. The subsequently deposited 1.5 µm-thick SiO_2 layer via PECVD exhibited highly conformal growth characteristics, almost entirely preserving the macroscopic height difference (with a variation of less than 20 nm). Consequently, direct chemical–mechanical polishing (CMP) at this stage would inevitably trigger severe pattern density effects and localized dishing. To circumvent this issue, this study employed a strategy involving overlay lithography combined with selective dry etching to precisely reduce the protruding oxide features. As shown by the second profile in Figure 3a, this dry etching step significantly reduced the steep macroscopic step height.

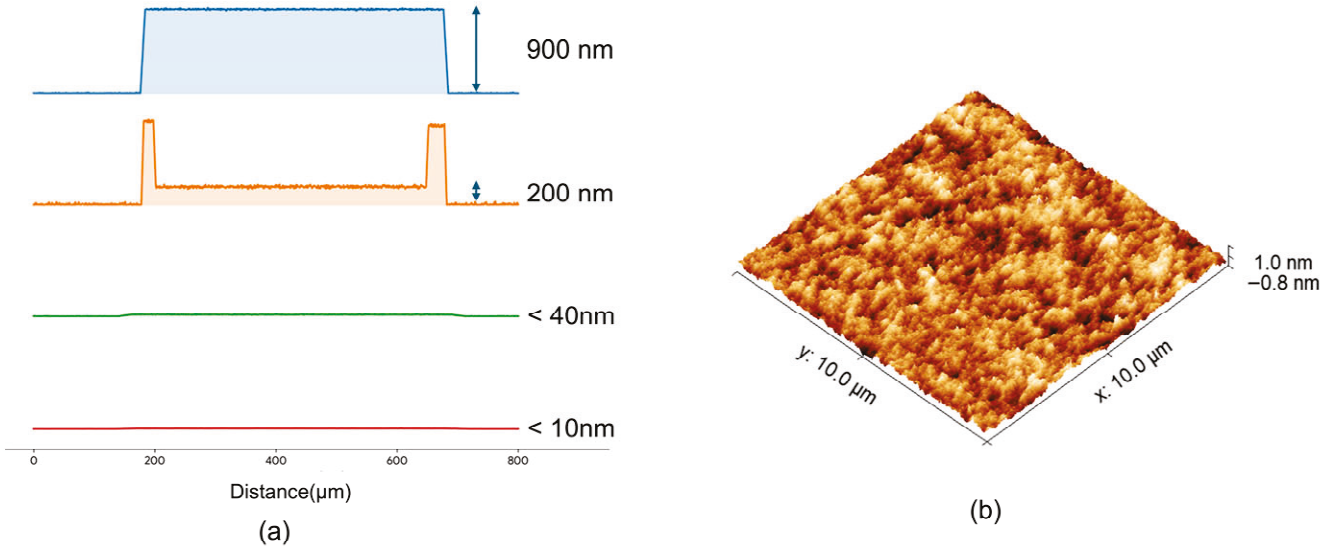


Figure 3. Surface morphology characterization of the planarization process: (**a**) the evolution of surface morphology at different stages of the hybrid planarization; (**b**) 3D AFM image of the final SiO_2 bonding surface after the second CMP treatment, indicating sub-nanometer roughness.

The pre-planarized surface then underwent the first round of CMP, followed by the conformal deposition of an additional 300 nm SiO_2 layer to repair any potential residual micro-scratches and provide a fresh, pristine oxide layer for final polishing. The third and fourth profiles in Figure 3a vividly illustrate the progressive elimination of the step height. After the second CMP treatment, a flat macroscopic surface was finally obtained, with the global height variation reduced to a negligible range of 10–20 nm.

Beyond macroscopic flatness, the microscopic surface roughness directly determines the density of the interfacial covalent bonds. Figure 3b displays the three-dimensional (3D) atomic force microscopy (AFM) morphology of the SiO_2 surface after the second CMP process, acquired over a scanning area of 10 µm × 10 µm with a resolution of 256 × 256 pixels. The 3D topography clearly reveals a uniformly dense surface feature without any visible macro-protrusions, residual particles, or scratches, demonstrating the effectiveness of the hybrid planarization process. The measured root-mean-square roughness (Sq) is 0.200 nm, while the average roughness (Sa) is 0.158 nm, and the maximum peak-to-valley height (Sz) is strictly limited to within 2.791 nm. These sub-nanometer roughness metrics perfectly meet the stringent requirements for spontaneous covalent SiO_2–SiO_2 bonding under room-temperature activation, fundamentally ensuring the high yield of the subsequent wafer-level bonding and transfer.

After the formation of the covalent SiO_2–SiO_2 interface, the bonded wafer pair underwent extremely rigorous mechanical grinding and reactive ion etching to completely remove the approximately 1 mm thick native bulk silicon substrate. This etching process

https://doi.org/10.3390/mi17050607

was precisely stopped at the AlN/AlGaN buffer layer. Such a harsh thinning process typically introduces enormous shear stress; if the bonding interface were weak, it would immediately trigger massive film delamination or catastrophic fracture. A full-wafer scanning acoustic microscopy (SAM) image of the bonded wafer pair is shown in Figure 4a, and a normal photograph of the wafer after bonding, removal of the native silicon substrate, and n-GaN thinning is provided in Figure 4b. Part of the wafer had been diced for subsequent experiments, so the remaining portion of the actual post-transfer wafer is shown. While the optical photograph provides an intuitive view of the wafer appearance after bonding and substrate removal, the SAM image provides clearer and more quantitative visualization of the bonding quality. Analysis of the SAM image using ImageJ (version 1.54g) identified 11 visible voids and showed that the void-affected area fraction is approximately 4.301%. In addition, the fraction of LED-patterned regions not overlapped by any voids was found to exceed 95%, indicating that the majority of the LED regions on the wafer were structurally preserved after bonding. Additionally, optical and electrical characterization was performed on devices selected from regions without visible bonding defects.

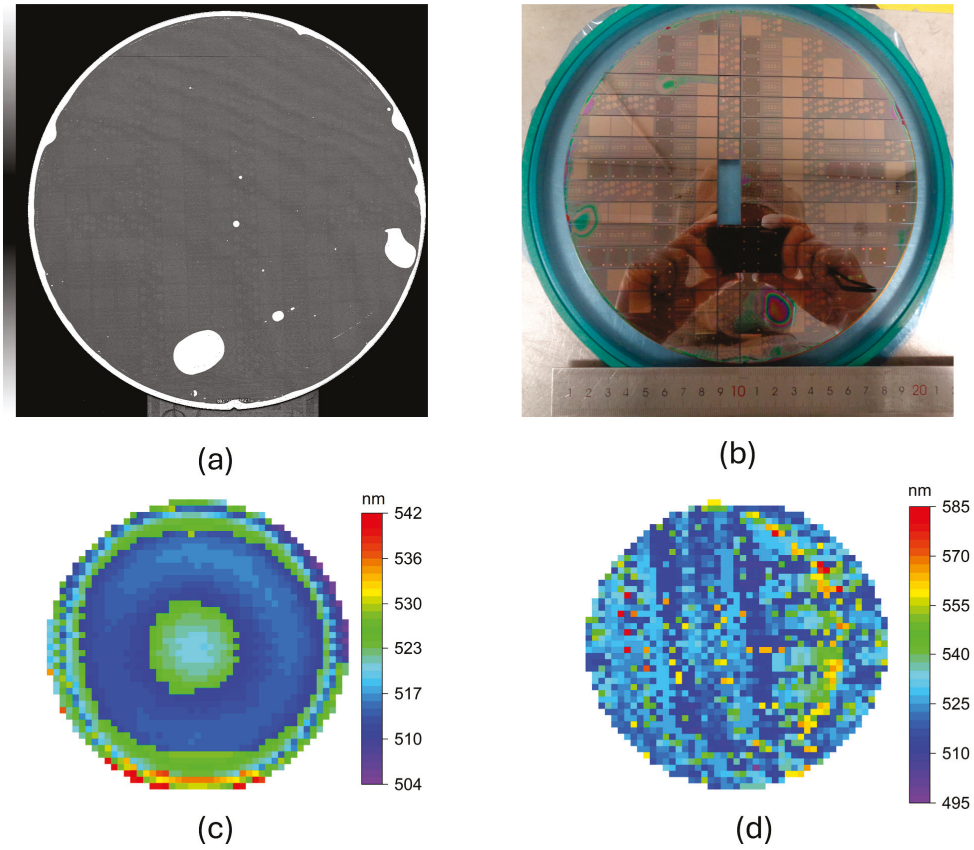


Figure 4. Evidence of the transfer yield at the macroscopic scale: (**a**) Post-bond full-wafer SAM image. (**b**) Normal optical photograph of the wafer after bonding, removal of the native silicon substrate, and n-GaN thinning. Part of the wafer was diced for subsequent experiments, and the remaining portion is shown. (**c**) The PL map of the initial GaN-on-Si epitaxial wafer before deice fabrication. (**d**) The PL map of the post-transfer wafer after SiO_2–SiO_2 direct bonding and complete removal of the native bulk silicon substrate.

Figure 4c and Figure 4d present the full-wafer PL peak wavelength mappings before and after substrate transfer, respectively. Figure 4c displays the typical concentric circular emission pattern of the initial GaN-on-Si epitaxial wafer, while Figure 4d shows that after complete removal of the native silicon substrate, the 8-inch ultrathin epitaxial film maintained a high degree of overall integrity on the carrier wafer. Combining the SAM

https://doi.org/10.3390/mi17050607

images and pl map, it can be concluded that although a small number of macroscopic bubbles or voids can be observed at the edges or in localized areas (which may originate from trace particle contamination or gas trapping during the room-temperature bonding process), they did not propagate to cause catastrophic large-area film peeling, nor did they significantly affect the core active light-emitting region. That macroscopic optical integrity conclusively proves that the sub-nanometer smooth surface achieved through hybrid planarization was successfully transformed into an extremely robust covalent bonding network, capable of withstanding the extreme mechanical stress challenges of the subsequent processes. Furthermore, a careful comparison of the two peak wavelength mappings reveals a global blue shift in the overall emission wavelength after the removal of the silicon substrate. This physical phenomenon will be analyzed in detail in the next section.

3.2. Strain Relaxation and Optical Evolution Analysis

The mechanical removal of the massive native silicon substrate and the severely lattice-mismatched buffer layer inevitably triggers a drastic redistribution of internal stress within the GaN epitaxial layer. High-resolution X-ray diffraction (HRXRD) would provide a direct measurement of lattice strain. However, the strain evolution in this study had to be monitored while maintaining the bonded sample as an intact 8-inch wafer during the sequential substrate-removal process. The available XRD system could not directly accommodate the full-size 8-inch bonded wafer. Although cleaving the wafer into small pieces would enable conventional XRD measurements, such a destructive process would partially release the wafer-scale mechanical constraint, introduce edge-related stress relaxation, and prevent continuous characterization on the same wafer during the subsequent thinning steps. Therefore, instead of XRD, we employed a non-destructive characterization strategy combining PL spectroscopy of the MQWs with wafer-scale warpage measurements using a non-contact thickness gauge. In this context, the PL peak shift and FWHM evolution are used as optical indicators of relative strain relaxation in the active region, while the warpage data reflect the macroscopic mechanical response of the bonded wafer stack. It should be specifically noted that due to localized stress modulation and slight process deviations introduced during the wafer bonding process, the global PL emission often exhibits a certain degree of spatial non-uniformity. Therefore, to strictly eliminate the interference of spatial variations and accurately track the intrinsic strain evolution, a fixed representative micro-area near the center of the wafer was selected for continuous in situ PL monitoring after each sequential thinning step in this study. Representative stacked PL spectra recorded during the progressive back-thinning process are shown in Figure 5.

The extracted PL peak wavelength, FWHM, and wafer warpage are summarized in Figure 6a,b. Interestingly, although the microscopic active region exhibited an extremely steady and monotonic strain relaxation, the macroscopic warpage fluctuated violently due to structural asymmetry. Specifically, as shown in Figure 6b, the warpage exhibited a dramatic peak at the remaining thickness of 2.8 μm. Based on the epitaxial design, it is hypothesized that the removal of the highly strained AlN/AlGaN buffer layer at this stage temporarily disrupts the stress balance, potentially causing the observed peak before further strain relaxation. Meanwhile, as shown in Figure 6a, the PL peak wavelength continuously blue-shifted from approximately 514 nm to 511 nm, accompanied by a noticeable narrowing of the full width at half maximum (FWHM). This microscopic evolution is consistent with the progressive release of the additional in-plane biaxial compressive stress within the InGaN/GaN MQWs during the removal of the underlying constraint layers. This strain relaxation is expected to weaken the piezoelectric polarization field, thereby mitigating the quantum-confined Stark effect (QCSE). The previously tilted energy bands consequently

https://doi.org/10.3390/mi17050607

recovered to a flatter state, resulting in an increased effective bandgap (wavelength blue shift). Meanwhile, the FWHM narrowing is primarily driven by the homogenization of local strain gradients and the reduced sensitivity of quantized energy levels to interfacial thickness fluctuations within the flattened band structure, which collectively suppresses the inhomogeneous broadening of the emission spectrum.

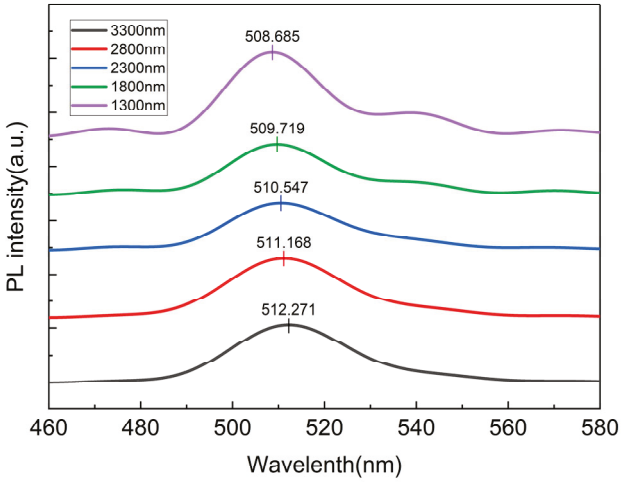


Figure 5. Stacked photoluminescence (PL) spectra of the InGaN/GaN MQWs at different remaining epitaxial thicknesses during the progressive back-thinning process.

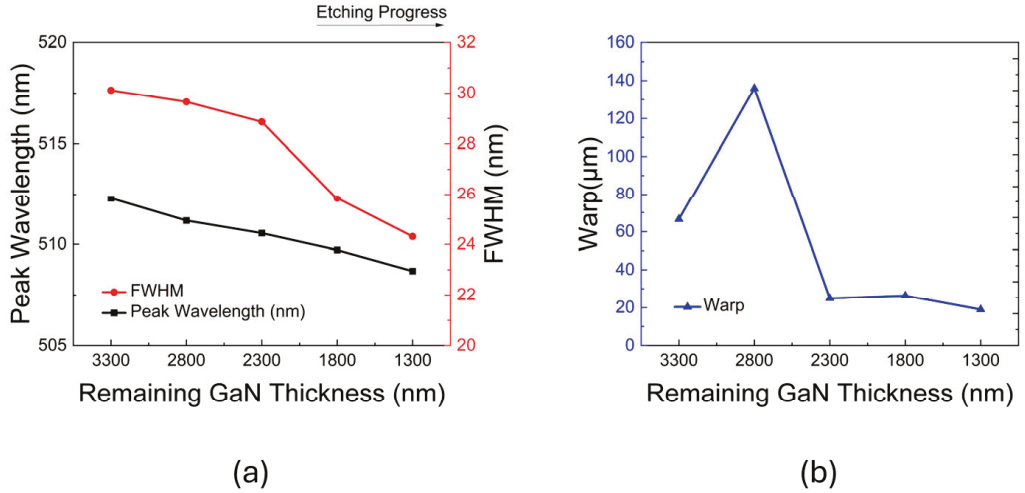


Figure 6. Decoupling of macroscopic structural deformation and microscopic localized strain: (**a**) Evolution of the PL peak wavelength and full width at half maximum (FWHM) as a function of the remaining GaN thickness. (**b**) Corresponding macroscopic wafer warpage measured by a non-contact thickness gauge.

3.3. Electrical Performance Analysis

To evaluate the electrical integrity of the Micro-LEDs after undergoing extreme physical and thermal processes, such as wafer bonding and substrate lift-off, the current-voltage characteristics before and after transfer were compared. As shown in Figure 7 (plotted on both linear and semi-logarithmic axes), although the electrical framework exhibited a certain degree of process-induced degradation, the core rectification characteristics of the p-n junction were successfully preserved. Specifically, in the reverse bias region, the transferred device exhibited a leakage current of approximately 3.1×10^{-4} A at 5 V, which is an increase of about three orders of magnitude compared to the pre-transfer baseline of 1.48×10^{-7} A. This increased leakage can be primarily attributed to two factors: first, the ICP etching performed to fabricate probe access via inevitably introduced plasma

https://doi.org/10.3390/mi17050607

damage and dense surface states on the sidewalls, which act as non-radiative Shockley–Read–Hall (SRH) leakage channels; second, the profound strain relaxation (as evidenced in Section 3.2), combined with thermal annealing at 300 °C, may have activated latent threading dislocations as conductive leakage paths.

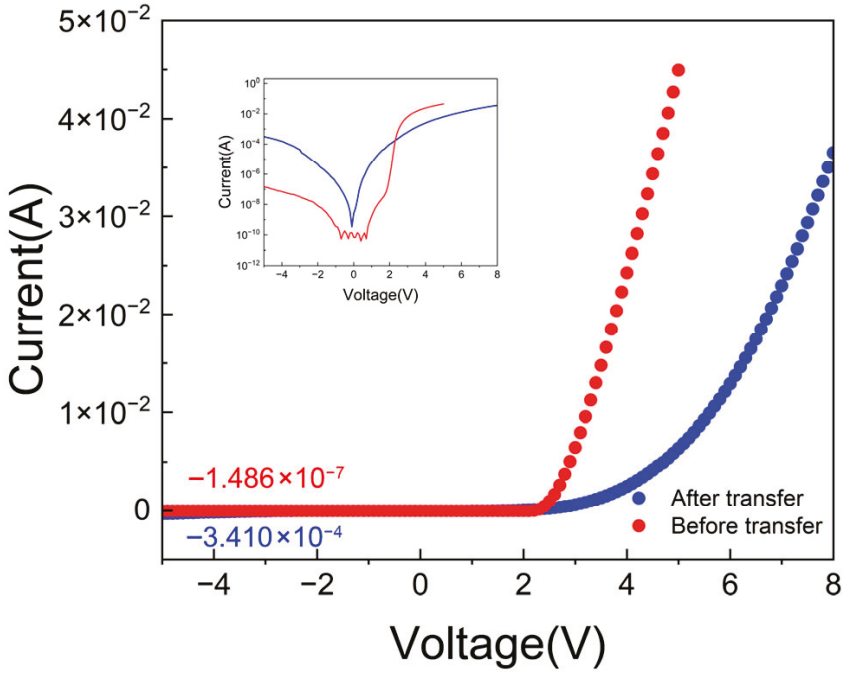


Figure 7. Current–voltage (I–V) characteristics of the Micro-LEDs before (red) and after (blue) the wafer-level transfer.

Furthermore, in the forward bias region, the turn-on voltage increased from approximately 2.5 V to 3.3 V, accompanied by a decrease in the slope of the I–V curve. This indicates a significant increase in the series resistance of the device, likely related to the slight degradation of the fragile p-GaN/ITO ohmic contact interface due to the thermal budget during the bonding process. To further evaluate device variation, turn-on voltage and reverse leakage current at −5 V were extracted from five devices before transfer and five devices after transfer, as summarized in Table A1. The statistical results show the same general trend as the representative I–V curves in Figure 7: the transferred devices remain functional but exhibit higher turn-on voltage and increased reverse leakage compared with the pre-transfer devices. Overall, the current transfer process successfully preserves the normal diode operation of the devices, allowing further optical-intensity measurements to be performed and thereby enabling evaluation of the effect of substrate transfer. However, for practical Micro-LED applications, this level of increased leakage current (by more than three orders of magnitude) and elevated turn-on voltage requires further optimization. The following electroluminescence analysis is therefore conducted to assess whether the transferred device architecture can still provide optical-performance enhancement despite the observed electrical degradation. Meanwhile, for future practical Micro-LED devices, the balance between optical enhancement and electrical degradation should also be carefully considered.

3.4. Optical Enhancement and Thermal Limitations

To verify the core objective of this wafer-level substrate transfer—namely, improving optical performance by replacing the strongly absorbing silicon substrate—a comprehensive analysis of the electroluminescence (EL) performance was conducted. Figure 8a compares the EL spectra at a low injection current density of 5 A/cm^2. To ensure a rigorous and fair

https://doi.org/10.3390/mi17050607

optical comparison, the baseline spectrum before transfer was mathematically smoothed and fitted to remove the strong Fabry–Pérot (FP) interference fringes originally formed by the GaN/air and GaN/Si interfaces, thereby accurately extracting its intrinsic spontaneous emission envelope.

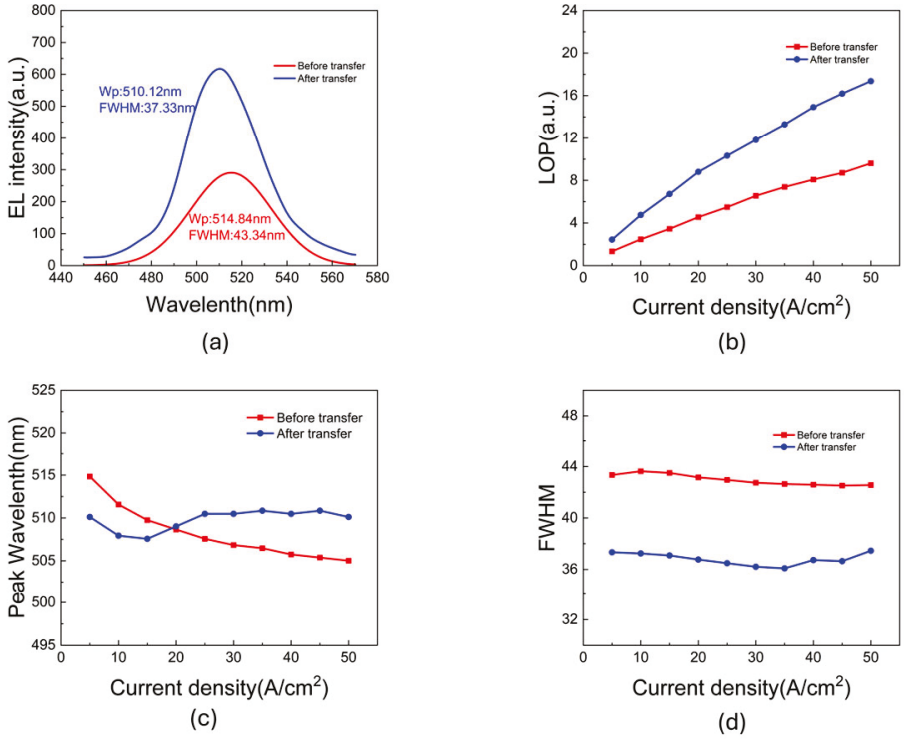


Figure 8. Optoelectronic luminescence characteristics before (red) and after (blue) the transfer: (**a**) EL spectra at a low injection current density of 5 A/cm^2. (**b**) Integrated EL intensity as a function of injection current density (L-J curves), (**c**) peak wavelength, and (**d**) FWHM evolution versus current density.

As shown in Figure 8a, the integrated EL intensity of the transferred device exhibited a remarkable 1.9-fold increase (nearly 100% enhancement) compared to the silicon-based reference device. The approximately 1.9-fold increase in EL intensity indicates improved light extraction in the transferred device architecture. Before transfer, photons emitted toward the substrate side could be absorbed by the native Si substrate. After substrate transfer and Si removal, the Ni/Al/Ti p-metal becomes the backside optical boundary beneath the light-emitting region, where it can partially redirect downward-propagating photons toward the emitting side. Therefore, the observed EL enhancement is attributed to the combined optical effect of removing the absorbing Si substrate and enabling a reflective backside boundary through the transfer process. These two changes occur simultaneously in the present device structure. The reflection efficiency may depend on the specific backside metal stack, and further optimization using different reflector materials will be considered in future work.

Remarkably, as revealed by the macroscopic integrated intensity versus current density curves in Figure 8b, this significant optical dividend is strongly maintained even at higher injection levels. Throughout the tested current range, the emission intensity maintained a growth trend without exhibiting significant efficiency droop. This continuous enhancement proves that within the current operating range, the optical gain provided by substrate transfer dominates the device performance. However, it is essential to objectively evaluate this optical success against the electrical degradation discussed in Section 3.3. While the 1.9-fold optical output enhancement successfully validates the transfer strategy for the

https://doi.org/10.3390/mi17050607

current test devices, the accompanying increase in reverse leakage current is a significant process-induced defect. When facing future applications of true Micro-LEDs, such a severe leakage current cannot be ignored, as it would severely compromise overall efficiency and reliability. This inherent trade-off explicitly indicates that although the optical architecture is successfully verified, the current process conditions must be rigorously optimized in future work. Despite the strong growth in macroscopic EL intensity, the evolution of the microscopic spectra—particularly the FWHM and peak wavelength—serves as an extremely sensitive probe revealing the underlying optothermal dynamics. As shown in Figure 8d, the FWHM of the transferred device remained narrower than the pre-transfer baseline across all injection currents. This phenomenon corroborates the PL results in Section 3.2, confirming that substrate lift-off and N-face thinning released the additional stress, thereby weakening the QCSE. The resulting band-flattening is directly manifested as a narrowing of the emission linewidth and an improvement in color purity.

However, the evolution of the peak wavelength (Figure 8c) reveals the competition between carrier dynamics and heat accumulation at high injection levels. At low current densities, the transferred device exhibited a shorter wavelength (blue shift) compared to the state before transfer, again consistent with the initial strain relaxation. But as the injection current increased, the pre-transfer device exhibited a typical and continuous blue shift due to the excellent heat dissipation of the bulk silicon. In comparison, the blue shift trend of the transferred device becomes less pronounced at high current densities, with the emission wavelength remaining near 510 nm. This behavior may be understood as the result of competing mechanisms under high-current injection. On one hand, increased carrier injection can weaken the QSCE in the InGaN/GaN quantum wells, leading to a blue shift of the EL peak. On the other hand, self-heating may become more pronounced in the transferred device structure, possibly due to the additional thermal resistance introduced by the bonding and interfacial layers. According to the temperature dependence of the semiconductor bandgap described by Varshni's empirical relation, an increase in junction temperature would reduce the effective bandgap and induce a red shift in the emission peak. Such a thermally induced red shift could partially compensate for the injection-induced blue shift, resulting in the observed stalled blue shift in the peak position at higher current densities. Since temperature-dependent EL measurements, thermal simulations, and direct junction-temperature extraction were not performed in this study, this interpretation should be regarded as a plausible explanation rather than a quantitative confirmation. This observation suggests that thermal management of the bonding and interfacial layers should be considered in future high-current Micro-LED designs.

4. Conclusions

In summary, by employing a customized hybrid planarization strategy combining selective dry etching and iterative chemical–mechanical polishing (CMP), this study successfully achieved the wafer-level substrate transfer of 8-inch GaN-on-Si green light-emitting devices via SiO_2–SiO_2 direct bonding. The combined PL and wafer-warpage results suggest that the sequential removal of the massive native silicon substrate and high-stress buffer layers induces strong macroscopic wafer-shape evolution while gradually relaxing the additional compressive strain in the MQW active region. This strain relaxation increases the intrinsic bandgap of the well layer via the deformation potential effect and effectively weakens the piezoelectric polarization field in the active region to significantly mitigate the QCSE, resulting in a continuous blue shift in the emission peak and a narrowing of the spectral linewidth.

Regarding the optoelectronic performance evolution, the extreme substrate transfer and thermal annealing processes inevitably led to an increase in reverse leakage current

https://doi.org/10.3390/mi17050607

and series resistance of the devices, while the core rectifying architecture of the p-n junction maintained robust integrity. More importantly, by eliminating the strongly light-absorbing native silicon substrate and incorporating a BSR, the transferred devices achieved a remarkable 1.9-fold enhancement in relative optical performance, showing a significant optical advantage over the original GaN-on-Si devices. However, as an inherent trade-off, the significant increase in leakage current indicates that the current transfer and processing conditions require further rigorous optimization to meet the stringent electrical demands of future micro-scale applications.

Furthermore, an analysis of the spectral evolution at high injection levels showed a stalled blue shift trend in the transferred devices. It is hypothesized that this behavior may arise from a competition between the injection-induced blue shift and potential localized self-heating caused by the additional thermal resistance of the bonding interface. This observation suggests that the thermal management of the bonded structure remains a crucial consideration for future high-current applications.

Ultimately, this work validates a high-yield wafer-level substrate transfer process for GaN-on-Si light-emitting devices and provides systematic experimental insights into stress control, optimization, and thermal management issues during the substrate transfer process. The relevant process and mechanism conclusions can also provide a reference for the subsequent fabrication and transfer of Micro-LED arrays with smaller pixel sizes.

Author Contributions: Conceptualization, S.Z. (Siyi Zhang), X.N., Q.F., S.Z. (Shuhan Zhang) and X.G.; methodology, S.Z. (Siyi Zhang), Q.F. and X.G.; formal analysis, S.Z. (Siyi Zhang), Q.F. and S.Z. (Shuhan Zhang); investigation, S.Z. (Siyi Zhang) and S.Z. (Shuhan Zhang); resources, X.N., Q.F., and X.G.; data curation, S.Z. (Siyi Zhang), Q.F., and S.Z. (Shuhan Zhang); writing—original draft preparation, S.Z. (Siyi Zhang); writing—review and editing, S.Z. (Siyi Zhang), X.N., Q.F., and X.G.; visualization, S.Z. (Siyi Zhang), Q.F., and X.G.; supervision, Q.F. and X.G.; project administration, Q.F. and X.G.; funding acquisition, Q.F. and X.G. All authors have read and agreed to the published version of the manuscript.

Funding: This research received no external funding.

Institutional Review Board Statement: Not applicable.

Informed Consent Statement: Not applicable.

Data Availability Statement: The original contributions presented in this study are included in the article. Further inquiries can be directed to the corresponding author.

Conflicts of Interest: The authors declare no conflicts of interest.

Appendix A

Table A1. Statistics of electrical characteristics before and after substrate transfer.

Device Group	No.	Turn-On Voltage (V)	Reverse Leakage Current at −5 V (A)
Before transfer	1	2.4	-3.962×10^{-7}
Before transfer	2	2.6	-7.893×10^{-8}
Before transfer	3	2.6	-2.852×10^{-8}
Before transfer	4	2.6	-1.486×10^{-7}
Before transfer	5	2.4	-1.578×10^{-8}
After transfer	1	3.3	-9.870×10^{-4}
After transfer	2	3.4	-1.719×10^{-4}
After transfer	3	3.3	-2.970×10^{-4}
After transfer	4	3.5	-3.410×10^{-4}
After transfer	5	3.4	-4.228×10^{-4}

https://doi.org/10.3390/mi17050607

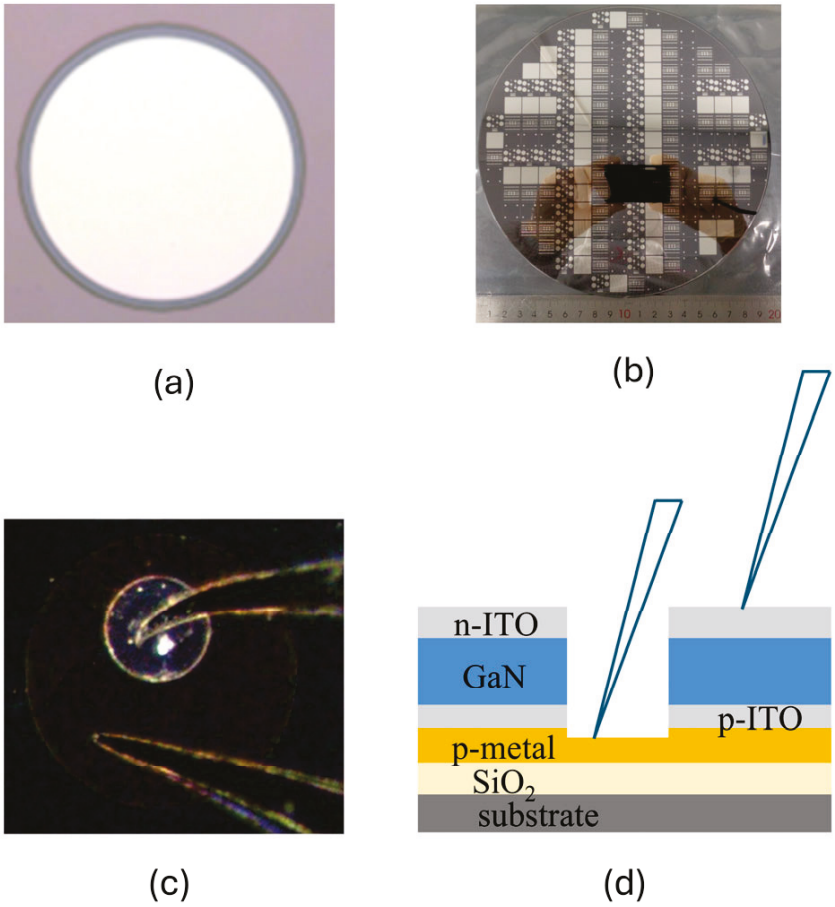


Figure A1. Real morphology of front-side LED structures and EL measurement configuration: (**a**) Optical microscopy image of the fabricated circular LED mesa. (**b**) Representative optical photograph of an 8-inch wafer with fabricated LED device structures. (**c**) Optical photograph of the actual EL testing process. (**d**) Cross-sectional schematic diagram illustrating the EL measurement setup.

References

1. Zhang, S.; Zheng, H.; Zhou, L.; Li, H.; Chen, Y.; Wei, C.; Wu, T.; Lv, W.; Zhang, G.; Zhang, S.; et al. Research progress of micro-led display technology. *Crystals* **2023**, *13*, 1001. [CrossRef]
2. Huang, Y.; Hsiang, E.-L.; Deng, M.-Y.; Wu, S.-T. Mini-led, micro-led and oled displays: Present status and future perspectives. *Light Sci. Appl.* **2020**, *9*, 105. [CrossRef] [PubMed]
3. Hsiang, E.-L.; Yang, Z.; Yang, Q.; Lan, Y.-F.; Wu, S.-T. Prospects and challenges of mini-led, oled, and micro-led displays. *J. Soc. Inf. Disp.* **2021**, *29*, 446–465. [CrossRef]
4. Behrman, K.; Kymissis, I. Micro light-emitting diodes. *Nat. Electron.* **2022**, *5*, 564–573. [CrossRef]
5. Wu, H.; Lin, X.; Shuai, Q.; Zhu, Y.; Fu, Y.; Liao, X.; Wang, Y.; Wang, Y.; Cheng, C.; Liu, Y.; et al. Ultra-high brightness micro-leds with wafer-scale uniform gan-on-silicon epilayers. *Light Sci. Appl.* **2024**, *13*, 284. [CrossRef]
6. Qi, L.; Zhang, X.; Chong, W.C.; Lau, K.M. Monolithically integrated high-resolution full-color gan-on-si micro-led microdisplay. *Photon. Res.* **2023**, *11*, 109–120. [CrossRef]
7. Tian, P.; McKendry, J.J.D.; Gu, E.; Chen, Z.; Sun, Y.; Zhang, G.; Dawson, M.D.; Liu, R. Fabrication, characterization and applications of flexible vertical ingan micro-light emitting diode arrays. *Opt. Express* **2016**, *24*, 699–707. [CrossRef]
8. Yin, L.; Zhou, H.; Ji, X.; Li, J.; Wang, K.; Li, C.; Zhang, J. Investigating the performance and reliability of Au-Sn bonded flip-chip micro-leds. *IEEE Trans. Electron Devices* **2024**, *71*, 1999–2004. [CrossRef]
9. Wang, Y.; Dong, X.; Han, S.; Song, Y.; Sheng, C.; Wang, C.; Huang, X.; Ge, Y. 25.6: A study on micro-led stamp transfer technology: Requirement and challenges. *SID Symp. Dig. Tech. Pap.* **2021**, *52*, 347–348. [CrossRef]
10. Carreira, J.F.C.; Xie, E.; Bian, R.; Herrnsdorf, J.; Haas, H.; Gu, E.; Strain, M.J.; Dawson, M.D. Gigabit per second visible light communication based on algainp red micro-led micro-transfer printed onto diamond and glass. *Opt. Express* **2020**, *28*, 12149–12156. [CrossRef] [PubMed]

https://doi.org/10.3390/mi17050607

11. Zhu, S.; Shan, X.; Lin, R.; Qiu, P.; Wang, Z.; Lu, X.; Yan, L.; Cui, X.; Zhang, G.; Tian, P. Characteristics of gan-on-si green micro-led for wide color gamut display and high-speed visible light communication. *ACS Photonics* **2023**, *10*, 92–100. [CrossRef]
12. Lau, J.H. Recent advances and trends in advanced packaging. *IEEE Trans. Compon. Packag. Manuf. Technol.* **2022**, *12*, 228–252. [CrossRef]
13. Trindade, A.J.; Guilhabert, B.; Xie, E.Y.; Ferreira, R.; McKendry, J.J.D.; Zhu, D.; Laurand, N.; Gu, E.; Wallis, D.J.; Watson, I.M.; et al. Heterogeneous integration of gallium nitride light-emitting diodes on diamond and silica by transfer printing. *Opt. Express* **2015**, *23*, 9329–9338. [CrossRef] [PubMed]
14. Lu, X.; Zhu, S.; Lin, R.; Sun, D.; Cui, X.; Tian, P. Performance improvement of red ingan micro-leds by transfer printing from si substrate onto glass substrate. *IEEE Electron Device Lett.* **2022**, *43*, 1491–1494. [CrossRef]
15. Yang, Z.; Ji, X.X.; Zhou, H.J.; Li, J.X.; Wang, X.Y.; Lu, X.Z.; Yin, L.Q.; Zhang, J.H. Research on au-in flip-chip bonding process of 2300 ppi micro-led arrays. *IEEE Trans. Electron Devices* **2024**, *71*, 7637–7643. [CrossRef]
16. Wang, C.; Yang, T.X.; Zhou, Y.J.; Yuan, J.W.; Guo, C.L.; Zhou, X.T.; Sun, J.; Yan, Q. A metal micro-dot array-based alignment-free flip-chip bonding technique for micro-led display fabrication. *Mater. Sci. Semicond. Process.* **2026**, *207*, 110466. [CrossRef]
17. Zhou, H.J.; Wang, K.F.; Ji, X.X.; Yin, L.Q.; Zhang, J.H. High resolution micro-led arrays using au-sn flip-chip bonding. *IEEE Trans. Electron Devices* **2023**, *70*, 3140–3144. [CrossRef]
18. Yin, L.Q.; Fu, H.; Yang, Z.; Zhou, H.J.; Wang, X.Y.; Ji, X.X.; Lu, X.Z.; Zhang, J.H. Research on micro-led heterogeneous integration and reliability based on copper pillar bumps. *IEEE Electron Device Lett.* **2026**, *47*, 124–127. [CrossRef]
19. Shi, J.; Chen, Y.; Miao, G.; Jiang, H.; Song, H. Recent progress in group III-nitride micro-led displays: From material improvement methods, device optimization techniques to full-color realization strategies. *Mater. Sci. Semicond. Process.* **2025**, *186*, 109090. [CrossRef]
20. Chen, D.; Chen, Y.-C.; Zeng, G.; Zhang, D.W.; Lu, H.-L. Integration technology of micro-led for next-generation display. *Research* **2023**, *6*, 0047. [CrossRef]
21. Liang, D.; Fang, A.W.; Park, H.; Reynolds, T.E.; Warner, K.; Oakley, D.C.; Bowers, J.E. Low-temperature, strong SiO_2–SiO_2 covalent wafer bonding for III–V compound semiconductors-to-silicon photonic integrated circuits. *J. Electron. Mater.* **2008**, *37*, 1552–1559. [CrossRef]
22. Wang, Q.; Ko, W.H. Si-to-Si fusion bonded touch mode capacitive pressure sensors. *Mechatronics* **1998**, *8*, 467–484. [CrossRef]
23. Calvez, A.; Larrey, V.; Noël, P.; Rieutord, F.; Fournel, F. Exploring chemical catalytic mechanisms for enhancing bonding energy in direct silicon dioxide wafer bonding. *Appl. Sci.* **2025**, *15*, 3883. [CrossRef]
24. Lee, H.; Kim, G.; Jeong, W.; Lee, Y.; Jeong, H.; Ahn, Y.; Kim, C.; Ha, D.H. Strategies for enhancing SiO_2 chemical-mechanical polishing (cmp): Functional nanoparticle abrasive design and integration. *Chem.-A Eur. J.* **2026**, *32*, e02584. [CrossRef]
25. Ryu, K.K.; Roberts, J.C.; Piner, E.L.; Palacios, T. Thin-body n-face gan transistor fabricated by direct wafer bonding. *IEEE Electron Device Lett.* **2011**, *32*, 895–897. [CrossRef]
26. Dragoi, V.; Razek, N.; Guiot, E.; Caulmilone, R.; Liao, M.; Wang, Y.S.; Goorsky, M.S.; Yates, L.; Graham, S. Direct wafer bonding of gan for power devices applications. *ECS Trans.* **2018**, *86*, 23. [CrossRef]
27. Uenuma, M.; Ando, R.; Furukawa, M.; Uraoka, Y. The influence of Ga–OH bond at initial GaN surface on the electrical characteristics of SiO_2/GaN interface. *Phys. Status Solidi (B)* **2019**, *257*, 1900368. [CrossRef]

Disclaimer/Publisher's Note: The statements, opinions and data contained in all publications are solely those of the individual author(s) and contributor(s) and not of MDPI and/or the editor(s). MDPI and/or the editor(s) disclaim responsibility for any injury to people or property resulting from any ideas, methods, instructions or products referred to in the content.

https://doi.org/10.3390/mi17050607

micromachines

MDPI

Article

All-Optical Terahertz Dual-Band Logic Gates Based on Unidirectional Modes

Dewang Guo [1], Yun You [1,*], Zhimin Liu [1] and Jie Xu [2,*]

[1] School of Science, East China Jiaotong University, Nanchang 330013, China
[2] School of Medical Information and Engineering, Southwest Medical University, Luzhou 646000, China
* Correspondence: youyun202003@163.com (Y.Y.); xujie011451@163.com (J.X.)

Abstract

All-optical logic gates have emerged as a critical technology for enabling broadband, low-loss, and high-speed communication systems, addressing the inherent bandwidth limitations of electronic counterparts. Here, we propose a Y-shaped structure leveraging unidirectional modes in the terahertz regime, which enables the realization of multifunctional all-optical logic gates within the lower- and upper-frequency bandwidth regions, including, but not limited to, AND, OR, NOT, and XNOR gates. Numerical simulations and theoretical analyses confirm that the proposed logic gates exhibit robust one-way propagation characteristics, with electromagnetic signals demonstrating complete immunity to backscattering even in the presence of structural defects. Furthermore, nonlocal effects are found to have a negligible impact on the operational bandwidths of our design. Building upon this Y-shaped configuration, we further develop an all-optical digital logic system (AODLS) capable of supporting bifrequency multi-input and multi-output logic operations. When lower- and upper-frequency signals are injected into separate input ports, their corresponding output signals remain fully independent, eliminating cross-talk and enabling true parallel computation. This dual-band parallel processing capability represents a significant advance over conventional single-band all-optical logic systems, opening new avenues for high-throughput all-optical computing and integrated photonic circuits.

Keywords: logic gates; surface magnetoplasmons (SMPs); unidirectional propagation; nonlocal effects

1. Introduction

Since the transistor was first invented in 1947, there has been great developments in electronic technology. However, affected by the constraints of both Moore's law and Joule's law, electronic communications suffer from defects such as cross-talk [1,2]. All-optical communications, owing to their ultra-fast data processing, error-free transmission [3], and minimal or even zero energy loss [4], reveal their potential as candidates for next-generation communication technology.

All-optical logic gates, which fulfill various logical functions, have received much attention for their potential applications in all-optical computing systems [5–7] and photonic integrated circuits [8,9]. Nowadays, there are several methods to realize all-optical logic functions, such as semiconductor optical amplifier (SOA) [10,11], optical interference effect [12,13], third-order nonlinear effect [14–16], and interferometry [17–19]. In fact, due to the unavoidable reflections in conventional optical logic gates, the contrast ratios (CRs) of most logic gates are typically below 30 dB. In numerous investigations focusing on

sub-wavelength all-optical logic gates, the conventional surface magnetoplasmons (SMPs) fail to be strictly unidirectional, and there will always be propagating modes in both directions once nonlocal effects are considered [20]. Note that in ref. [21], while in certain frequency regimes SMPs modes clearly lose their unidirectionality owing to nonlocal effects, spatial dispersion does not always prevent the existence of unidirectional surface waves. Indeed, it can be shown that the upper bulk mode bandgap (opened due to time-reversal-symmetry breaking) is characterized by a nonzero topological invariant number; topologically protected unidirectional surface waves can emerge when an interface is formed with a material having a bulk mode bandgap with different topological properties. In addition, while the conventional SMPs are not strictly unidirectional in the lower bulk mode bandgap, in most cases of interest they may be practically unidirectional due to the unavoidable losses that would largely attenuate the backward propagating modes. The one-way electromagnetic (EM) modes are theoretically topologically protected, which has been theoretically demonstrated [22,23] and experimentally proven [24,25] by many groups. Notably, in recent microwave-related research based on unidirectional waveguides, they have successfully implemented AND and OR logic operations under a unified logic-level definition, which is more suitable for cascading applications [26].

In this paper, we propose a robust AODLS based on unidirectional modes in the terahertz regime. The Y-shaped module of the AODLS enables the implementation of fundamental logic gates across distinct lower- and upper-frequency bands, including, AND, OR, NOT, and XNOR gates. Since nonlocality-immune SMPs modes are unidirectional and immune to backscattering, this implies an ultra-high contrast ratio. Most importantly, the AODLS supports bifrequency multi-input multi-output logic operations, where upper- and lower-frequency signals can be processed simultaneously with signal isolation between input and output ports. This intrinsic signal decoupling enables true parallel computation, a capability that surpasses the performance of single-band all-optical logic systems reported in the existing literature. This work establishes a new paradigm for all-optical calculations, offering a scalable solution for the development of high-throughput integrated photonic circuits and next-generation optical information processing systems.

2. Physical Model

The Y-shaped structure is a widely adopted physical model in the field of all-optical logic devices; it has been extensively studied over the past few decades [27–30]. As schematically illustrated in Figure 1, the proposed structure consists of three symmetric straight arms (labeled ‘A’, ‘B’, and ‘C’), each constructed from alternating layers of dielectric (Si) and semiconductor (InSb), with both layers having a uniform thickness d. The Si layer is bounded by a perfect electric conductor (PEC), while the InSb layer is terminated by a perfect magnetic conductor (PMC). Notably, the InSb segments are divided into two regions (InSb-a and InSb-b) with distinct magnetic configurations. The blue-colored InSb-a is magnetized along the +z direction by an external magnetic field B_0, whereas the brown-colored InSb-b is magnetized along the -z direction. The equivalent magnetic bias configurations could potentially be realized through engineered current-driven electromagnetic fields (patterned current arrays) to generate spatially varying effective magnetic fields with opposite orientations. The z-direction thickness of the InSb layers is treated as infinitely extended in the two-dimensional model, with all results readily extending to three-dimensional structures by adjusting the z-dimension boundary conditions. To implement basic logical operations based on unidirectional modes, the key lies in establishing two independent unidirectional channels to achieve efficient EM wave transmission.

https://doi.org/10.3390/mi17050509

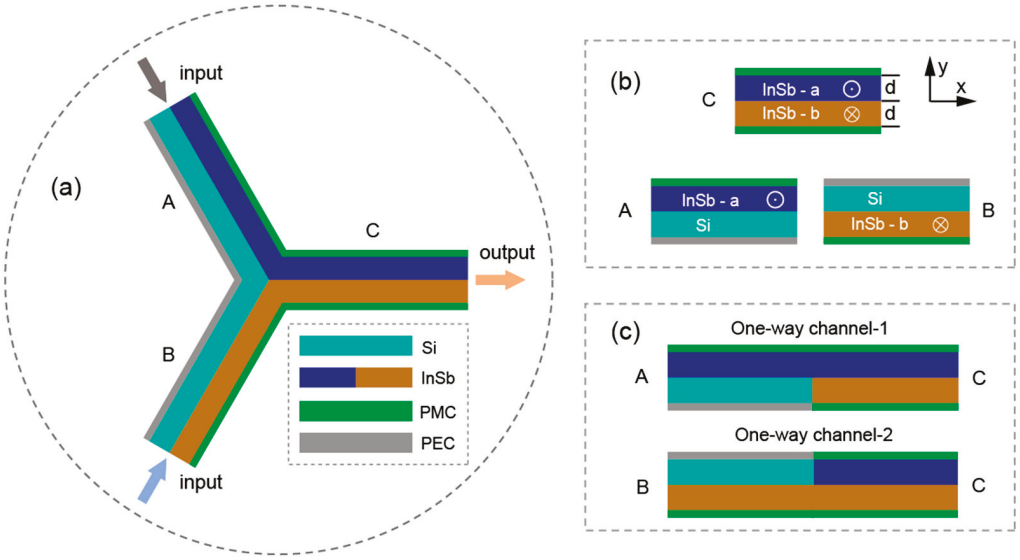


Figure 1. (**a**) The schematic of the Y-shaped structure of all-optical logic operations. (**b**) The three types of arms. (**c**) Pre-designed two one-way channels. Note that we use ${\omega_c}^a$, ${\omega_c}^b$ to clarify the procession ω_c for blue-colored InSb-a, and brown-colored InSb-b layers, respectively.

In our work, the relative permittivity of InSb-a, and InSb-b, influenced by the magnetic field, are given by:

$$\overleftrightarrow{\varepsilon}_a = \begin{bmatrix} \varepsilon_1^a & \mathrm{i}\varepsilon_2^a & 0 \\ -\mathrm{i}\varepsilon_2^a & \varepsilon_1^a & 0 \\ 0 & 0 & \varepsilon_3^a \end{bmatrix}, \quad \overleftrightarrow{\varepsilon}_b = \begin{bmatrix} \varepsilon_1^b & -\mathrm{i}\varepsilon_2^b & 0 \\ \mathrm{i}\varepsilon_2^b & \varepsilon_1^b & 0 \\ 0 & 0 & \varepsilon_3^b \end{bmatrix} \tag{1}$$

with

$$\varepsilon_1 = \varepsilon_\infty\left(1 - \frac{(\omega + \mathrm{i}\nu){\omega_p}^2}{\omega[(\omega + \mathrm{i}\nu)^2 - {\omega_c}^2]}\right), \quad \varepsilon_2 = \varepsilon_\infty \frac{\omega_c {\omega_p}^2}{\omega[(\omega + \mathrm{i}\nu)^2 - {\omega_c}^2]}, \quad \varepsilon_3 = \varepsilon_\infty\left(1 - \frac{{\omega_p}^2}{\omega(\omega + \mathrm{i}\nu)}\right) \tag{2}$$

where ε_∞ denotes the high-frequency permittivity of the semiconductor, ω_p is the plasma frequency of the semiconductor, ω is the angular frequency, and $\omega_c = eB_0/m^*$ (e and m^* represent the charge and effective mass of the electron) is the electron cyclotron frequency. In this paper, ε_∞ = 15.6 (InSb), ε_d = 11.68 (Si). In the following analytical derivation, the semiconductor is assumed to be lossless for clarity, while the realistic material loss will be incorporated into subsequent full-wave transmission simulations. To establish two independent unidirectional channels for efficient EM signal transmission, it is essential to characterize the dispersion relation of the SMPs in those arms. According to Maxwell's equations with appropriate boundary conditions, one may readily calculate the dispersion equations in the above three arms using:

$$\frac{\varepsilon_2^a}{\varepsilon_1^a}k + \frac{\alpha_a}{\tanh(\alpha_a d)} + \frac{\varepsilon_v^a}{\varepsilon_d}\alpha_d \tanh(\alpha_d d) = 0, \qquad (\text{'A'}) \tag{3}$$

$$\frac{\varepsilon_2^b}{\varepsilon_1^b}k + \frac{\alpha_b}{\tanh(\alpha_b d)} + \frac{\varepsilon_v^b}{\varepsilon_d}\alpha_d \tanh(\alpha_d d) = 0, \qquad (\text{'B'}) \tag{4}$$

$$\varepsilon_v^b\left[\frac{\varepsilon_2^a}{\varepsilon_1^a}k + \frac{\alpha_a}{\tanh(\alpha_a d)}\right] + \varepsilon_v^a\left[\frac{\varepsilon_2^b}{\varepsilon_1^b}k + \frac{\alpha_b}{\tanh(\alpha_b d)}\right] = 0, \qquad (\text{'C'}) \tag{5}$$

https://doi.org/10.3390/mi17050509

where $\alpha_a = \sqrt{k^2 - \varepsilon_v^a \, {k_0}^2}$, $\alpha_b = \sqrt{k^2 - \varepsilon_v^b \, {k_0}^2}$, and $\alpha_d = \sqrt{k^2 - \varepsilon_d \, {k_0}^2}$ respectively represent the transverse attenuation coefficients of the SMPs in the InSb-a, InSb-b, and Si layers. From the dispersion equations, it is evident that the SMPs in the arms exhibit contrasting propagation properties for opposite wavenumbers, reflecting the nonreciprocity effect. Crucially, tuning the external magnetic field enables the creation of a unidirectional propagation region, where EM waves are confined to travel exclusively along a single direction. With the dispersion equation of the SMPs derived, the asymptotic frequencies (AFs) can be readily calculated. These AFs define the boundaries of the complete one-way propagation (COWP) bands, within which we observe that:

$$\omega_{sp}^{(+)} = \begin{cases} \omega_{sp}^{(+1)} = \omega_a = \frac{1}{2}(\sqrt{{\omega_c}^2 + 4{\omega_p}^2} - \omega_c) \\ \omega_{sp}^{(+2)} = \frac{1}{2}(\sqrt{{\omega_c}^2 + 4{\omega_p}^2 \frac{\varepsilon_\infty}{\varepsilon_\infty + \varepsilon_d}} + \omega_c) \end{cases} \tag{6}$$

$$\omega_{sp}^{(-)} = \begin{cases} \omega_{sp}^{(-1)} = \frac{1}{2}(\sqrt{{\omega_c}^2 + 4{\omega_p}^2 \frac{\varepsilon_\infty}{\varepsilon_\infty + \varepsilon_d}} - \omega_c) \\ \omega_{sp}^{(-2)} = \omega_b = \frac{1}{2}(\sqrt{{\omega_c}^2 + 4{\omega_p}^2} + \omega_c) \end{cases} \tag{7}$$

for arms 'A'/'B'. ${\omega_{sp}}^{(+)}$ and ${\omega_{sp}}^{(-)}$ indicate the AFs in the limits of $k \to +\infty$ and $k \to -\infty$, respectively. In fact, the values of ω_a and ω_b correspond to the zero point of ε_v. And

$$\omega_{sp}^{(+)} = \begin{cases} \omega_{sp}^{(+1)} = \omega_c \\ \omega_{sp}^{(+2)} = \omega_a = \frac{1}{2}(\sqrt{{\omega_c}^2 + 4{\omega_p}^2} - \omega_c) \end{cases} \tag{8}$$

$$\omega_{sp}^{(-)} = \omega_b = \frac{1}{2}(\sqrt{{\omega_c}^2 + 4{\omega_p}^2} + \omega_c) \tag{9}$$

for 'C', where the cyclotron frequencies of InSb-a and InSb-b are equal (${\omega_c}^a = {\omega_c}^b$), analyses of Equations (6)–(9) reveal that the three arms share identical AFs, denoted as ω_a and ω_b, significantly simplifying the design process for effective broadband.

The implementation of broadband all-optical logic operations based on unidirectional SMPs modes necessitates the establishment of independent one-way propagation channels and sufficiently broad COWP bands. We choose ${\omega_c}^a = {\omega_c}^b = 0.7\omega_p$ ($\omega_p = 4\pi \times 10^{12}$ rad/s), $d = 0.05\lambda_p$ ($\lambda_p = 2\pi c/\omega_p$) in the following work. Under this parameter configuration, the dispersion curves for the SMPs in the arms 'A'/'B' and 'C' are calculated and plotted in Figures 2a and 2b, respectively. In these figures, the red solid lines represent the dispersion curves of the SMPs modes, while the blue solid curves correspond to the lowest-order bulk modes within the green-shaded bulk zones, and the black dashed lines indicate light-lines in the medium. Black horizontal arrows mark the values of AFs, and black dots denote cutoff frequencies ω_{cf}, which are influenced by the dielectric thickness d. Based on our calculations, the bandwidths of the COWP bands in the arms 'A'/'B' are $0.48\omega_p < \omega < 0.71\omega_p$ (COWP_1), $1.22\omega_p < \omega < 1.41\omega_p$ (COWP_2). For arm 'C', the COWP band bandwidths are $0 < \omega < 0.7\omega_p$ (COWP_1), $1.22\omega_p < \omega < 1.41\omega_p$ (COWP_2). Consequently, two distinct unidirectional propagation channels are established ('A $\to$ C' and 'B $\to$ C') in the lower one-way regions ($0.48\omega_p < \omega < 0.7\omega_p$). Conversely, the EM signal transmission from arm 'A' to arm 'B' is effectively suppressed, demonstrating the non-reciprocal characteristic essential for optical logic isolation. Here, the propagation direction is reversed in the upper one-way regions ($1.22\omega_p < \omega < 1.41\omega_p$), enabling two one-way channels ('C $\to$ A' and 'C $\to$ B'), while the signal transmission between arms 'A' and 'B' remains prohibited.

https://doi.org/10.3390/mi17050509

Actually, the designed bandwidths are sufficiently broad to ensure operational robustness and facilitate practical device implementation.

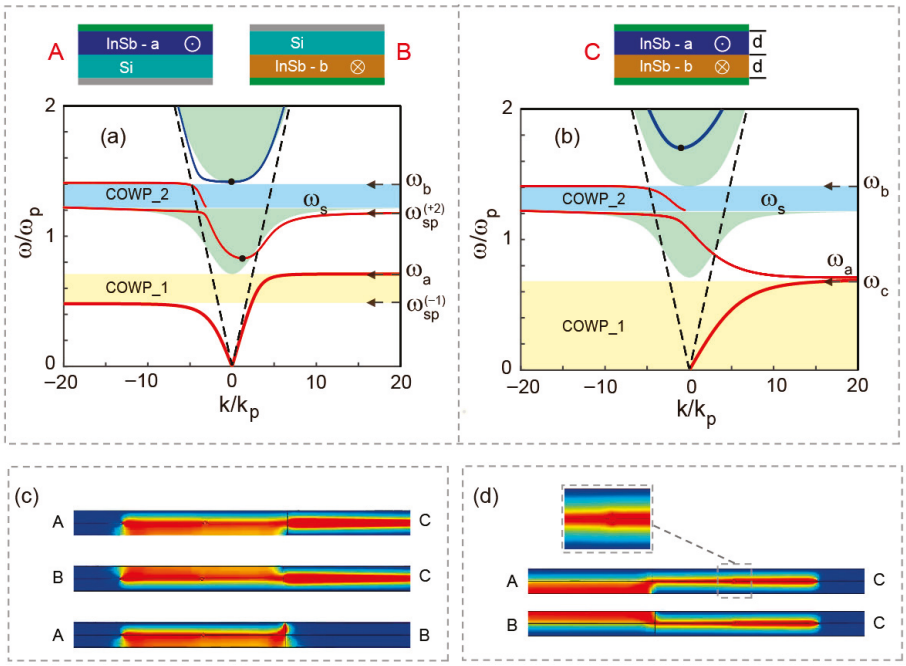


Figure 2. (**a**) The dispersion diagrams of arms 'A'/'B', ${\omega_c}^a = {\omega_c}^b = 0.7\omega_p$ and $d = 0.05\lambda_p$. (**b**) The dispersion diagrams of arm 'C', ${\omega_c}^a = {\omega_c}^b = 0.7\omega_p$ and $d = 0.05\lambda_p$. (**c**,**d**) Electromagnetic signal transmission through channels operating at $0.6f_p$ and $1.3f_p$, respectively.

To verify the theoretical predictions regarding the unidirectional propagation characteristics of SMPs and the inter-arm coupling effects, full-wave EM simulations were conducted using finite element method (FEM). The simulation setup, as illustrated in Figure 2c,d, incorporates structural perturbations in the form of air holes (radius $r = 1.5$ um) placed at the InSb-InSb interfaces with $\nu = 0.002\omega_p$, and SMPs are excited using a magnetic current source. We chose two frequencies $f = 0.6f_p$ and $f = 1.3f_p$, corresponding to the lower and upper unidirectional frequency bands of interest. The simulated magnetic field distributions confirm the robust one-way channeling behavior. As shown in Figure 2c, the EM signal is efficiently guided through the unidirectional channels 'A $\rightarrow$ C' and 'B $\rightarrow$ C', while the propagation from arm 'A' to arm 'B' is effectively suppressed at their interface for $f = 0.6f_p$. This observation validates the predicted lower-band isolation. Similarly, Figure 2d demonstrates that at $f = 1.3f_p$, the EM signal propagates exclusively from arm 'C' to arms 'A' or 'B', with no signal transfer occurring between arms 'A' and 'B'. These results are in excellent agreement with the theoretical dispersion analysis. In addition, the EM signal is observed to circumvent the introduced air-hole defects entirely, with the defects exerting a negligible influence on the transmission characteristics of the one-way SMPs, further demonstrating the remarkable robustness of the unidirectional propagation against structural imperfections. The proposed design exhibits robust tolerance to material defects and realistic fabrication tolerances, thereby verifying its practical feasibility for real-world implementation.

The bandwidths of the unidirectional propagation region in the three arms can be effectively tuned by adjusting the external magnetic field (B_0). To systematically investigate the influence of the magneto-static field on the COWP bands, we plot the AFs as functions of the cyclotron frequency ω_c for $d = 0.05\lambda_p$. As shown in Figure 3a, for arms 'A'/'B', increasing B_0 initially broadens and subsequently narrows the COWP_1 band, while the COWP_2 band exhibits a monotonic expansion in bandwidth. In contrast, Figure 3b

https://doi.org/10.3390/mi17050509

reveals more complex variations in the COWP bands for arm 'C', with the maximum total bandwidth achieved at $\omega_c = 0.7\omega_p$.

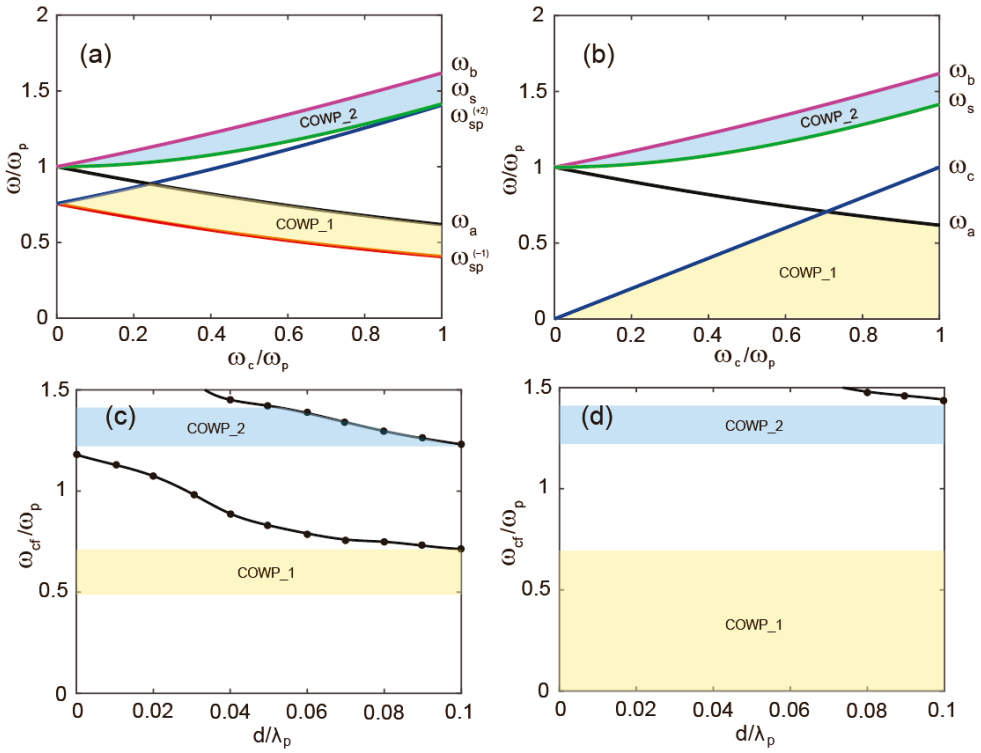


Figure 3. (**a**) The asymptotic frequencies (AFs) are plotted as functions of ω_c in the arms 'A'/'B'. (**b**) AFs are plotted as functions of ω_c in the arm 'C'. (**c**,**d**) The cutoff frequencies ω_{cf} as functions of the thickness d in the arms 'A'/'B', 'C', respectively.

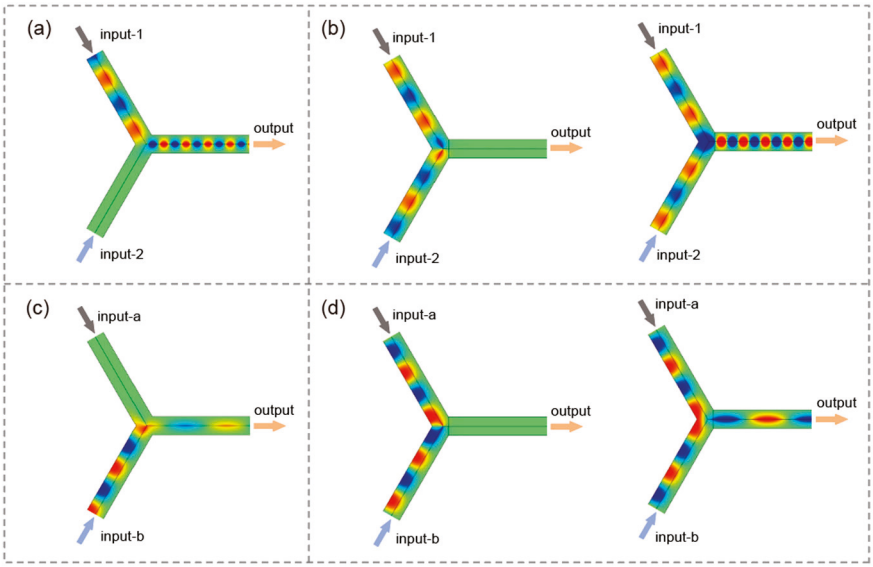
In addition to the magnetic field, the dielectric layer thickness d also plays a critical role in shaping the COWP bands, as the excitation of reverse-propagating SMPs can reduce the effective unidirectional window. The relationship between d and ω_{cf} at $\omega_c = 0.7\omega_p$ is examined in Figure 3c,d. The results indicate that for $d < 0.053\lambda_p$, the COWP bands in arms 'A'/'B' and 'C' remain largely unaffected. However, once $d > 0.053\lambda_p$, the upper-frequency COWP_2 band in arms 'A'/'B' undergo significant narrowing. Therefore, to ensure adequate operational bandwidths in both the lower- and upper-frequency regimes while maintaining strong unidirectional confinement, we select the optimal parameter of $d = 0.05\lambda_p$ and $\omega_c = 0.7\omega_p$ for the subsequent design and analysis of the proposed all-optical logic device.

3. Realization of Basic Logic Gates

As discussed in the context of Figure 2, the arms 'A', 'B', and 'C' support unidirectional forward propagation modes within the operational frequency range of $0.48\omega_p < \omega < 0.7\omega_p$. Leveraging the two distinct one-way channels established in this frequency band, the proposed Y-shaped structure can function as a platform for all-optical logic gates, including, but not limited to, AND, OR, NOT, and XNOR gates, as schematically illustrated in Figure 4a,b. In the logic operation scheme, arms 'A' and 'B' serve as input ports, while arm 'C' acts as the output port. Figure 4a presents simulated field distributions for the Y-shaped structure at $f = 0.6f_p$ when the EM signal is excited in only one of the input ports. For the OR gate implementation under positive logic convention, the presence of an EM signal in an arm is defined as logic '1', whereas the absence of signal (zero-energy state) corresponds to logic '0'. Accordingly, when any input port receives a logic '1' (unidirectional EM signal),

https://doi.org/10.3390/mi17050509

the output port also exhibits logic '1', thereby realizing the OR gate function. Specifically, for input combinations '10' or '01', the output power reaches 0.426 mW with a transmittance of 0.316, corresponding to logic state '1'; for input '11', the output power increases to 1.7 mW with a transmittance of 0.63, also corresponding to logic state '1'; and for input '00', no output power (0 mW) or transmittance (0) is detected, corresponding to logic state '0'. In contrast, the AND gate operation requires the adoption of a negative logic scheme. Here, the propagation of EM signal is interpreted as logic '0', while the absence of energy flow is regarded as logic '1'. Under this principle, if any input port is excited with EM signal (logic '0'), the output will correspondingly yield logic '0'. This logical inversion, combined with the unidirectional transmission characteristics of the structure, enables the realization of the AND gate within the same physical layout.



(e)

OR operation			AND operation			NOT operation			XNOR operation		
input-a	input-b	output	input-a	input-b	output	input-a	input-b	output	input-a	input-b	output
'1'	'0'	'1'	'0'	'1'	'0'	'1'		'0'	'0'	'1'	'0'
'0'	'1'	'1'	'1'	'0'	'0'		'1'	'0'	'0'	'0'	'1'

Figure 4. (**a**) Simulated field distributions of the Y-shaped structure at $f = 0.6f_p$, with EM signal excitation applied to a single input port. (**b**) Two input ports are excited with EM signals of phases 3*pi/2 and pi/2 in the left figure, and both input ports are driven by signals with the phase of 3*pi/2 in the right figure. (**c**,**d**) The external magnetic field direction applied to the InSb-a and InSb-b layers are reversed, with simulated field distributions at $f = 1.3f_p$. (**e**) The truth tables of the OR, AND, NOT, and XNOR operations.

Similarly, the NOT gate operation is implemented using the negative logic scheme, wherein the presence of EM energy at the input port is defined as logic '1', while the output port yields logic '0'. Under this convention, the input logic '1' is converted to the output logic '0', thereby realizing the logical inversion characteristic of the NOT gate. Furthermore, the XNOR gate can be achieved by injecting EM signals with distinct phases into the two input ports. In this scheme, the signal phase of pi/2 is assigned to logic '1', and the phase of 3*pi/2 corresponds to logic '0'. Two representative simulations are performed on the Y-shaped structure, as shown in Figure 4b. In the left figure, when the two input ports are excited with EM signals of phases 3*pi/2 and pi/2, respectively, the zero-energy state is observed at the output port. In the right figure, when both input ports are driven by signals with the phase of 3*pi/2, the EM energy couples unidirectionally into arm 'C', resulting in a clear output signal. Notably, input combinations '10' or '01' yield an output

https://doi.org/10.3390/mi17050509

power of 1.04×10^{-7} mW with a transmittance of 7.7×10^{-8}, representing logic '0', while inputs '11' or '00' result in an output power of 1.7073 mW with a transmittance of 0.63, corresponding to logic '1'. The output characteristics of the unidirectional SMPs are highly dependent on the applied magnetic field, which enables tolerance to phase deviations via fine-tuning. The corresponding truth tables for the OR, AND, NOT, and XNOR operations are summarized in Figure 4e. All simulation results align closely with the theoretical predictions, demonstrating the reliable logic-level response of the proposed structure. Accordingly, the Y-shaped module is capable of performing multiple logic operations and acts as a multifunction logic gate, which has potential for high-performance optical communication or calculation.

Notably, the arms 'A', 'B', and 'C' also support unidirectional propagation modes within the upper-frequency operating band of $1.22\omega_p < \omega < 1.41\omega_p$, where the EM energy propagates in the backward direction. To implement logic operations in this frequency regime, the external magnetic field direction applied to the InSb-a and InSb-b layers can be reversed, thereby inverting the propagation direction in the three arms. Following the analogous analysis that presents in Figure 4a,b, the OR, AND, NOT, and XNOR logic functions are successfully demonstrated in Figure 4c,d when $f = 1.3f_p$. In the OR gate, for inputs '10' or '01', the output power is 0.475 mW with a transmittance of 0.416, representing logic '1'; for input '11', the output power rises to 1.9 mW with a transmittance of 0.832, representing logic '1'; and input '00' produces no detectable output power or transmittance, representing logic '0'. In the XNOR gate, inputs '10' or '01' result in 1.35×10^{-10} mW output power and 1.18×10^{-10} transmittance, corresponding to logic '0', while inputs '11' or '00' yield an output power of 1.9 mW with a transmittance of 0.832, corresponding to logic '1'. The operational principle of these gates relies exclusively on stable unidirectional EM signals, which afford significantly higher discrimination precision compared to alternative approaches. For example, in the simulated OR gate operation, the logic '1' state corresponds to a clearly defined EM signal, whereas the logic '0' state exhibits no detectable energy, resulting in a sharply distinct contrast. A distinctive feature of this work is that the SMPs-based logic gates can operate within two continuous and relatively broad complete COWP bands. The dual-band capability enables flexible, frequency-selective logic functionality without altering the physical geometry, thereby enhancing the adaptability of the device for programmable photonic circuits.

To evaluate the fundamental impact of nonlocal effects on the operational integrity of the proposed all-optical logic gates, a comparative analysis of the pattern distributions in arms 'A'/'B' and 'C' is conducted under both local and nonlocal models at $f = 0.6f_p$ and $1.3f_p$, as shown in Figures 5 and 6. These findings collectively reveal the pronounced robustness of both Si-InSb and InSb-InSb structures against nonlocal perturbations. For the Si-InSb configuration, nonlocal interactions induce a weak excitation of reverse-propagating SMPs at $0.6f_p$ in Figure 5a, with only minor deviations from the one-dimensional magnetic field distribution predicted by the local model. This indicates that the core unidirectional transmission property of SMPs remains effectively preserved for practical device applications. In contrast, Figure 5b reveals that the Si-InSb structure demonstrates complete immunity to nonlocal effects at $1.3f_p$, sustaining topologically protected unidirectional surface waves without any observable degradation in propagation direction. The InSb-InSb structure displays even stronger robustness, as illustrated in Figure 6. At both the lower ($f = 0.6f_p$) and upper ($f = 1.3f_p$) operational frequencies, the field distribution curves predicted by the nonlocal model show perfect consistency with those from the local model. The perfect agreement confirms the broadband immunity of the InSb-InSb structure to nonlocal effects, underscoring its exceptional stability for sustaining unidirectional transmission modes. These findings demonstrate that nonlocal effects neither compromise the estab-

https://doi.org/10.3390/mi17050509

lished unidirectional channels nor degrade the computational performance of all-optical logic gates.

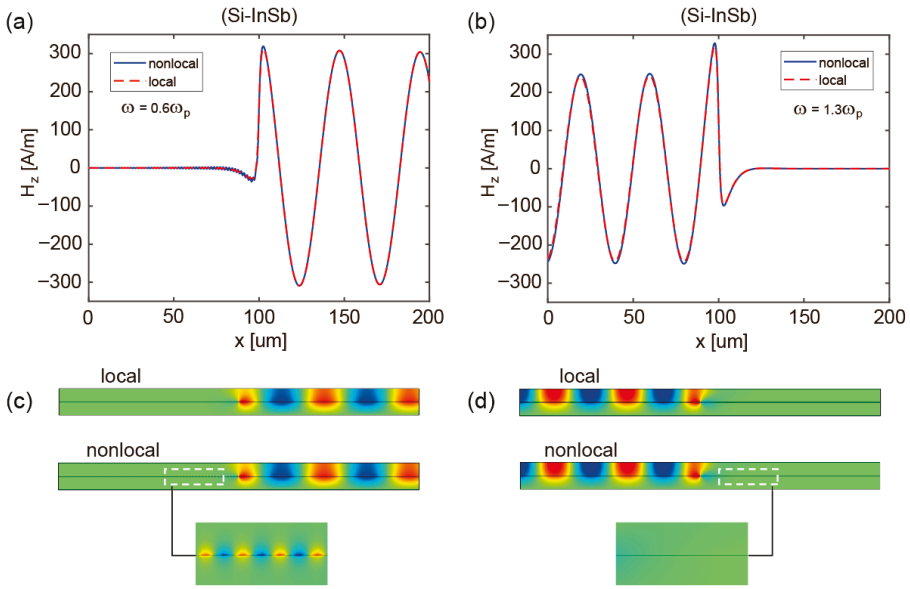


Figure 5. (**a**,**b**) The one-dimensional magnetic-field profiles of Si-InSb structure at $0.6f_p$ and $1.3f_p$, respectively. (**c**,**d**) Corresponding magnetic-field distributions of the Si-InSb structure under local and nonlocal models at $0.6f_p$ and $1.3f_p$.

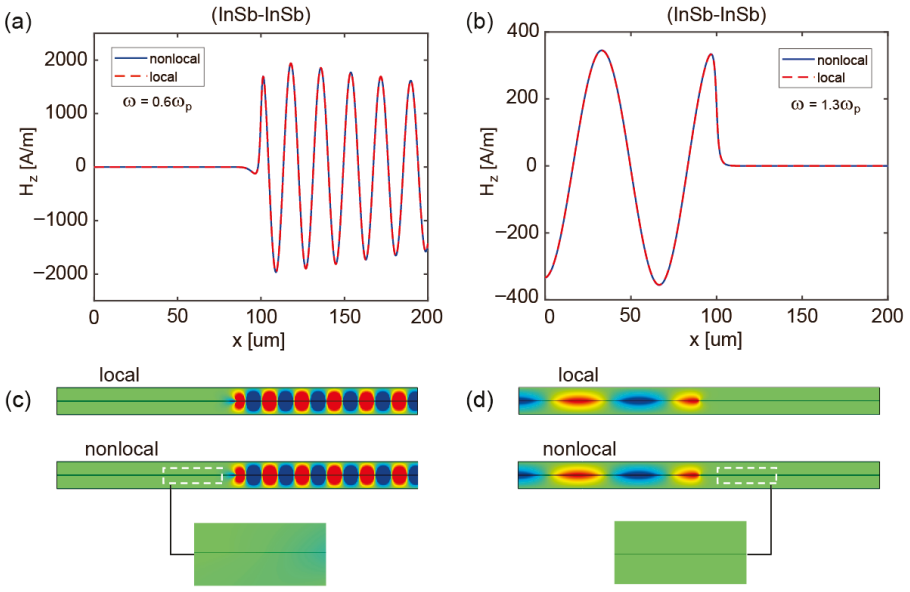


Figure 6. (**a**,**b**) The one-dimensional magnetic-field profiles of InSb-InSb structure at $0.6f_p$ and $1.3f_p$, respectively. (**c**,**d**) Corresponding magnetic-field distributions of the InSb-InSb structure under local and nonlocal models at $0.6f_p$ and $1.3f_p$.

4. The AODLS for Multi-Input Logic Operations

Optical computations are characterized by super-fast data transmissions relying on fan-in and fan-out, and our proposed unidirectional-modes-based logic gates have two broad operating bands. Building on this foundational capability, we now present a systematic design approach for integrating this module into AODLS. The schematic diagram of the proposed all-optical AODLS is presented in Figure 7a. To clearly illustrate the signal flow, arrows have been incorporated into the schematic, indicating the propagation directions

https://doi.org/10.3390/mi17050509

within the unidirectional channels. The system architecture supports four distinct input configurations for two independent output ports, enabling versatile logic operations. At the lower-frequency band operations ($0.48f_p < f < 0.7f_p$), the EM signals are injected into the 'input-1' and 'input-2' ports. The corresponding output signal is collected from the 'output-3' port. When operating in this upper-frequency band ($1.22f_p < f < 1.41f_p$), the input signals are directed into the 'input-a' and 'input-b' ports, with the output retrieved from the 'output-c' port.

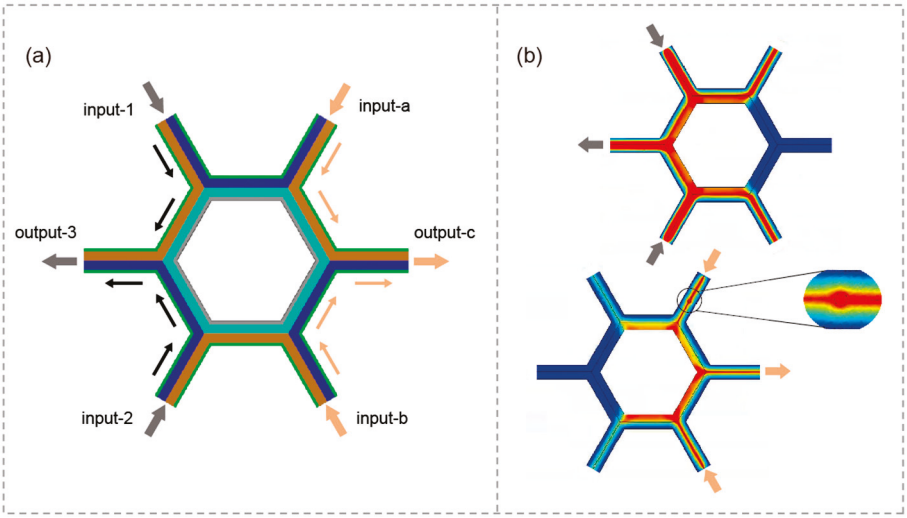


Figure 7. (**a**) The schematic of AODLS structure. (**b**) Transmission of EM wave in AODLS.

To experimentally validate the functionality and robustness of the proposed AODLS, full-wave EM simulations were performed using FEM, with the schematic and simulated field distributions presented in Figure 7b. Imperfections on the InSb-InSb interface are introduced as air holes with r = 1.5 um to demonstrate the robust unidirectionality of the incident EM modes. The input EM wave perfectly bypasses the introduced air hole defects at the input port and subsequently splits into two guided waves. This confirms the robustness of the topological one-way channels against backscattering and localization induced by interface disorders. Notably, virtually no inter-channel cross-talk or spurious noise is observed during the entire logic operation process. The input/output propagation characteristics align perfectly with the theoretical predictions based on the dispersion analysis. Most importantly, inputs applied at 'input-1' and 'input-2' have no measurable effect on 'output-c'. Similarly, signals injected into 'input-a' and 'input-b' do not influence 'output-3', allowing for concurrent operation. Hence, the signal inputs and outputs are independent, which is promising for parallel computation. Surely, the OR, AND, NOT, and XNOR logical operations are also implemented in AODLS. It is worth mentioning that the AODLS works with two outputs and could be easily extended to the four-output logic device by suitably assembling the Y-shaped modules at the output ports. The AODLS shows significant promise in complex logic operations due to its expansibility, precision, and broadband characteristics. Compared to conventional electronic logic gates, which rely on distinguishing between relatively high and low voltage levels, the unidirectional all-optical logic gates offer a distinct advantage, given that the logical state is defined by the presence or absence of the EM signal.

5. Conclusions

In this work, we have proposed a novel, robust, AODLS operating in the terahertz regime. Theoretical analysis and full-wave simulations demonstrate that the Y-shaped

https://doi.org/10.3390/mi17050509

module of the AODLS can independently implement fundamental logic functions (not limited to, AND, OR, NOT, and XNOR gates) within the lower- and upper-frequency regions. The lower- and upper-frequency bands are defined by $0.48\omega_p < \omega < 0.7\omega_p$ and $1.22\omega_p < \omega < 1.41\omega_p$, respectively. The unidirectional propagation characteristics remain robust against structural imperfections and operational bandwidths are completely unaffected by nonlocal effects, ensuring operational stability. In addition, by connecting Y-shaped modules at the output ports, the AODLS can be extended to the four-output logic device. The upper-frequency and lower-frequency operational modes are entirely independent, with no cross-talk observed on their output ports. This intrinsic port isolation enables genuine parallel computation on a single integrated platform. Owing to the broad operating band, error-free transmission and ultra-fast data processing, our proposed AODLS could become a novel platform for optical calculations and optical communication.

Author Contributions: Conceptualization, Y.Y. and J.X.; formal analysis, D.G. and Z.L.; writing—original draft preparation, D.G.; writing—review and editing, D.G. and Y.Y.; visualization, D.G. and Z.L.; funding acquisition, Y.Y. and J.X. All authors have read and agreed to the published version of the manuscript.

Funding: This research was funded by the National Natural Science Foundation of China, grant numbers 62101496 and 12404143.

Institutional Review Board Statement: Not applicable.

Informed Consent Statement: Not applicable.

Data Availability Statement: The original contributions presented in this study are included in the article. Further inquiries can be directed to the corresponding authors.

Conflicts of Interest: The authors declare no conflicts of interest.

References

1. Markov, I.L. Limits on fundamental limits to computation. *Nature* **2014**, *512*, 147–154. [CrossRef]
2. Yang, H.; Khayrudinov, V.; Dhaka, V.; Jiang, H.; Autere, A.; Lipsanen, H.; Sun, Z.; Jussila, H. Nanowire network–based multifunctional all-optical logic gates. *Sci. Adv.* **2018**, *4*, eaar7954. [CrossRef]
3. Mueller, T.; Xia, F.; Avouris, P. Graphene photodetectors for high-speed optical communications. *Nat. Photonics* **2010**, *4*, 297–301. [CrossRef]
4. Hardy, J.; Shamir, J. Optics inspired logic architecture. *Opt. Express* **2007**, *15*, 150–165. [CrossRef]
5. Kotb, A.; Wang, Z.; Zoiros, K.E. High-performance all-optical logic gates based on silicon racetrack and microring resonators. *Electronics* **2025**, *14*, 2961. [CrossRef]
6. Kotb, A.; Hatziefremidis, A.; Zoiros, K.E. Silicon-on-Silica Microring Resonators for High-Quality, High-Contrast, High-Speed All-Optical Logic Gates. *Nanomaterials* **2025**, *15*, 1736. [CrossRef]
7. Swarnakar, S.; Palacharla, V.; Muduli, A.; Kumar, S. Design and optimization of photonic crystal based all-optical logic gate with enhanced contrast ratio. *Opt. Quant. Electron.* **2023**, *55*, 623. [CrossRef]
8. Rao, D.G.S.; Swarnakar, S.; Kumar, S. Design of all-optical reversible logic gates using photonic crystal waveguides for optical computing and photonic integrated circuits. *Appl. Opt.* **2020**, *59*, 11003–11012. [CrossRef]
9. Lipton, J.; Yurash, B.; Sorensen, A.; Vajo, J.; Whiteley, S.; Wang, T.; Huang, B.; Bai, X.; Portales, A.; Rubin, S.; et al. Low-Loss Nanophotonic Devices with Chip-Level Uniformity and Integrated Color Centers in SiC-On-Insulator. *ACS Photonics* **2025**, *12*, 2397–2405. [CrossRef]
10. Kim, J.Y.; Kang, J.M.; Kim, T.Y.; Han, S.K. 10 Gbit/s all-optical composite logic gates with XOR, NOR, OR and NAND functions using SOA-MZI structures. *Electron. Lett.* **2006**, *42*, 303–304. [CrossRef]
11. Cui, J.; Zoiros, K.E.; Kotb, A. Advances in Semiconductor Optical Amplifier Technologies for All-Optical Logic Gate Implementations: A Comprehensive Review. *Nanomaterials* **2026**, *16*, 202. [CrossRef]
12. Li, Z.; Chen, Z.; Li, B. Optical pulse controlled all-optical logic gates in SiGe/Si multimode interference. *Opt. Express* **2005**, *13*, 1033–1038. [CrossRef]
13. Wang, L.A.; Chang, S.H.; Lin, Y.F. Novel implementation method to realize all-optical logic gates. *Opt. Eng.* **1998**, *37*, 1011–1018. [CrossRef]

https://doi.org/10.3390/mi17050509

14. Fujisawa, T.; Koshiba, M. All-optical logic gates based on nonlinear slot-waveguide couplers. *J. Opt. Soc. Am. B* **2006**, *23*, 684–691. [CrossRef]
15. Liang, T.K.; Nunes, L.R.; Tsuchiya, M.; Abedin, K.S.; Miyazaki, T.; Van Thourhout, D.; Bogaerts, W.; Dumon, P.; Baets, R.; Tsang, H.K. High speed logic gate using two-photon absorption in silicon waveguides. *Opt. Commun.* **2006**, *265*, 171–174. [CrossRef]
16. Passaro, V.M.N.; De Passaro, F. All-optical AND gate based on Raman effect in silicon-on-insulator waveguide. *Opt. Quantum Electron.* **2006**, *38*, 877–888. [CrossRef]
17. He, L.; Zhang, W.X.; Zhang, X.D. Topological all-optical logic gates based on two-dimensional photonic crystals. *Opt. Express* **2019**, *27*, 25841–25859. [CrossRef]
18. Gao, X.; Chen, B.J.; Shum, K.M.; Zhang, Q.L.; Ma, Q.; Cui, W.Y.; Cui, T.J.; Chan, C.H. Logic gates of terahertz spoof surface plasmons. *Adv. Mater. Technol.* **2023**, *8*, 2201225. [CrossRef]
19. Wang, Y.; Liu, W.; Ji, Z.; Modi, G.; Hwang, M.; Agarwal, R. Coherent interactions in one-dimensional topological photonic systems and their applications in all-optical logic operation. *Nano Lett.* **2020**, *20*, 8796–8802. [CrossRef]
20. Buddhiraju, S.; Shi, Y.; Song, A.; Wojcik, C.; Minkov, M.; Williamson, I.A.D.; Dutt, A.; Fan, S. Absence of unidirectionally propagating surface plasmon-polaritons at nonreciprocal metal-dielectric interfaces. *Nat. Commun.* **2020**, *11*, 674. [CrossRef]
21. Hassani Gangaraj, S.A.; Monticone, F. Do truly unidirectional surface plasmon-polaritons exist? *Optica* **2019**, *6*, 1158–1165. [CrossRef]
22. Wang, Z.; Chong, Y.D.; Joannopoulos, J.D.; Soljačić, M. Reflection-free one-way edge modes in a gyromagnetic photonic crystal. *Phys. Rev. Lett.* **2008**, *100*, 013905. [CrossRef]
23. Silveirinha, M.G. Chern invariants for continuous media. *Phys. Rev. B* **2015**, *92*, 125153. [CrossRef]
24. Wang, Z.; Chong, Y.; Joannopoulos, J.D.; Soljačić, M. Observation of unidirectional backscattering-immune topological electromagnetic states. *Nature* **2009**, *461*, 772–775. [CrossRef] [PubMed]
25. Wang, M.; Zhang, R.Y.; Zhang, L.; Wang, D.; Guo, Q.; Zhang, Z.Q.; Chan, C.T. Topological one-way large-area waveguide states in magnetic photonic crystals. *Phys. Rev. Lett.* **2021**, *126*, 067401. [CrossRef]
26. Xu, J.; You, Y.; Xiao, S.; Hong, L.; Shen, Y.; Tsakmakidis, K.L.; Luo, Y. Assembling magneto-optical heterostructures for all-optical multi-functional devices. *Opt. Laser Technol.* **2025**, *188*, 112858. [CrossRef]
27. Song, X.; Yang, C.; Yuan, R.; Xiang, Y. Electrochemical label-free biomolecular logic gates regulated by distinct inputs. *Biosens. Bioelectron.* **2022**, *202*, 114000. [CrossRef]
28. Gao, L.; Chen, L.; Wei, H.; Xu, H. Lithographically fabricated gold nanowire waveguides for plasmonic routers and logic gates. *Nanoscale* **2018**, *10*, 11923–11929. [CrossRef] [PubMed]
29. Pan, D.; Wei, H.; Xu, H. Optical interferometric logic gates based on metal slot waveguide network realizing whole fundamental logic operations. *Opt. Express* **2013**, *21*, 9556–9562. [CrossRef] [PubMed]
30. Assunção, T.F.; Nascimento, E.M.; Sombra, A.S.B.; Lyra, M.L. Phase-shift-controlled logic gates in y-shaped nonlinearly coupled chains. *Phys. Rev. E* **2016**, *93*, 022218. [CrossRef]

Disclaimer/Publisher's Note: The statements, opinions and data contained in all publications are solely those of the individual author(s) and contributor(s) and not of MDPI and/or the editor(s). MDPI and/or the editor(s) disclaim responsibility for any injury to people or property resulting from any ideas, methods, instructions or products referred to in the content.

https://doi.org/10.3390/mi17050509

micromachines

MDPI

Article

Polydimethylsiloxane-Based Quantum Dot Color Conversion Layers for QD-OLED Applications

Sang-Uk Byun, Su-Been Lee, Seo-Young Kim, Yu-Lim Seok, Gun Park and Dae-Gyu Moon *

Department of Electronic Materials, Device, and Equipment Engineering, Soonchunhyang University, Asan-si 31538, Chungcheongnam-do, Republic of Korea
* Correspondence: dgmoon@sch.ac.kr; Tel.: +82-41-530-1312

Abstract

Quantum dot (QD)-based color conversion layers are key components in QD-OLED displays because they can provide high color purity and simplified pixel architectures by converting blue emission from OLEDs into red or green light. The performance of the color conversion layer strongly depends on the blue light absorption, blue leakage, and overall emission efficiency of the display. We fabricated the color conversion layers using a thermally curable polydimethylsiloxane (PDMS) matrix, and their color conversion characteristics were systematically compared with those of QD-only layers. In the QD-only layers, the intensity of the converted green emission increased with increasing QD concentration due to enhanced absorption of blue light emitted from the OLED. However, a large fraction of blue light was transmitted through the layer without being absorbed by the QDs, resulting in a significant blue leakage and a relatively low output/input efficiency below 10%. In contrast, PDMS-based QD color conversion layers exhibited substantially improved color conversion characteristics. By varying the QD concentration and controlling the layer thickness, blue leakage was significantly suppressed and the green emission intensity increased. The maximum color conversion efficiency of 30.0% was obtained at a QD concentration of 8.3 wt% with a layer thickness of 35.9 μm.

Keywords: quantum dot; color conversion layer; PDMS; blue leakage; color conversion efficiency; output/input efficiency

1. Introduction

Quantum dots (QDs) are nanoscale semiconductor particles that exhibit discrete energy levels and size-dependent optical properties due to quantum confinement effects [1–3]. QDs have been extensively studied during past decades because of their superior characteristics such as size-tunable wavelengths, high photoluminescence quantum yield, and narrow emission bandwidth in display applications [4–9]. In particular, QDs have attracted much attention in recent years as color conversion materials for the blue organic light-emitting devices (OLEDs), since they can provide high-quality displays by combining the advantages of OLEDs, such as self-emission and high contrast ratio, with the excellent characteristics of QDs, including high color purity and spectral tunability [10–12]. In the QD-OLEDs, the blue OLED serves as the excitation source and the QDs act as the color conversion layer. QDs absorb the blue light emitted from OLED and re-emit red or green light from QDs. Since red and green pixels originate from a single blue OLED, there is no need to use a fine metal mask for sub-pixel formation, offering a simpler pixel patterning process compared to RGB OLED arrays [7]. QD-OLEDs possess all the excellent

characteristics of OLEDs, such as a high contrast ratio, fast response time, thin form factor, and mechanical flexibility [13–15]. In addition, QD-OLEDs provide better color mixing and a wider color gamut compared to conventional OLEDs due to symmetric and sharp emission characteristics of QDs [16–18].

In QD-OLEDs, QDs are integrated into a stable and efficient color conversion layer that is optically transparent, mechanically robust, and compatible with the OLED substrate. One of the key issues in fabricating color conversion layers is color conversion efficiency, which determines how effectively blue light is converted into green and red light. QDs exhibit superior color conversion efficiency compared to traditional phosphors due to their high quantum yield and narrow emission spectra [7]. This efficiency directly impacts the overall brightness of displays. The most common approach for fabricating a color conversion layer is to formulate QD ink by dispersing QDs in polymer solutions and forming a thin film using a solution coating method [19–26]. Among the polymer candidates, UV-curable resins have been widely used due to their simple processing, patterning capabilities, and fast curing time [21–26]. Photopolymer resin-based QD inks allow for layer-by-layer printing, making it easy to control the thickness [26]. However, UV-curable QD–polymer composites face several limitations when applied to QD-OLEDs. Prolonged exposure to UV light can degrade both the polymer and the QDs themselves, reducing photoluminescence efficiency and spectral stability [27,28]. In addition, the rapid curing process can lead to internal stresses, non-uniform QD dispersion, and shrinkage-induced cracks [29]. These effects are particularly problematic when scaling to large-area displays or achieving high pixel density in high-resolution displays. Moreover, some UV-curable resins absorb part of the blue light emitted by the OLED, decreasing the excitation efficiency of QDs and thus lowering the conversion efficiency [30].

In this paper, we investigated a color conversion layer in which QDs were dispersed in a thermally curable polydimethylsiloxane (PDMS). PDMS is a silicon-based elastomer known for its high optical transparency in the visible and near UV range, excellent thermal and environmental stability, and low elastic modulus [31]. Unlike UV-cured systems, PDMS curing does not require irradiation and proceeds uniformly through thermal crosslinking, minimizing light-induced degradation and allowing more homogenous QD dispersion [32]. Although several authors have demonstrated color conversion layers fabricated using the nanocomposites composed of QDs dispersed in PDMS, most of the research has focused on color conversion for the white LEDs [33–35]. In this paper, we report on a PDMS-based QD color conversion layer for use as a pixel component in QD-OLEDs. By varying the QD concentration and layer thickness, we fabricated PDMS-based QD color conversion layers and investigated their color conversion characteristics, including color conversion spectrum, conversion efficiency, and blue leakage.

2. Materials and Methods

Blue OLEDs were fabricated using ITO-coated glass substrates with a sheet resistance of about 10 Ω/sq. ITO anode patterns were defined using a photolithography process. The patterned ITO substrates were cleaned with acetone, isopropyl alcohol, and deionized water, followed by oxygen plasma treatment to remove organic residues before evaporating the organic materials. Organic and metal layers were deposited by the vacuum thermal evaporation method at a base pressure of 10^{-6} Torr. After depositing a 50 nm thick N,N′-bis(naphthalen-1-yl)-N,N′-bis(phenyl)-benzidine (NPB) hole transport layer, a 50 nm thick 4,4′-bis(2,2-diphenylethenyl)-1,1′-biphenyl (DPVBi) luminescent layer was evaporated. Finally, 0.5 nm thick LiF and a 100 nm thick Al layer were sequentially evaporated to define the cathodes through a shadow mask without breaking the vacuum. The completed device structure is ITO/NPB (50 nm)/DPVBi (50 nm)/LiF (0.5 nm)/Al. The devices were

https://doi.org/10.3390/mi17050505

encapsulated in a nitrogen glove box. The electroluminescence (EL) spectra of the devices were measured using a spectroradiometer (CS1000, Minolta, Tokyo, Japan). To ensure measurement accuracy, the spectroradiometer was periodically calibrated using a standard luminance source traceable to national standards by the supplier. The spectroradiometer was warmed up for at least 30 min prior to data acquisition. Dark calibration was performed prior to each measurement to eliminate the influence of dark current and electronic noise. All measurements were conducted in a light-tight dark box under fixed optical geometry to minimize ambient light and systematic errors.

Green-emitting CdSe/ZnS QDs (ZEUS, Hwaseong, Republic of Korea) with oleic acid ligands were used for fabricating the PDMS-based QD color conversion layers. PDMS and curing agent were purchased from Sewang Hitech Silicone (Kimpo, Republic of Korea). To ensure uniform dispersion, the QDs were first dispersed in octane, which is a nonpolar solvent suitable for stabilizing ligand-capped QDs. Four different QD concentrations of 100, 200, 400, and 800 mg were each dissolved in 1 mL of octane and stirred at 1500 rpm for over 3 h. The QD-octane solution was then mixed with 1 g of PDMS base and 0.1 g of a thermal curing agent, followed by stirring at 300 rpm for 30 min. The resulting PDMS-QD solution was spin-coated and cured on a hot plate at 150 °C for 30 min to form the QD color conversion layers. The fabricated color conversion layer was placed on top of a blue OLED, and its conversion spectrum was measured using a spectroradiometer. The layer thickness was measured using a surface profilometer (Surfcorder ET3000, Kosaka Laboratory, Tokyo, Japan). The shape and size distributions of the QDs were investigated by transmission electron microscopy (TEM, JEM-ARM200F, JEOL, Tokyo, Japan). Time-resolved photoluminescence (TRPL) was measured using a modular research fluorometer for lifetime and steady state measurements (HORIBA, Fluorolog-QM, Kyoto, Japan)

3. Results and Discussion

Figure 1 shows the TEM image, particle size distribution, photoluminescence (PL), and absorption spectra of the green-emitting CdSe/ZnS QDs, as well as the EL spectrum of the blue OLED. The QDs exhibit nearly spherical shapes. The particle sizes of QDs range from 6.5 to 10.0 nm, with the highest population in the range of 8.0–8.5 nm. The average particle size was measured to be 8.1 nm. The PL spectrum of QDs dispersed in octane exhibits an emission peak at 534 nm with a full width half maximum (FWHM) of the spectrum was 45 nm. The blue OLED with a structure of ITO/NPB/DPVBi/LiF/Al exhibits an EL emission peak at 464 nm with a FWHM of 68 nm. In addition, the emission spectrum of the blue OLED significantly overlaps with the absorption region of the QDs, enabling efficient excitation.

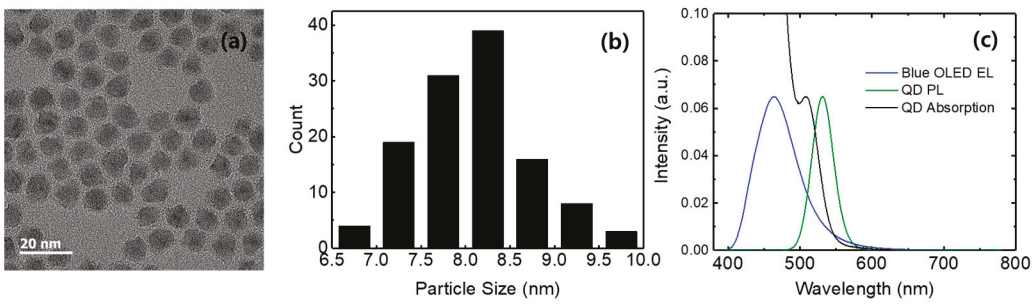


Figure 1. (**a**) TEM image, (**b**) particle size distribution, and (**c**) PL and absorption spectra of the green-emitting CdSe/ZnS QDs, and EL spectrum of the blue OLED.

To investigate the effect of the PDMS matrix on color conversion, the color conversion characteristics of a QD-only layer were first examined. A QD solution was prepared by dispersing QDs in octane, and a QD-only layer was formed via spin coating. Figure 2a

https://doi.org/10.3390/mi17050505

shows a schematic illustration of the QD layer fabrication process and the color conversion process using the blue OLED. The concentration of QDs dispersed in octane was varied to 100, 200, 400, and 800 mg/mL. Figure 2b shows the thickness of the spin-coated QD-only layers as a function of QD concentration. As the QD concentration increases, more QDs accumulate after spin coating, resulting in an increase in the layer thickness.

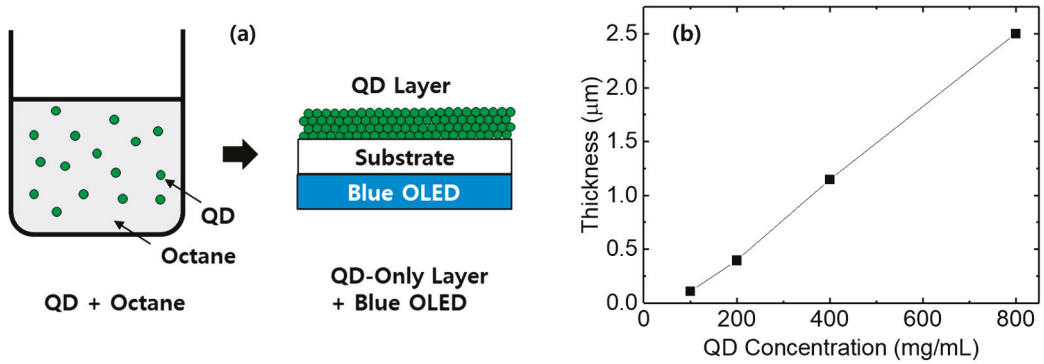


Figure 2. (**a**) Schematic illustration of the fabrication of QD-only layer for color conversion of the blue OLED and (**b**) thickness of the QD-only layer as a function of QD concentration.

Figure 3a shows the color conversion spectra of QD-only layers prepared with different concentrations of QDs. The color conversion of the blue OLED by the QDs occurs as the QDs absorb the light emitted from the blue OLED, and the absorption of blue light depends on the thickness of the QD layer. When the QD concentration is 100 mg/mL, the QD layer is too thin, resulting in almost no color conversion. On the other hand, a clearly distinguished green peak from the QDs is observed when the QD concentration increases to 800 mg/mL. In addition, the peak wavelength of the transmitted blue light moves toward the longer wavelength region as the QD concentration increases. For example, the emission peak wavelength of the blue OLED is 464 nm, whereas the QD conversion layer at 800 mg/mL exhibits a peak wavelength of 480 nm. This red shift is considered to be due to the wavelength-dependent absorption characteristics of the QDs. Since QDs exhibit stronger absorption at shorter wavelengths within the blue emission range of the OLED, the higher energy components of the blue emission are preferentially absorbed as the QD layer becomes thicker, while the lower components are relatively less attenuated. This difference in absorption leads to an apparent red shift.

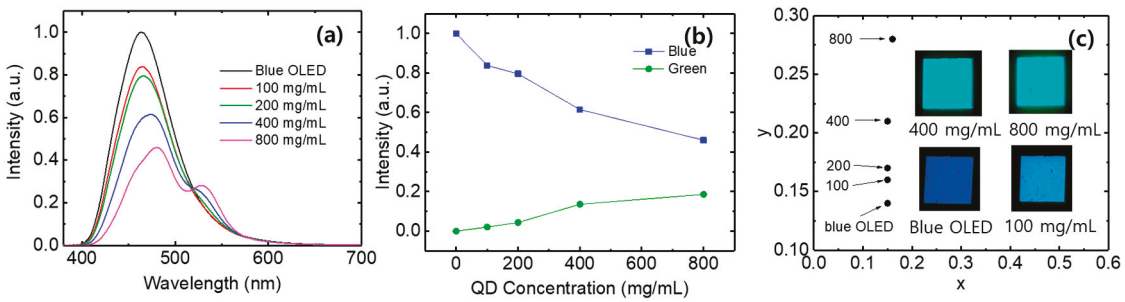


Figure 3. (**a**) Color conversion spectra, (**b**) blue and green emission intensities, (**c**) color coordinates and emission images of QD-only layers fabricated with different QD concentrations.

Figure 3b shows the maximum intensities of the transmitted blue light and the converted green light as a function of QD concentration. As the QD concentration increases, the thickness of the QD layer increases, resulting in greater absorption of blue light by the QDs. Consequently, the intensity of the converted green light increases, while the intensity of the transmitted blue light decreases. Figure 3c shows the color coordinates and

https://doi.org/10.3390/mi17050505

emission images of the light converted by the QD-only layers. The blue OLED exhibits color coordinates of (0.15, 0.14). At a QD concentration of 100 mg/mL, little color conversion occurs, and the color coordinates are nearly identical to those of the blue OLED, at (0.15, 0.16). As the QD concentration increases, more blue light is absorbed by the QDs, causing the color coordinates to shift toward the green region. At a QD concentration of 800 mg/mL, the color coordinates are (0.16, 0.28). Although the color coordinates shift toward the green region, the blue emission remains dominant and the green emission is relatively weak, resulting in a greenish-blue color. In addition, the color-converted images become increasingly blurred and diffused with increasing QD concentration, indicating enhanced light scattering within the layer.

Figure 4 shows the color conversion efficiencies and the output/input efficiencies of the QD-only layer as a function of QD concentration. The color conversion efficiency is defined as follows [24]: $\eta_{CCE} = A_{QD}/(A_{bOLED} - A_{btrans}) \times 100$, where η_{CCE} is the color conversion efficiency, A_{QD} is the integrated area of the converted green emission spectrum, A_{bOLED} is the integrated area of the blue light spectrum incident from the OLED onto the QD layer, and A_{btrans} is the integrated area of the blue light spectrum transmitted through the QD layer. The output/input efficiency is defined as follows [24]: $\eta_{out/in} = A_{QD}/A_{bOLED} \times 100$, where $\eta_{out/in}$ is the output/input efficiency. A_{QD} and A_{bOLED} are the same as defined above.

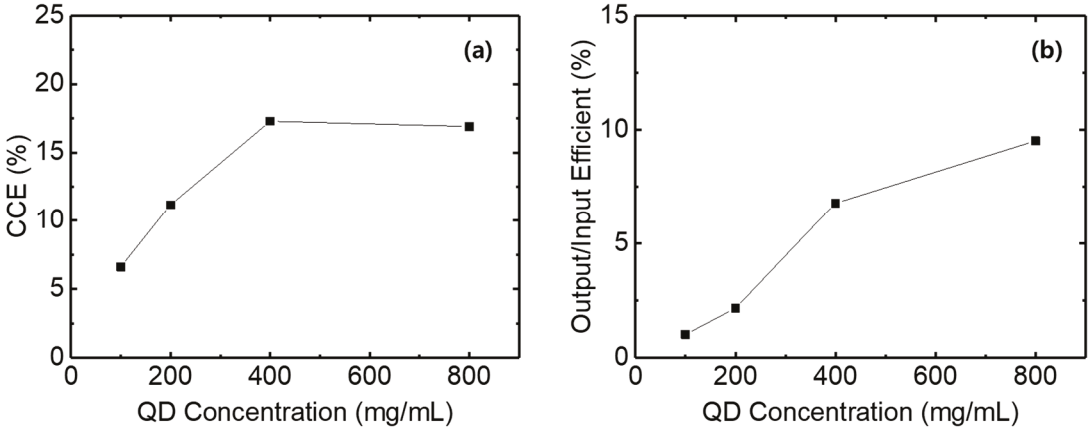


Figure 4. (**a**) Color conversion efficiencies and (**b**) output/input efficiencies of QD-only layers fabricated with different QD concentrations.

The QD-only layer exhibits a low color conversion efficiency of 6.6% due to the thin thickness at a QD concentration of 100 mg/mL. As the QD concentration increases to 400 mg/mL, the thickness of the QD-only layer increases, and the color conversion efficiency rises to 17.3%. When the QD concentration reaches 800 mg/mL, the color conversion efficiency slightly decreases to 16.9%. In contrast, the output/input efficiency exhibits lower values than the color conversion efficiency, because it does not account for the transmitted blue light, i.e., blue leakage. At a QD concentration of 100 mg/mL, about 85% of the blue light is leaked without being absorbed by the QDs, resulting in a very low proportion of converted light, approximately 1%. As the QD concentration increases, a higher proportion of blue light is absorbed by the QDs. Consequently, the output/input efficiency increases, reaching 9.5% at a QD concentration of 800 mg/mL.

To fabricate the color conversion layers by dispersing QDs in PDMS, QDs were first added to octane to prepare a QD solution, which was then mixed with PDMS containing a curing agent. Figure 5a shows a schematic illustration of the fabrication process of the color conversion layer in which QDs are dispersed in PDMS, as well as a schematic of the color conversion process using a blue OLED. For the color conversion layers, 1 g of PDMS

https://doi.org/10.3390/mi17050505

and 0.1 g of curing agent were used. In addition, the concentration of QDs in 1 mL of octane was varied to 100, 200, 400, and 800 mg/mL. Therefore, the concentrations of QDs dispersed in PDMS were 8.3, 15.4, 26.7, and 42.1 wt%, respectively. After spin-coating the solution containing PDMS, curing agent, octane, and QDs, the coated films were cured at 150 °C for 30 min to form the color conversion layers. The thickness of the color conversion layers was controlled by repeating the spin-coating and curing processes.

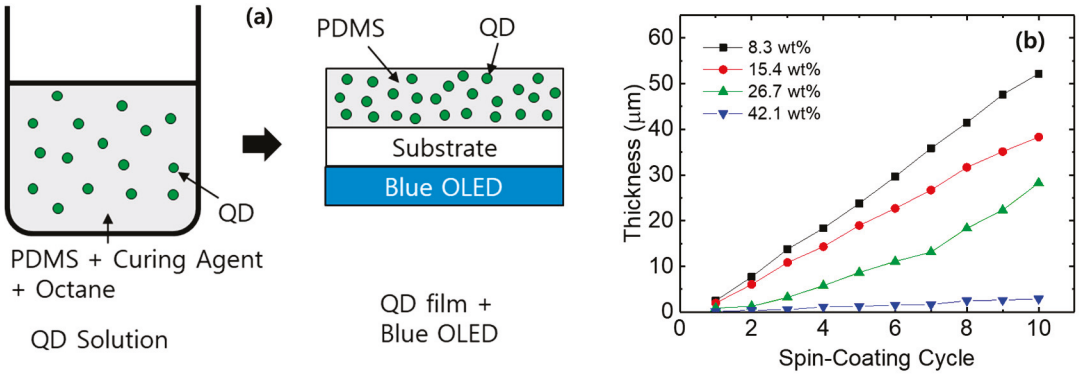


Figure 5. (**a**) Schematic illustration of the fabrication of the PDMS-based QD color conversion layer, and (**b**) thickness of the PDMS-based color conversion layer as a function of spin-coating cycle.

Figure 5b shows the thickness of the color conversion layers as a function of the number of repeated spin-coating and curing cycles. The thickness of the layer increases as the number of spin-coating cycles increases, as the layer cured at 150 °C remains undamaged when subsequent PDMS-QD mixtures are spin-coated onto it. It should be noted that the thickness of the color conversion layer decreases with increasing QD concentration despite the higher solid content. The decrease in the thickness of the color conversion layer at higher QD concentrations is presumed to be related to the plasticizing effect of oleic acid ligands coordinated on the QDs [36]. As the QD concentration increases, the amount of oleic acid also increases, which is believed to reduce the viscosity and surface tension of the PDMS-QD solution [36,37]. The QD ligands can also delay the PDMS curing kinetics, allowing the wet film to flow for a longer time during spin-coating, which can result in the formation of a thinner layer [38]. We observed a noticeable increase in the fluidity of the PDMS-QD mixture with high QD loading. This reduced viscosity allows the solution to spread more thinly during the spin coating process, resulting in a decrease in the final film thickness. On the other hand, we observed that when the QD concentration exceeded 42.1 wt%, it was impossible to measure the thickness of the layer using a surface profiler because curing of the layer did not occur. This result suggests that an excessive amount of oleic acid ligands hinders the network formation of the PDMS matrix.

Figure 6 shows the color conversion spectra of the PDMS-based QD color conversion layers. As the layer thickness increases, the transmitted blue emission decreases and the converted green emission increases for all QD concentrations. At a low concentration of 8.3 wt%, the blue emission dominates due to the limited absorption of the incident blue light. As the QD concentration increases to 15.4 wt% and 26.7 wt%, the QD emission progressively increases, while the blue leakage correspondingly decreases. At the highest concentration of 42.1 wt%, the blue emission is significantly suppressed, and the QD emission becomes dominant. These results indicate that the PDMS-based QD color conversion layers exhibit significantly lower blue leakage and improved color conversion characteristics compared with the QD-only layers.

Figure 7 shows the variation in the maximum intensities of transmitted blue light and converted green light for PDMS-based QD color conversion layers with different

https://doi.org/10.3390/mi17050505

QD concentrations. As the thickness increases, the blue intensity decreases for all QD concentrations, indicating the enhanced absorption of the incident blue light within the QD conversion layer. This trend becomes more pronounced at higher QD concentrations, where the stronger absorption leads to a more rapid attenuation of the blue emission with increasing thickness. The corresponding green emission intensity increases with increasing layer thickness due to the enhanced color conversion by the QDs. However, beyond a certain thickness, the green emission intensity begins to saturate or slightly decreases. In addition, at higher QD concentrations, the green emission reaches its maximum at a relatively smaller thickness.

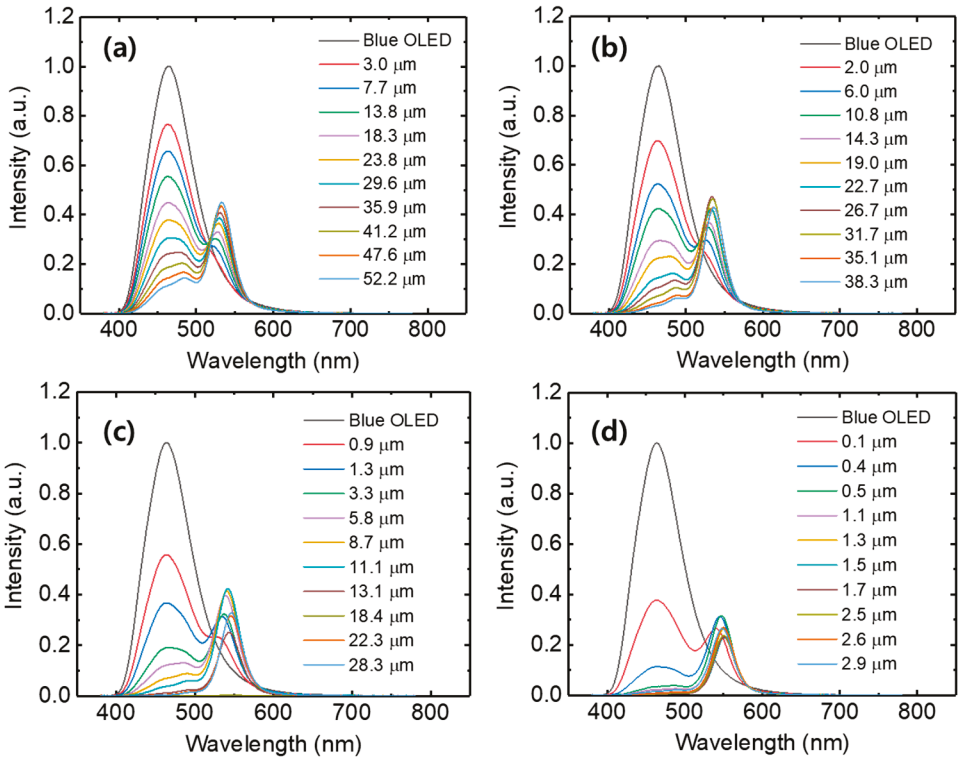


Figure 6. Color conversion spectra of PDMS-based QD color conversion layers with QD concentrations of (**a**) 8.3 wt%, (**b**) 15.4 wt%, (**c**) 26.7 wt%, and (**d**) 42.1 wt%.

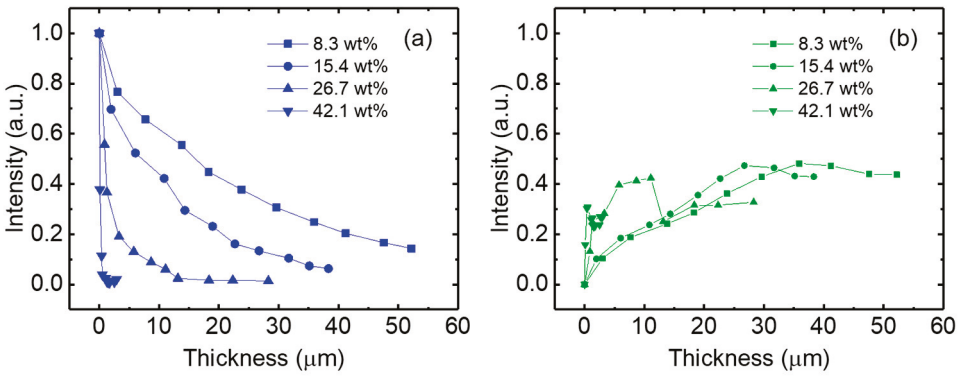


Figure 7. (**a**) blue and (**b**) green emission intensities of PDMS-based QD color conversion layers with different QD concentrations.

Figure 8a shows the color coordinates of the PDMS-based QD color conversion layers with different concentrations of QDs. As the layer thickness and the QD concentration increase, the emission color systematically shifts from the blue region toward the green region. This result directly reflects the progressive suppression of the blue leakage and

https://doi.org/10.3390/mi17050505

the enhancement of the green emission. For example, the color coordinates are (0.23, 0.61) in the 25.1 μm layer with 15.4 wt% QDs. Therefore, the color coordinates of the PDMS-based QD layer are significantly improved compared to those of the QD-only layer and are closer to the standard green coordinates (0.19, 0.80) of Rec. 2020. Figure 8b shows the corresponding color conversion images. As the QD concentration and thickness increase, the emission color gradually shifts from bluish green to a more saturated green. Figure 8b also represents that the color-converted images become increasingly blurred and diffused with increasing QD concentration and layer thickness, indicating enhanced light scattering within the PDMS-based QD layer. This suggests that the QDs act as scattering centers in the PDMS matrix, inducing multiple scattering of blue light. This scattering increases the effective optical path length of blue photons within the layer. This light-trapping effect enhances the probability of blue light absorption by the QDs. Consequently, blue leakage is significantly suppressed, and the green emission is correspondingly improved. However, spatial inhomogeneities can be observed in the color conversion images of 42.1 wt% QDs, which may be attributed to QD aggregation within the PDMS matrix. This aggregation results in non-uniform emission and slight degradation of color purity.

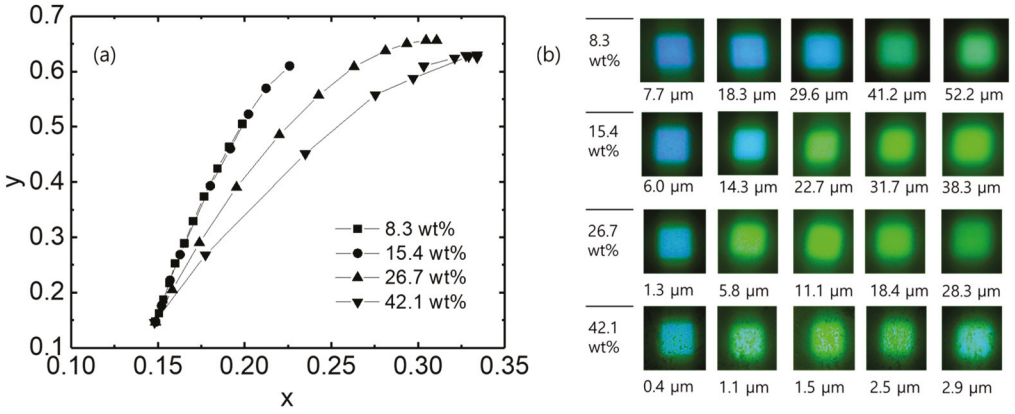


Figure 8. (**a**) Color coordinates and (**b**) color conversion images of PDMS-based QD color conversion layers with different QD concentrations.

Figure 9 shows the color conversion efficiencies and output/input efficiencies of PDMS-based QD color conversion layers, and TRPL decay curves of the PDMS-QD solutions. The color conversion efficiency increases with increasing thickness, reaches a maximum value, and then slightly decreases for all QD concentrations. The 8.3 wt% layer exhibits a maximum color conversion efficiency of 30.0% at a thickness of 35.9 μm, while the 15.4 wt% and 26.7 wt% layers show maximum color conversion efficiencies of 26.7% and 25.7% at thicknesses of 27.9 and 5.8 μm, respectively. The 42.1 wt% layer exhibits a maximum color conversion efficiency of 19.0% at a thickness of 0.4 μm. This result indicates that the optimal thickness for maximum color conversion efficiency decreases with increasing QD concentration. Furthermore, the maximum color conversion efficiency also decreases as the QD concentration increases. A similar trend is observed in the output/input efficiency, where both the maximum output/input efficiency and corresponding optimal thickness decrease with increasing QD concentration.

To further investigate these efficiency characteristics, TRPL measurements of the PDMS-QD solutions were performed. The PL decay is significantly prolonged as the QD concentration increases from 8.3 wt% to 42.1 wt%, indicating enhanced self-absorption in the dense QD environment. In such a high-density QD system, photons emitted by the QDs are likely to be reabsorbed by neighboring QDs before escaping the sample, thereby extending the measured decay time [39]. These results suggest that the PDMS-QD

https://doi.org/10.3390/mi17050505

system effectively traps and recycles photons through multiple scattering and reabsorption events. In the PDMS-QD layer, multiple scattering increases the effective optical path length, thereby enhancing the probability of blue photon absorption and improving color conversion efficiency while suppressing blue leakage compared to QD-only films. However, at higher QD concentrations, excessive self-absorption leads to repeated photon recycling processes, during which photons are increasingly lost via non-radiative recombination pathways. In addition, serious QD agglomeration in the 42.1 wt% layers may further exacerbate self-absorption and reduce the maximum color conversion efficiency.

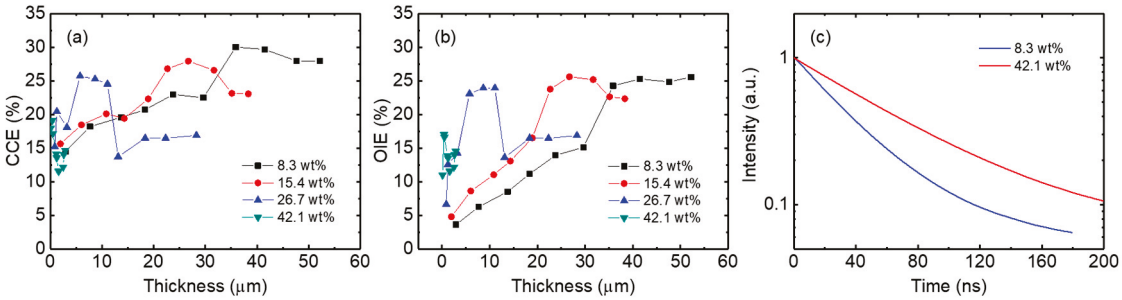


Figure 9. (**a**) Color conversion efficiencies, (**b**) output/input efficiencies of PDMS-based QD color conversion layers with different QD concentrations, and (**c**) TRPL decay curves of PDMS-QD solutions.

4. Conclusions

Color conversion layers were fabricated by dispersing QDs in a thermally curable PDMS matrix, and the color conversion characteristics of blue light emitted from a blue OLED were compared with those of QD-only layers. QD-only layers were prepared by spin-coating a QD solution dispersed in octane. As the QD concentration in octane increased from 100 to 800 mg/mL, the thickness of the QD-only layer increased from 0.11 to 2.51 μm, resulting in enhanced absorption of blue light by the QDs. Consequently, the green emission increased while the blue leakage decreased. However, a considerable amount of blue light was transmitted through the layer, resulting in a relatively low maximum color conversion efficiency of 17.3%. In contrast, the PDMS-based QD color conversion layer exhibited significantly improved color conversion characteristics. PDMS-based layers were fabricated by spin-coating a mixture of thermally curable PDMS, a curing agent, octane, and QDs. The concentration of QDs varied from 8.3 to 42.1 wt%, and the thickness of the QD layer was controlled by repeating the spin-coating and thermal curing processes. The PDMS-based QD layers exhibited significantly reduced blue leakage and substantially increased green emission intensity compared with the QD-only layers. At a QD concentration of 8.3 wt% and a layer thickness of 35.9 μm, the PDMS-based layer exhibited a maximum color conversion efficiency of 30.0%. Higher QD concentrations slightly reduced the maximum efficiency due to the photon loss caused by excessive self-absorption, although blue leakage was suppressed even with thinner layers. These results indicate that the PDMS-based QD color conversion layer provides improved blue light absorption, reduced blue leakage, and enhanced color conversion efficiency, demonstrating its strong potential for high-performance QD-OLED display applications.

Author Contributions: Conceptualization, D.-G.M.; methodology, S.-U.B., S.-B.L. and S.-Y.K.; validation, D.-G.M.; data curation, S.-U.B., Y.-L.S. and G.P.; writing—original draft preparation, S.-U.B.; writing—review and editing, D.-G.M.; supervision, D.-G.M.; project administration, D.-G.M.; funding acquisition, D.-G.M. All authors have read and agreed to the published version of the manuscript.

https://doi.org/10.3390/mi17050505

Funding: This work was supported by the Soonchunhyang University Research Fund and Korea Institute for Advancement of Technology (KIAT) grant funded by the Korea government (MOTIE) (RS-2025-02263458, HRD Program for Industrial Innovation), and the Super-Gap R&D Project (RS-2024-00420455) of MOTIE/KEIT.

Institutional Review Board Statement: Not applicable.

Informed Consent Statement: Not applicable.

Data Availability Statement: The original contributions presented in this study are included in the article. Further inquiries can be directed to the corresponding author.

Conflicts of Interest: The authors declare no conflicts of interest.

References

1. Alivisatos, A.P. Semiconductor clusters, nanocrystals, and quantum dots. *Science* **1996**, *271*, 933–937. [CrossRef]
2. Dabbousi, B.O.; Rodriguez-Vejo, J.; Mikulec, F.V.; Hine, J.R.; Mattoussi, H.; Ober, R.; Jensen, K.F.; Bawendi, M.G. (CdSe)ZnS core-shell quantum dots: Synthesis and characterization of a size series of highly luminescent nanocrystallites. *J. Phys. Chem. B* **1997**, *101*, 9463–9475. [CrossRef]
3. Reiss, P.; Protière, M.; Li, L. Core/shell seminconductor nanocrystals. *Small* **2009**, *5*, 154–168. [CrossRef]
4. Arquer, F.P.G.; Talapin, D.V.; Klimov, I.; Arakawa, Y.; Bayer, M.; Sargent, E.H. Semiconductor quantum dots: Technological progress and future challenges. *Science* **2021**, *373*, 640. [CrossRef]
5. Jang, E.; Jang, H. Review: Quantum dot light-emitting diodes. *Chem. Rev.* **2023**, *123*, 4663–4692. [CrossRef]
6. Tian, D.; Ma, H.; Huang, G.; Gao, M.; Cai, F.; Fang, Y.; Li, C.; Jiang, X.; Wang, A.; Wang, S.; et al. A review on quantum dot light-emitting diodes: From materials to applications. *Adv. Opt. Mater.* **2023**, *11*, 2201965. [CrossRef]
7. Li, G.; Tseng, M.C.; Chen, Y.; Yeung, F.S.; He, H.; Cheng, Y.; Cai, J.; Chen, E.; Kowk, H.S. Color-conversion displays: Current status and future outlook. *Light Sci. Appl.* **2024**, *13*, 301. [CrossRef] [PubMed]
8. Chen, J.; Zhao, Q.; Yu, B.; Lemmer, U. A review on quantum dot-based color conversion layers for mini/micro-LED displays: Packaging, light management, and pixelation. *Adv. Opt. Mater.* **2024**, *12*, 2300873. [CrossRef]
9. Tessier, M.D.; Dupont, D.; Nolf, K.D.; Roo, J.D.; Hens, Z. Economic and size-tunable synthesis of InP/ZnE (E = S, Se) colloidal quantum dots. *Chem. Mater.* **2015**, *27*, 4893–4898. [CrossRef]
10. Hu, Z.; Yin, Y.; Ali, M.U.; Peng, W.; Zhang, S.; Zou, T.; Li, Y.; Jiao, S.; Chen, S.J.; Lee, C.Y.; et al. Inkjet printed uniform quantum dots as color conversion layers for full-color OLED displays. *Nanoscale* **2020**, *12*, 2103–2110. [CrossRef]
11. Kim, D.Y.; Han, Y.J.; Choi, J.; Sakong, C.; Ju, B.K.; Cho, K.H. Inkjet printed quantum dot film formed by controlling surface wettability for blue-to-green color conversion. *Org. Electron.* **2020**, *84*, 105814. [CrossRef]
12. Yin, M.; Pen, T.; Yu, Z.; Peng, X.; Zhang, X.; Xie, W.; Liu, S.; Zhang, L. Color-stable WRGB emission from blue OLEDs with quantum dots-based patterned down-conversion layer. *Org. Electron.* **2018**, *62*, 407–411. [CrossRef]
13. Tang, C.W.; VanSlyke, S.A. Organic electroluminescent diodes. *Appl. Phys. Lett.* **1987**, *51*, 913–915. [CrossRef]
14. Hong, G.; Gan, X.; Leonhardt, C.; Zhang, Z.; Seibert, J.; Busch, J.M.; Bräse, S. A brief history of OLEDs-emitter development and industry milestones. *Adv. Mater.* **2021**, *33*, 2005630. [CrossRef] [PubMed]
15. Huang, Y.; Hsiang, E.L.; Deng, M.Y.; Wu, S.T. Mini-LED, micro-LED and OLED displays: Present status and future perspectives. *Light Sci. Appl.* **2020**, *9*, 105. [CrossRef] [PubMed]
16. Shirasaki, Y.; Supran, G.J.; Bawendi, M.G.; Bulović, V. Emergence of colloidal quantum-dot light-emitting technologies. *Nat. Photon.* **2013**, *7*, 13–23. [CrossRef]
17. Yang, S.; Ren, Y.; Luo, D.; Shang, X.; Fang, W.; Ye, S.; Liu, B. Research progress in hybrid light-emitting diodes based on quantum dots and organic emitters. *J. Lumin.* **2024**, *270*, 120560. [CrossRef]
18. Kim, J.; Roh, J.; Park, M.; Lee, C. Recent advances and challenges of colloidal quantum dot light-emitting diodes for display applications. *Adv. Mater.* **2024**, *36*, 2212220. [CrossRef]
19. Lee, S.Y.; Sakong, C.; Choi, S.; Ju, B.; Cho, K.H. Controlling the surface modification by CF_4 plasma treatment for inkjet printed color conversion layer with InP-based QDs ink. *Adv. Mater. Interfaces* **2023**, *10*, 2201851. [CrossRef]
20. Nam, E.; Lee, C.; Kim, S.J.; Chung, H.K.; Chae, H. Stability and dispersion improvement of quantum-dot films by hydrosilylation between quantum-dot ligands and a siloxane matrix. *Opt. Express* **2019**, *27*, 20037–20046. [CrossRef] [PubMed]
21. Huang, Y.M.; Singh, K.J.; Liu, A.C.; Lin, C.C.; Chen, Z.; Wang, K.; Lin, Y.; Liu, Z.; Wu, T.; Kuo, H.C. Advances in quantum-dot displays. *Nanomaterials* **2020**, *10*, 1327. [CrossRef]
22. Lee, S.Y.; Sakong, C.; Ju, B.K.; Cho, K.H. Enhancing the reliability of InP-based QD color conversion layer through a uniform organic encapsulation layer via inkjet printing. *Org. Electron.* **2024**, *135*, 107136. [CrossRef]

https://doi.org/10.3390/mi17050505

23. Hyun, B.R.; Sher, C.W.; Chang, Y.W.; Lin, Y.; Liu, Z.; Kuo, H.C. Dual role of quantum dots as color conversion layer and suppression of input light for full-color micro-LED displays. *J. Phys. Chem. Lett.* **2021**, *12*, 6946–6954. [CrossRef]
24. Park, H.; Hahm, D.; Cho, H.; Shin, J.-W.; Kang, C.-M.; Ahn, D.-H.; Joo, C.W.; Kwon, B.-H.; Kim, K.; Kim, J.Y.; et al. Efficient quantum dot color conversion layer with mixed spherical/rod-shaped scattering particles. *ACS Appl. Opt. Mater.* **2023**, *1*, 289–297. [CrossRef]
25. Lin, C.T.; Zhuan, Y.L.; Jung, N.T.; Hoang, M.S.; Chen, H.S. Design of quantum dot color converters for inkjet-printed optoelectronic devices: Violet-converted full color mini-LED. *Adv. Mater. Technol.* **2024**, *9*, 2301370. [CrossRef]
26. Elliott, A.M.; Ivanova, O.S.; Williams, C.B.; Campbell, T.A. Inkjet printing of quantum dots in photopolymer for use in additive manufacturing of nanocomposites. *Adv. Eng. Mater.* **2013**, *15*, 903–907. [CrossRef]
27. Moon, H.; Lee, C.; Lee, W.; Kim, J.; Chae, H. Stability of quantum dots, quantum dot films, and quantum dot light-emitting diodes for display applications. *Adv. Mater.* **2019**, *31*, 1804294. [CrossRef] [PubMed]
28. Baek, H.; Kang, S.; Heo, J.; Choi, S.; Kim, R.; Kim, K.; Ahn, N.; Yoon, Y.G.; Lee, T.; Chang, J.B.; et al. Insights into structural defect formation in individual InP/ZnSe/ZnS quantum dots under UV oxidation. *Nat. Commun.* **2024**, *15*, 1671. [CrossRef] [PubMed]
29. Choi, Y.; Choi, C.; Bae, J.; Park, J.; Shin, K. Synthesis of gallium phosphide quantum dots with high photoluminescence quantum yield and their application as color converters for LEDs. *J. Ind. Eng. Chem.* **2023**, *123*, 509–516. [CrossRef]
30. Ozdemir, R.; Avermaet, H.V.; Erdem, O.; Schiettecatte, P.; Hens, Z.; Aubert, T. Quantum dot patterning and encapsulation by maskless lithography for display technologies. *ACS Appl. Mater. Interfaces* **2023**, *15*, 9629–9637. [CrossRef]
31. Li, S.; Zhang, J.; He, J.; Liu, W.; Wang, Y.; Huang, Z.; Pang, H.; Chen, Y. Functional PDMS elastomers: Bulk composites, surface engineering, and precision fabrication. *Adv. Sci.* **2023**, *10*, 2304506. [CrossRef]
32. Kim, K.; Kim, D.R.; Kim, D.; Song, H.H.; Lee, S.; Choi, Y.; Lee, K.; Lee, G.H.; Lee, J.; Kim, H.H.; et al. Intrinsically-stretchable and patternable quantum dot conversion layers for stretchable displays in robotic skin and wearable electronics. *Adv. Mater.* **2025**, *37*, 2420633. [CrossRef]
33. Yu, S.; Tang, Y.; Li, Z.; Chen, K.; Ding, X.; Yu, B. Enhanced optical and thermal performance of white light-emitting diodes with horizontally layered quantum dots phosphor nano-composites. *Photonics Res.* **2018**, *6*, 90–98. [CrossRef]
34. Li, J.; Tang, Y.; Li, Z.; Ding, X.; Yu, S.; Yu, B. Improvement in color-conversion efficiency and stability for quantum-dot-based light-emitting diodes using a blue anti-transmission film. *Nanomaterials* **2018**, *8*, 508. [CrossRef]
35. Li, Z.-T.; Li, J.-X.; Li, J.-S.; Deng, Z.-H.; Deng, Y.-H.; Tang, Y. Scattering effect on optical properties of quantum dot white light-emitting diodes incorporating SiO_2 nanoparticles. *IEEE J. Quantum Electron.* **2020**, *56*, 3600109. [CrossRef]
36. Sander, M.M.; Nicolau, A.; Guzatto, R.; Samios, D. Plasticiser effect of oleic acid polyester on polyethylene and polypropylene. *Polym. Test.* **2012**, *31*, 1077–1082. [CrossRef]
37. Liu, L.; He, S.; Tang, L.; Yang, S.; Ma, T.; Su, X. Application of CO_2-switchable oleic-acid-based surfactant for reducing viscosity of heavy oil. *Nanomaterials* **2021**, *26*, 6273. [CrossRef]
38. Mourdikoudis, S.; Menelaou, M.; Fiuza-Maneiro, N.; Zheng, G.; Wei, S.; Pérez-Juste, J.; Polavarapu, L.; Sofer, Z. Oleic acid/oleylamine ligand pair: A versatile combination in the synthesis of colloidal nanoparticles. *Nanoscale Horiz.* **2022**, *7*, 941–1015. [CrossRef] [PubMed]
39. Hu, X.; Xie, Y.; Geng, C.; Xu, S.; Bi, W. Study on the color compensation effect of composite orange-red quantum dots in WLED application. *Nanoscale Res. Lett.* **2020**, *15*, 118. [CrossRef] [PubMed]

Disclaimer/Publisher's Note: The statements, opinions and data contained in all publications are solely those of the individual author(s) and contributor(s) and not of MDPI and/or the editor(s). MDPI and/or the editor(s) disclaim responsibility for any injury to people or property resulting from any ideas, methods, instructions or products referred to in the content.

https://doi.org/10.3390/mi17050505

micromachines

MDPI

Article

Design and Ultra-Precision Fabrication of Freeform Fresnel Lenses for Generating Rectangular Dark Hollow Beams

Juan Zhang [1,2], Qilu Huang [1,3,4,*], Yingxin Xu [1,2], Chaocheng Yang [1] and Tingdi Liao [1,3,4]

[1] Institute for Photonics Technology, Quanzhou Normal University, Quanzhou 362000, China
[2] College of Photonic and Electronic Information Engineering, Fujian Normal University, Fuzhou 350000, China
[3] Fujian Provincial Collaborative Innovation Center for Ultra-Precision Optical Engineering and Applications, Quanzhou 362000, China
[4] Fujian Provincial Key Laboratory for Advanced Micro-Nano Photonics Technology and Devices, Quanzhou 362000, China
* Correspondence: qilu_huang@qztc.edu.cn

Abstract

Freeform Fresnel lenses combine the powerful beam-shaping capability of freeform optics with the lightweight and compact characteristics of conventional Fresnel structures, leading to their increasing adoption across diverse applications. This paper proposes and experimentally validates a method for generating rectangular dark hollow beams using a freeform Fresnel lens. The lens is divided into multiple fan-shaped sectors centered on the optical axis, with each sector generating a defocused spot at a distinct spatial location. Based on geometrical optics, a freeform Fresnel lens with a 25 mm aperture is designed to produce a square hollow beam with a side length of 10 mm. A lens with a division angle of 5° was fabricated using ultra-precision diamond turning. The angular form error was measured to be below 0.1°, and the surface roughness was found to be below 10 nm. An optical testing system was established to characterize the generated beam profile. The experimental results successfully demonstrate the formation of the desired rectangular dark hollow beam. The measured results agree well with the simulations, confirming the feasibility and practical potential of the proposed method.

Keywords: freeform Fresnel lens; rectangular dark hollow beam; beam shaping; ultra-precision diamond turning

1. Introduction

Dark hollow beams (DHBs) are structured optical fields characterized by low on-axis intensity and a surrounding high-intensity boundary. They have been widely studied in atom optics [1,2], optical communications [3], laser material processing [4], and optical manipulation of particles [5,6]. Most existing studies focus on DHBs with circular symmetry. However, several theoretical models for DHBs with non-circular symmetry have also been reported [7–10]. Elliptical hollow beams can be used to trap microscopic particles and guide them along elliptical trajectories. They can also trap and rotate single elongated objects [11]. In addition, under certain conditions in weak atmospheric turbulence, rectangular DHBs exhibit a lower scintillation index than Gaussian, elliptical Gaussian, and rectangular flat-topped beams [12]. Freeform DHBs are particularly suitable for manipulating non-spherical objects in optical tweezers, as they help suppress unwanted rotational motion of trapped micro-objects [13].

Various methods have been proposed to generate DHBs, including phase plates [14,15], holograms [16], mode conversion techniques [17], axicon lenses [18,19], and hollow fibers [20]. Freeform Fresnel optics has recently emerged as a promising class of optical components. It combines the advanced wavefront control of freeform optics with the compact form factor of Fresnel structures. Goldstein proposed a design method for faceted freeform Fresnel lenses capable of producing prescribed output intensity distributions [21]. With the steady development of freeform Fresnel lens fabrication processes [22–24], they have been applied to compact wireless communication systems [25], irradiance shaping [26,27], and head-up displays [28].

In this study, we propose a method to generate a rectangular dark hollow beam using a freeform Fresnel lens. The lens aperture is divided into multiple fan-shaped sectors, each consisting of serrated annular Fresnel zones. A topological mapping is established between the sectorized sub-apertures and the target rectangular hollow pattern. This mapping allows each sector to redirect incident light to designated off-axis positions along the rectangular boundary. The lens is fabricated by ultra-precision diamond turning with a slow tool servo technique. Experimental results demonstrate that the generated beam profile is in good agreement with the simulations, validating the proposed method as a compact and manufacturable solution for structured beam generation.

2. Theoretical Design Method

The fundamental principle for generating a rectangular DHB using a freeform Fresnel lens is illustrated in Figure 1a. The lens is divided into several sector-shaped regions with its center as the origin. Each sector generates an off-axis focal spot at a prescribed spatial location, and each sector consists of serrated annular zones. The superposition of these off-axis focal spots forms a rectangular intensity distribution on the detection plane. The topological mapping from the fan-shaped lens sectors to the target plane is shown in Figure 1b. A freeform Fresnel lens with a division angle of $\boldsymbol{\omega}$ converts the normally incident light into a rectangular pattern with a side length of d. Light incident on a sector at an azimuth angle $\boldsymbol{\theta}$ is mapped to a point on the rectangular pattern with the corresponding azimuth angle.

The rectangular pattern is both center-symmetric and diagonally symmetric. Therefore, the design range can be restricted to azimuth angles from 0 to $\pi/4$. If the design region is divided into n fan-shaped sectors, the angle ω of each sector is $\pi/(4n)$. The distance r_n from the focal point generated by the nth fan-shaped lens sector to the origin is given by

$$r_n = \frac{d}{2\cos(\theta_n)} \tag{1}$$

where θ_n denotes the azimuth angle of the nth fan-shaped lens sector, given by

$$\theta_n = (n-1)\omega \tag{2}$$

A 2D ray diagram of light incident on the lens facets is shown in Figure 2. The freeform Fresnel lens consists of planar and groove surfaces, with the groove surfaces facing the receiver. A collimated incident light beam is refracted by the groove facet with a slope angle of α underneath the lens plane. For the nth fan-shaped lens sector, the facet angle α is given as

$$tan(\alpha) = \frac{N_1 sin(\beta)}{N_2 - N_1 cos(\beta)} \tag{3}$$

where

$$\beta = arctan[(l - r_n)/f] \tag{4}$$

https://doi.org/10.3390/mi17040448

Here, N_1, N_2 are representative refractive index of the air and the Fresnel lens material respectively, l is the distance from the center of the facet to the center axis, and f is the focal length. If we denote the groove width of Fresnel lens as w, the height of the facet h can therefore be defined as follows:

$$h = w \times tan(\alpha) \tag{5}$$

Monte Carlo ray-tracing simulations were performed using software TracePro ® 7.0 (Lambda Research Corporation, Littleton, MA, USA) to evaluate the optical performance of the modular Fresnel lenses. The key parameters of the proposed freeform Fresnel lens are as follows: lens aperture $D = 25$ mm, focal length $f = 125$ mm, two grooves per millimeter ($w = 0.5$ mm), groove height $h < 0.3$ mm, material polymethyl methacrylate (PMMA, $n = 1.49$, T = 92.4% @ 640 nm), and side length of the rectangular DHB $d = 10$ mm. A collimated light source with an output power of 1 W and a wavelength of 640 nm was used for simulation. The number of simulated rays is 500,000, and the receiving surface is a square plane with a side length of 15 mm and grid size of 128 × 128.

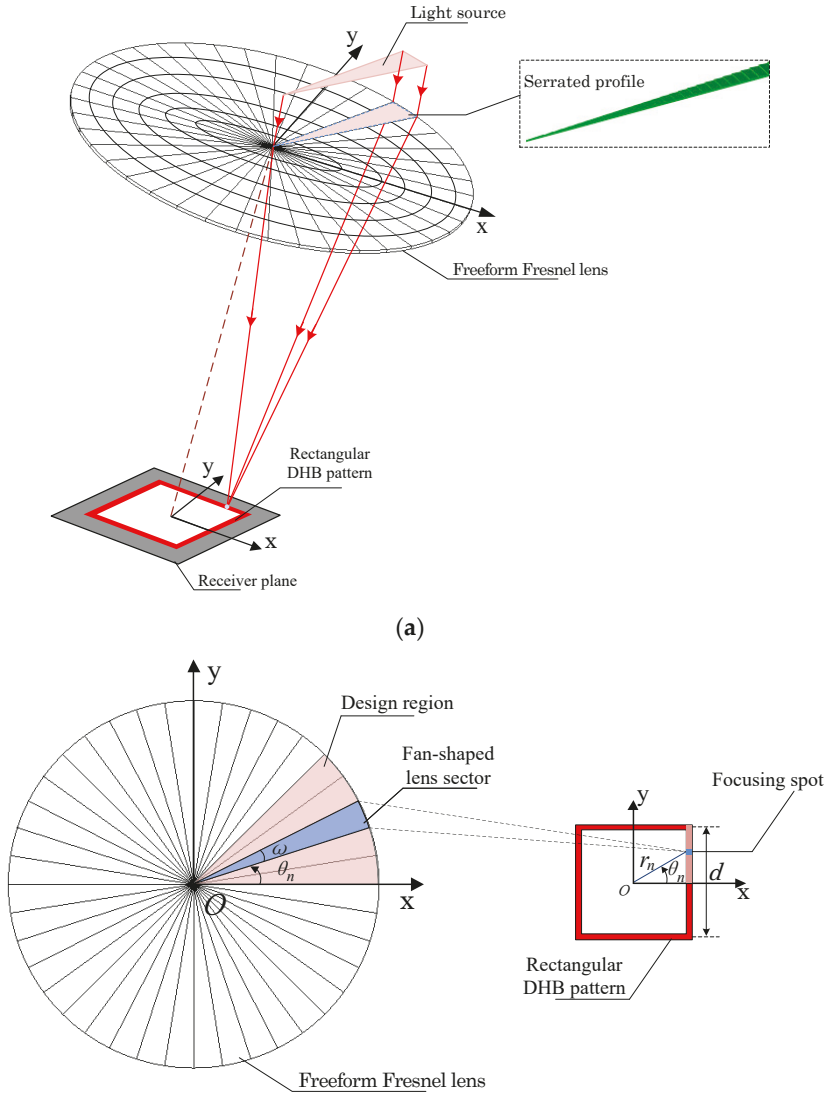


Figure 1. (**a**) Three-dimensional schematic diagram of the freeform Fresnel lens generating a rectangular DHB. (**b**) Topological mapping from fan-shaped lens sector to the receiver plane.

https://doi.org/10.3390/mi17040448

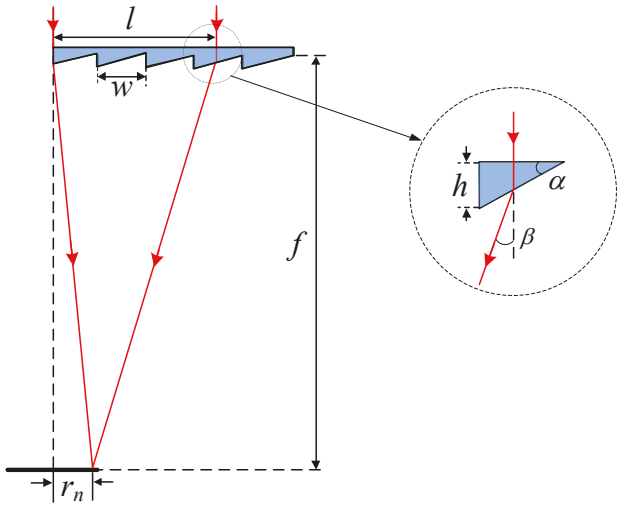
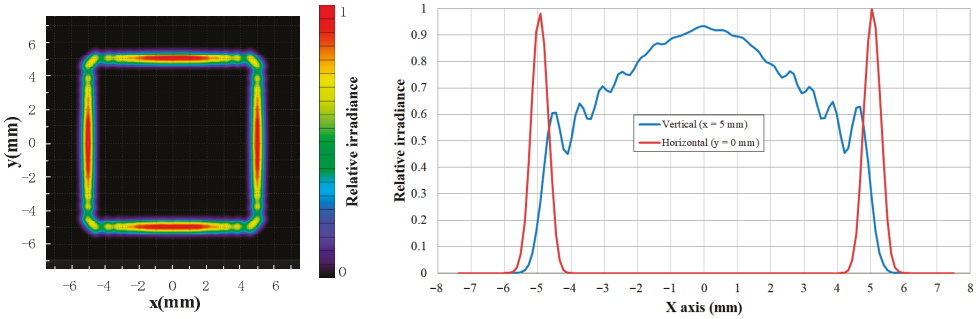


Figure 2. 2D ray diagram of light incident on the lens facets.

Figure 3a shows the two-dimensional relative irradiance distribution of the rectangular DHB for a division angle of 5° (Total 72 sectors over the lens region). The simulation indicates that a square hollow spot with a side length of 10 mm and a hollow width of approximately 1 mm can be formed on the receiver plane. The irradiance distribution exhibits higher intensity along the central regions of each side, with noticeable stitching artifacts of focused spots at the corners. Figure 3b presents the cross-sectional irradiance profiles along $x = 5$ mm and $y = 0$ mm. The results confirm the absence of stray light within the hollow region. The minimum irradiance within the effective spot area is about 50% lower than the maximum intensity.



(**a**) (**b**)

Figure 3. Relative irradiance distribution of the rectangular DHB for division angle of 5°. (**a**) Two-dimensional irradiance distribution. (**b**) Cross-sectional irradiance distribution curve.

The design principle of the proposed method is to focus the light from each fan-shaped sector into an individual spot, such that a linear intensity distribution is formed by superposing these focal spots. Owing to the finite angular span of each sector, the focal spot deviates from an ideal point and instead exhibits an arc-like profile. Accordingly, the precision of the angular division between sectors directly influences the beam intensity distribution on the receiver plane. To enhance the irradiance distribution uniformity of the rectangular DHB, the segmentation accuracy was increased to 2.5°. Figure 4 shows the corresponding relative irradiance distribution on the receiver plane. As seen in the figure, the intensity along the edges of the spot is significantly improved, leading to a more uniform rectangular pattern. Although reducing the division angle improves irradiance uniformity, it simultaneously increases machining complexity by narrowing the spacing between adjacent fan-shaped regions.

https://doi.org/10.3390/mi17040448

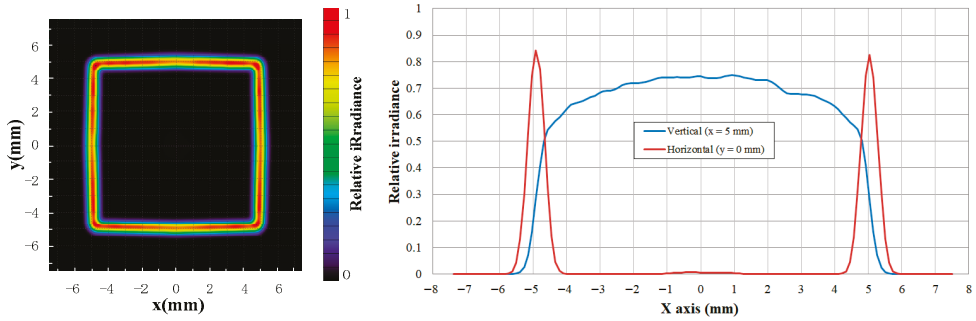


Figure 4. Relative irradiance distribution of the rectangular DHB for division angle of 2.5°. (**a**) Two-dimensional irradiance distribution. (**b**) Cross-sectional irradiance distribution curve.

The cross-sectional profiles of the irradiance distribution of the rectangular DHB in free space were calculated at various propagation distances z for a division angle of 5°, as shown in Figure 5. As the propagation distance increases, the hollow region of the optical spot gradually expands, reaching its designed maximum at the focal plane. At this position, the beam is most concentrated and its width is minimal. The hollow region gradually decreases beyond the focal plane. Although a focused spot distribution appears at the rear focal plane ($z = 215$ mm), the beam as a whole has already diverged.

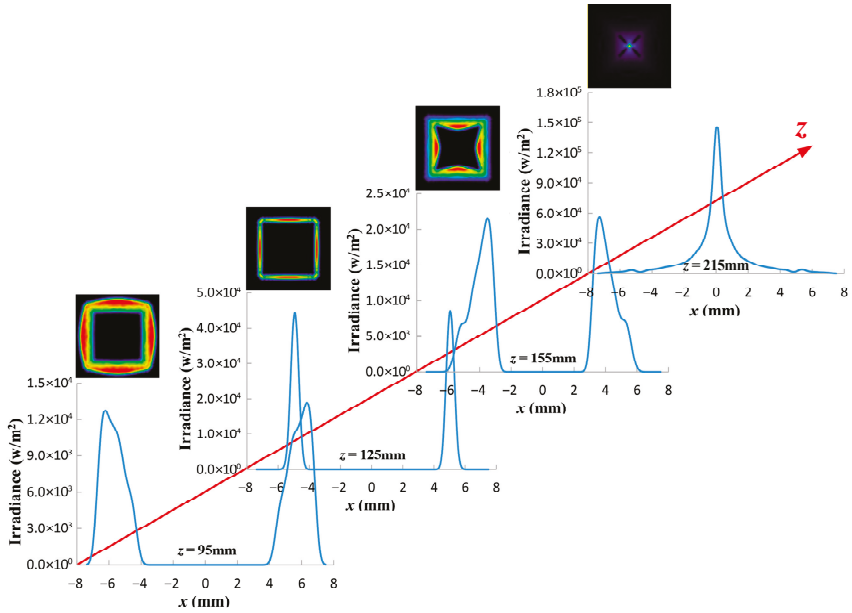


Figure 5. Cross line ($y = 0$ mm) of the irradiance distribution of a rectangular DHB at various propagation distances of 5°.

3. Experimental Verification

3.1. Experimental Setup

To validate the feasibility of the proposed method, a freeform Fresnel lens with a division angle of 5° was chosen for experimental fabrication, as it involves less machining complexity. The experiments were conducted on an ultra-precision lathe (Nanotech 650FG, Moore, Swanzey, NH, USA) equipped with three linear axes (X, Y, Z) and a rotational axis (C), as shown in Figure 6. A commercially manufactured single-crystal diamond tool was employed, with a rake angle of 0°, a nose radius of 10 μm, and an included angle of 70°.

https://doi.org/10.3390/mi17040448

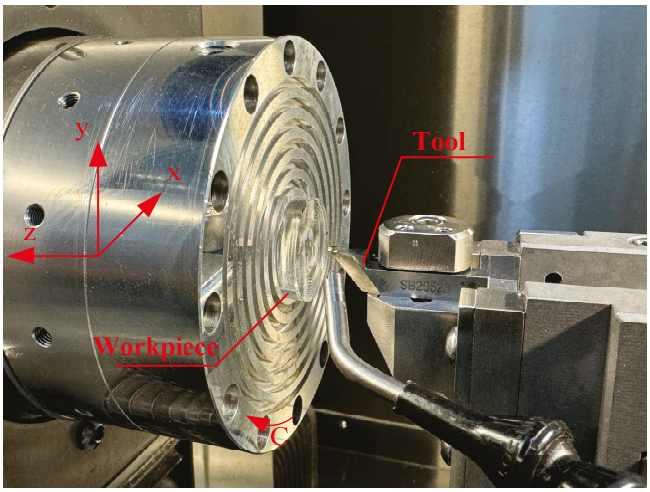


Figure 6. Experimental setup and coordinate configuration.

3.2. Verification of the Exemplary Freeform Fresnel Optics

The freeform Fresnel lens with a division angle of 5°, introduced in Section 2, was successfully fabricated using ultra-precision machining, as shown in Figure 7. Due to the relatively small facet angles in the central region of the designed freeform Fresnel lens, the central area with a diameter of 2 mm was fabricated as a planar surface. A cross-sectional profile comprising 23 facets was measured using a probe-type optical instrument (Form Talysurf PGI, Taylor Hobson, Leicester, UK). Two line segments at azimuth angles of 0° and 45° were selected for analysis, with the testing starting points set at the central origin of the optical element (the X-axis of the ultra-precision lathe as the reference axis). The resulting contour lines, presented in Figure 8, were compared with the intended design, and the forming angular error was calculated. During measurement of the groove tip morphology, interference between the probe and the workpiece caused noise in the tip region. Therefore, only the valid data region was used for analysis. The maximum forming angular error was within 0.1°, demonstrating that the proposed fabrication process achieved high machining accuracy.

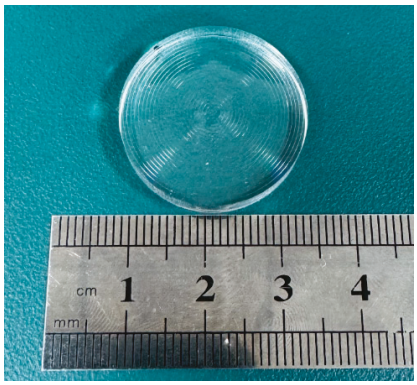


Figure 7. Photograph of the fabricated freeform Fresnel lens.

Based on the surface profile measurement results shown in Figure 8a, roughness analysis was performed on three grooves. Figure 9 presents the roughness curves of the inclined surfaces for the 1st, 11th, and 23rd grooves. The results indicate that the surface roughness values of the three groove inclined surfaces are 8.9 nm, 9.5 nm, and 8.2 nm, respectively. The experimental findings reveal that the surface roughness of groove-inclined facets is strictly confined to the nanometer scale, indicating excellent machining consistency and superior surface finishing quality.

https://doi.org/10.3390/mi17040448

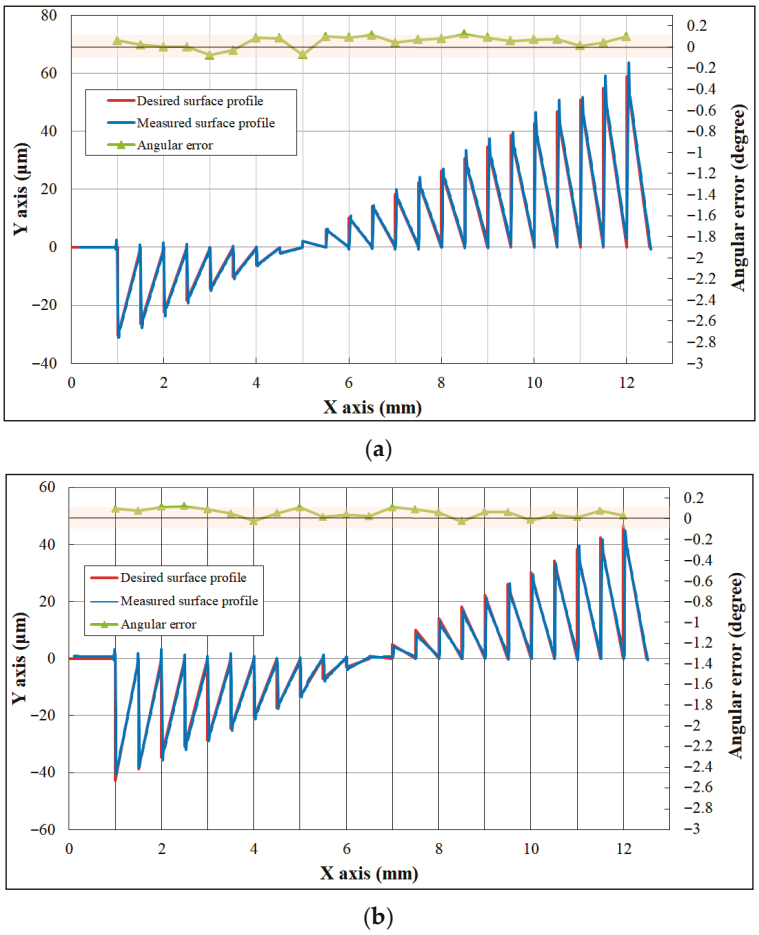


Figure 8. Comparison of the desired profile and measured profile of the freeform Fresnel optics on depth direction and corresponding forming error: (**a**) azimuth angles of 0°, (**b**) azimuth angles of 45°.

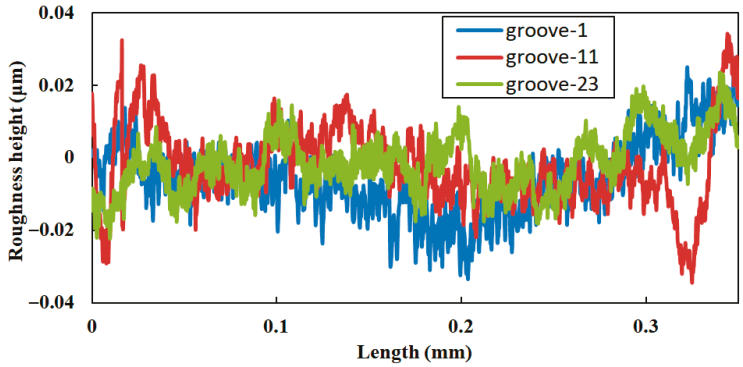


Figure 9. Measurement of surface roughness.

A freeform Fresnel lens with division angle of 5°, fabricated from PMMA material, was processed to assess its optical performance, and an optical test setup was established as shown in Figure 10. The experimental test setup was assembled on a vibration-isolated optical platform, with all auxiliary testing components mounted on a graduated optical linear rail to enable precise positional alignment throughout the measurement process. A 640 nm laser integrated with a collimating lens was employed as the illumination source, which irradiated the machined freeform Fresnel lens; the transmitted beam was then imaged onto a receiving surface, and the corresponding light spot on this surface was subsequently captured by a beam analyzer (SP300, Ophir-Spiricon, North Logan, UT, USA). The freeform Fresnel lens was firmly fixed on a precision lens mount, with its grooved

https://doi.org/10.3390/mi17040448

surface facing the receiving surface. The receiver employed herein is a ground glass slide, featuring a light-scattering surface on one side and a flat transparent surface on the other. The light spot was projected onto the scattering surface of the ground glass, while the beam analyzer acquired the spot image through its transparent flat side. This beam analyzer is equipped with a 7.1 mm × 5.3 mm CCD detector and a 5× magnification focusing lens.

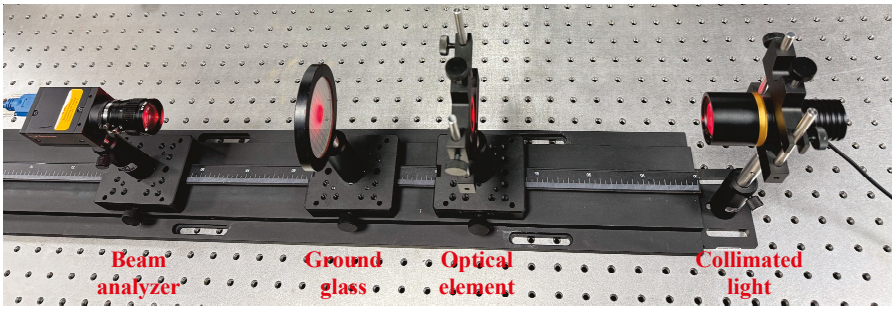
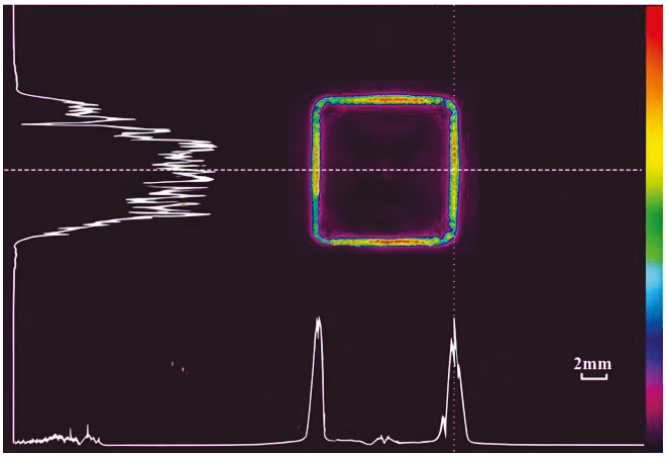


Figure 10. Photograph of the optical test setup.

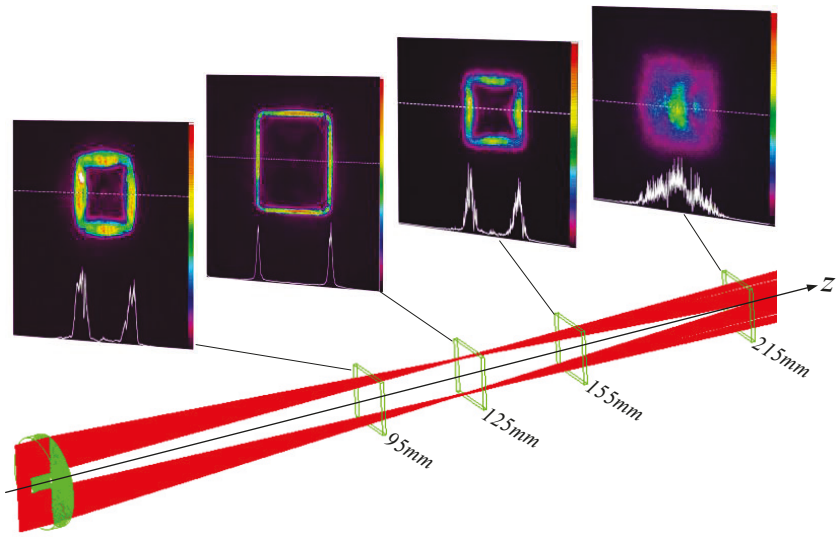
Figure 11 presents the experimentally measured optical performance of the fabricated freeform Fresnel lens. As shown in Figure 11a, a rectangular dark hollow beam with a side length of 10.3 mm and a width of approximately 1.2 mm was obtained at the focal plane, where the central intensity is significantly suppressed and the boundary exhibits a continuous closed high-intensity distribution. The overall beam profile shows good agreement with the simulated result (Figure 3a), demonstrating that the proposed design method can effectively achieve the desired beam shaping after fabrication. Meanwhile, noticeable intensity of non-uniformity is observed along the boundary, particularly near the rectangular corners. This behavior is consistent with the simulation results, where the non-uniform energy distribution is attributed to the finite division angle accuracy of the fan-shaped sectors. Figure 11b further illustrates the evolution of the beam at different propagation distances. As the propagation distance increases from 95 mm to 125 mm (focal plane), the hollow region gradually expands and stabilizes, and the rectangular profile becomes more distinct. At the focal plane, the beam exhibits the most concentrated size and highest contrast. With further propagation to 155 mm and 215 mm, the beam begins to diverge, the contrast of the hollow region decreases, and the boundary becomes blurred, indicating a strong focal-plane dependence of the structure.



(**a**)

Figure 11. *Cont.*

https://doi.org/10.3390/mi17040448



(**b**)

Figure 11. Optical performance test. (**a**) Measured beam profile test image at focal plane. (**b**) Cross-sectional optical path of beam propagation and spot distributions at different transmission positions.

4. Conclusions

This study presents a design method for freeform Fresnel lenses to generate rectangular dark hollow beams. The approach is validated through theoretical modeling, ray-tracing simulations, and experimental characterization. The proposed method divides the lens into multiple fan-shaped sectors and establishes a topological mapping between each sector and the target rectangular hollow pattern. By redirecting light to off-axis positions through serrated Fresnel zones, the desired beam profile is formed via spot superposition. A freeform Fresnel lens with a division angle of 5° was successfully designed and fabricated. The experimental results agree well with the simulations, confirming the feasibility and effectiveness of the proposed method. Although reducing the division angle can improve irradiance uniformity, it also increases machining complexity. Therefore, a trade-off between optical performance and fabrication difficulty must be considered. The proposed design strategy is not limited to rectangular beams and can be extended to hollow beams with arbitrary geometries.

A concentric design with a constant groove width was adopted in this work, and when combined with the ultra-precision slow tool servo machining process, it effectively reduces machining difficulty and enables the convenient and efficient fabrication of the required surface profile. The fabricated lens exhibits an angular error below 0.1° and a surface roughness below 10 nm, demonstrating excellent machining performance.

Freeform Fresnel lenses replace continuous surfaces with segmented facets, significantly reducing thickness and weight. Although this may slightly compromise surface continuity, it enables lightweight and compact optical designs. Furthermore, such structures are generally considered compatible with fabrication techniques such as injection molding and nanoimprint lithography, indicating their potential for large-scale production. However, this aspect was not experimentally investigated in the present study and will be addressed in future work.

Author Contributions: Conceptualization, J.Z. and Q.H.; methodology, Q.H.; software, C.Y. and Y.X.; investigation, J.Z. and Y.X.; resources, Q.H.; data curation, J.Z. and Q.H.; writing—original draft preparation, J.Z.; writing—review and editing, Q.H. and T.L.; All authors have read and agreed to the published version of the manuscript.

https://doi.org/10.3390/mi17040448

Funding: This research was funded by Higher Education Institution-Industry-Research Collaboration Program of Fujian Province (grant number: 2025H61010041) and Quanzhou Major Science and Technology Special Project (grant number: 2024QZGZ3).

Institutional Review Board Statement: Not applicable.

Informed Consent Statement: Not applicable.

Data Availability Statement: The original contributions presented in this study are included in the article. Further inquiries can be directed to the corresponding author.

Conflicts of Interest: The authors declare no conflicts of interest.

References

1. Yin, J.P.; Zhu, Y.F.; Wang, W.B.; Wang, Y.Z.; Jhe, W. Optical potential for atom guidance in a dark hollow laser beam. *J. Opt. Soc. Am. B* **1998**, *15*, 25–33. [PubMed]
2. Porfirev, A.P.; Skidanov, R.V. Dark-hollow optical beams with a controllable shape for optical trapping in air. *Opt. Express* **2015**, *23*, 8373–8384. [CrossRef] [PubMed]
3. Yan, X.; Zhang, P.F.; Zhang, J.H.; Qiao, C.H.; Fan, C.Y. Quantum polarization fluctuations of partially coherent dark hollow beams in non-Kolmogorov turbulence atmosphere. *Chin. Phys. B* **2016**, *25*, 084204. [CrossRef]
4. Drevinskas, R.; Zhang, J.; Beresna, M.; Gecevičius, M.; Kazanskii, A.G.; Svirko, Y.P.; Kazansky, P.G. Laser material processing with tightly focused cylindrical vector beams. *Appl. Phys. Lett.* **2016**, *108*, 221107. [CrossRef]
5. Zhang, W.; Lin, Y.; Gao, Y.; Guo, Z.; Li, X.; Hu, Y.; Dong, P.; Zhang, Q.; Fang, X.; Zhang, M. Numerical and Experimental Investigation on the Optical Manipulation from an Axicon Lensed Fiber. *Micromachines* **2021**, *12*, 187. [CrossRef]
6. Ovchinnikov, Y.B.; Manek, I.; Sidorov, A.I.; Wasik, G.; Grimm, R. Gravito-optical atom trap based on a conical hollow beam. *Europhys. Lett.* **1998**, *43*, 510–515. [CrossRef]
7. Cai, Y.; Lin, Q. Hollow elliptical Gaussian beam and its propagation through aligned and misaligned paraxial optical systems. *J. Opt. Soc. Am. A* **2004**, *21*, 1058–1065. [CrossRef]
8. Cai, Y.; Zhang, L. Coherent and partially coherent dark hollow beams with rectangular symmetry and paraxial propagation properties. *J. Opt. Soc. Am. B* **2006**, *23*, 1398–1407. [CrossRef]
9. Wang, H.; Li, X. Propagation of partially coherent controllable dark hollow beams with various symmetries in turbulent atmosphere. *Opt. Lasers Eng.* **2010**, *48*, 48–57. [CrossRef]
10. Liang, G.; Shu, F.J.; Ma, S.S.; Cheng, W.J.; Sun, C.Z. Spiraling elliptic hollow beams with cross phase. *New J. Phys.* **2023**, *25*, 033011. [CrossRef]
11. Lin, J.; Zhong, S.; Shen, J. Propagation of elliptical Gaussian vortex beam based on angular spectrum representation. *J. Quant. Spectrosc. Radiat. Transf.* **2024**, *324*, 109062. [CrossRef]
12. Cai, Y.; Zhang, Y. Scintillation properties of a rectangular dark hollow beam. *J. Mod. Opt.* **2009**, *56*, 502–507. [CrossRef]
13. Piccirillo, B.; Piedipalumbo, E.; Santamato, E. Geometric-Phase Waveplates for Free-Form Dark Hollow Beams. *Front. Phys.* **2020**, *8*, 94. [CrossRef]
14. Heckenberg, N.R.; McDuff, R.; Smith, C.P.; White, A.G. Generation of optical phase singularities by computer-generated holograms. *Opt. Lett.* **1992**, *17*, 221–223. [CrossRef]
15. Xia, Y.; Yin, J.P. Generation of a focused hollow beam by an 2 pi-phase plate and its application in atom or molecule optics. *J. Opt. Soc. Am. B* **2005**, *22*, 529–536. [CrossRef]
16. Paterson, C.; Smith, R. Higher-order Bessel waves produced by axicon-type computer-generated holograms. *Opt. Commun.* **1996**, *124*, 121–130. [CrossRef]
17. Power, W.L.; Allen, L.; Babiker, M.; Lembessis, V.E. Atomic motion in light beams possessing orbital angular momentum. *Phys. Rev. A* **1995**, *52*, 479. [CrossRef]
18. Monk, S.; Arlt, J.; Robertson, D.; Courtial, J.; Padgett, M. The generation of Bessel beams at millimetre-wave frequencies by use of an axicon. *Opt. Commun.* **1999**, *170*, 213–215. [CrossRef]
19. Joshi, S.; Yadav, B.K.; Shahid Khan, M.; Kandpal, H.C. Effect of coherence and polarization on the polychromatic partially coherent dark hollow beam generated from axicon-lens system. *J. Opt.* **2014**, *16*, 2433–2439. [CrossRef]
20. Hu, M.; Wang, C.; Song, Y.; Li, Y.; Chai, L.; Serebryannikov, E.; Zheltikov, A. A hollow beam from a holey fiber. *Opt. Express* **2006**, *14*, 4128–4134. [CrossRef]
21. Goldstein, P. Process for designing a freeform Fresnel lens. *Opt. Eng.* **2011**, *50*, 895–900. [CrossRef]
22. Tan, N.Y.J.; Zhang, X.; Neo, D.W.K.; Huang, R.; Liu, K.; Kumar, A.S. A review of recent advances in fabrication of optical Fresnel lenses. *J. Manuf. Process.* **2021**, *71*, 113–133. [CrossRef]

https://doi.org/10.3390/mi17040448

23. Wang, Y.; Wang, J.; Guo, P. Generic fabrication solution of freeform Fresnel optics using ultra-precision turning. *Opt. Express* **2023**, *31*, 44622–44647. [CrossRef]
24. Chen, J.; Yu, Y.; Gu, P.; Zhu, L.; Zhang, Z.; Zhang, X. Fabrication of the freeform Fresnel lens by swinging-rotating diamond ruling. *J. Manuf. Process.* **2024**, *119*, 130–145. [CrossRef]
25. Kirrbach, R.; Faulwaßer, M.; Jakob, B. Non-rotationally symmetric freeform Fresnel-lenses for arbitrary shaped li-fi communication channels. In Proceedings of the 2019 Global LIFI Congress (GLC), Paris, France, 12–13 June 2019.
26. Hui, X.; Liu, J.; Wan, Y.; Lin, H. Realization of uniform and collimated light distribution in a single freeform-Fresnel double surface led lens. *Appl. Opt.* **2017**, *56*, 4561–4565. [CrossRef]
27. Desnijder, K.; Hanselaer, P.; Meuret, Y. Freeform Fresnel lenses with a low number of discontinuities for tailored illumination applications. *Opt. Express* **2020**, *28*, 24489–24500. [CrossRef]
28. Dahlmanns, J.; Völl, A.; Wester, R.; Stollenwerk, J.; Loosen, P.; Holly, C. Simulation and design of a Fresnelized freeform optic for a head-up display. *Illum. Opt. VI* **2021**, *11874*, 118740Q.

Disclaimer/Publisher's Note: The statements, opinions and data contained in all publications are solely those of the individual author(s) and contributor(s) and not of MDPI and/or the editor(s). MDPI and/or the editor(s) disclaim responsibility for any injury to people or property resulting from any ideas, methods, instructions or products referred to in the content.

https://doi.org/10.3390/mi17040448

micromachines

MDPI

Article

Triple-Cation Perovskite Photoanodes for Solar Water Splitting: From Photovoltaic-Assisted to Immersed Photoelectrochemical Operation

Vera La Ferrara [1,*], Marco Martino [1], Antonio Marino [1], Giovanni Landi [2], Silvano Del Gobbo [3], Nicola Lisi [3], Rosanna Viscardi [3], Alberto Giaconia [3] and Giulia Monteleone [3]

[1] Energy Technologies and Renewable Sources Department, ENEA Portici Research Center, 80055 Portici, Italy; marco.martino@enea.it (M.M.); antonio.marino@enea.it (A.M.)
[2] Energy Efficiency Unit Department, ENEA Portici Research Center, 80055 Portici, Italy; giovanni.landi@enea.it
[3] Energy Technologies and Renewable Sources Department, ENEA Casaccia Research Center, 00123 Rome, Italy; silvano.delgobbo@enea.it (S.D.G.); nicola.lisi@enea.it (N.L.); rosanna.viscardi@enea.it (R.V.); alberto.giaconia@enea.it (A.G.); giulia.monteleone@enea.it (G.M.)
* Correspondence: vera.laferrara@enea.it

Abstract

Mixed-halide perovskite solar cells with the composition $Cs_{0.1}(MA_{0.17}FA_{0.83})_{0.9}Pb(I_{0.83}Br_{0.17})_3$ were fabricated obtaining solar cells as glass/ITO/SnO_2/triple-cation perovskite/HTL/Au, and subsequently used as photoanodes for efficient solar-driven water splitting by attaching commercial catalytic nickel foils to the Au back-contact pads of solar cells. To enable operation in alkaline media, the devices were encapsulated using commercial PET–EVA multilayer films, providing an effective barrier while leaving the Ni foils exposed as the electrochemically active interface. Two operating configurations were investigated and compared: (i) an outside configuration, where the perovskite device powered the external electrochemical cell, and (ii) an immersed configuration, in which the encapsulated perovskite solar cell was directly integrated, together with the Ni catalyst, into the electrolyte. In both configurations, the onset potential for the oxygen evolution reaction shifted from ~1.32 V vs. RHE, when the Ni electrode was not powered by the perovskite solar cell, to ~0.34 V vs. RHE, when the perovskite device powered the Ni foil for both immersed and outside configurations. The immersed configuration delivered the highest performance, achieving a maximum Applied Bias Photon-to-Current Efficiency of ~20% under AM 1.5 G illumination (100 mW cm^{-2}), among the highest values reported for perovskite-based photoanodes. Importantly, the enhanced performance does not arise from changes in catalyst composition or direct semiconductor–electrolyte interaction, but from improved photovoltage delivery and reduced resistive losses enabled by the integrated device architecture. These results demonstrate that device architecture is a key factor in controlling photovoltage utilization and charge-transfer kinetics, providing a viable strategy for efficient and scalable perovskite-based photoelectrochemical systems.

Keywords: perovskite photoanode; solar water splitting; hydrogen evolution; encapsulation; ABPE; mixed-halide perovskite; photoelectrochemical devices; PET–EVA

1. Introduction

Organic–inorganic hybrid perovskite solar cells (PSCs) have attracted remarkable attention as next-generation photovoltaic materials due to their high-power conversion

efficiencies, low-cost fabrication, and tunable optoelectronic properties [1–3]. Despite these advantages, most perovskite devices suffer from rapid degradation upon exposure to moisture, oxygen, and light, which severely limits their operational stability and long-term performance [4]. This challenge underscores the need for innovative encapsulation strategies and device integration that can simultaneously ensure high efficiency and environmental robustness. These intrinsic vulnerabilities remain one of the main obstacles to the commercialization of perovskite-based technologies. To enhance device durability, several strategies have been proposed, including compositional engineering, interface passivation, and the use of flexible polymeric encapsulants [5–9]. Polymeric barriers improve resistance to humidity and oxygen while enabling lightweight, robust, and portable devices compared to heavier commercial alternatives. These encapsulation approaches allow perovskite-based systems to operate in conditions unsuitable for unprotected devices [10]. Encapsulation also enables the integration of PSCs with photoelectrochemical (PEC) systems for solar-driven water splitting, where protection from aqueous environment is essential. Such integrated configurations allow hydrogen production directly from sunlight while avoiding both the intrinsic instability of perovskites in liquid electrolytes and the need for an external power supply. Integrating the light absorber and catalytic electrodes within a compact architecture simplifies the device design, reduces energy losses, and potentially improves conversion efficiency. The adoption of a PEC approach enables the direct conversion of solar energy into chemical fuels, offering a pathway toward integrated Solar-to-Hydrogen systems. This approach has been widely recognized as a promising route toward sustainable hydrogen production, as it allows direct coupling between light absorption and catalytic reactions without intermediate electrical conversion steps [11]. In solar fuel research, water splitting can be achieved through either photocatalytic or photoelectrochemical (PEC) approaches. In photocatalysis, light absorption, charge separation, and catalytic reactions occur within suspended semiconductor particles, often making charge extraction and interfacial processes difficult to control. In contrast, PEC systems rely on photoelectrodes connected to an external circuit, enabling spatial separation of redox reactions and direct measurement of photocurrent and applied bias. This configuration provides a more controlled and quantitative platform to investigate charge-transfer kinetics and photovoltage utilization. In this context, the PEC approach was specifically chosen to evaluate how effectively the photovoltage generated by encapsulated perovskite solar cells can be delivered to the catalytic interface and exploited to drive water-splitting reactions under alkaline conditions. This is particularly relevant for understanding the role of device architecture in governing photovoltage delivery, interfacial charge-transfer kinetics and overall device performance. Perovskite-based devices can provide high photovoltages, but their effective utilization strongly depends on the device integration and on how efficiently the photovoltage is transferred to drive interfacial electrochemical reactions. Moreover, the bandgap tunability of hybrid perovskites, combined with their high absorption coefficients, makes them promising photoanode materials capable of driving the oxygen evolution reaction (OER) efficiently under alkaline conditions [12–16].

The use of perovskite materials as photoanodes has gained increasing importance due to their unique combination of optoelectronic and structural properties that can overcome the limitations of conventional metal oxides. Traditional metal oxide-based photoanodes such as $BiVO_4$, WO_3, and Fe_2O_3 exhibit high stability but suffer from wide bandgaps and sluggish charge transport. In contrast, halide perovskites exhibit high absorption coefficients, long carrier diffusion lengths, and tunable bandgaps (1.5–2.2 eV), making them suitable for solar water splitting [12]. Recent studies have demonstrated that perovskite-based photoanodes can achieve outstanding photoelectrocatalytic activity when properly protected and integrated with efficient catalysts. For instance, Hansora et al. [13] reported

https://doi.org/10.3390/mi17040431

$FAPbI_3$/NiFeOOH photoanode with Applied Bias Photon-to-Current Efficiency (ABPE) of 7.9%. Similarly, Yang et al. [14] demonstrated that perovskite with carbon/graphite conductive protection layers and NiFe catalyst can achieve unassisted water splitting with a high ABPE of 8.5%. More recently, Fehr et al. [15] demonstrated scalable perovskite PEC systems with Solar-to-Hydrogen (STH) efficiencies of up to 20.8% in tandem configurations, while Song et al. [16] reported all-perovskite tandem systems with STH efficiencies up to 15% and operational stability exceeding 120 h. These advances highlight the capability of perovskite materials to deliver high photovoltage (>2.0 V) and high photocurrent densities (>12 mA cm^{-2}), while maintaining low fabrication costs. However, their integration into aqueous PEC environments remains challenging. Direct exposure to electrolytes often results in structural degradation and performance loss due to ion migration and dissolution of the perovskite layer. Therefore, the development of encapsulation approaches that combine environmental stability with efficient electronic coupling to catalytic electrodes is critical for advancing this technology. Among the various perovskite compositions, triple-cation mixed-halide systems (e.g., Cs/MA/FA-based) have emerged as particularly suitable for applications requiring enhanced operational stability. Compared to single- or double-cation perovskites, triple-cation formulations exhibit improved phase stability, reduced defect density, and suppressed ion migration, leading to enhanced charge transport and reduced non-radiative recombination losses. These effects were systematically demonstrated by Saliba et al. [17], who showed that the incorporation of cesium into mixed-cation perovskites significantly enhances thermal and structural stability. These advantages are particularly relevant under PEC conditions, where the device is subjected to additional stress factors such as continuous illumination, applied bias, and proximity to aqueous electrolytes. In such environments, less stable perovskite compositions tend to degrade rapidly due to structural instability and interfacial reactions. Therefore, the use of triple-cation perovskites represents a rational and strategic choice to enhance both device durability and performance in PEC configurations. To date, only limited studies have demonstrated their feasibility for water splitting [15] often without a detailed photoelectrochemical characterization or a systematic analysis of device integration. In particular, a direct comparison between perovskite solar cells operating externally to an electrochemical cell and those integrated within the electrolyte has not been reported. As a result, the role of device configuration in governing photovoltage delivery, interfacial charge-transfer kinetics, and overall PEC performance remains unclear. In this context, the present work addresses this gap by providing a systematic comparison between outside (OS) and immersed (IS) configurations using the same encapsulated triple-cation perovskite device. The OS configuration corresponds to a photovoltaic-assisted electrochemical cell setup, whereas the IS configuration involves direct integration of the solar cell-based device, together with the Ni catalyst, into the electrolyte. This approach allows the effect of device architecture to be isolated. Furthermore, we demonstrate that the enhancement in PEC performance does not originate from changes in catalyst composition or direct semiconductor–electrolyte interaction, but rather from improved photovoltage delivery and reduced resistive losses enabled by the integrated device. Finally, this work provides one of the first comprehensive photoelectrochemical characterizations of triple-cation perovskites under alkaline conditions, including cyclic voltammetry, onset potential analysis, photocurrent response, and ABPE evaluation. In this work, we employ a triple-cation mixed-halide perovskite, $Cs_{0.1}(MA_{0.17}FA_{0.83})_{0.9}Pb(I_{0.83}Br_{0.17})_3$, as a light absorber layer in n-i-p solar cells, glass/ITO/SnO_2/triple-cation perovskite/HTL/Au and subsequently adapted to operate as photoanodes. This formulation of triple-cation perovskite, with a higher cesium content and optimized halide ratio, enhances structural stability and interfacial charge transfer [17,18]. To enable operation in alkaline electrolyte, the devices were encapsulated

https://doi.org/10.3390/mi17040431

using commercially available PET–EVA multilayer films, forming the final architecture glass/ITO/SnO_2/perovskite/HTL/Au/Ni, where Ni acts as the catalytic interface.

2. Materials and Methods

2.1. Materials

SnO_2 colloid precursor (tin (IV) oxide 15% H_2O colloidal dispersion), PbI_2 (≥99.999%, ultradry) and $PbBr_2$ (Puratronic, ≥99.998%) were purchased from Alfa Aesar (Thermo Fisher Scientific, Rodano, Italy). CsI (≥99.999%, anhydrous), acetonitrile (ACN anhydrous), anisole (≥99.7% anhydrous), N,N-dimethylformamide (DMF anhydrous), dimethyl sulfoxide (DMSO anhydrous), formamidinium iodide (FAI anhydrous), methylammonium bromide (MABr, ≥99%, anhydrous), Spiro-OMeTAD, chlorobenzene (CB anhydrous), 4-tert-butylpyridine (TBPy), bis(trifluoromethane)sulfonimide lithium salt (Li-TFSI), and FK209 Co (III) TFSI salt were purchased from Sigma Aldrich (Merck Life Science S.r.l., Milano, Italy). All chemicals were used without further purification. Glass/ITO substrates (2×2 cm^2, 10 Ω sq^{-1}) were used as conductive supports and purchased from Kintec (Hong Kong, China).

2.2. Preparation of Precursors

The SnO_2 solution was prepared by diluting the commercial SnO_2 colloidal dispersion with deionized water (1:5). The perovskite precursor solution $Cs_{0.1}(MA_{0.17}FA_{0.83})_{0.9}Pb(I_{0.83}Br_{0.17})_3$ was obtained by mixing PbI_2 (1.10 M), $PbBr_2$ (0.22 M), FAI (1.05 M), and MABr (0.20 M) in DMF/DMSO (4:1 v/v). A 1.50 M CsI solution in DMSO was added to achieve 10 mol% Cs content. The hole transport material (HTM) solution consisted of 73 mg Spiro-OMeTAD in 1 mL CB, 27 μL TBPy, 17 μL Li-TFSI solution (520 mg Li-TFSI in 1 mL ACN), and 7 μL FK209 Co (III) TFSI solution (375 mg in 1 mL ACN). The alkaline electrolyte (1 M KOH) was prepared by dissolving 5.61 g KOH pellets (≥99.99%), purchased from Sigma Aldrich (Merck Life Science S.r.l., Milano, Italy) in 100 mL deionized water with stirring, cooled to room temperature, and freshly used.

2.3. Perovskite-Based Solar Cell and Photoanode Fabrication

ITO substrates were sequentially sonicated in acetone and 2-propanol for 15 min each, dried with nitrogen, and treated under UV–ozone for 20 min. SnO_2 electron transport layers (ETLs) were spin-coated at 6000 rpm for 30 s and annealed at 130 °C for 1 h. The substrates were then transferred into a nitrogen glovebox for perovskite and hole transport layer (HTL) deposition. The perovskite layer was spin-coated using a two-step program (1000 rpm for 10 s and 6000 rpm for 20 s), with 200 μL anisole added dropwise as an antisolvent. Films were annealed at 100 °C for 1 h. The Spiro-OMeTAD layer, as HTL, was spin-coated at 4000 rpm for 30 s, followed by thermal evaporation of 80 nm Au back contact [16]. To use the pristine perovskite solar cell as a photoanode for PEC testing, the device was modified by adding two nickel foils onto its existing electrical contacts, one on the Au pad and one on the ITO-coated glass substrate, named Ni (+) and Ni (−) respectively (Figure 1a). Given the higher rigidity and hardness of nickel compared to gold, small drops of silver conductive paste were applied between the Au pads (or ITO) and the Ni foils to improve electrical contact. To evaluate a suitable thickness of nickel foils for photoelectrocatalytic integration, the current density–voltage (J–V) characteristics of pristine perovskite devices were first recorded under standard illumination (AM 1.5 G, 100 mW cm^{-2}) and compared with PSCs with nickel foils of varying thicknesses as the electrode. Among the thicknesses, 20 μm thick nickel foil exhibited the best performance. The perovskite devices were then encapsulated using multilayer polymeric film lamination between two PET–EVA sheets and laminated using a hot-press laminator (PlastiEVO, Tosingraf S.r.l., Rosà, Italy). The lamination process

https://doi.org/10.3390/mi17040431

was carried out at 100 °C for 5 min, forming an effective barrier against moisture and oxygen. The PET layer provided mechanical stability and optical transparency, whereas the EVA layer ensured strong adhesion and air- and watertight sealing. A Kapton polyimide tape was first applied to protect the active area from direct exposure to the encapsulant. Front- and back-view images of the encapsulated devices are shown (Figure 1b).

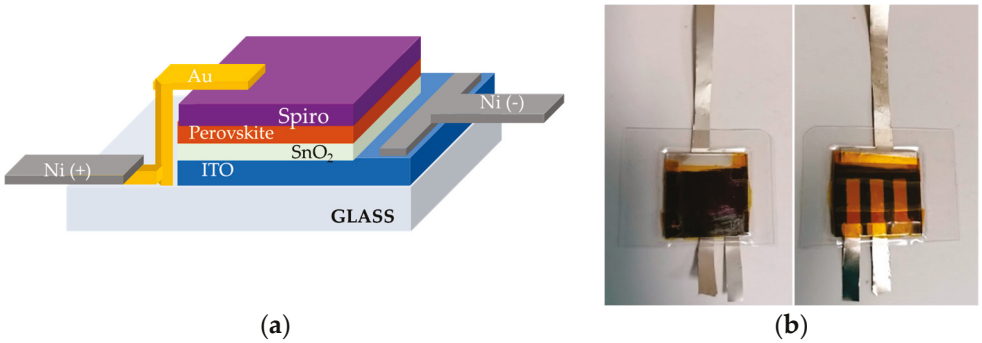


Figure 1. (**a**) Schematic representation of the n-i-p perovskite solar cell architecture (Glass/ITO/SnO_2/Perovskite/Spiro-OMeTAD/Au) showing the placement of nickel electrodes in contact with Au and ITO terminals of the device. (**b**) Photographs of the typical perovskite device encapsulated using multilayer polymeric films (PET–EVA). (Left) front, where glass is illuminated by solar simulator, and (right) back, where Nickel foils are deposited on Au pads and on ITO.

3. Results and Discussion

3.1. Perovskite-Based PEC Configurations and Characterization of Standard Electrochemical Cell

The photoelectrochemical performance of the encapsulated PSCs was evaluated in two operational configurations: (i) outside (OS) configuration, where the perovskite cell powered an external standard electrochemical cell, and (ii) immersed (IS) configuration, where the encapsulated device was directly integrated into the electrolyte. The Ni foil in contact with the Au terminal was used as the working electrode. Illumination was provided by a LED AM 1.5 G solar simulator (Ossila B.V. Leiden, Netherlands), irradiance 100 mW cm^{-2} (Figure 2). The standard electrochemical had three-electrode configuration with 1 M KOH electrolyte, with Ni as the working electrode, Pt as the counter electrode, and Ag/AgCl as reference (Figure 3). The nickel electrode drove the oxygen evolution reaction (OER) at the anode ($4OH^- \rightarrow O_2 + 2H_2O + 4e^-$), while the platinum counter electrode catalyzed the hydrogen evolution reaction (HER) at the cathode ($4H_2O + 4e^- \rightarrow 2H_2 + 4OH^-$). The overall process corresponded to water splitting ($2H_2O \rightarrow 2H_2 + O_2$). The cyclic voltammetry (CV) recorded on the Ni/Pt electrodes, biased with a potentiostat, but in the absence of the perovskite solar cell (i.e., without any photovoltage contribution) shows the characteristic behavior of alkaline OER, with an anodic onset potential appearing at approximately $E_{(onset\ (vs.\ Ag/AgCl))}$ = +0.30 V vs. Ag/AgCl. The onset potential (E_{onset}) is conventionally defined as the potential at which the photocurrent density reaches a small but measurable value (typically 0.0001–0.0002 A cm^{-2} above the baseline), and represents the minimum external bias required to initiate the electrochemical reaction.

To demonstrate the analyzed results, the measured potentials are converted into potential versus reversible hydrogen electrode (RHE) using [19]

$$E_{RHE} = E_{Ag/AgCl} + E^0_{Ag/AgCl} + 0.059 \times pH \quad (1)$$

The potential of the reference electrode, concerning the standard hydrogen electrode at 25 °C (0.197 V for Ag/AgCl), is denoted as $E^0_{Ag/AgCl}$, while the working potential measured versus the reference electrode is represented as $E_{Ag/AgCl}$. Thus, the OER onset corresponds

https://doi.org/10.3390/mi17040431

to approximately 1.32 V vs. RHE for nickel-based catalysts in alkaline media (1 M KOH, pH = 14) (Figure 4). The $Ni(OH)_2/NiOOH$ redox transition, which reflects the formation of active NiOOH sites, occurs at a lower potential of around 1.1 V vs. RHE.

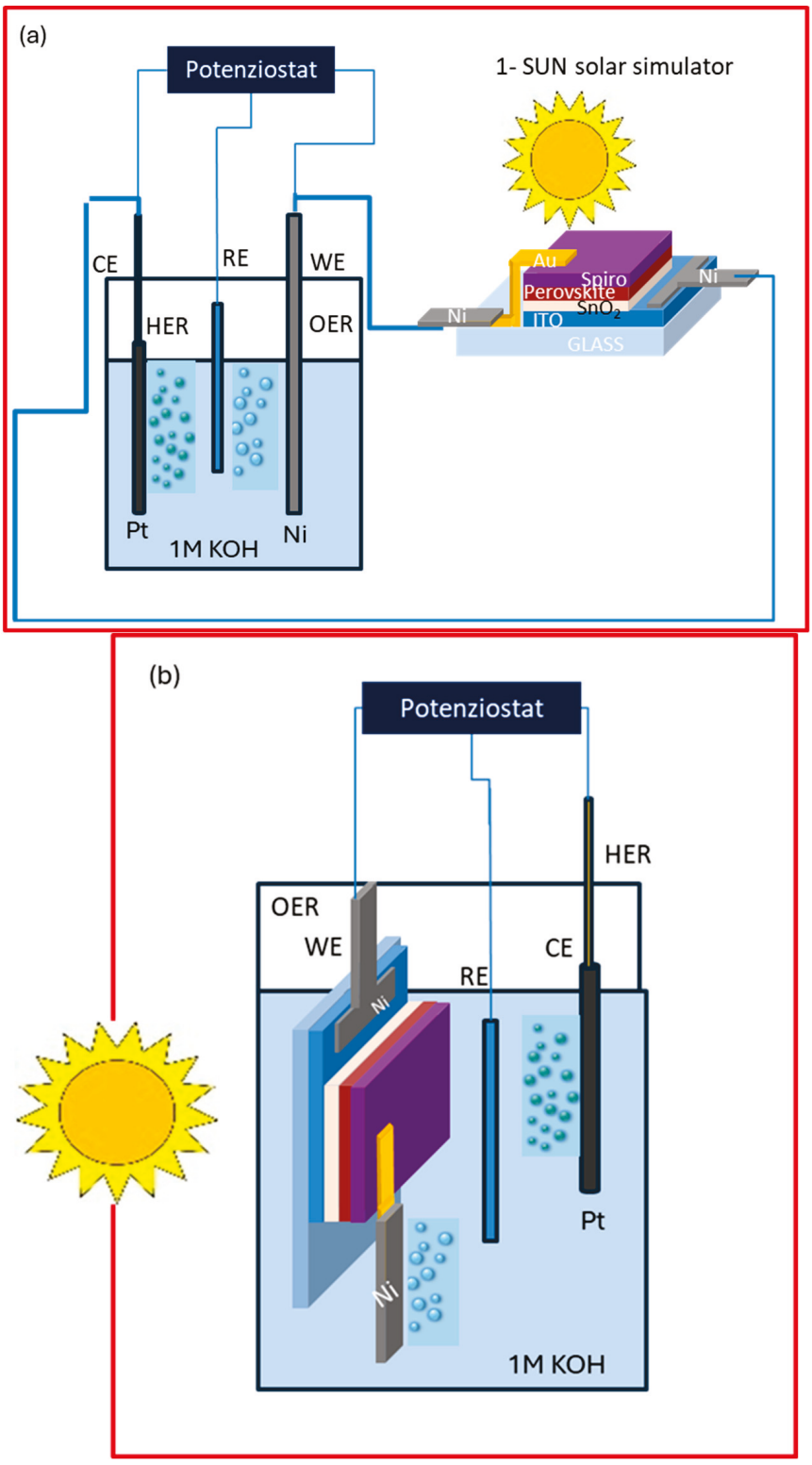


Figure 2. Schematic representation of the encapsulated PSC in (**a**) outside and (**b**) immersed configuration with Nickel as the working electrode and platinum as the counter electrode and the third electrode as reference.

https://doi.org/10.3390/mi17040431

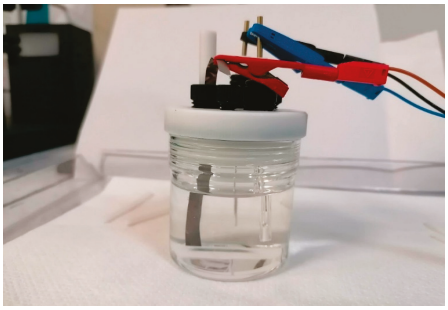


Figure 3. Standard photoelectrochemical cell used for water-splitting experiments in 1 M KOH aqueous electrolyte. The electrodes are biased to the potentiostat via alligator clips.

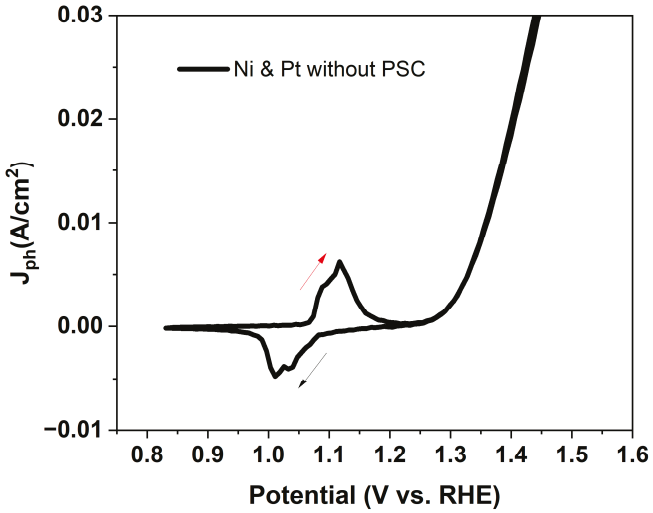


Figure 4. Cyclic voltammetry curve of a standard electrochemical cell, biased with a potentiostat, employing nickel as the working electrode and platinum as the counter electrode in 1 M KOH aqueous solution, at scan rate 100 mV/s. The arrows indicate the direction: from positive to negative voltages (dark arrow, reduction) and from negative to positive voltages (red arrow, oxidation).

3.2. Encapsulated Device Characterization for PEC Applications

After fabrication of PSCs, the J–V characteristics under LED solar simulator, recorded before and after encapsulation, are shown in Figure 5. The nearly overlapping curves confirm that the encapsulation processes do not affect the electrical performance of the devices. To assess whether the encapsulation procedure alters the photovoltaic performance of the devices, a statistical comparison of the key photovoltaic (PV) parameters (short-circuit current density, J_{sc}, open-circuit voltage, V_{oc}, fill factor, FF, and power conversion efficiency, PCE) was carried out before and after encapsulation. Figure 6 shows the distribution of each parameter across multiple devices, represented as box-and-whisker plots with the individual datapoints overlaid. This analysis allows a direct evaluation of potential degradation or variability induced by the encapsulation process.

The distributions of PV parameters reveal that encapsulation does not negatively affect the photovoltaic performance of the PSCs. A slight increase in J_{sc} is observed after encapsulation. This improvement is attributed to a reduction in surface and interfacial recombination losses. In particular, the encapsulation layers act as an effective barrier against moisture and oxygen, which are known to induce trap states and accelerate interfacial degradation in perovskite devices. In addition, the lamination process can improve interfacial contact between layers, particularly at the back contact, thereby facilitating more efficient charge extraction. A minor contribution from enhanced optical confinement within the encapsulated structure may also play a role. Similar trends have been reported in

https://doi.org/10.3390/mi17040431

the literature, where encapsulation strategies were shown not only to enhance environmental stability, but also to suppress non-radiative recombination and ion migration at perovskite interfaces, leading to improved photovoltaic performance, although different encapsulation chemistries were used [20]. Overall, these effects contribute to more efficient carrier collection, resulting in the observed increase in photocurrent. These results confirm the robustness of the encapsulation strategy and demonstrate that the devices retain full photovoltaic functionality prior to their implementation as photoanodes in PEC measurements.

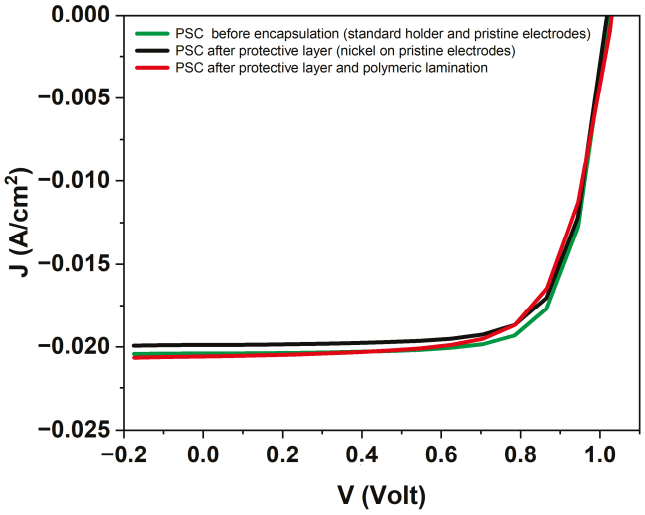


Figure 5. Typical J–V characteristics of PSCs recorded before and after encapsulation. The green curve corresponds to the pristine device measured in the standard holder with original electrodes (gold as positive and ITO as negative electrode); the black curve represents the device after applying the protective Kapton layer and catalytic nickel foil electrodes on the pristine contacts; and the red curve shows the device after full encapsulation with the polymeric multilayer lamination (PET–EVA).

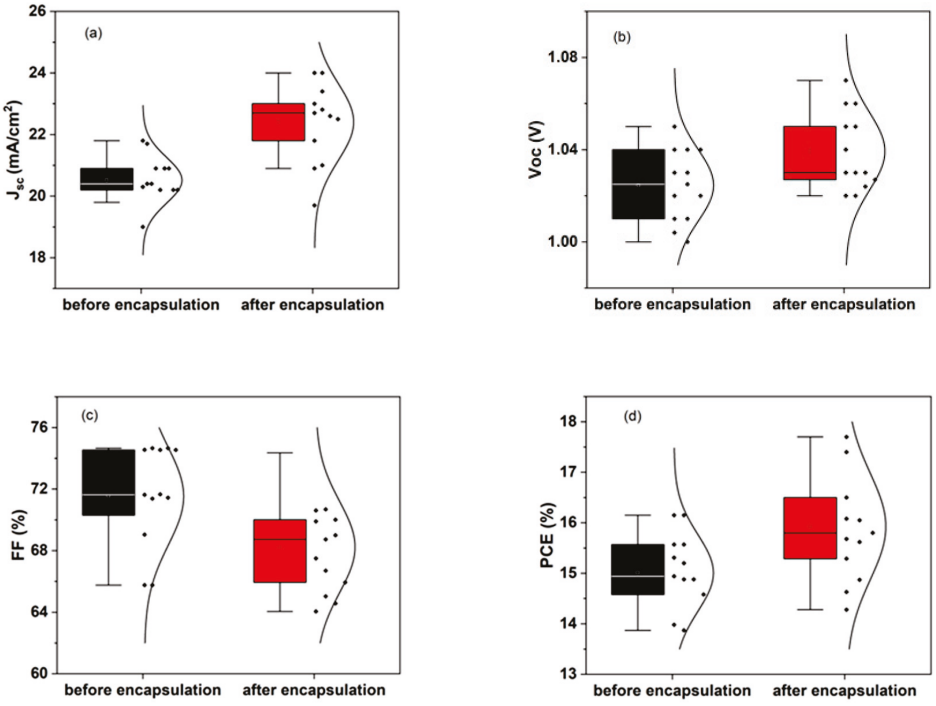


Figure 6. Statistical distribution of photovoltaic parameters before and after encapsulation: (**a**) short-circuit current density (J_{sc}), (**b**) open-circuit voltage (V_{oc}), (**c**) fill factor (FF) and (**d**) power conversion efficiency (PCE).

https://doi.org/10.3390/mi17040431

3.3. Experimental Setup for Perovskite Solar Cells in Outside and Immersed Configurations

The photoelectrochemical performance of the encapsulated PSCs (called PSC A, PSC B, PSC C and PSC D) was evaluated in two operational configurations: outside and immersed.

3.3.1. Outside Configuration

In the OS configuration, the encapsulated PSCs operated as independent light-harvesting units, directly powering the external electrochemical cell for water splitting. Figure 7 shows the corresponding photographs. The left panel displays the full experimental setup, including the electrochemical cell, the solar simulator, and the microprobes used to contact the external perovskite solar cell. In the central image, a single external PSC is contacted with two microprobes, while the right image shows two PSCs connected in series and contacted in the same manner, both illuminated under identical conditions.

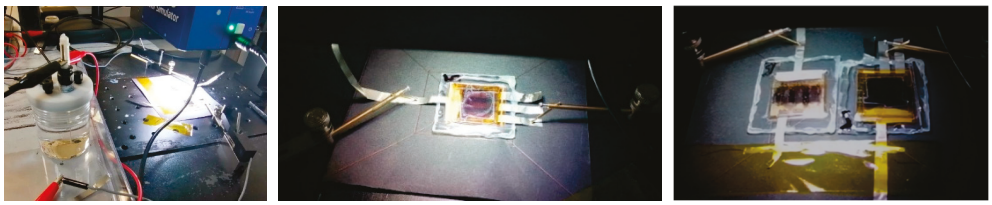


Figure 7. Photographs of the experimental setup used for testing PSCs in outside configuration under LED solar illumination. (**Left**) The encapsulated PSC is connected externally to the standard electrochemical cell. (**Center**) Single perovskite solar cell. (**Right**) Two PSCs connected in series.

Typical J–V curves (Figure 8) confirm that connecting two PSCs in series increases the open-circuit voltage (V_{oc}) as expected, while the current density (J) decreases slightly due to additional contact resistance introduced by the series connection. In the OS configuration, the only driving force for the reaction was the photovoltage delivered by the perovskite solar cell placed outside the electrolyte, which powered the Ni/Pt electrochemical cell. All measurements in alkaline electrolyte were performed under zero applied bias from the potentiostat. No hydrogen evolution was detected in the dark, confirming the absence of spontaneous electrochemical activity. Under illumination, the photocurrent was observed, demonstrating that the photovoltage generated by external PSCs was sufficient to autonomously power the water-splitting reaction. The chronoamperometric response (Figure 9) clearly shows a marked increase in photocurrent (J_{ph}) upon illumination, corresponding to hydrogen generation, and a return to baseline in the dark.

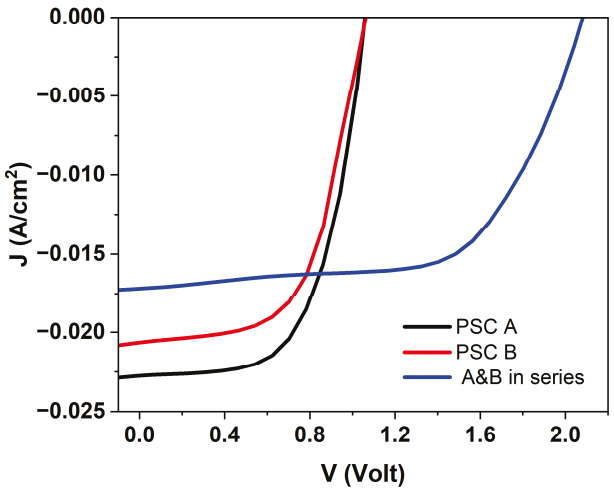


Figure 8. Typical current density–voltage (J–V) characteristics of one PSC and of the two devices connected in series, lighted with LED solar simulator.

https://doi.org/10.3390/mi17040431

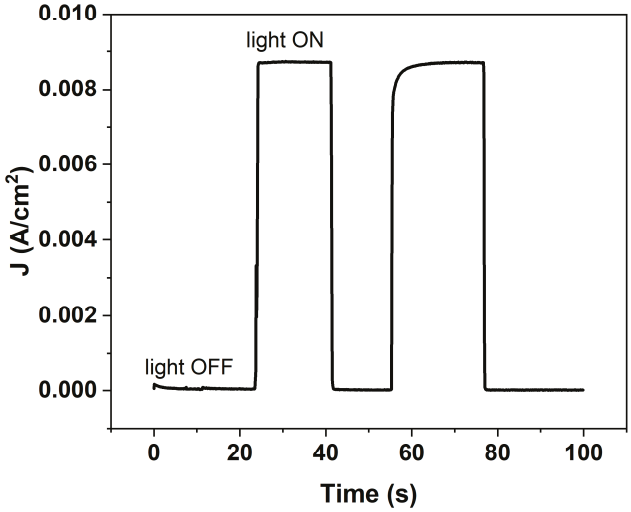


Figure 9. Photocurrent density of the photoelectrochemical cell connected to PSCs in series, lighted by LED solar simulator and no bias with potentiostat.

3.3.2. Immersed Configuration

In the IS configuration, the encapsulated perovskite solar cell was directly placed in the alkaline electrolyte, serving simultaneously as the photovoltaic absorber and as the mechanical support for the nickel electrode that defined the active area, and no bias is applied from the potentiostat. In this arrangement, the PSC was fully integrated within the electrochemical environment. Photographs of the experimental setup are presented in Figures 10 and 11, where LED solar simulator lighted through the substrate glass side. The light beam was oriented perpendicularly to the photoanode surface to ensure uniform illumination of the active area. Figure 12 compares the transient photocurrent generated (J_{ph}) by one PSC when contacted with either one or two nickel foils. When two Ni foils are connected to the two Au pads of the PSC (red curve), the photocurrent nearly doubles relative to the configuration with a single Ni foil (black curve). This increase is consistent with the increasing of the electrochemically active area while the operating voltage remains unchanged, confirming that the photocurrent scales proportionally with the area of active Ni contact interfaces participating in the OER process. The transient J_{ph}–t profiles exhibited clear ON/OFF photoresponses synchronized with light modulation, confirming that no reaction occurred in the dark and unbiased (see Videos S1 and S2 recorded with a single nickel foil and two nickel foils, respectively).

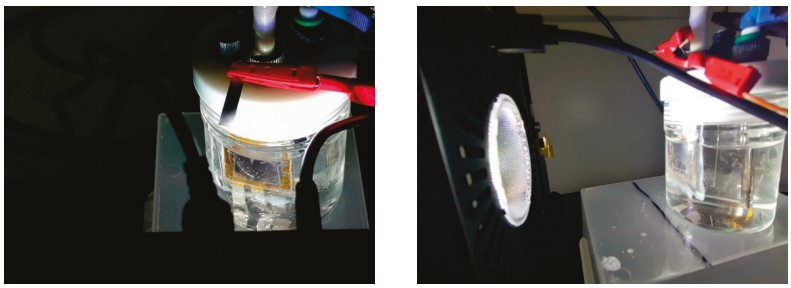
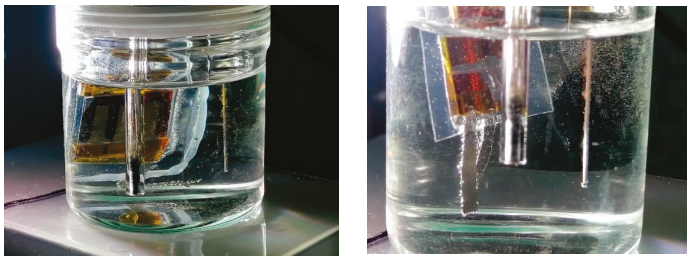


Figure 10. Photographs of the photoelectrochemical setup when perovskite-based photoanode was immersed. (**Left**) The encapsulated perovskite-based photoanode illuminated through the glass substrate using the LED solar simulator. (**Right**) Another view of the same setup during operation.

The influence of externally applied bias from the potentiostat on the PEC performance was also examined (Figure 13). As expected, the photocurrent increased if 300 mV bias was applied, indicating improved charge separation and enhanced interfacial charge-transfer

https://doi.org/10.3390/mi17040431

kinetics. No measurable current or hydrogen evolution was observed in the dark, even under applied bias, confirming the strictly photoinduced nature of the process.



(**a**) (**b**)

Figure 11. Magnified views of the perovskite-based photoanode showing the actual placement of the nickel electrodes on the Au terminals after encapsulation. (**a**) Configuration with a single Ni electrode placed on one Au pad of the device. (**b**) Configuration with two Ni electrodes positioned on two separate Au pads, defining independent photoactive areas sharing a common ITO contact.

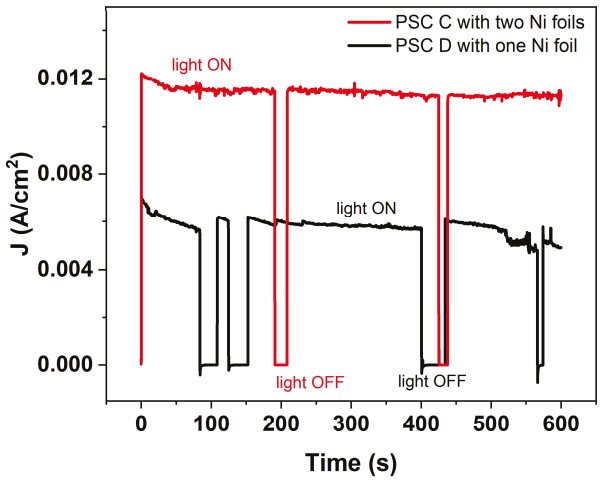


Figure 12. Photocurrent–time (J_{ph}–t) response of photoanode under illumination but no bias with potentiostat. The black curve corresponds to a device with a single Ni foil electrode placed on one Au pad, while the red curve refers to a device with two Ni foil electrodes positioned on two separate Au pads. PSC C-Ni foil 0.56 cm^2 each, PSC D-Ni foil 0.6 cm^2.

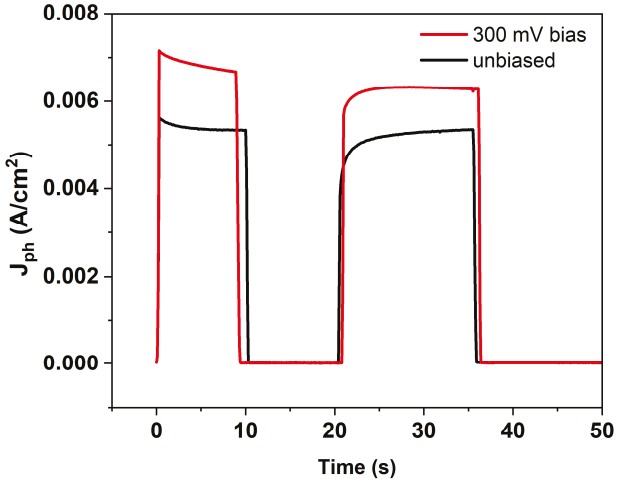


Figure 13. Photocurrent–time response of the immersed perovskite photoanode under chopped illumination. The black curve corresponds to measurements performed at 0 V bias, while the red curve represents data acquired under an applied bias of +300 mV. PSC had 3 Nickel foils, 0.5 cm^2 each.

https://doi.org/10.3390/mi17040431

3.4. Photoelectrochemical Response: Outside vs. Immersed Configuration

A comparative CV analysis was performed on the same encapsulated PSC, first operated outside the electrolyte and then immersed in the electrolyte to enable a direct comparison. The measurements were also compared with those of a standard Ni electrode measured without the perovskite solar cell. (Figure 14). The CV curves were recorded without iR compensation; however, the series resistance of the system (4–7 Ω) results in a negligible uncompensated drop, making this correction unnecessary for interpreting the data. Both configurations, OS and IS, exhibit hysteresis between the reduction and oxidation scans, a characteristic of perovskite-based photoelectrodes associated with ionic migration and capacitive charging within the halide perovskite absorber [21]. However, hysteresis is noticeably more pronounced in the OS configuration (dark curve Figure 14), indicating slower interfacial equilibration and higher recombination losses when the device is electrically connected through external wiring. In contrast, the immersed device shows a more stable and reproducible CV shape, suggesting improved charge-transfer kinetics. This difference can be rationalized considering the electrical and electrochemical coupling in the two configurations. In the OS configuration, the photovoltage generated by the perovskite is delivered through external wiring and metallic contacts before reaching the electrolyte, introducing additional series resistance, contact losses, and potential drops at multiple interfaces. These effects reduce the effective driving force available for the electrochemical reaction and slow down interfacial charge transfer. In contrast, in the IS configuration, the catalyst is directly integrated within the electrochemical environment and electrically coupled to the perovskite back contact, minimizing resistive losses and enabling a more efficient transfer of photogenerated holes to the NiOOH active sites. This improved coupling enhances the kinetics of the $Ni(OH)_2$/NiOOH redox transition and facilitates faster charge injection into the electrolyte. These effects contribute to the observed history-dependent electrochemical response, which is absent in the standard electrochemical cell where the Ni and Pt electrodes are not powered by the perovskite solar cell (blue curve; Figure 14). Moreover, in the IS configuration (red curve; Figure 14), the photocurrent increases more rapidly and reaches higher values compared to the OS configuration. The onset potential for oxygen evolution shifts dramatically when the PSC is used for powering the nickel foil electrode for both IS and OS configurations. While the Ni/Pt electrochemical cell, not powered by the perovskite absorber, exhibits an onset around 1.32 V vs. RHE (Figure 14; blue curve), both the IS and OS PSC–Ni configurations show a much earlier onset at ~0.34 V vs. RHE (Figure 14; black and red curves).

This strong reduction in overpotential does not originate from the Ni–electrolyte interface itself, as nickel already forms $Ni(OH)_2$/NiOOH in the standard cell, but rather from the photovoltage and photogenerated holes supplied by the perovskite absorber directly into the NiOOH catalytic sites, triggering the $Ni(OH)_2$/NiOOH redox transition at approximately 177 mV (Figure 14; black and red curves). This value is markedly lower than the anodic peak observed at ~1.1 V in the configuration where the electrochemical cell operates without being powered by the PSC (Figure 14; blue curve). This comparison clearly shows that the photovoltage provided by the perovskite significantly lowers the energetic threshold required for Ni activation in alkaline media. This behavior indicates that the photovoltage generated by the perovskite effectively shifts the Fermi level of the electrode under illumination, enabling earlier activation of the catalytic cycle. In this sense, the perovskite does not merely act as a power source but actively modulates the electrochemical potential at the catalyst interface. Furthermore, the IS configuration shows the highest photocurrents and the most favorable kinetics, whereas the OS configuration still benefits from photovoltage assistance but is limited by additional resistive and interfacial losses. Taken together, the comparison demonstrates that the perovskite solar cell is responsible

https://doi.org/10.3390/mi17040431

for the drastic reduction in OER onset potential and that direct immersion maximizes the efficiency of photovoltage transfer to the catalytic interface and reduces hysteresis compared to the OS configuration. Overall, these results demonstrate that the observed enhancement in the IS configuration is not due to changes in catalyst composition or intrinsic activity, but rather to improved photovoltage delivery and reduced resistive losses enabled by the integrated device architecture. This highlights the critical role of device design in maximizing the utilization of photogenerated charge carriers in perovskite-based PEC systems. Although the CV curves highlight clear differences in onset potential and photocurrent behavior between the two configurations, a quantitative metric is needed to determine how effectively the devices convert absorbed photons into chemical output.

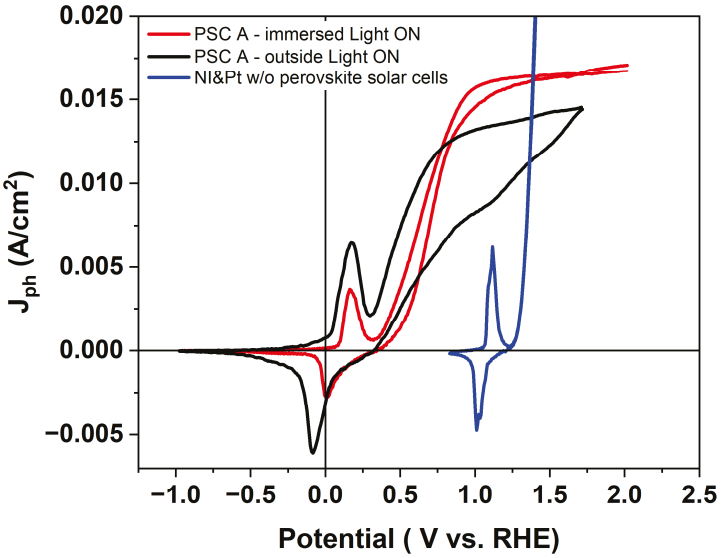


Figure 14. Cyclic voltammetry curves of the encapsulated perovskite in both OS and IS configurations, dark and red curves respectively, compared to the cyclic voltammetry of a standard electrochemical cell (the blue one).

Although direct quantification of H_2/O_2 and Faradaic efficiency was beyond the scope of the present study, these measurements will be necessary in future work to validate practical energy conversion and determine the corresponding Solar-to-Hydrogen (STH) efficiency. Therefore, in this study, the Applied Bias Photon-to-Current Efficiency (ABPE) was used as a direct and reliable metric of photoelectrochemical performance.

The ABPE is defined as

$$\mathrm{ABPE}(\%) = \frac{J_{ph} \times (1.23 - V_{bias})}{P_{in}} \times 100 \quad (2)$$

where J_{ph} is the photocurrent density (A cm^{-2}), 1.23 V is the thermodynamic potential required for water splitting, V_{bias} is the applied bias potential, and P_{in} is the incident light power density (100 mW cm^{-2} under standard AM 1.5 G solar illumination). The potential corresponding to the maximum of the ABPE curve is referred to as the optimal bias (V_{opt}), which represents the point of maximum conversion efficiency (Figure 15).

The IS configuration delivers the highest ABPE (~19.9%) because it minimizes contact resistance and enables more efficient photovoltage transfer to the Ni/NiOOH interface, whereas the OS configuration (~17.8%) remains limited by additional wiring and interfacial losses. Table 1 summarizes the photoelectrochemical parameters obtained for both the IS and OS configurations.

https://doi.org/10.3390/mi17040431

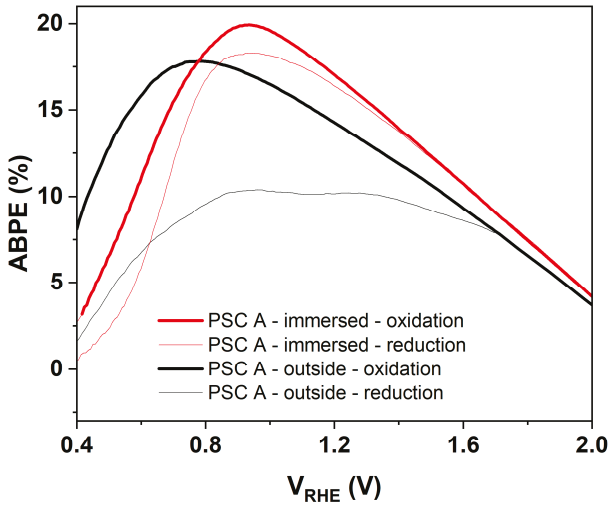


Figure 15. Applied Bias Photon-to-Current Efficiency curves for the PSC operated in the OS and IS configurations.

Table 1. Summary of key photoelectrochemical parameters for the PSC operated in the OS and IS configurations.

Configuration	V_{Onset} (V vs. RHE)	V_{opt} (V vs. RHE)	Jph (mA/cm^2)	$ABPE_{max}$ (%)
IS (oxidation curve)	0.34	0.93	15.7	~19.93
IS (reduction curve)	0.34	0.93	15.7	~18.31
OS (oxidation curve)	0.34	0.75	13.6	~17.80
OS (reduction curve)	0.34	0.93	9.9	~10.39

To examine the effective operating conditions of the device in different configurations, the J–V curve, measured for pristine PSC in photovoltaic (PV) mode (before immersion), was overlaid with the photocurrent–potential characteristics extracted from cyclic voltammetry in the IS and OS configurations (Figure 16). This combined representation directly shows how much of the photovoltage generated by the perovskite can be transferred to the electrochemical reaction under each operating mode.

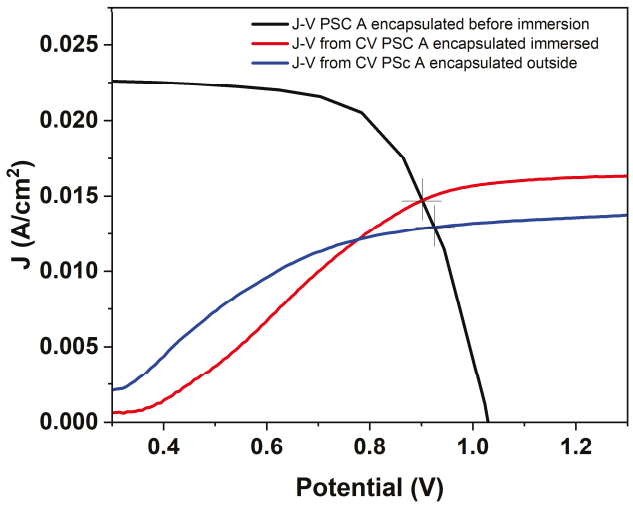


Figure 16. J–V curve of the perovskite solar cell (black, before immersion) overlaid with the photocurrent–potential responses extracted from CV in the IS (red) and OS (blue) configurations. The intersection point indicates the self-driven operating condition for OER without external bias.

https://doi.org/10.3390/mi17040431

In PV mode (black curve), the device shows V_{oc} of ~1.05 V and short-circuit current density exceeding 20 mA cm^{-2}, representing the maximum power available from the perovskite absorber. When the same device operates as an immersed photoanode (red curve), the anodic photocurrent follows a markedly different J–V trajectory, intersecting the PV curve at approximately 0.89 V and ~14.7 mA cm^{-2}. This intersection defines the potential operating point at which the photovoltage generated by the perovskite is sufficient to sustain OER without external bias. The higher current at the intersection reflects the more efficient transfer of photovoltage to the Ni/NiOOH interface in the IS configuration, in accordance with improved charge-transfer kinetics and reduced interfacial losses. In contrast, the OS configuration (blue curve) exhibits lower photocurrent and its intersection with the PV curve occurs at a much smaller current density and at a higher voltage, 0.93 V, closer to V_{oc}. This indicates that only a limited fraction of the available photovoltage is effectively transferred to the electrochemical cell when the device is not immersed, due to additional series resistance and wiring losses, and the absence of direct semiconductor–electrolyte coupling. As a result, the OS configuration operates close to the OER onset, which explains why only a few high-performing cells can drive oxygen evolution in this configuration.

3.5. Stability of Immersed Device

To evaluate the operational long-term stability of the immersed perovskite-based photoanode, an aging test was carried out under continuous illumination with an LED solar simulator in 1 M KOH, with simultaneous monitoring of the photocurrent and visual inspection of the device over time (Figure 17).

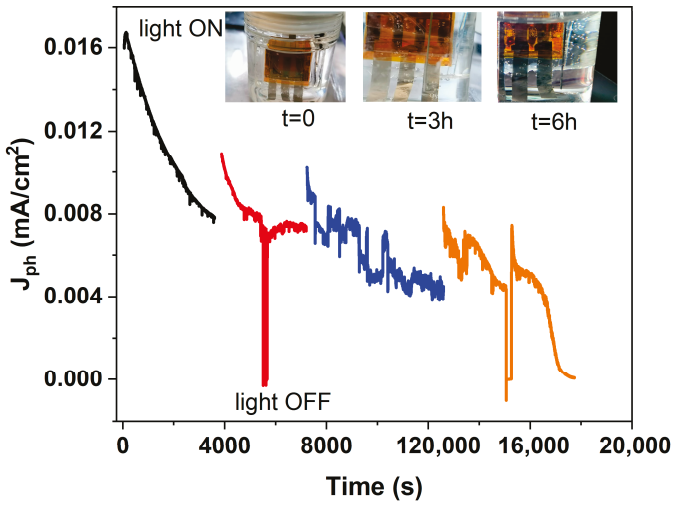


Figure 17. Photocurrent stability of the immersed perovskite-based photoanode under continuous illumination in 1 M KOH. The photocurrent density (J_{ph}) is shown as a function of time, with different colors corresponding to consecutive measurement intervals. Photographs of the device at t = 0 h, 3 h, and 6 h during immersion are reported above the graph, highlighting the physical evolution of the sample over time.

At t = 0 h, the photograph (inset of Figure 17) shows the device at the beginning of the immersion. After ~3 h of immersion, a yellowish coloration becomes visible along the edges of the encapsulation, indicating that although the PET–EVA lamination provides a good barrier against moisture and alkaline exposure, it is insufficient on its own to fully protect the device edges from electrolyte penetration. Additionally, epoxy resin was applied at the borders to reinforce edge sealing, but partial penetration still occurred during prolonged operation. After 6 h, the perovskite layer shows complete degradation, accompanied by a

https://doi.org/10.3390/mi17040431

sharp decrease in photocurrent, confirming that device failure occurs once the electrolyte reaches the active layer. The observed edge degradation likely originates from electrolyte penetration through imperfect sealing, leading to perovskite dissolution and ion migration. Future work should explore advanced edge-sealing materials or multilayer encapsulation strategies. Previous studies have shown that PET–EVA encapsulation can offer effective environmental protection in alkaline media [22,23], suggesting that the operational stability observed here could be further extended through improved edge-sealing strategies.

3.6. Comparison with Literature-Reported Approaches

Table 2 compares the IS configuration presented in this study with representative perovskite-based photoelectrodes reported in the literature under similar alkaline conditions (1 M KOH, AM 1.5 G illumination). A direct comparison highlights that the present device achieves among the highest ABPE values reported for single photoanode configurations, reaching ~20%, significantly exceeding previously reported values (typically $\leq$8.5% for standalone perovskite photoanodes [13,14]). It is important to note that higher efficiencies reported in the literature are often achieved in tandem architectures (e.g., perovskite/silicon systems [15]), where additional photovoltage is provided by a second absorber. In contrast, the performance reported here is obtained using a single perovskite-based photoanode, emphasizing the effectiveness of the proposed device architecture in maximizing photovoltage utilization. Compared to previous immersed configurations, the improved performance can be primarily attributed to the combined effect of the triple-cation composition, which enhances electronic quality and stability, and the optimized device integration that minimizes resistive losses and improves charge-transfer kinetics at the catalyst interface. In terms of operational stability, the device exhibits a degradation timescale of approximately 5 h, comparable to other triple-cation perovskite systems [15], while longer stability reported for single-cation systems is generally associated with significantly lower efficiencies. This highlights the current trade-off between performance and durability in perovskite-based PEC systems. Overall, this comparison demonstrates that high PEC performance can be achieved without relying on complex tandem architectures, but rather through optimized device integration and efficient photovoltage utilization.

Table 2. Recent literature data obtained with the best perovskite photoelectrodes in 1 M KOH, illumination 100 mW cm^{-2}.

Photoelectrode Configuration	Jph (mA/cm^2) at 1.23 V vs. RHE	ABPE (%)	STH (%)	Aging	Ref.
$Cs_{0.1}(MA_{0.17}FA_{0.83})_{0.9}Pb(I_{0.83}Br_{0.17})_3$ immersed photoanode/Nickel foil	16.4	19.9		5 h	This work
$MAPbI_3$–$BiVO_4$ photoanode tandem–outside PSC	5.01	6.2			[12]
$FAPbI_3$/Ni/NiFeOOH—immersed photoanode	22.8		9.8	3 days	[13]
$FAPbBr_3$/carbon/graphite/NiFe immersed photoanode	9.12	8.5		100 h	[14]
$Cs_{0.05}FA_{0.85}MA_{0.1}Pb(I_{0.95}Br_{0.05})_3$ & $FA(PbI_3)_{0.97}(MAPbI_3)_{0.03}$ immersed photocathode & photoanode	20	13.4 *		5 h	[15]
Tandem perovskite/silicon phoanode	16.9 10	20.8 * 13.4 *		1 h 102 h	

* Fehr et al. [15] reported STH efficiencies assuming a 100% Faradaic efficiency for the catalysts, which corresponds to an ABPE.

https://doi.org/10.3390/mi17040431

Further improvements in encapsulation and edge sealing will be required to extend operational lifetimes while maintaining the high efficiency demonstrated here.

4. Conclusions

This work presents a systematic comparison between outside (OS) and immersed (IS) configurations of encapsulated triple-cation perovskite solar cells operating as photoanodes for solar-driven water splitting. The OS configuration corresponds to a photovoltaic-assisted electrochemical cell setup, whereas the IS configuration involves direct integration of the solar cell-based device, together with the Ni catalyst, into the electrolyte. The results clearly demonstrate that device architecture plays a decisive role in governing the photoelectrochemical response. In particular, the immersed configuration significantly enhances charge-transfer kinetics, reduces hysteresis, and increases photocurrent density and overall PEC efficiency compared to the outside configuration. A key finding of this study is that the observed performance enhancement does not originate from changes in catalyst composition or from direct semiconductor–electrolyte interaction, as the perovskite absorber remains fully encapsulated. Instead, the improvement arises from more efficient photovoltage delivery and reduced resistive losses enabled by the integrated device architecture. This provides direct experimental evidence that photovoltage utilization, rather than catalyst modification, is a critical factor in determining the performance of perovskite-based PEC systems. Under AM 1.5 G illumination, the immersed configuration achieves an ABPE of approximately 20%, among the highest values reported for perovskite-based photoanodes, while simultaneously reducing the OER onset potential by nearly 1 V compared to a standard Ni/Pt electrochemical system. From a broader perspective, this study introduces three main advances: (i) the first systematic comparison between outside and immersed configurations, enabling isolation of architectural effects; (ii) the identification of photovoltage delivery and resistive losses as the dominant factors governing PEC performance; and (iii) one of the first comprehensive photoelectrochemical characterizations of triple-cation perovskites under alkaline conditions. In addition to these fundamental insights, the proposed architecture outlines a viable route toward scalable PEC systems, based on solution-processed perovskite absorbers, commercially available PET–EVA encapsulation materials, and a simplified monolithic design that minimizes external wiring and associated losses. Future work should focus on improving long-term operational stability through advanced encapsulation and edge-sealing strategies, as well as on direct quantification of hydrogen and oxygen evolution to determine Solar-to-Hydrogen and Faradaic efficiencies. These developments will be essential to translate the demonstrated performance into practical and scalable solar fuel technologies.

Supplementary Materials: The following supporting information can be downloaded at: https://www.mdpi.com/article/10.3390/mi17040431/s1, Video S1: One Nickel foil and PSC immersed; Video S2: Two Nickel foils and PSC immersed.

Author Contributions: Conceptualization, V.L.F., N.L., S.D.G. and M.M.; methodology, V.L.F., N.L., S.D.G., M.M. and A.M.; validation, V.L.F., M.M., A.M., G.L., S.D.G., N.L., R.V., A.G. and G.M.; formal analysis, V.L.F., G.L., S.D.G. and R.V.; investigation, V.L.F. and A.M.; writing—original draft preparation, V.L.F.; writing—review and editing, V.L.F., M.M., G.L., S.D.G., N.L., R.V., A.G. and G.M.; project administration, A.G.; funding acquisition, G.M. All authors have read and agreed to the published version of the manuscript.

Funding: This research was funded by the European Union—NextGeneration EU from the Italian Ministry of Environment and Energy Security, POR H2 AdP MEES/ENEA with involvement of CNR and RSE, PNRR—Mission 2, Component 2, Investment 3.5 "Ricerca e sviluppo sull'idrogeno", CUP: I83C22001170006.

https://doi.org/10.3390/mi17040431

Institutional Review Board Statement: Not applicable.

Informed Consent Statement: Not applicable.

Data Availability Statement: The data presented in this study are available on request from the corresponding author.

Conflicts of Interest: The authors declare no conflicts of interest.

Abbreviations

The following abbreviations are used in this manuscript:

OS	Outside
IS	Immersed
OER	Oxygen Evolution Reaction
HER	Hydrogen Evolution Reaction
ABPE	Applied Bias Photon-to-Current Efficiency
RHE	Reversible Hydrogen Electrode
PET–EVA	poly (ethylene terephthalate)–ethylene vinylacetate
AM	Air Mass
PSC	Perovskite Solar Cell
PEC	Photoelectrochemical
STH	Solar-to-Hydrogen
CV	Cyclic Voltammetry
ITO	Indium tin oxide
n-i-p	negative-intrinsic-positive
ETL	Electron Transport Layer
HTL	Hole Transport Layer
J–V	Current Density–Voltage
LED	Light Emitting Diode
J_{sc}	Short-Circuit Current Density
V_{oc}	Open-Circuit Voltage
FF	Fill Factor
PCE	Power Conversion Efficiency
J_{ph}	Photocurrent Density
PV	Photovoltaic
V_{opt}	Optimal Bias

References

1. NREL Best Research-Cell Efficiency Chart. Available online: https://www.nrel.gov/pv/cell-efficiency.html (accessed on 15 January 2026).
2. Green, M.; Ho-Baillie, A.; Snaith, H. The emergence of perovskite solar cells. *Nat. Photon.* **2014**, *8*, 506–514. [CrossRef]
3. Park, N.-G.; Zhu, K. Scalable fabrication and coating methods for perovskite solar cells and solar modules. *Nat. Rev. Mater.* **2020**, *5*, 333–350. [CrossRef]
4. Niu, G.; Li, W.; Li, J.; Liang, X.; Wang, L. Enhancement of thermal stability for perovskite solar cells through cesium doping. *RSC Adv.* **2017**, *7*, 17473–17479. [CrossRef]
5. Jeong, M.; Choi, I.W.; Go, E.M.; Cho, Y.; Kim, M.; Lee, B.; Jeong, S.; Jo, Y.; Choi, H.W.; Lee, J.; et al. Stable perovskite solar cells with efficiency exceeding 24.8% and 0.3-V voltage loss. *Science* **2020**, *369*, 1615–1620. [CrossRef]
6. Ahn, N.; Son, D.Y.; Jang, I.H.; Kang, S.M.; Choi, M.; Park, N.-G. Highly reproducible perovskite solar cells with average efficiency of 18.3% and best efficiency of 19.7% fabricated via Lewis base adduct of lead(II) iodide. *J. Am. Chem. Soc.* **2015**, *137*, 8696–8699. [CrossRef] [PubMed]
7. Yang, Y.; Song, X.; Liu, H.; Zhang, A.; Cao, J.; Wu, C. Encapsulation-driven stability in perovskite solar cells: Suppressing degradation through hermetic sealing. *ACS Appl. Mater. Interfaces* **2025**, *17*, 34119–34128. [CrossRef] [PubMed]
8. Aitola, K.; Gava Sonai, G.; Markkanen, M.; Kaschuk, J.J.; Hou, X.; Miettunen, K.; Lund, P.D. Encapsulation of commercial and emerging solar cells with focus on perovskite solar cells. *Sol. Energy* **2022**, *237*, 264–283. [CrossRef]

https://doi.org/10.3390/mi17040431

9. Dipta, S.S.; Rahim, M.A.; Uddin, A. Encapsulating perovskite solar cells for long-term stability and prevention of lead toxicity. *Appl. Phys. Rev.* **2024**, *11*, 021301. [CrossRef]
10. Chu, Q.-Q.; Sun, Z.; Wang, D.; Cheng, B.; Wang, H.; Wong, C.-P.; Fang, B. Encapsulation: The path to commercialization of stable perovskite solar cells. *Matter* **2023**, *6*, 3838–3863. [CrossRef]
11. Walter, M.G.; Warren, E.L.; McKone, J.R.; Boettcher, S.W.; Mi, Q.; Santori, E.A.; Lewis, N.S. Solar Water Splitting Cells. *Chem. Rev.* **2010**, *110*, 6446–6473. [CrossRef]
12. Qiu, Y.; Liu, W.; Chen, W.; Zhou, G.; Hsu, P.-C.; Zhang, R.; Liang, Z.; Fan, S.; Zhang, Y.; Cui, Y. Efficient solar-driven water splitting by nanocone $BiVO_4$–perovskite tandem cells. *Sci. Adv.* **2016**, *2*, e1501764. [CrossRef]
13. Hansora, D.; Yoo, J.W.; Mehrotra, R.; Byun, W.J.; Lim, D.; Kim, Y.K.; Noh, E.; Lim, H.; Jang, J.W.; Seok, S.I.; et al. All-perovskite-based unassisted photoelectrochemical water splitting system for efficient, stable and scalable solar hydrogen production. *Nat. Energy* **2024**, *9*, 272–284. [CrossRef]
14. Yang, H.; Liu, Y.; Ding, Y.; Li, F.; Wang, L.; Cai, B.; Zhang, F.; Liu, T.; Boschloo, G.; Johansson, E.M.J.; et al. Monolithic $FAPbBr_3$ photoanode for photoelectrochemical water oxidation with low onset-potential and enhanced stability. *Nat. Commun.* **2023**, *14*, 5486. [CrossRef]
15. Fehr, A.M.K.; Agrawal, A.; Mandani, F.; Conrad, C.L.; Jiang, Q.; Park, S.Y.; Alley, O.; Li, B.; Sidhik, S.; Metcalf, I.; et al. Integrated halide perovskite photoelectrochemical cells with solar-driven water-splitting efficiency of 20.8%. *Nat. Commun.* **2023**, *14*, 3797. [CrossRef]
16. Song, Z.; Li, C.; Chen, L.; Dolia, K.; Fu, S.; Sun, N.; Li, Y.; Wyatt, K.; Young, J.L.; Deutsch, T.G.; et al. All-perovskite tandem photoelectrodes for unassisted solar hydrogen production. *ACS Energy Lett.* **2023**, *8*, 2611–2619. [CrossRef]
17. Saliba, M.; Matsui, T.; Seo, J.Y.; Domanski, K.; Correa-Baena, J.P.; Nazeeruddin, M.K.; Zakeeruddin, S.M.; Tress, W.; Abate, A.; Hagfeldt, A.; et al. Cesium-containing triple cation perovskite solar cells: Improved stability, reproducibility and high efficiency. *Energy Environ. Sci.* **2016**, *9*, 1989–1997. [CrossRef] [PubMed]
18. La Ferrara, V.; De Maria, A.; Rametta, G. Green anisole as antisolvent in planar triple-cation perovskite solar cells with varying cesium concentrations. *Micromachines* **2024**, *15*, 136. [CrossRef]
19. Garcia, A.C.; Koper, M.T.M. Effect of saturating the electrolyte with oxygen on the activity for the oxygen evolution reaction. *ACS Catal.* **2018**, *8*, 9359–9363. [CrossRef]
20. Li, W.; Bao, X.; Zhu, A.; Gu, H.; Mao, Y.; Wang, B.; Wang, G.; Guo, J.; Li, Y.; Xing, G. Internal Encapsulation Enables Efficient and Stable Perovskite Solar Cells. *Adv. Funct. Mater.* **2025**, *35*, 2414004. [CrossRef]
21. Tress, W.; Marinova, N.; Inganäs, O.; Nazeeruddin, M.K.; Zakeeruddin, S.M.; Grätzel, M. Understanding the rate-dependent J–V hysteresis, slow time component, and aging in $CH_3NH_3PbI_3$ perovskite solar cells. *Energy Environ. Sci.* **2015**, *8*, 995–1004. [CrossRef]
22. Ocaña, L.; Montes, C.; González-Díaz, B.; González-Pérez, S.; Llarena, E. Evaluation of ethylene-vinyl acetate, methyl methacrylate, and polyvinylidene fluoride as encapsulating materials for perovskite-based solar cells using the low-temperature encapsulation method in a cleanroom environment. *Energies* **2024**, *17*, 60. [CrossRef]
23. Emery, Q.; Dagault, L.; Khenkin, M.; Kyranaki, N.; Bernardes de Araújo, W.M.; Erdil, U.; Demuylder, M.; Cros, S.; Schlatmann, R.; Stannowski, B.; et al. Tips and tricks for a good encapsulation for perovskite-based solar cells. *Prog. Photovolt. Res. Appl.* **2025**, *33*, 551–559. [CrossRef]

Disclaimer/Publisher's Note: The statements, opinions and data contained in all publications are solely those of the individual author(s) and contributor(s) and not of MDPI and/or the editor(s). MDPI and/or the editor(s) disclaim responsibility for any injury to people or property resulting from any ideas, methods, instructions or products referred to in the content.

https://doi.org/10.3390/mi17040431

micromachines

MDPI

Article

A Novel Spiral Si Drift Detector with a Constant Cathode Gap and Arbitrary Cathode Pitch Profiles

Hongfei Wang [1,2,3] and Zheng Li [2,3,*]

[1] School of Physics and Physical Engineering, Qufu Normal University, Qufu 273165, China; wanghf.20@163.com
[2] School of Integrated Circuits, Ludong University, Yantai 264025, China
[3] Engineering Research Center of Photodetector Special Chip in Universities of Shandong, Ludong University, Yantai 264025, China
* Correspondence: 3636@ldu.edu.cn

Abstract

In this paper, an innovative design of a silicon spiral drift detector (SDD) has been proposed. In this design, gaps under the SiO_2 layer between the cathode rings are kept constant, with a minimum value to reduce the surface leakage current. The cathode pitch profile $P(r)$ as a function of radius r is allowed to change in an arbitrary way to achieve the optimum field distribution. The concept, design considerations, modeling and electrical simulations have been carried out for this novel structure with a hexagonal spiral silicon drift detector. Using one-dimensional analyses, we obtain the exact solution of the spiral design $r = r(\theta)$ with a near-arbitrary pitch profile $P(r) = P_1\left(\frac{r}{r_1}\right)^{\frac{1}{\eta}}$, with η as an arbitrary real number. We also obtained the electric potential and field profiles on both surfaces of the detector. Using a Technology Computer-Aided Design (TCAD) tool, we made 3D simulations of the detector's electrical properties. The hexagonal spiral silicon drift detector has excellent electrical properties: a uniform electric field, smooth distribution of electric potential and electron concentration, and a clear electron drift channel. The distributions of the electric field, electric potential, and electron concentration are symmetrical and smooth, which is beneficial for applications in photon sciences (X-ray) and safeguards and homeland security (particle radiation). The theoretical work and simulation results serve as solid foundations for the detector design and the expansion of semiconductor technology.

Keywords: spiral silicon drift detector; Arbitrary Pitch Profiles; constant cathode gap; electric field distribution; electric potential distributions; electron concentration distribution

1. Introduction

The concept of the silicon drift detector (SDD) was first introduced by E. Gatti and P. Rehak in the 1980s [1], marking a significant advancement in radiation detection technology. Since their emergence in 1983, SDDs have evolved as a pivotal tool across numerous scientific and industrial domains due to their exceptional performance and technological maturity. These detectors are fabricated using planar processing techniques and the principle of lateral depletion on ultra-pure, high-resistivity silicon substrates. In contrast to conventional silicon-based detectors like micro-strip or pixel devices, SDDs offer distinct benefits including rapid response times, high energy resolution, ease of integration, low capacitance, minimal noise, and uniform internal drift characteristics. Moreover, they operate effectively without the need for liquid nitrogen cooling, and under a nearly parallel surface drift field, the electrons move toward the anode at an approximately constant velocity.

SDDs have found extensive applications in cutting-edge fields such as in experiments at CERN's LEP NA45 in 1992 and BNL's Relativistic Heavy Ion Collider [2–4] in 2001, as well as in photon and nuclear physics [5,6], dark matter detection [7], X-ray fluorescence spectroscopy [8–10], medical imaging [11–15], and X-ray pulsar navigation [15–19]. For instance, pulsar-based navigation techniques leverage SDDs for deep space exploration and autonomous satellite guidance, with collaborative efforts like those between NASA and BNL focusing on modular X-ray spectrometers for lunar surface mapping. The historical progression of detector technology, beginning with single crystals, bipolar transistors, germanium crystal counters, lithium-drift detectors, and charge-coupled devices in the 1950s, culminated in the development of SDDs, underscoring their transformative impact.

Structurally, SDDs have advanced from initial silicon strip designs to concentric ring and spiral configurations. Traditional concentric ring SDDs feature a central anode surrounded by cathode rings but require manual voltage biasing for each ring to establish a potential gradient, leading to challenges such as nonlinear potential distribution and complex resistor selection. In response, the spiral SDD was developed to address the limitation of automatic voltage division. By utilizing a spiral cathode ring that functions simultaneously as a rectifying junction and voltage divider, this design generates a potential gradient (or transverse drift field), enabling incident carriers to drift efficiently to the collection anode [20,21] without external dividers. This innovation significantly simplifies operation and mitigates issues like high power consumption and heating, which are prevalent in large-area SDDs or arrays. The main advantages of the spiral SDDs are less surface leakage current (less noise, better resolution) and better drift field for fast charge collection. Consequently, the spiral SDD has become a mainstream technology.

In our novel design method, the cathode gaps (g) under SiO_2 are kept constant to minimize surface leakage current. We allow the pitch profile $P(r)$ to vary in an arbitrary way to obtain the optimum electric field distribution. Our design is different from that in [22], where a constant electric surface field is imposed. Although cathode gaps were kept constant in both cases, our electric field is allowed to change to obtain the optimal profile. Exact solutions of SDD of spiral design $r = r(\theta)$ can be obtained for the hexagonal spiral SDD. Based on the theoretically calculated coordinates of each point on the spiral ring, the SDD structure diagram can be drawn. Technology Computer-Aided Design (TCAD) is used for simulation in this work. We have systematically researched its respective electrical properties, such as the electric field and potential distributions, and the electron concentration distribution.

2. The Novel Spiral Silicon Drift Detector (SDD) Concept and Design Considerations

Figure 1 presents the top and bottom views of the novel spiral SDD. The structural parameters and the foundational rules of the detector's design can be seen clearly in Figure 2. In a spiral SDD, the cathode pitch $P(r)$, the cathode width $w(r)$, and the gap between cathode rings $g(r)$ can be written as, on the top surface:

$$P(r) = g(r) + w(r) = g + w(r) \tag{1}$$

Here, we use constant gap g, and on the bottom surface

$$P_B(r) = g_B(r) + w_B(r) = g_B + w_B(r) \tag{2}$$

https://doi.org/10.3390/mi17030354

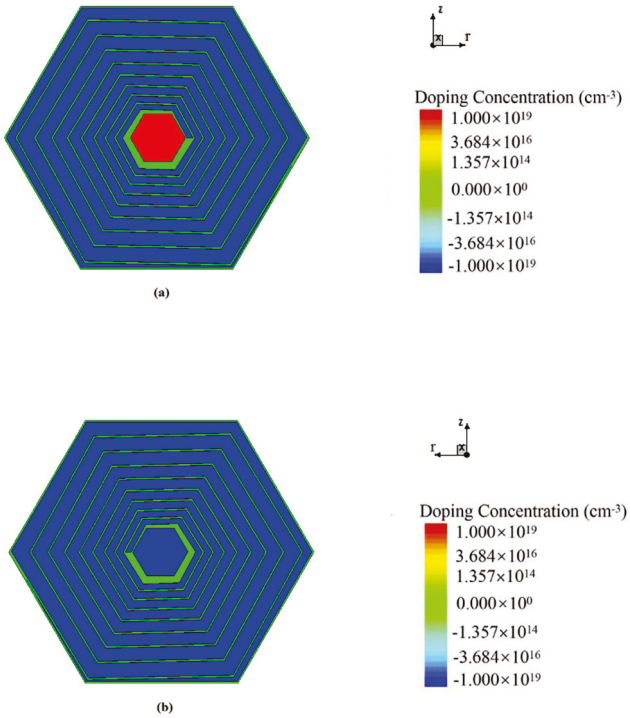


Figure 1. (**a**) The top view of the novel spiral SDD unit cell. (**b**) The bottom view of the unit cell.

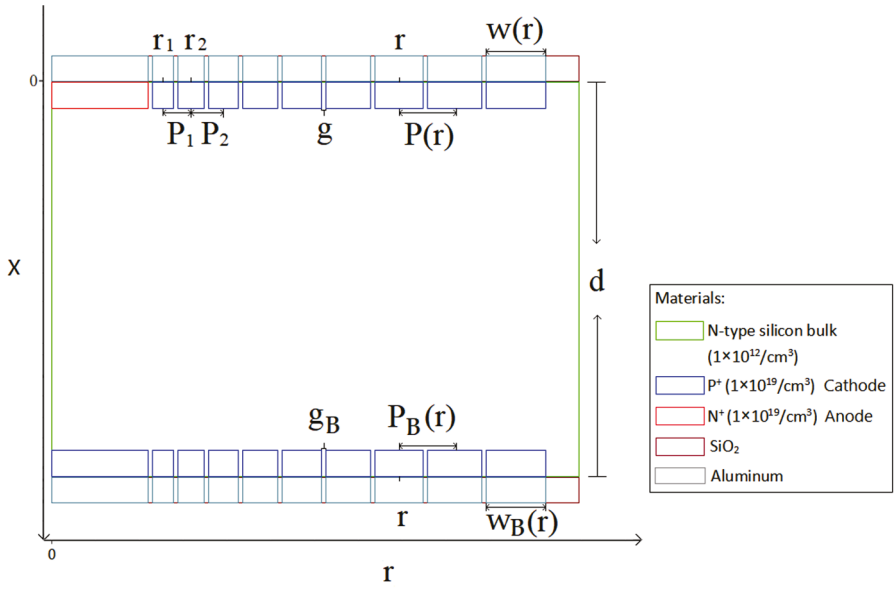


Figure 2. The cross-section view and the structural parameters of the novel spiral SDD.

In our work, we chose the constant and minimum gap values for both surfaces to reduce surface leakage current. On the top surface, let $E(r)$ as the electric field profile on the surface; then, the voltage drop between r and $r + \Delta r$ is $\Delta V(r)$:

$$\Delta V(r) = E(r) \cdot P(r) = I\frac{\rho_s}{w(r)} \cdot \alpha r \tag{3}$$

where ρ_s denotes the sheet resistance of the cathode ion implant, and I represents the ohmic current in the spiral, and

$$\alpha = \begin{cases} 2\pi \text{ (circle)} \\ 6 \text{ (hexagon)} \end{cases}$$

https://doi.org/10.3390/mi17030354

where α is a parameter for different spiral shapes.

We have:

$$E(r) = \frac{\alpha I \rho_s r}{P(r)w(r)} \tag{4}$$

From Equations (1) and (4), we have:

$$E(r) = \frac{\alpha I \rho_s r}{P(r)[P(r) - g]} \tag{5}$$

We can obtain the electric potential profile $\phi(r)$ on the top surface:

$$\phi(r) = \int_{r_1}^{r} E(r)dr = \alpha I \rho_s \int_{r_1}^{r} \frac{rdr}{P(r)[P(r) - g]} \tag{6}$$

We chose the following cathode pitch profile:

$$P(r) = P_1 \left(\frac{r}{r_1}\right)^{\frac{1}{\eta}} \tag{7}$$

where a real number (near arbitrary) ($0 < \eta < \infty$), and η defines how fast $P(r)$ changes with r. Let

$$x = \left(\frac{r}{r_1}\right)^{\frac{1}{\eta}} \tag{8}$$

We have:

$$P(x) = P_1 x$$

and

$$r = r_1 x^{\eta}$$

where r_1 denotes the radius of the first ring of the spiral, and P_1 represents the pitch of the first ring.

Equation (6) becomes:

$$\phi(r) = \int_1^x \rho_s \alpha I r_1 \eta \frac{x^{\eta-1} dx r_1 x^{\eta}}{P_1 x(P_1 x - g)}$$

or

$$\phi(r) = \frac{\rho_s \alpha I {r_1}^2 \eta}{P_1} \int_1^x \frac{x^{2\eta-2} dx}{P_1 x - g} \tag{9}$$

If $\eta = 1$,

$$\phi(r) = \frac{2\alpha \rho_s I {r_1}^2 \eta}{{P_1}^2} \ln \frac{\left(\frac{r}{r_1}\right)^{\frac{1}{2}} - \frac{g}{P_1}}{1 - \frac{g}{P_1}} \tag{10}$$

$(\eta = 1)$

For $\eta \neq 1$.

For

$$g < \frac{P_1}{2} \tag{11}$$

Let

$$y = \left(\frac{r}{r_1}\right)^{\frac{1}{\eta}} - \frac{g}{P_1} > \frac{g}{P_1} \left(\text{sincer} \geq r_1, \left(\frac{r}{r_1}\right)^{\frac{1}{\eta}} \geq 1\right) \tag{12}$$

i.e.,

$$r > r_1 \left(2\frac{g}{P_1}\right)^{\eta} (0 < \eta < \infty) \text{always stands}$$

https://doi.org/10.3390/mi17030354

Since $y = x - \frac{g}{P_1}$, $x = y + \frac{g}{P_1}$,$dx = dy$
Equation (9) becomes

$$\phi(r) = \frac{\alpha\rho_s {Ir_1}^2 \eta}{{P_1}^2}\int_1^x \frac{x^{2\eta-2}dx}{x-\frac{g}{P_1}} = \frac{\alpha\rho_s {Ir_1}^2}{{P_1}^2}\int_{y_1}^y \frac{\left(y+\frac{g}{P_1}\right)^{2\eta-2}}{y}dy$$

$$\phi(r) = \frac{\alpha\rho_s {Ir_1}^2 \eta}{{P_1}^2}\int_{y_1}^y y^{2\eta-3}\left(1+\frac{g}{P_1 y}\right)^{2\eta-2}dy \tag{13}$$

From Equation (12), we have

$$\frac{g}{P_1 y} < 1 \tag{14}$$

So, we can use the Taylor expansion to express:

$$\begin{gathered}\left(1+\tfrac{g}{P_1 y}\right)^{2\eta-2} = 1 + \tfrac{(2\eta-2)}{1!}\left(\tfrac{g}{P_1 y}\right) + \\ + \tfrac{(2\eta-2)(2\eta-3)}{2!}\left(\tfrac{g}{P_1 y}\right)^2 + \ldots \\ + \tfrac{(2\eta-2)(2\eta-3)(2\eta-4)\ldots(2\eta-i-1)}{i!}\left(\tfrac{g}{P_1 y}\right)^i + \ldots \\ (i \to \infty)\end{gathered} \tag{15}$$

Equation (13) becomes

$$\phi(r) = \tfrac{\alpha\rho_s {Ir_1}^2 \eta}{{P_1}^2}\int_{y_1}^y y^{2\eta-3}dy[1+ \textstyle\sum_{i=1}^{\infty} \tfrac{(2\eta-2)(2\eta-3)\ldots(2\eta-i-1)}{i!}\left(\tfrac{g}{P_1 y}\right)^i] \tag{16}$$

Carry out integration, we have

$$\begin{gathered}\phi(r) = \tfrac{\alpha\rho_s {Ir_1}^2 \eta}{{P_1}^2}\left[\tfrac{\left(y^{2\eta-2}-y_1^{2\eta-2}\right)}{2\eta-2} + \right. \\ \left. + \textstyle\sum_{i=1}^{\infty} \tfrac{(2\eta-2)(2\eta-3)\ldots(2\eta-i-1)}{(2\eta-2-i)i!}\left(y^{2\eta-2-i}-y_1^{2\eta-2-i}\right)\right] + V_{E1}\end{gathered} \tag{17}$$

where

$$\begin{cases} y = \left(\frac{r}{r_1}\right)^{\frac{1}{\eta}} - \frac{g}{P_1} \\ y_1 = 1 - \frac{g}{P_1} \end{cases} \tag{18}$$

We can use the boundary conditions (we already used one of them in Equation (17)):

$$\begin{cases} \phi(r = r_1) = V_{E_1} \\ \phi(r = R) = V_{out} \end{cases} \tag{19}$$

Let

$$A = \frac{\alpha\rho_s {Ir_1}^2 \eta}{{P_1}^2}$$

and

$$\begin{gathered}B\left(\tfrac{r}{r_1}\right) = \tfrac{\left(y^{2\eta-2}-y_1^{2\eta-2}\right)}{2\eta-2} + \\ + \textstyle\sum_{i=1}^{\infty} \tfrac{(2\eta-2)(2\eta-3)\cdots(2\eta-i-1)}{(2\eta-2-i)i!}\left(y^{2\eta-2-i}-y_1^{2\eta-2-i}\right)\end{gathered}$$

https://doi.org/10.3390/mi17030354

We can rewrite Equations (17) and (19) as:

$$\begin{cases} \phi(r) = A \cdot B\left(\frac{r}{r_1}\right) + V_{E1} \\ \phi(r = r_1) = A \cdot B(1) + V_{E1} = V_{E1} \\ \phi(r = R) = A \cdot B\left(\frac{R}{r_1}\right) + V_{E1} = V_{out} \end{cases} \tag{20}$$

We have:

$$V_{out} - V_{E1} = A \cdot B\left(\frac{R}{r_1}\right)$$

Finally, we have the design value of P_1:

$$P_1 = \sqrt{\frac{\alpha \rho_s I {r_1}^2 \eta}{V_{out} - V_{E1}} \cdot B\left(\frac{R}{r_1}\right)} \tag{21}$$

For the backside, we let the backside surface electric potential

$$\Psi_B(r) = V_B + \gamma \phi(r) \quad (\gamma < 1) \tag{22}$$

V_B is the voltage on the central cathode on the backside. We can calculate the circular SDD spiral rings' polar angle $\theta(r)$ (top surface) [19]:

$$\theta(r) = \int_{r_1}^{r} \frac{2\pi dr}{P(r)} \tag{23}$$

Using Equation (7), we have:

$$\theta(r) = \frac{2\pi r_1}{P_1} \frac{1}{1 - \frac{1}{\eta}} [(\frac{r}{r_1})^{1 - \frac{1}{\eta}} - 1] \tag{24}$$

Then, for SDD spiral rings we have

$$\theta(r) = \begin{cases} 2\pi \frac{r_1}{P_1} \ln \frac{r}{r_1} & (\eta = 1) \\ 2\pi \frac{r_1}{P_1} \frac{1}{1 - \frac{1}{\eta}} \left[\left(\frac{r}{r_1} \right)^{1 - \frac{1}{\eta}} - 1 \right] & (\eta > 1) \end{cases} \tag{25}$$

Solve r as the function of θ,

$$r = \begin{cases} r_1 e^{\frac{P_1}{r_1} \frac{\theta}{2\pi}} & (\eta = 1) \\ r_1 \left[1 + \frac{P_1}{2\pi r_1} \frac{\eta - 1}{\eta} \theta \right]^{\frac{\eta}{\eta - 1}} & (\eta > 1) \end{cases} \tag{26}$$

For the backside, from Equation (22), we have the backside electric field:

$$E_B(r) = \gamma E(r) \tag{27}$$

Let

$$P_B(r) = P(r) \tag{28}$$

then

$$\theta_B(r) = \int_{r_{1B}}^{r} \frac{2\pi dr}{P_B(r)} = \int_{r_{1B}}^{r} \frac{2\pi dr}{P(r)} \tag{29}$$

Similarly to Equation (2), we have:

$$\theta_B(r) = \frac{2\pi r_{1B}}{P_1} \frac{1}{1 - \frac{1}{\eta}} \cdot \left[r^{1 - \frac{1}{\eta}} - {r_{1B}}^{1 - \frac{1}{\eta}} \right] \tag{30}$$

https://doi.org/10.3390/mi17030354

Let

$$r_{1B} = r_1 \tag{31}$$

We have

$$\theta_B(r) = \theta(r) \tag{32}$$

$$r_B = \begin{cases} r_1 e^{\frac{P_1}{r_1}\frac{\varphi}{2\pi}} \\ r_1\left[1 + \frac{P_1}{2\pi r_1}\frac{\eta-1}{\eta}\varphi\right]^{\frac{\eta}{\eta-1}} \end{cases} \tag{33}$$

Since:

$$P_B(r) = g_B + w_B(r) \tag{34}$$

Let $g_B = g$, $w_B = N$, we get:

$$P_B(r) = g + w_B(r) = g + w(r) = P(r) \tag{35}$$

and

$$\begin{cases} P_B(r) = P_1\left(\frac{r}{r_1}\right)^{\frac{1}{\eta}} \\ w_B(r) = P_1\left(\frac{r}{r_1}\right)^{\frac{1}{\eta}} - g \end{cases} \tag{36}$$

Now, back to Equations (17) and (18). Let $\frac{g}{P_1} = 0.1$ ($g = 10$ μm, $P_1 = 100$ μm), $\eta = 1.6$, we have:

$$\begin{cases} y(r) = \left(\frac{r}{r_1}\right)^{\frac{1}{1.6}} - 0.1 \\ y_1 = 1 - 0.1 = 0.9 \end{cases} \tag{37}$$

Starting from the fourth term, the subsequent contributions are negligible due to their diminishing magnitude; thus, the truncated formula retains only the first three terms. Equation (17) is now:

$$\begin{aligned} \phi(r) = V_{E1} + \frac{1.6\rho_s {I r_1}^2}{P_1}\frac{y^{1.2} - y_1^{1.2}}{1.2} + \frac{1.6\rho_s {I r_1}^2}{P_1}\cdot 0.6\left(y^{0.2} - y_1^{0.2}\right) \\ + \quad + \frac{1.6\rho_s {I r_1}^2}{P_1}\cdot\left[-0.015\left(y^{-0.8} - y_1^{-0.8}\right)\right] \end{aligned} \tag{38}$$

Here, we only take $i = 3$ to achieve enough accuracy.

On the backside, we have:

$$\Psi(r) = V_B + 0.3\phi(r) \tag{39}$$

The detector full-depletion voltage is V_{fd}:

$$V_{fd} = \frac{eN_{eff}d^2}{2\varepsilon\varepsilon_0} \tag{40}$$

Let $V_B = V_{fd}$, $d = 0.03$ cm, we have $V_{fd} = 72.09$ V.

For $R = 1200$ μm $= 0.12$ cm, $\alpha = 6$, $\rho_s = 2000$, $I = 10 \times 10^{-5}$ A, $\eta = 1.6$, $g = 0.001$ cm, $r_1 = 0.0255$ cm, $V_{out} = 30$ V, and $V_{E1} = 18$ V, we have:

$$\begin{cases} y(R) = \left(\frac{R}{r_1}\right)^{\frac{1}{1.6}} - 0.1 = 2.633 \\ y_1 = 1 - 0.1 = 0.9 \end{cases}$$

$$B\left(\frac{R}{r_1}\right) = \frac{y^{1.2} - y_1^{1.2}}{1.2} + 0.6\left(y^{0.2} - y_1^{0.2}\right) - 0.015\left(y^{-0.8} - y_1^{-0.8}\right) = 2.0787$$

https://doi.org/10.3390/mi17030354

From Equation (21) we obtain:

$$P_1 = 0.014706 \text{ cm} \approx 147.1 \text{ μm}$$

Due to the fact that the hexagonal shape is the closest to the circular shape and can also be arranged in an array to make a pixel detector, we select the hexagonal shape for the detector unit. An n-type silicon substrate with a doping level of 1×10^{12} cm^{-3} is used. The spiral SDD cell has a thickness of 300 μm. Figure 3 is a 2D cross-sectional view at $Z = 0$ μm (due to symmetry, only half of the cross-section is shown). The structure of the spiral SDD anode (near $r = 0$) and the cathode rings on both sides can be shown clearly. The aluminum electrode contact layers and the silicon dioxide protective layers are also observable. We can see that the central feature on the cell's top surface is a heavily doped N-type region, which serves as the collecting anode and has a radius of 220.4 μm. The doped layer exhibits a concentration of $1 \times 10^{19}/cm^3$ and the doping depth is 1 μm. Heavily doped P-type spiral rings, with a doping depth of 1 μm and a doping concentration of $1 \times 10^{19}/cm^3$, are around the anode. The detector anode surface is covered with a 1 μm aluminum layer. Likewise, the start and end points of the spiral ring are also aluminized to the same thickness. The remaining surfaces are coated with a 1 μm silicon dioxide layer, utilizing the material's inherent stability and chemical inertness. At the bottom of the silicon bulk, there is a heavily doped hexagonal P-type cathode with a radius of 220.4 μm near $r = 0$. The doping concentration is $1 \times 10^{19}/cm^3$ and the doping depth is 1 μm. A heavily doped P-type spiral ring with a doping depth of 1 μm and a doping concentration of $1 \times 10^{19}/cm^3$ is surrounding the central cathode. The spiral ring on the top surface, along with the central hexagonal cathode on the bottom surface and the spiral ring jointly constitutes the cathode of this detector. The electrode contact points of the structure are positioned at the central positions of the anode top surface, the central cathode (bottom surface), the starting point of the first ring of the spiral cathode, and the ending point of the spiral cathode on both surfaces, respectively.

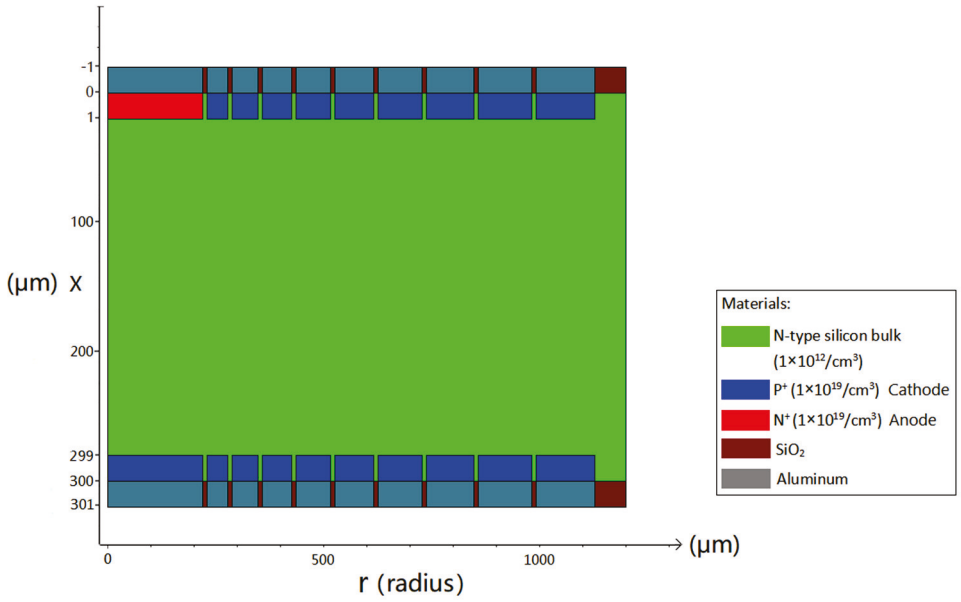


Figure 3. A two-dimensional cross-section view of the novel spiral SDD.

https://doi.org/10.3390/mi17030354

3. Electrical Characteristic Results

To investigate the electrical behavior performance of the spiral SDD in more detail, we carried out 3D simulations of detector electrical properties including the profiles of electric field, potential, and electron concentration by TCAD (Sentaurus 2019).

3.1. Electric Field Distribution of the Spiral SDD

To reveal the internal electric field distribution more clearly, we created a 2D cross-section at Z = 0 μm through the detector cell shown in Figure 4. The red zones indicate strong electric field regions corresponding to the anode positions, while the central regions exhibit nearly stable electric field intensity with distinct drift channels, indicating the complete depletion of the detector. We can obviously see a nearly stable and uniform electric field distribution on the carrier drift channel, demonstrating a superior electric field uniformity that can enhance the detector performance.

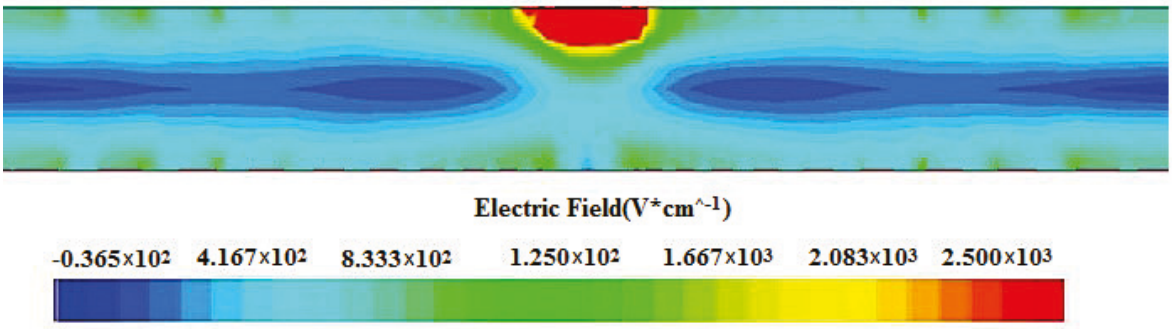


Figure 4. Electric field distribution of a cross-section at Z = 0 μm through the detector cell.

Figure 5 presents a one-dimensional curve for a cut at the X = 160 μm position from Figure 4. It is evident that the detector's electric field intensity distribution exhibits an anode-symmetric pattern; the detector's electric field is between 100 V/cm near the outer ring (r = R) and close to 600 V/cm near the anode.

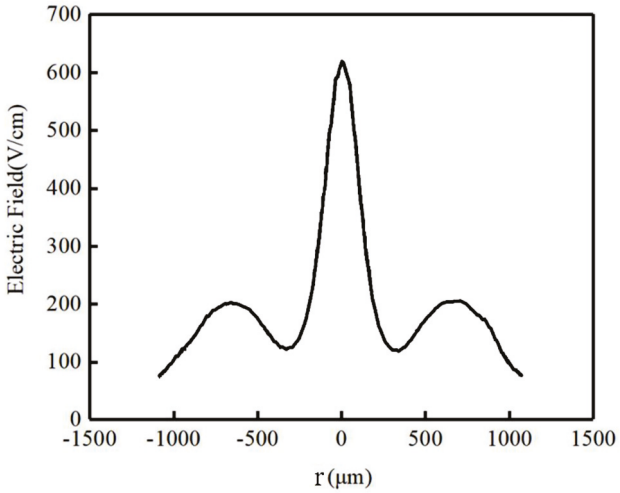


Figure 5. Electric field profile of the one-dimensional cross-section of the novel detector (X = 160 μm).

3.2. Electric Potential Distribution of the Spiral SDD

An analysis of the electric potential distribution across a two-dimensional cross-section of the spiral SDD at Z = 0 μm is shown in Figure 6. It is evident that the potential distribution is highly symmetrical. The figure shows that the potential is the highest in the collector anode region (red area), while the surrounding areas exhibit lower potential.

https://doi.org/10.3390/mi17030354

Under the electric field force, carriers drift from low-potential regions to high-potential regions, moving from the periphery toward the detector center. They ultimately reach the collector anode to complete the charge collection. It demonstrates a good gradient distribution of potential.

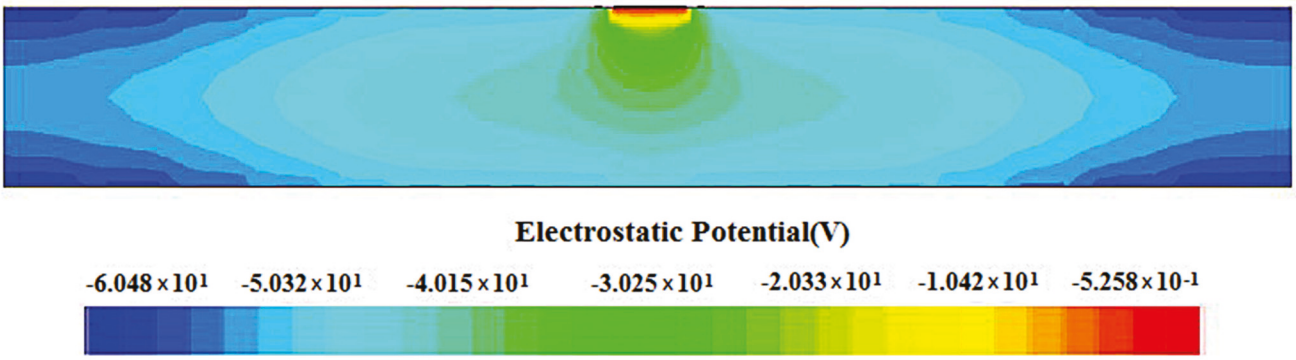


Figure 6. Electric potential profile of a cross-section at Z = 0 μm through the detector cell.

In Figure 7, we can see the one-dimensional potential distribution at a cut at X = 160 μm from Figure 6. It is evident that the potential reaches its maximum at the anode and gradually decreases from the center toward both ends, exhibiting a smooth potential grading for electrons drifting towards the anode.

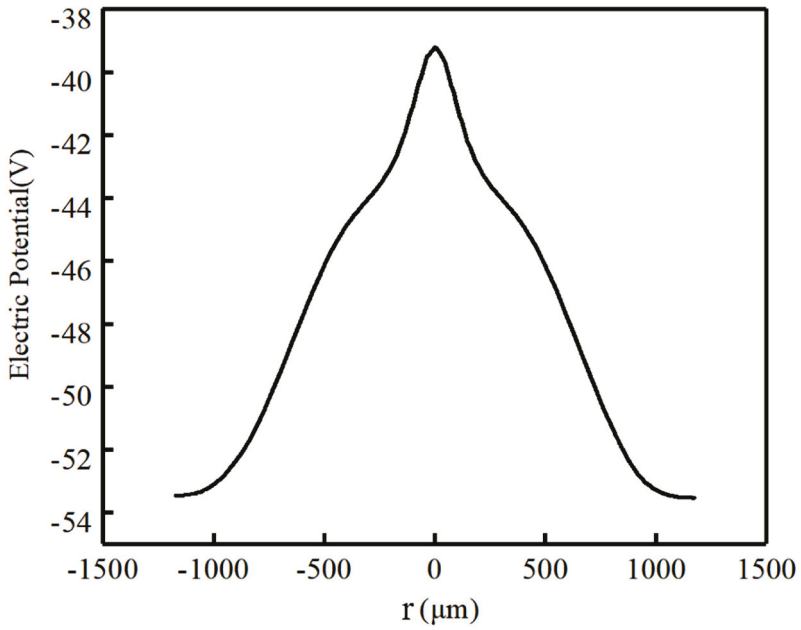


Figure 7. Electric potential profile of the one-dimensional cross-section of the novel detector (X = 160 μm).

3.3. Electron Concentration Profile for the Spiral SDD

The 2D electron concentration distributions of the spiral SDD under full-depletion conditions are shown in Figure 8 (cut at Z = 0). We can see that the electron concentration is the highest in the collector anode region, forming a clear drifting channel for the electrons (red area in the figure) in the detector's central region, consistent with the drift channel demonstrated by the electric field distribution shown in Figure 4.

https://doi.org/10.3390/mi17030354

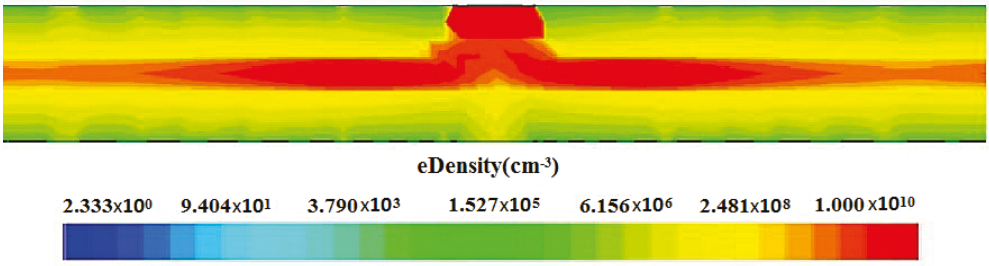


Figure 8. Electric concentration profile for the spiral SDD.

4. The Novel Spiral Silicon Drift Detector (SDD) Concept and Design Considerations from the Second Arbitrary P(r) Profile

A second arbitrary $P(r)$ profile:

Let

$$P(r) = \frac{\xi P_1}{\xi + \sin\frac{r-r_1}{r_1}} \quad (\xi \geq 2) \tag{41}$$

Then the spiral angle $\theta(r)$ is

$$\theta(r) = \int_{r_1}^{r} \frac{2\pi}{P(r)} dr = \frac{2\pi}{\xi P_1} \int_{r_1}^{r} \left[\xi + \sin\frac{r-r_1}{r_1}\right] dr$$

$$\theta(r) = \frac{2\pi}{\xi P_1}\left[\xi(r-r_1) + r_1\left(1 - \cos\frac{r-r_1}{r_1}\right)\right] \tag{42}$$

For a SDD front surface field $E(r)$,

since

$$E(r) \cdot P(r) = \frac{\alpha I \rho_s r}{w(r)} \tag{43}$$

Let

$$w(r) = \beta P(r) \tag{44}$$

Then we have

$$E(r) = \frac{\alpha I \rho_s r}{\beta P(r)^2} \tag{45}$$

The SDD front surface potential is

$$\phi(r) = \int_{r_1}^{r} E(r) dr + V_{E1} \tag{46}$$

From Equations (41) and (45) we get:

$$\phi(r) = \frac{\alpha I \rho_s}{\beta \xi P_1} \int_{r_1}^{r} \left[\xi + \sin\frac{r-r_1}{r_1}\right]^2 dr + V_{E1}$$

$$\phi(r) = \frac{\alpha I \rho_s}{\beta \xi P_1}\left[\left(\xi^2 + \frac{1}{2}\right)(r-r_1) + 2\xi r_1 \cdot \left(1 - \cos\frac{r-r_1}{r_1}\right) - \frac{r_1}{4}\sin\frac{2(r-r_1)}{r_1} + V_{E1}\right] \tag{47}$$

$$\phi(R) = V_{out}$$

We have:

$$V_{out} - V_{E1} = \frac{\alpha I \rho_s}{\beta \xi P_1}\left[\left(\xi^2 + \frac{1}{2}\right)(R-r_1) + 2\xi r_1 \cdot \left(1 - \cos\frac{r-r_1}{r_1}\right) - \frac{r_1}{4}\sin\frac{2(r-r_1)}{r_1}\right] \tag{48}$$

https://doi.org/10.3390/mi17030354

This equation can be used to determine ξ or P_1 (if one or the other is fixed).
On the backside surface, we let:

$$\begin{cases} P_B(r) = P(r) \\ w_B(r) = w(r) \\ \theta_B(r) = \theta(r) \\ \Psi(r) = V_B + \gamma\phi(r) \qquad (0 < \gamma < 1) \end{cases} \tag{49}$$

We can use the method of iteration to calculate r as a function of θ as the following:

$$\text{① let } r^{(0)} = r_1 \tag{50}$$

$$\text{② } r^{(1)} = r_1 + \frac{\theta}{2\pi} P_1 \tag{51}$$

$$\text{③ } r^{(2)} = r_1 + \frac{1}{\xi}\left\{\frac{\xi P_1 \theta}{2\pi} - r_1\left(1 - \cos\frac{r^{(1)} - r_1}{r_1}\right)\right\} \tag{52}$$

$$\text{④ } r^{(n)} = r_1 + \frac{1}{\xi}\left\{\frac{\xi P_1 \theta}{2\pi} - r_1\left(1 - \cos\frac{r^{(n-1)} - r_1}{r_1}\right)\right\} \tag{53}$$

$$\text{⑤ stop till : } \left|\frac{r^{(n)} - r^{(n-1)}}{r^{(n)}}\right| \leq 10^{-4} \tag{54}$$

We used the following parameters for SDD calculations:

$P_1 = 0.00638$ cm, $r_1 = 0.0255$ cm, $R = 1200$ μm $= 0.12$ cm, $\xi = 2$, $\beta = 0.85$, we get a SDD with 21 turns of spiral.

Figure 9 presents the top and bottom views of the novel spiral SDD from the second arbitrary P(r) profile. The structural parameters and the foundational rules of the detector's design from the second arbitrary P(r) profile can be seen clearly in Figure 10. Figure 11 is a 2D cross-sectional view at $Z = 0$ μm from the second arbitrary P(r) profile (due to symmetry, only half of the cross-section is shown).

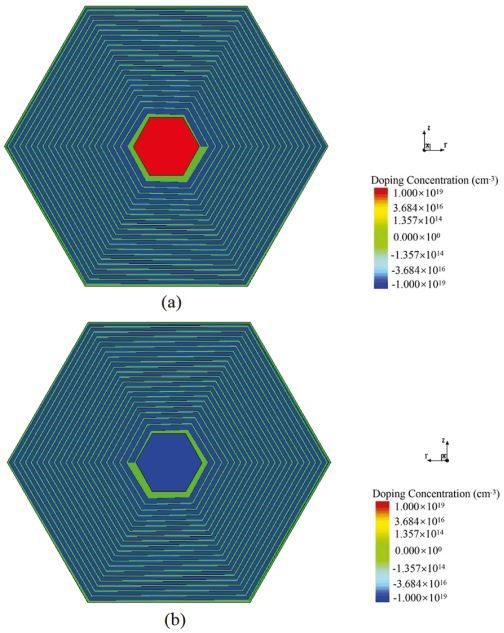


Figure 9. (**a**) The top view of the novel spiral SDD unit cell from the second arbitrary P(r) profile. (**b**) The bottom view of the unit cell from the second arbitrary P(r) profile.

https://doi.org/10.3390/mi17030354

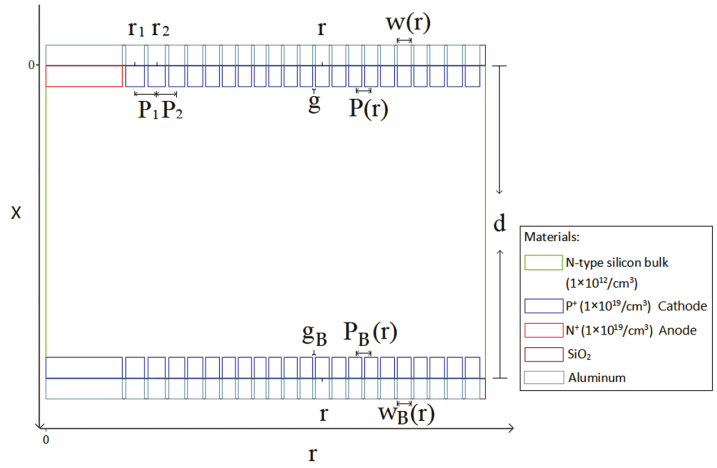


Figure 10. The cross-section view and structural parameters of the novel spiral SDD from the second arbitrary P(r) profile.

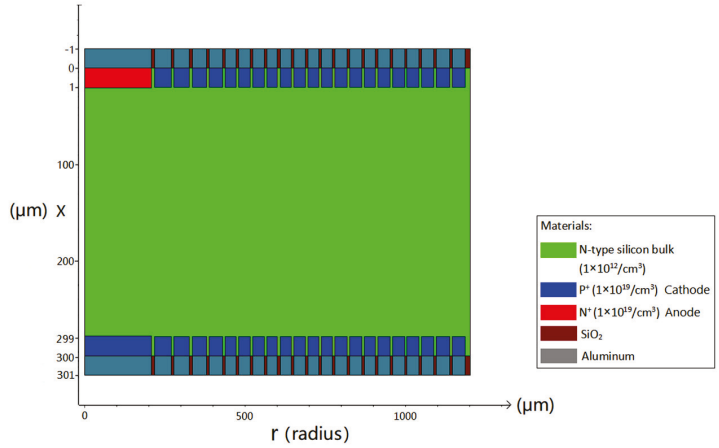


Figure 11. A two-dimensional cross section view of the novel spiral SDD from the second arbitrary P(r) profile.

5. Electrical Characteristic Results from the Second Arbitrary P(r) Profile

5.1. Electric Field Distribution of the Spiral SDD from the Second Arbitrary P(r) Profile

Due to the appropriate pressure applied to the contact points of the electrodes of the double-sided spiral SDD, the detector has a reasonable potential distribution, and a good electric field distribution can be formed within the detector. Figure 12 shows the electric field distribution inside the P(r) and the second P(r) structures of the spiral SDDs, respectively. The red area is the strong electric field area where the detector anode is located. The electric field intensity in the middle area is almost stable and forms a distinct drift channel, indicating that the detector has been completely exhausted. It can clearly be seen from the figure that there is an uneven distribution of the electric field at the position of the carrier drift channel in the middle of the P(r) detector, while the electric field distribution in the middle area of the second P(r) detector is uniform and the carrier drift channel is nearly straight, indicating that the second P(r) detector has a higher uniformity of the electric field and better detector performance.

https://doi.org/10.3390/mi17030354

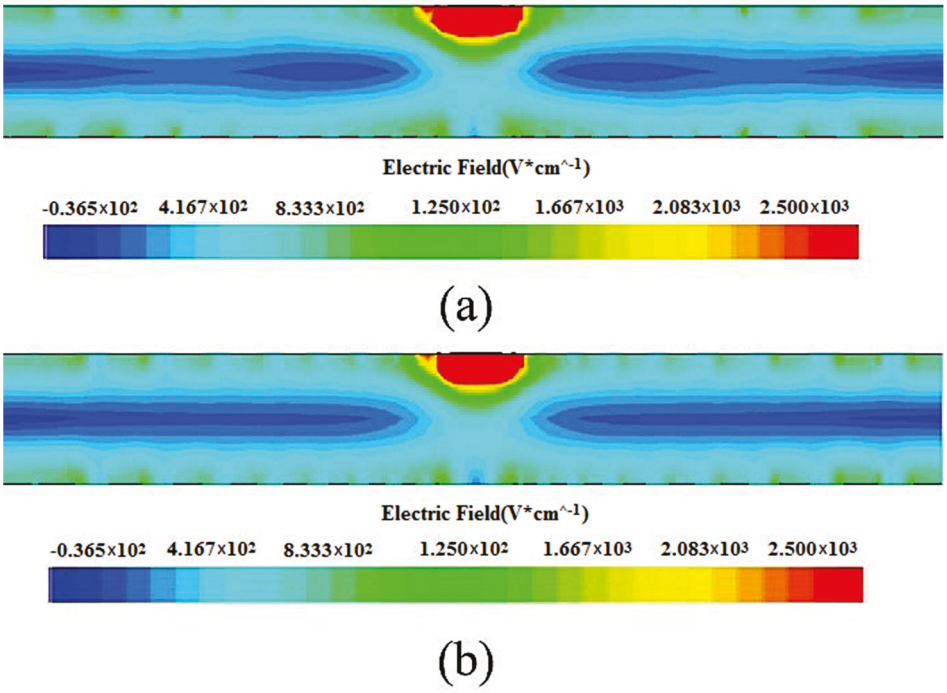


Figure 12. The electric field distribution diagrams of the spiral SDDs: (**a**) the P(r), (**b**) the second P(r).

To compare the uniformity of the electric field distribution of the P(r) and the second P(r) detectors, Figure 13 shows a one-dimensional curve comparison of the electric field distribution at $X = 160$ μm, with the red curve representing the electric field distribution of the P(r) detector and the black curve representing the electric field distribution of the second P(r) detector. It can be clearly observed that the electric field intensity distribution of the second P(r) detector is symmetrical about the anode, there is a peak in the electric field distribution curve, and the magnitude of the electric field decreases with the increase in detector radius, and the curve is smooth. The electric field intensity distribution of the P(r) detector has three peaks including the anode area, and the electric field variation trend is unstable with fluctuations. Thus, it is verified that the electric field distribution of the second P(r) detector is more uniform and has better electrical performance than that of the P(r) detector.

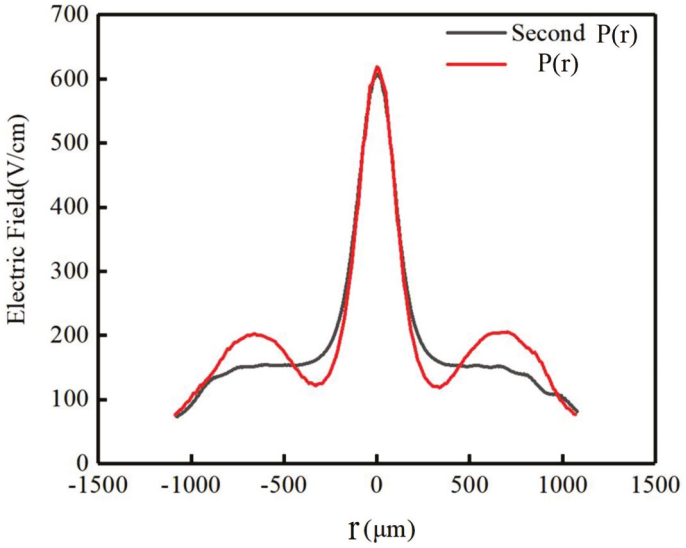


Figure 13. Electric field distribution curves of the spiral SDDs.

https://doi.org/10.3390/mi17030354

5.2. Electric Potential Distribution of the Spiral SDD from the Second Arbitrary P(r) Profile

Figure 14 shows the two-dimensional cross-sectional potential distribution of the P(r) and the second P(r) structures of the double-sided spiral SDDs, respectively. It can be seen from the figure that the area where the collected anode is located has the highest potential (the red area in the figure), while the potential around it is low. The carriers drift under the force of the electric field, moving the path from the low-potential area to the high-potential area, that is, the carriers drift from the periphery to the center of the detector, and finally reach the collection anode to complete the signal readout. The second P(r) detector shown in Figure 14b has a more uniform, symmetrical and better gradient distribution of potential than the P(r) detector.

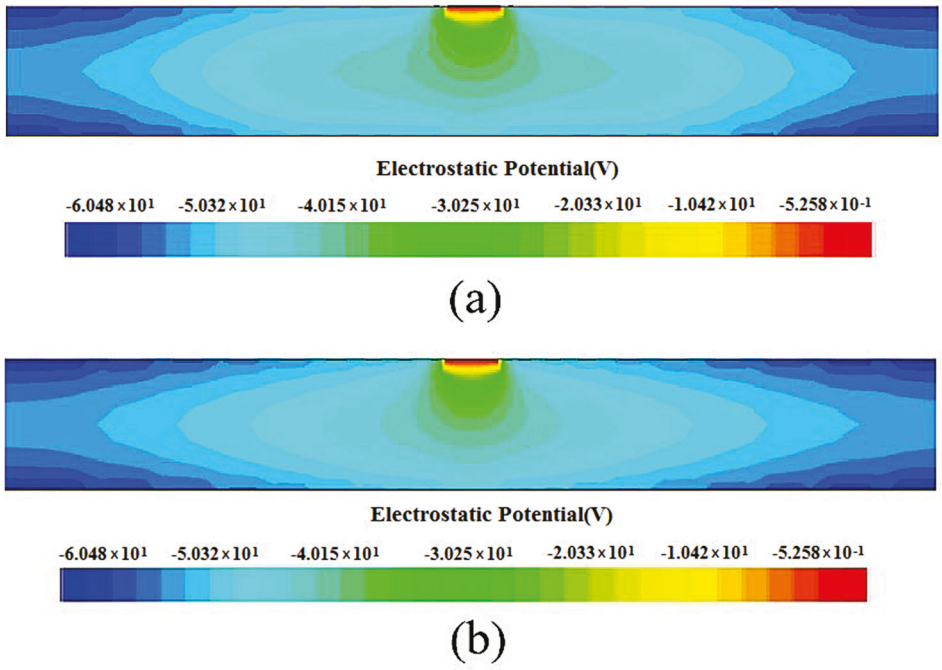


Figure 14. The two-dimensional cross-section potential distribution of the spiral SDDs: (**a**) the P(r), (**b**) the second P(r).

To highlight the difference in potential distribution between the P(r) and the second P(r) detectors, the potential distribution of the detector was cut at X = 160 μm to obtain the one-dimensional curve of potential with radius as shown in Figure 15. It can be clearly observed that the potential is highest at the anode and gradually decreases from the middle to both ends. The potential distribution curve of the second P(r) detector is smoother than that of the P(r) detector, meaning that the potential distribution of the second P(r) detector is more uniform.

5.3. Electron Concentration Profile for the Spiral SDD from the Second Arbitrary P(r) Profile

Figure 16 respectively shows the electron concentration distribution of the P(r) and the second P(r) structures of the spiral SDDs in the fully exhausted state, with the highest electron concentration in the collected anode region and a high electron concentration channel (the red area in the figure) generated in the middle region inside the detector, which is consistent with the drift channel generated in the electric field distribution. A comparison of the electron concentration distribution of the P(r) and the second P(r) detectors shown in Figure 16a,b reveals that the second P(r) detector has a more uniform electron concentration distribution, indicating superior electrical performance of the detector.

https://doi.org/10.3390/mi17030354

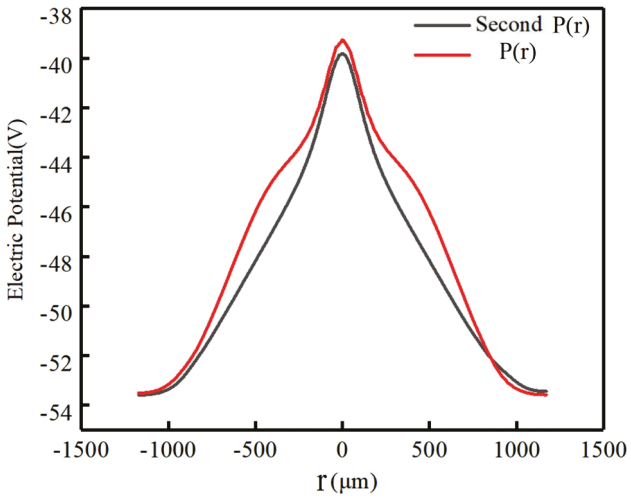


Figure 15. Potential distribution curves of the spiral SDDs.

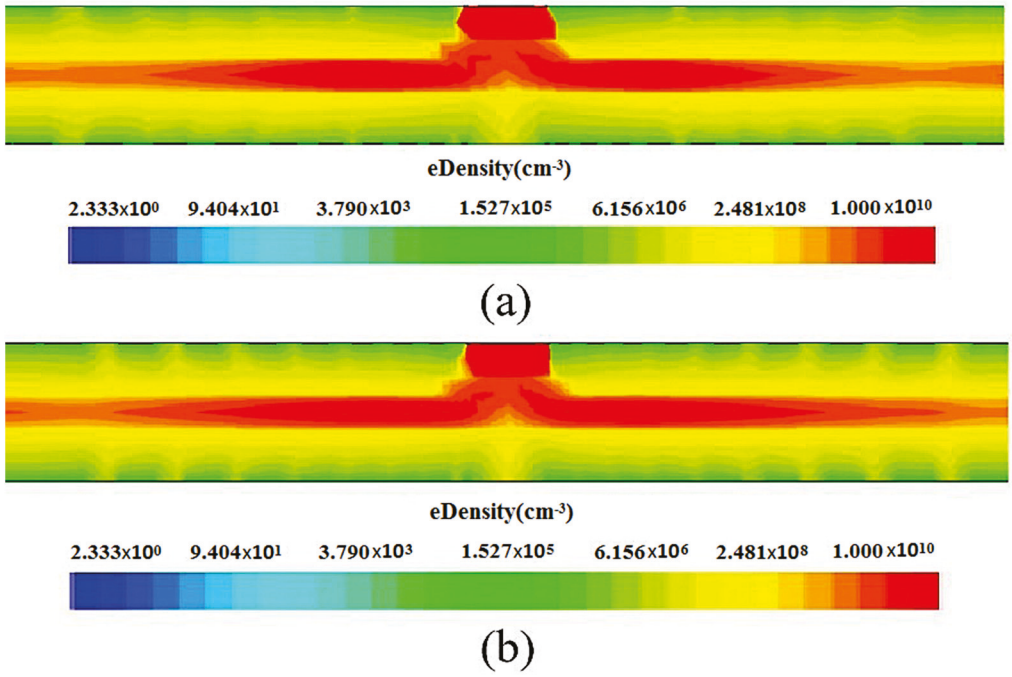


Figure 16. Electron concentration distribution diagrams of the spiral SDDs: (**a**) the P(r), (**b**) the second P(r).

6. Conclusions

In this paper, an innovative design of the silicon spiral drift detector (SDD) has been proposed. In our design method, the cathode gaps (g) under SiO_2 are kept constant to minimize the surface leakage current. We allow the pitch profile $P(r)$ to vary in an arbitrary way to obtain the optimum electric field distribution. Exact solutions for the SDD with a spiral design $r = r(\theta)$ can be obtained for the hexagonal spiral SDD. According to the coordinates of each point of the spiral ring obtained by theoretical calculation, the SDD structure diagram can be drawn. Technology Computer-Aided Design (TCAD) is used to simulate the novel SDD in this work. We have systematically researched its respective electrical properties, such as electric field distribution, electric potential distribution, and electron concentration distribution. Simulation results have shown a uniform electric field and smooth electric potential and electron concentration profiles. It makes the SDD particularly outstanding in fields of space physics and photon science, such as pulsar

https://doi.org/10.3390/mi17030354

X-ray detection and X-ray fluorescence spectrometers. This new design can be realized with the current SDD-processing technology, such as epitaxy, photolithography and ion implantation. In summary, our novel design of the silicon spiral drift detector can serve as a valuable method for the further improvement of SDD's fields.

Author Contributions: Conceptualization, H.W. and Z.L.; methodology, Z.L.; software, H.W.; validation, Z.L.; formal analysis, H.W.; investigation, Z.L.; resources, Z.L.; data curation, H.W.; writing—original draft preparation, H.W.; writing—review and editing, H.W.; visualization, Z.L.; supervision, Z.L.; project administration, Z.L.; funding acquisition, Z.L. All authors have read and agreed to the published version of the manuscript.

Funding: This research was funded by the National Key R&D Program of China (2023YFF0719600).

Institutional Review Board Statement: Not applicable.

Informed Consent Statement: Not applicable.

Data Availability Statement: The original contributions presented in the study are included in the article, further inquiries can be directed to the corresponding author.

Conflicts of Interest: The authors declare no conflicts of interest.

References

1. Gatti, E.; Rehak, P. Semiconductor drift chamber—An application of a novel charge transport scheme. *Nucl. Instrum. Methods* **1984**, *225*, 608–614. [CrossRef]
2. Rolandi, G. The LHC machine and experiments. *Int. J. Mod. Phys. A* **2008**, *21*, 1654–1656. [CrossRef]
3. Chabaud, V.; Dijkstra, H.; Gröne, M.; Flohr, M.; Horisberger, R.; Hubbeling, L.; Maehlum, G.; Peisert, A.; Sandvik, A.; Weilhammer, P. Beam test results from a prototype for the delphi microvertex detector. *Nucl. Instrum. Methods Phys. Res. Sect. A Accel. Spectrometers Detect. Assoc. Equip.* **1990**, *292*, 75–80. [CrossRef]
4. Biolcati, E. Measurement of identified charged hadron spectra in proton-proton collisions using the Inner Tracking System of the ALICE experiment at the LHC. In *AIP Conference Proceedings*; American Institute of Physics: College Park, MD, USA, 2011; pp. 483–485.
5. Klein, S.R.; Steinberg, P. Photonuclear and Two-Photon Interactions at High-Energy Nuclear Colliders. *Annu. Rev. Nucl. Part. Sci.* **2020**, *70*, 323–354. [CrossRef]
6. Habs, D.; Tajima, T.; Zamfir, V. Extreme Light Infrastructure–Nuclear Physics (ELI–NP): New Horizons for Photon Physics in Europe. *Nucl. Phys. News* **2011**, *21*, 23–29. [CrossRef]
7. Collar, J.; Puibasset, J.; Girard, T.; Miley, H.; Limagne, D.; Waysand, G. Preliminary dark matter limits from a large-mass, low-background SDD. *Nucl. Phys. B Proc. Suppl.* **2000**, *87*, 120–122. [CrossRef]
8. Utica, G.; Fabbrica, E.; Carminati, M.; Borghi, G.; Zorzi, N.; Ficorella, F.; Picciotto, A.; Allegretta, I.; Falkenberg, G.; Fiorini, C. ARDESIA-16: A 16-channel SDD-based spectrometer for energy dispersive X-ray fluorescence spectroscopy. *J. Instrum.* **2021**, *16*, P07057.
9. Newbury, D.E.; Ritchie, N.W.M. Performing elemental microanalysis with high accuracy and high precision by scanning electron microscopy/silicon drift detector energy-dispersive X-ray spectrometry (SEM/SDD-EDS). *J. Mater. Sci.* **2015**, *50*, 493–518. [CrossRef]
10. Hafizh, I.; Bellotti, G.; Carminati, M.; Utica, G.; Gugiatti, M.; Balerna, A.; Tullio, V.; Lepore, G.O.; Borghi, G.; Ficorella, F.; et al. Characterization of ARDESIA: A 4-channel SDD X-ray spectrometer for synchrotron measurements at high count rates. *J. Instrum.* **2019**, *14*, P06027. [CrossRef]
11. Metzger, W.; Engdahl, J.; Rossner, W.; Boslau, O.; Kemmer, J. Large-area silicon drift detectors for new applications in nuclear medicine imaging. *IEEE Trans. Nucl. Sci.* **2004**, *51*, 1631–1635. [CrossRef]
12. Fiorini, C.; Gola, A.; Longoni, A.; Zanchi, M.; Restelli, A.; Perotti, F. A large-area monolithic array of silicon drift detectors for medical imaging. *Nucl. Instrum. Methods Phys. Res. Sect. A Accel. Spectrometers Detect. Assoc. Equip.* **2006**, *568*, 96–100.
13. Pourmorteza, A.; Symons, R.; Sandfort, V.; Mallek, M.; Fuld, M.K.; Henderson, G. Abdominal imaging with contrast-enhanced photon-counting CT: First human experience. *Radiology* **2016**, *279*, 239–245. [CrossRef]
14. Kalender, W.A.; Kolditz, D.; Steiding, C.; Ruth, V.; Luck, F.; Rossler, A.C. Technical feasibility proof for high-resolution low-dose photon-counting CT of the breast. *Eur. Radiol.* **2017**, *27*, 1081–1086. [CrossRef]
15. Li, X.; Liu, M.; Li, Z. Design and simulation of silicon detector cells with spiral ring electrode structures. *AIP Adv.* **2021**, *11*, 045127. [CrossRef]

https://doi.org/10.3390/mi17030354

16. Kern, J.; Alonso-Mori, R.; Tran, R.; Hattne, J.; Gildea, R.J.; Echols, N.; Glöckner, C.; Hellmich, J.; Laksmono, H.; Sierra, R.G.; et al. Simultaneous Femtosecond X-ray Spectroscopy and Diffraction of Photosystem II at Room Temperature. *Science* **2013**, *340*, 491–495. [CrossRef]
17. Guazzoni, C. The first 25 years of silicon drift detectors: A personal view. *Nucl. Instrum. Methods Phys. Res. Sect. A Accel. Spectrometers Detect. Assoc. Equip.* **2010**, *624*, 247–254. [CrossRef]
18. Witze, A. NASA test proves pulsars can function as a celestial GPS. *Nature* **2018**, *553*, 261–262. [CrossRef]
19. Liu, M.; Li, Z.; Deng, Z.; He, L.; Xiong, B.; Li, Y. 314 mm^2 hexagonal double-sided spiral silicon drift detector for soft X-ray detection based on ultra-pure high resistance silicon. *Front. Mater.* **2021**, *8*, 700137. [CrossRef]
20. Li, Z. Generalization of the modeling and design considerations of concentric and spiral Si drift detectors. *Nucl. Instrum. Methods Phys. Res. Sect. A Accel. Spectrometers Detect. Assoc. Equip.* **2013**, *730*, 73–78. [CrossRef]
21. Zhang, X.; Li, Z.; Liu, M.; Mu, H. Electrical characteristics analysis of a 314 mm^2 double-sided spiral SDD for x-ray pulsar navigation. *Mater. Res. Express.* **2020**, *7*, 085903. [CrossRef]
22. Sun, J.; Li, Z.; Li, X.; Li, X.; Cai, X.; Tan, Z.; Liu, M.; Wang, H. Novel Spiral Silicon Drift Detector with Equal Cathode Ring Gap and Given Surface Electric Fields. *Micromachines* **2022**, *13*, 1682. [CrossRef] [PubMed]

Disclaimer/Publisher's Note: The statements, opinions and data contained in all publications are solely those of the individual author(s) and contributor(s) and not of MDPI and/or the editor(s). MDPI and/or the editor(s) disclaim responsibility for any injury to people or property resulting from any ideas, methods, instructions or products referred to in the content.

https://doi.org/10.3390/mi17030354

micromachines

MDPI

Article

High-Extinction-Ratio Chiral Mid-Wave Infrared Photodetector Using Trapezoidal Si Pillars

Yingsong Zheng [1], Longfeng Lv [2], Yuxiao Zou [3,4], Bo Cheng [5], Hanxiao Shao [2,*], Guofeng Song [2] and Kunpeng Zhai [6,*]

1 Chengdu Entrepreneurship College, Chengdu Polytechnic, 83 Tianyi Street, Chengdu 610041, China; 18109090666@163.com
2 Institute of Semiconductors, Chinese Academy of Sciences, Beijing 100083, China; lflv@semi.ac.cn (L.L.); sgf@semi.ac.cn (G.S.)
3 Kunming Institute of Physics, Kunming 650223, China; 13307110322@fudan.edu.cn
4 National Key Laboratory of Infrared Detection Technologies, Kunming Institute of Physics, Kunming 650223, China
5 Sichuan Provincial Engineering Research Center of Thermoelectric Materials and Devices, Chengdu 610041, China
6 Institute of Intelligent Photonics, Nankai University, Tianjin 300071, China
* Correspondence: shaohanxiao@semi.ac.cn (H.S.); kpzhai@nankai.edu.cn (K.Z.)

Abstract

Although the polarization state, as a key physical dimension of light, plays an irreplaceable role in many frontier fields such as quantum communication and chiral sensing, traditional photodetectors are limited by the inherent optical isotropy of materials and thus are unable to directly distinguish circular polarization information. This paper numerically reports a miniature circular polarization photodetector based on chiral metasurfaces, which achieves an excellent extinction ratio of up to 31 dB through the collaborative regulation of geometric displacement manipulation and tilt angle operation. This device utilizes the symmetry-breaking effect to construct significantly different transmission spectral responses between left circularly polarized light (LCP) and right circularly polarized light (RCP). Our research not only provides a high-performance implementation solution for on-chip polarization detection but also opens up new paths for the future development of quantum optics, integrated sensing, and ultra-compact polarization optical systems.

Keywords: MWIR photodetector; metasurface; circular polarization extinction ratio

1. Introduction

Polarization of light, as a fundamental optical degree of freedom of light, carries key information required in fields such as quantum cryptography, biomedical imaging, and remote sensing [1–3]. Traditional polarization detection techniques usually rely on bulky discrete optical components such as wave plates and polarizing beam splitters, facing inherent limitations such as complex system alignment and difficulty in integration [4]. In recent years, compact linear polarization photodetectors based on anisotropic nanomaterials (such as two-dimensional perovskites and nanowires) have made significant progress [5,6]. However, due to their intrinsic symmetry, these materials cannot directly distinguish circular polarization states—yet the precise detection of circular polarization is a core requirement in cutting-edge fields such as chiral photonics and spin-optical computing [7].

To address this challenge, metasurfaces [8–12], with their ability to flexibly manipulate light fields at subwavelength scales, offer a promising solution for on-chip polarization

optics. Dielectric metasurfaces, through their subwavelength-scale "meta-atom" arrays, can precisely control the phase, amplitude, polarization, and frequency of light in unprecedented ways, providing a powerful platform for achieving compact and efficient photonic devices [13–16]. In terms of linear polarization detection, a polarization extinction ratio exceeding 15 dB has been achieved by designing metasurfaces with in-plane asymmetry [17]. However, distinguishing between circular polarizations requires metasurfaces with chiral responses [18–23], which need to exhibit significant asymmetric transmission characteristics for LCP and RCP. Previous studies, such as designs based on plasmonic helical gratings or multilayer twisted metamaterials, have often been limited by complex multilayer fabrication processes or low efficiency [24–28]. On the other hand, although single-layer metasurfaces based on dielectric materials have achieved excellent circular dichroism, their light typically needs to be incident from the substrate side [29–32], which is incompatible with the conventional top-integration process of detectors. Therefore, the core challenge lies in designing a single-chip integrated chiral metasurface that combines high extinction ratio, small size, and high efficiency.

Here, we report a compact circularly polarized photodetector (CPPD) that achieves a circular polarization extinction ratio (CPER) of 31 dB at a wavelength of 4.3 μm by monolithically integrating a chiral metasurface with a type-II superlattice detector. By cooperatively regulating the symmetry breaking introduced by geometric displacement and tilt angle, the designed metasurface unit generates highly differentiated transmission responses to left- and right-handed circularly polarized light, with a circular dichroism (CD) exceeding 80%. The chiral metasurface is fabricated using silicon materials that are fully compatible with semiconductor processes and can be directly embedded in standard photodetector fabrication processes. Additionally, this paper systematically analyzes the impact of key process errors on the final performance of the device.

2. Materials and Methods

Figure 1a shows the three-dimensional structure of the mid-wave circularly polarized photodetector, which consists of a type-II superlattice photodetector at the bottom and a chiral silicon metasurface at the top. Figure 1b indicates that the chiral silicon metasurface is composed of a MgF2 film and a silicon pattern array. Figure 1c is the xy cross-sectional view of the silicon metasurface, which shows that the unit cell of the metasurface is composed of two right-angled trapezoids and a rectangular strip. The lower trapezoid can be obtained by rotating the upper trapezoid counterclockwise by 180 degrees. Figure 1d is the xz cross-sectional view of the circularly polarized photodetector, highlighting the functionality of each layer. Additionally, the structure information of the type-II superlattice photodetector from bottom to top is a 500 μm GaSb substrate, a 500 nm AlGaSb buffer layer, a 230 nm P-type doped GaSb, 400 pairs of 2.5 nm InAs/2.5 nm GaSb type-II superlattice absorption layers, a 240 nm AlGaSb barrier layer, and a 500 nm InAs top contact layer. The optical refractive indices of silicon and MgF2 at a wavelength of 4.3 μm are 3.48 and 1.38, respectively. The real part of the refractive index of the absorption layer in the type-II superlattice photodetector at a wavelength of 4.3 μm is 3.8, and the optical absorption length is approximately 1.7 μm. The absorption rate of the device is calculated by commercial software COMSOL 5.6, which is equal to 1 minus the transmission rate minus the reflection rate. Moreover, the specific structure of the optical model is a cube with a typical size of the operating wavelength. Periodic boundary conditions and (perfectly matched layers) are, respectively, applied to the four sides and (top and bottom) surfaces of the cube to reduce the computational load. The polarization information of the incident light is regulated by the incident port. The reflection rate and transmission rate are the area integrals of the Poynting vector at the reflection port and transmission port, respectively.

https://doi.org/10.3390/mi17020181

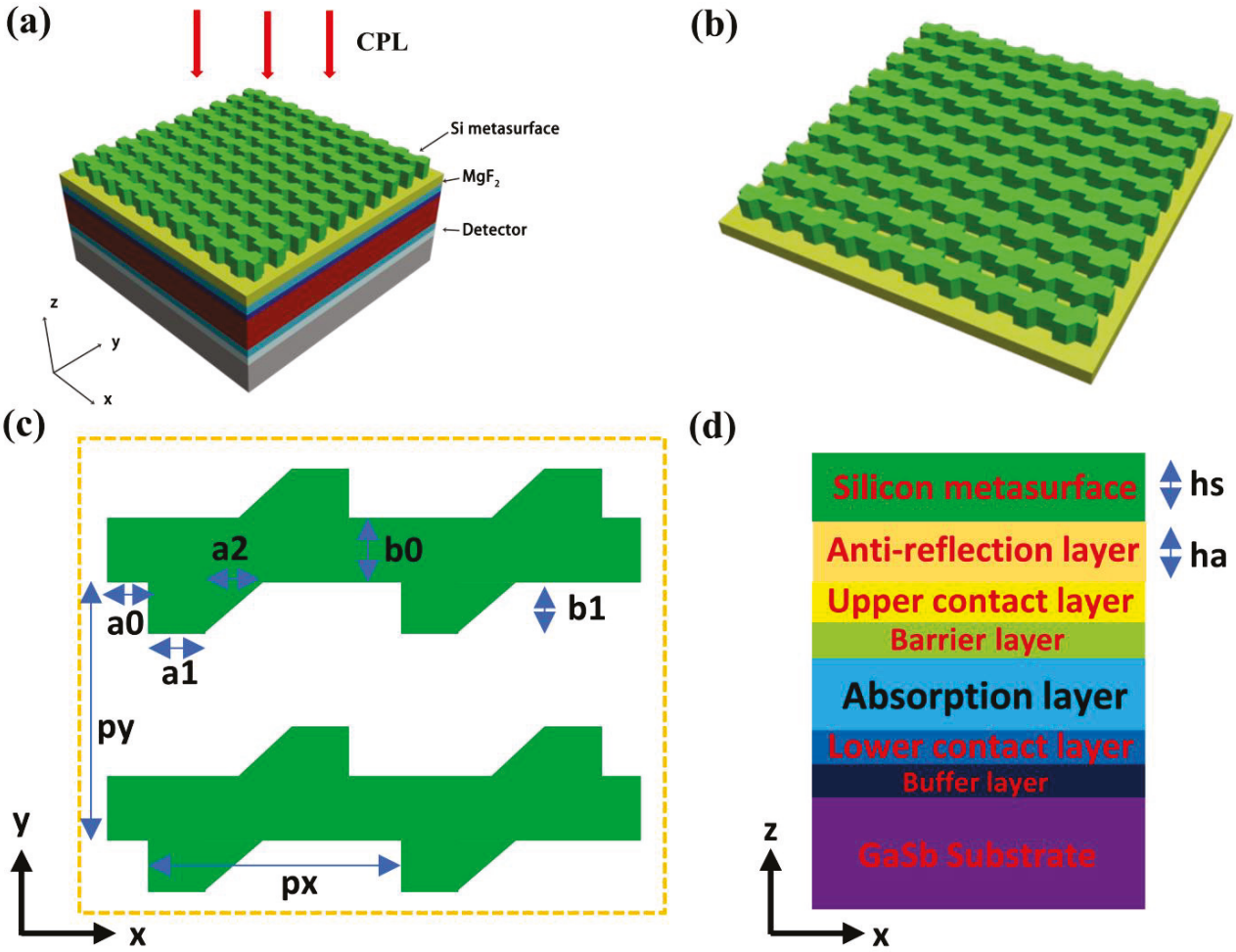


Figure 1. The structure and material information of the mid-wave CPPD. (**a**) Three-dimensional structure diagram of the mid-wave CPPD. The incident light is circularly polarized light (CPL), and the direction of the incident light is the Z-axis. (**b**) Three-dimensional structure diagram of the top chiral silicon metasurface. (**c**) The cross-sectional view of the silicon metasurface in the xy plane. The px = 2.35 μm, py = 2.35 μm, a0 = 0.92 μm, a1 = 2.91 μm, a2 = 1.33 μm, b0 = 2.76 μm, b1 = 1.68 μm. (**d**) The cross-sectional view of the mid-wave CPPD in the xz plane, which can show the thickness and material composition of the device. The hs = 1.61 μm, ha = 2.68 μm.

3. Results

Figure 2 shows the absorption spectrum and CPER spectrum of CPPD in Figure 1. Here, $CPER = 10 \times log_{10}(A_L/A_R)$, where A_L and A_R represent the optical absorption rates of CPPD under LCP and RCP incident conditions, respectively. The light red curve and the green curve represent the absorption rates, and their corresponding Y-axis is on the left. For the RCP incident case, there are three typical absorption valleys in the spectrum within the 4 to 4.6 μm band, located near 4.21 μm, 4.3 μm, and 4.53 μm. The absorption peak at 4.6 μm is extremely weak, almost approaching the failure state where the detector does not respond. For the LCP incident case, when the wavelength is less than 4.23 μm, the spectral line is almost the same as that of RCP, corresponding to an insignificant CD. However, when the wavelength is greater than 4.23 μm, the spectral lines of RCP and LCP are approximately mirror images of each other, corresponding to a significant CD. Additionally, the highest efficiency of CPPD is approximately 0.72. The blue solid line shows the CPER information of CPPD. There are three peaks in the CPER spectrum, but the peak exceeding 10 dB only exists at the operating wavelength of 4.3 μm, corresponding to a super-large 31 dB. The phenomenon that the peak positions of CPER

https://doi.org/10.3390/mi17020181

almost correspond one-to-one with the absorption valleys in the RCP absorption spectrum also exists. This is because the value of CPER is usually determined by the small quantity A_R in the denominator.

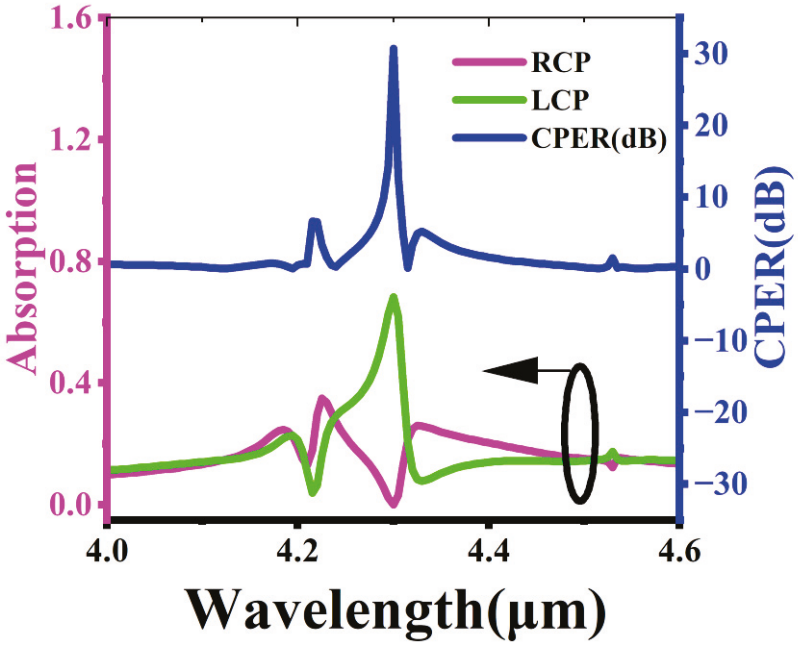


Figure 2. Absorption spectra and CPER spectra of CPPD. The combination of the black circle and arrow in the lower right corner pointing to the left indicates that the two curves below correspond to the left axis of the dual Y-axis.

3.1. Structural Evolution of the Unit Cell of the Metasurface

The geometric unit cell design of chiral metasurfaces is generally a chiral symmetric structure to break mirror symmetry and thereby generate differentiated optical responses when light interacts with the structure, achieving selective control of LCP/RCP. Figure 3a–c shows the entire process of the evolution of the unit cell of metasurfaces from a non-chiral symmetric structure to a chiral symmetric structure. Figure 3a corresponds to the case where the metasurface unit cell is a silicon bar. The silicon bar has C_2 rotational symmetry and does not belong to a typical chiral symmetric structure. As shown in Figure 3b, when two rectangles are placed on the upper and lower sides of the silicon bar, due to the horizontal misalignment of the two rectangles, the metasurface unit cell becomes a chiral symmetric structure. Figure 3c shows the case where two triangles are added, which can enhance the chiral symmetry. Figure 3d shows the CD spectra of the metasurface under different unit cell structures. It can be found that the intensity of the CD spectrum corresponding to the unit cell in Figure 3a is zero, the peak intensity of the CD peak corresponding to the unit cell composed of the silicon bar and the two rectangles does not exceed 0.6, while the CD intensity corresponding to the combination of the rectangle and the triangle can reach 0.9. This increasing CD intensity is likely due to the introduction of complex geometric structures, which increases the chiral symmetry of the metasurface. Additionally, for dielectric metasurfaces, they generally require a high refractive index difference Δn to enable subwavelength structures to accumulate sufficient phase differences within an extremely short propagation distance, thereby efficiently controlling the light wavefront [33]. Figure 3e shows the influence of Δn on CD. When Δn is greater than 0.62, the metasurface no longer has chiral modulation capability. Here, $\Delta n = n_{MgF2} - n_S$, where n_{MgF2} is the refractive index of MgF_2 and n_S is the refractive index of the other substrate. Figure 3f shows the transmission spectrum and CPER spectrum of the metasurface in

https://doi.org/10.3390/mi17020181

Figure 3c. The maximum transmission peak of LCP is peak a, with an intensity close to 100%, while the minimum intensity of the RCP valley corresponds to valley b, which is approximately 0. The maximum value of CPER occurs at a wavelength of 4.3 μm, approximately 31 dB. Here, $CPER = 10 \times \log(T_{LCP}/T_{RCP})$ where T_{LCP} and T_{RCP} are the transmission rates of the metasurface for LCP and RCP, respectively.

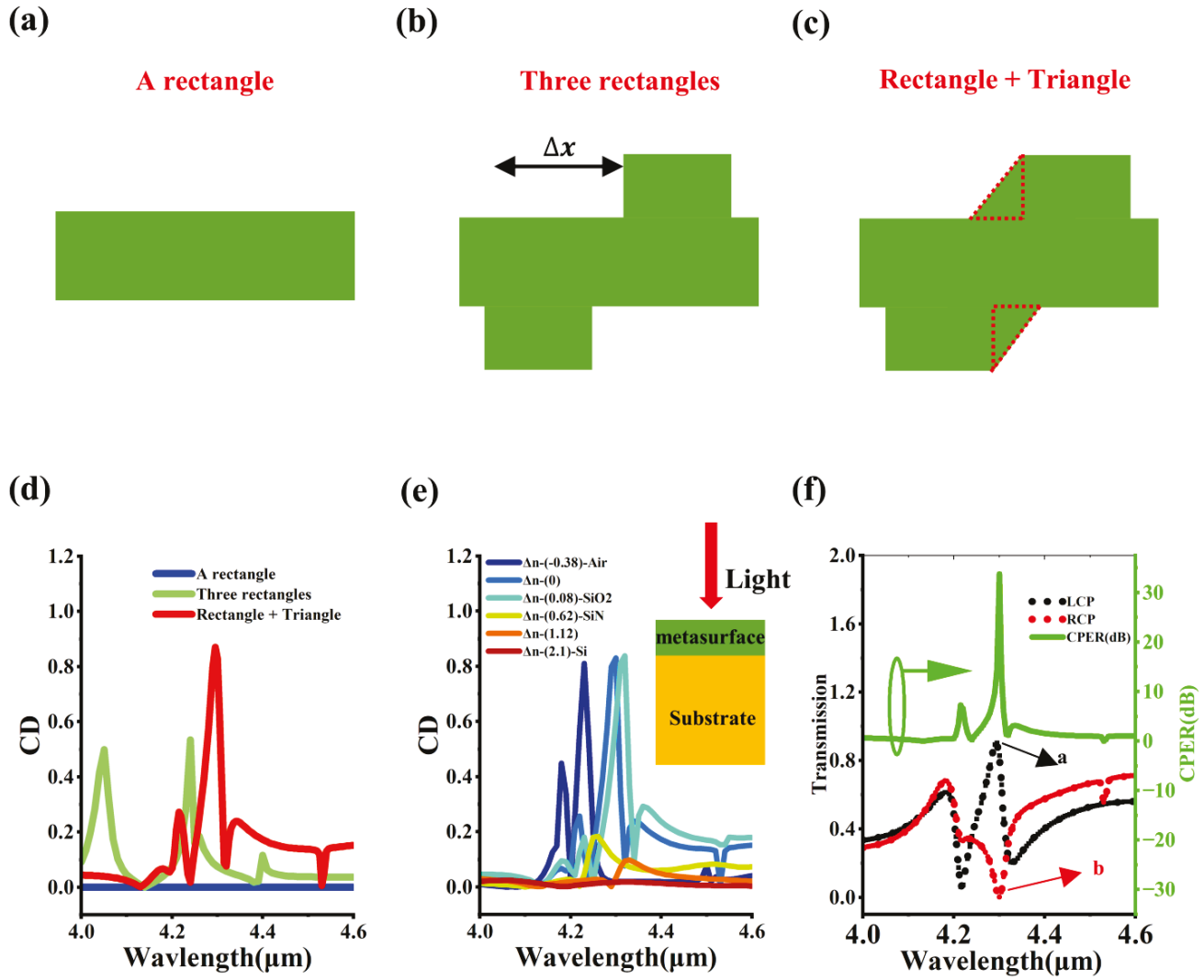


Figure 3. Structural variations and CD spectra. (**a**) a single rectangular unit cell. (**b**) three rectangular unit cells. (**c**) a combination of rectangular and triangular. (**d**) CD spectra of the metasurface corresponding to the three different unit cells. (**e**) CD spectra corresponding to different substrates. (**f**) Transmission and CPER spectra of the optimized structure. The combination of a green arrow and a green circle indicates that CPER corresponds to the right axis of the dual Y-axis. The letters a and b respectively represent the wavelength corresponding to the extreme values of the transmittance.

3.2. Analysis of Optical Resonance Modes

Multipole expansion [34] can precisely reveal the complex electromagnetic resonant modes in metasurface units, which is crucial for understanding and optimizing the interaction between light and subwavelength structures and achieving efficient light field control. The multipole expansion method is a theoretical approach that decomposes the overall electromagnetic response of a complex source (such as a metasurface unit) into the sum of contributions from basic radiation units such as electric dipoles (ED), magnetic dipoles (MD), electric quadrupoles (EQ), and magnetic quadrupoles (MQ). Figure 4a shows the normalized multipole expansion spectrum intensity of the metasurface under LCP

https://doi.org/10.3390/mi17020181

incidence. It can be observed that near peak a, the intensities of ED, MD, EQ, and MQ all correspond to a minimum value, which can be simply understood as no resonances occurring within the metasurface. This extremely weak resonance phenomenon may imply that at this time, the metasurface can be equivalently regarded as a dielectric film with an impedance matching air, corresponding to a transmission peak. Figure 4b shows the multipole expansion spectrum of the metasurface under RCP incidence, where the intensities of ED and EQ are most significant at valley b. It can be considered that the destructive interference of the ED and EQ modes leads to a transmission valley close to 0. Figure 4c presents the magnetic field intensity distribution of the metasurface at peak a and valley b. Regardless of whether the cross-section is the XZ plane or the YZ plane, there are significant red spheres appearing within the metasurface, indicating that a standing wave effect of the guided mode resonance type has occurred, which explains the extreme values of the spectral transmittance.

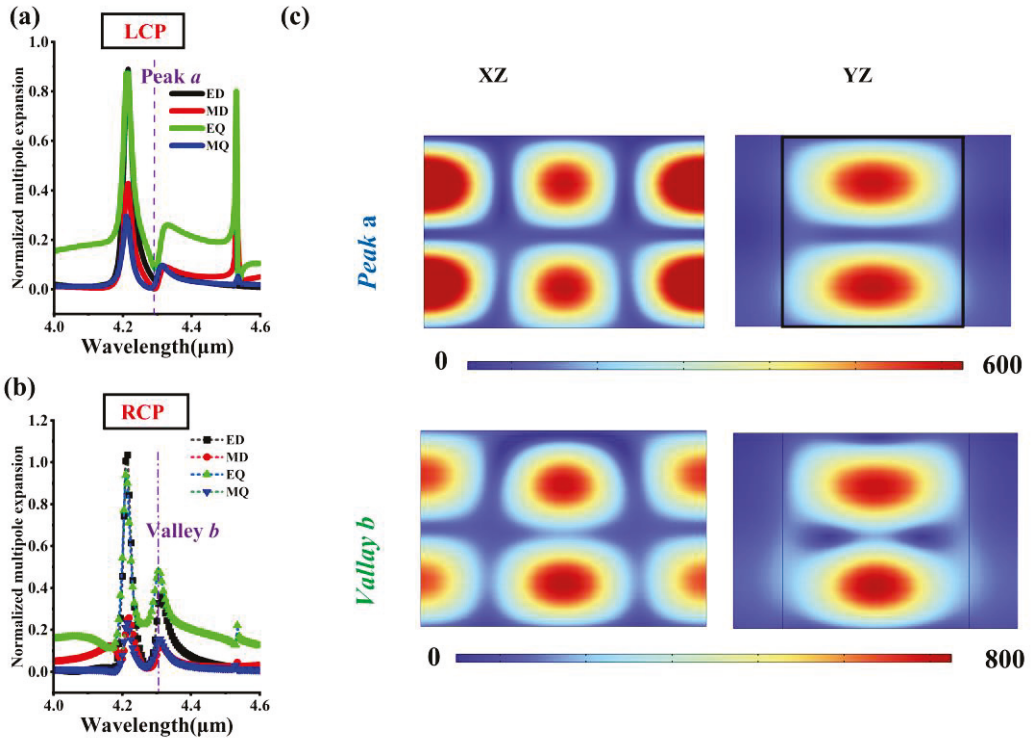


Figure 4. Multipole expansion and magnetic field intensity distribution. (**a**) Multipole expansion of the chiral metasurface under LCP incidence. (**b**) Multipole expansion of the chiral metasurface under RCP incidence. (**c**) Magnetic field distribution of the cross-section of the metasurface at peak *a* and valley *b*. Define peak a as the maximum value of the LCP transmittance near the 4.3 μm wavelength in Figure 3f, and valley *b* as the minimum value of the RCP transmittance near the 4.3 μm wavelength in Figure 3f.

3.3. Analysis of Vertical Coupling Effect

To ensure the efficient transmission of 4.3 μm wavelength light to the detector, it is necessary to simulate the thickness of the MgF_2 anti-reflection layer between the chiral metasurface and the detector to guarantee the minimum coupling between them. Figure 5a shows the influence of the MgF_2 film thickness *hs* on the absorption rate of the CPPD. For the case of RCP incidence, the absorption rate first decreases and then remains constant as *hs* increases. For the case of LCP incidence, the absorption rate shows periodic oscillations as *hs* increases. Additionally, considering the requirements for the quality of the MgF2 film formation, *hs* cannot be too large. Ultimately, an optimal *hs* of 2.68 μm is marked by a green box. Figure 5b shows the magnetic field intensity of the CPPD at peak *a*. It

https://doi.org/10.3390/mi17020181

can be found that the magnetic field can penetrate the metasurface and enter the detector below. However, as shown in Figure 5c, when the incident light corresponds to valley *b*, the metasurface exhibits the characteristics of a perfect reflector, prohibiting any photons from entering the detector.

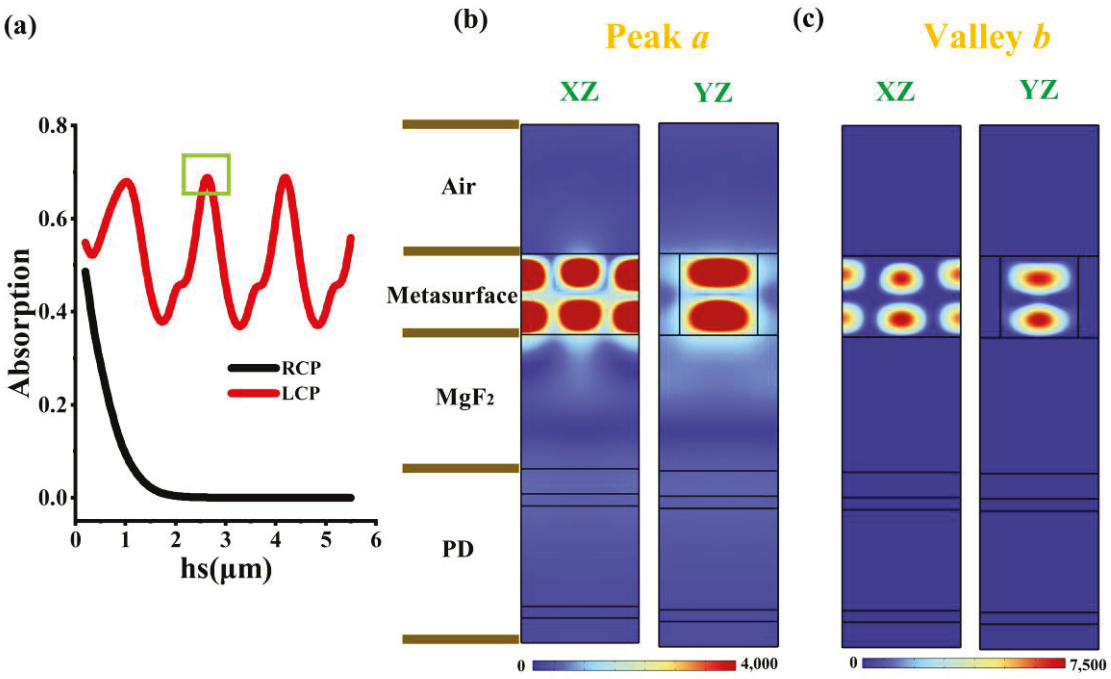


Figure 5. (**a**) The influence of the thickness hs of the dielectric layer between the chiral metasurface and the detector on the CPPD. The green box refers to the best hs. (**b**) The magnetic field distribution diagram of the CPPD at the peak a. (**c**) The magnetic field distribution diagram of the CPPD at valley *b*.

3.4. Analysis of Potential Errors

In addition to considering the influence of MgF_2 film thickness, CPPD also needs to take into account other factors, such as the degree of the polynomial in the optical model, mesh size, under-etching depth error, and over-etching depth error, etc. Figure 6a shows the influence of the degree of the polynomial function in the electromagnetic finite element algorithm on the absorption rate. When the degree of the polynomial is greater than or equal to 2, the calculation results of COMSOL tend to be stable. Figure 6b shows the influence of the mesh size of MgF_2 and silicon on the CPPD. It is obvious that when the mesh size is less than 40 nm, the simulation results are convergent. However, for silicon metasurfaces, large mesh sizes will cause significant result fluctuations. Figure 6c,d, respectively, show the influence of under-etching depth error and over-etching depth error on the device. Both cases have significant damage effects. Especially for the under-etching situation, when the etching error exceeds 60 nm, the device almost loses its chirality. Therefore, in the formal processing of the device, the etching rate and time can be precisely controlled, high-selectivity etching processes can be adopted, and real-time endpoint detection can be used to ensure that the etched structure size is as consistent as possible with the design target, thereby achieving the ideal etching state.

https://doi.org/10.3390/mi17020181

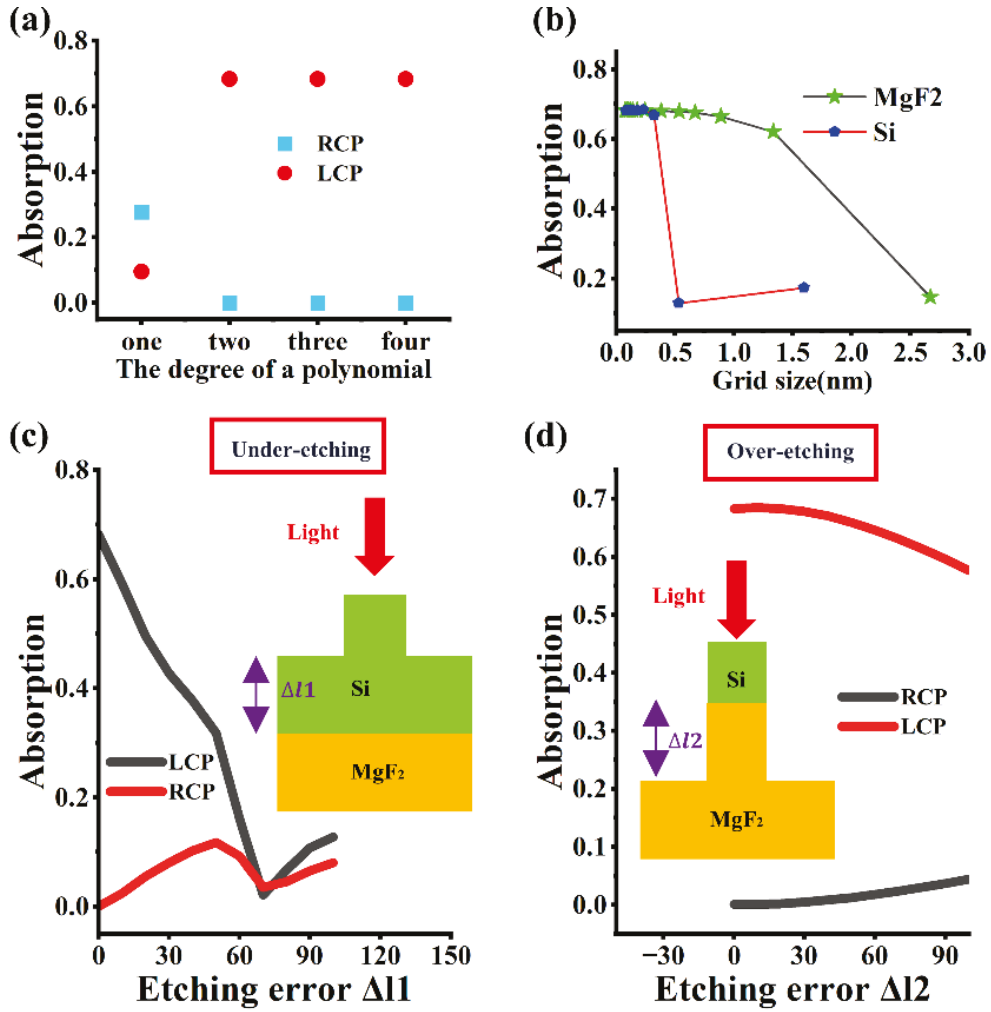


Figure 6. The influence of (**a**): polynomial degree, (**b**): mesh size, (**c**): under-etching depth error, (**d**): over-etching depth error.

4. Conclusions

In summary, we report a CPPD with a simple fabrication process. This device achieves a circular polarization extinction ratio of up to 31 dB at a wavelength of 4.3 μm by monolithically integrating a precisely designed chiral silicon metasurface with a type-II superlattice absorber. Our design constructs a metasurface with a strong chiral response by regulating the displacement and tilt angle of the structural units, resulting in highly differentiated transmission spectra for LCP and RCP, with a circular dichroism exceeding 80%. Moreover, the all-dielectric metasurface is fabricated using a technology compatible with complementary metal-oxide-semiconductor processes, providing an expandable path for the development of chip-level polarization detection systems. The design principles revealed in this work can be further extended to other spectral bands by adjusting the metasurface configuration and absorption materials, thus opening up new possibilities for wide-spectrum detection of all Stokes parameters.

Author Contributions: Conceptualization, Y.Z. (Yingsong Zheng) and B.C.; methodology, L.L.; software, G.S.; validation, L.L., Y.Z. (Yuxiao Zou) and K.Z.; formal analysis, H.S.; investigation, H.S.; resources, K.Z.; data curation, Y.Z. (Yingsong Zheng); writing—original draft preparation, Y.Z. (Yingsong Zheng) and L.L.; writing—review and editing, K.Z. and H.S.; visualization, H.S.; supervision, Y.Z. (Yingsong Zheng); project administration, Y.Z. (Yingsong Zheng); funding acquisition, K.Z. All authors have read and agreed to the published version of the manuscript.

https://doi.org/10.3390/mi17020181

Funding: This research was funded by the National Key Research and Development Program of China (2024YFB2807803). This research was the Natural Science Foundation of Tianjin, grant number NO. 24JCQNJC01880. This research was funded by the Research on Optoelectronic Fusion Technology, ZB253015. This research was funded by the Young Elite Scientists Sponsorship Program of Cast, grant number NO. YESS20240775. This research was funded by the Strategic Priority Research Program of the Chinese Academy of Sciences (grant no. XDB0980000).

Institutional Review Board Statement: Not applicable.

Informed Consent Statement: Not applicable.

Data Availability Statement: The raw data supporting the conclusions of this article will be made available by the authors on request.

Acknowledgments: The authors are grateful to Jietao Liu from Nankai University.

Conflicts of Interest: The authors declare no conflicts of interest.

References

1. Huard, S. Polarization of Light. *Med. Oncol.* **2011**, *28*, 547–552.
2. Huffman, P. Polarization of Light Scattered by Ice Crystals. *J. Atmos. Sci.* **2010**, *27*, 1207–1208. [CrossRef]
3. Petrova, E.V.; Tishkovets, V.P.; Jockers, K. Polarization of Light Scattered by Solar System Bodies and the Aggregate Model of Dust Particles. *Sol. Syst. Res.* **2004**, *38*, 309–324. [CrossRef]
4. Li, Z.; Ji, W. Research progress of short-wavelength infrared polarization imaging technologies. *J. Appl. Opt.* **2023**, *44*, 643–654. [CrossRef]
5. Hu, Y.; He, J.; Yan, Z.; Xu, C.; Li, X.; Wei, N.; Wang, Y.; Dong, N.; Wang, J. High Performance Balanced Linear Polarization Photodetector Based on 2D ReS_2. *Laser Photon. Rev.* **2024**, *18*, 2400661. [CrossRef]
6. Lin, Z.; Yang, X.; He, J.; Dong, N.; Li, B. Structural and optoelectronic characterization of anisotropic two-dimensional materials and applications in polarization-sensitive photodetectors. *Appl. Phys. Rev.* **2025**, *12*, 011301. [CrossRef]
7. Liu, S.; Yu, F.; Liu, X.; Zhang, H.; Ma, M.; Zhang, S.; Guo, H.; Hu, H.; Yuan, C.; Zheng, Z. High-performance integrated circularly polarized light detection using soft-helix-decorated perovskite diodes. *Newton* **2024**, *1*, 100003. [CrossRef]
8. Ji, J.; Li, J.; Wang, Z.; Li, X.; Sun, J.; Wang, J.; Fang, B.; Chen, C.; Ye, X.; Zhu, S. On-chip multifunctional metasurfaces with full-parametric multiplexed Jones matrix. *Nat. Commun.* **2024**, *15*, 8271. [CrossRef]
9. Zheng, J.P.; Zheng, L.Y.; Yu, S.Y.; Yang, S.L.; Sun, X.C.; Liu, L.; Lu, M.H.; Chen, Y.F.; Christensen, J. Focusing Micromechanical Polaritons in Topologically Nontrivial Hyperbolic Metasurfaces. *Adv. Mater.* **2024**, *36*, 2311599. [CrossRef]
10. Yang, J.; Cui, K.; Huang, Y.; Zhang, W.; Feng, X.; Liu, F. Angle-Insensitive Spectral Imaging Based on Topology-Optimized Plasmonic Metasurfaces. *Laser Photon. Rev.* **2024**, *18*, 2400255. [CrossRef]
11. Xu, Y.; Zhang, P.; Ma, Y.; Liu, J.; Zhu, L.; Wang, L.; Huang, X. Multifunctional Metasurfaces for Multispectral Infrared Detection With Radiative Cooling. *IEEE Photon. Technol. Lett.* **2025**, *37*, 53–56. [CrossRef]
12. Chen, Q.; Luo, X.; Xu, M.; Yan, X.; Zhang, Y.; Yu, S.; Zeng, Q.; Pu, M.; Guo, Y.; Zhang, F. Generation of high-complexity laser chaos with asymmetric filtered feedback enabled by Fano metasurfaces. *Opt. Express* **2025**, *33*, 33738–33749. [CrossRef]
13. Rocco, D.; Locatelli, A.; Carletti, L.; Vincenti, M.A.; Angelis, C.D. Nonlinear asymmetric imaging with AlGaAs metasurface. *Opt. Express* **2024**, *32*, 11673–11680. [CrossRef] [PubMed]
14. Marino, G.; Gigli, C.; Rocco, D.; Lemaître, A.; Favero, I.; De Angelis, C.; Leo, G. Zero-Order Second Harmonic Generation from AlGaAs-on-Insulator Metasurfaces. *ACS Photon.* **2019**, *6*, 1226–1231. [CrossRef]
15. Jung, C.; Lee, E.; Rho, J. The rise of electrically tunable metasurfaces. *Sci. Adv.* **2024**, *10*, eado8964. [CrossRef] [PubMed]
16. Ha, S.T.; Li, Q.; Yang, J.K.W.; Demir, H.V.; Brongersma, M.L.; Kuznetsov, A.I. Optoelectronic metadevices. *Science* **2024**, *386*, eadm7442. [CrossRef]
17. Afshinmanesh, F.; White, J.S.; Cai, W.; Brongersma, M.L. Measurement of the polarization state of light using an integrated plasmonic polarimeter. *Nanophotonics* **2012**, *1*, 125–129. [CrossRef]
18. Li, N.; Zhao, J.; Tang, P.; Cheng, Y. Triple-broadband asymmetric transmission via cross-polarization conversion based on composite chiral metasurface structure. *Opt. Commun.* **2024**, *560*, 130445. [CrossRef]
19. Xing, D.; Chen, M.H.; Wang, Z.; Lin, B.W.; Tabata, H.; Delaunay, J.J. Chiral Lasing Emission from a Simple Two-Unit Supercell Metasurface. *Laser Photon. Rev.* **2025**, *19*, e00530. [CrossRef]
20. Li, J.; Ding, J.; Dong, Q.; He, Y.; Zhou, L.; Zou, Y.; Chen, C.; Li, H.; Xu, W.; Tan, Q. Full Poincaré sphere vectorial polarization transformation of terahertz wave based on chiral metasurfaces. *Opt. Express* **2025**, *33*, 33067–33076. [CrossRef]

https://doi.org/10.3390/mi17020181

21. Luo, L.; Zhou, L.; Zou, Y.; Yang, J.; Huo, J.; Yang, X.; Lv, Y.; Bian, J.; Peng, S.; Liu, B. Terahertz polarization modulator based on chiral metasurface integrated with vanadium dioxide. *Opt. Lett.* **2025**, *50*, 3345–3348. [CrossRef]
22. Zhou, X.; Yang, H.; Zhao, R.; Fu, Y.; Yang, Y.; Zhou, X.; Liang, J. Dual-band chiral metasurface for spin-selective absorption and temperature-induced electromagnetic chameleon. *Appl. Surf. Sci.* **2025**, *682*, 161666. [CrossRef]
23. Wang, C.; Cheng, X.; Wang, R.; Hu, X.; Wang, C. Flexibly Designable 2D Chiral Metasurfaces with Pixelated Topological Structure Based on Machine Learning. *Laser Photon. Rev.* **2024**, *18*, 2300958. [CrossRef]
24. Li, W.; Coppens, Z.J.; Besteiro, L.V.; Wang, W.; Govorov, A.O.; Valentine, J. Circularly polarized light detection with hot electrons in chiral plasmonic metamaterials. *Nat. Commun.* **2015**, *6*, 8379. [CrossRef]
25. Gansel, J.K.; Thiel, M.; Rill, M.S.; Decker, M.; Bade, K.; Saile, V.; Freymann, G.V.; Linden, S.; Wegener, M. Gold Helix Photonic Metamaterial as Broadband Circular Polarizer. *Science* **2009**, *325*, 1513–1515. [CrossRef]
26. Yang, Z.Y.; Zhao, M.; Lu, P.X.; Lu, Y.F. Ultrabroadband optical circular polarizers consisting of double-helical nanowire structures. *Opt. Lett.* **2010**, *35*, 2588–2590. [CrossRef] [PubMed]
27. Ji, R.; Wang, S.W.; Liu, X.; Guo, H.; Lu, W. Hybrid Helix Metamaterials for Giant and Ultrawide Circular Dichroism. *ACS Photon.* **2016**, *3*, 2368–2374. [CrossRef]
28. Basiri, A.; Chen, X.; Bai, J.; Amrollahi, P.; Carpenter, J.; Holman, Z.; Wang, C.; Yao, Y. Nature-inspired chiral metasurfaces for circular polarization detection and full-Stokes polarimetric measurements. *Light Sci. Appl.* **2019**, *8*, 78. [CrossRef]
29. Hu, J.; Zhao, X.; Lin, Y.; Zhu, A.; Zhu, X.; Guo, P.; Cao, B.; Wang, C. All-dielectric metasurface circular dichroism waveplate. *Sci. Rep.* **2017**, *7*, 41893. [CrossRef]
30. Hu, J.; Zhang, C.; Dong, Y.; Zeng, A.; Wang, C. High efficiency all-dielectric pixelated metasurface for near-infrared full-Stokes polarization detection. *Photon. Res.* **2021**, *9*, 583–589.
31. Cheng, B.; Liu, L.; Zou, Y.; Song, G.; Li, S.; Zhai, K. Large circular dichroic long-wave infrared polarization photodetector based on rotationally operated chiral metasurfaces. *Opt. Commun.* **2025**, *583*, 131680. [CrossRef]
32. Cheng, B.; Zou, Y.; Song, G. Ultra-large bandwidth fully polarized photodetectors based on displacement-induced chiral dielectric metasurfaces. *Appl. Opt.* **2025**, *64*, 2332–2338. [CrossRef] [PubMed]
33. Pors, A.; Ding, F.; Chen, Y.; Radko, I.P.; Bozhevolnyi, S.I. Random-phase metasurfaces at optical wavelengths. *Sci. Rep.* **2016**, *6*, 28448. [CrossRef] [PubMed]
34. Dhawan, A.; Norton, S.J.; Gerhold, M.D.; Vo-Dinh, T. Comparison of FDTD numerical computations and analytical multipole expansion method for plasmonics-active nanosphere dimers. *Opt. Express* **2009**, *17*, 9688–9703. [CrossRef]

Disclaimer/Publisher's Note: The statements, opinions and data contained in all publications are solely those of the individual author(s) and contributor(s) and not of MDPI and/or the editor(s). MDPI and/or the editor(s) disclaim responsibility for any injury to people or property resulting from any ideas, methods, instructions or products referred to in the content.

https://doi.org/10.3390/mi17020181

micromachines

MDPI

Article

PN Tandem Solar Cells Based on Combination of Dye-Sensitized TiO_2 Photoanode and Perovskite-Sensitized NiO Photocathode

Huan Wang [1,*], Weicheng Tang [1,2], Mengru Li [1,2] and Xiaoli Mao [1,2,*]

[1] School of Electrical Engineering and Automation, Hefei University of Technology, Hefei 230009, China
[2] School of Physics, Hefei University of Technology, Hefei 230009, China
* Correspondence: wanghuan@hfut.edu.cn (H.W.); maoxiaolili@foxmail.com (X.M.)

Abstract

Dye-sensitized solar cells (DSSCs) have attracted significant attention as next-generation photovoltaic devices due to their low cost, simple fabrication process, use of earth-abundant materials, and potential for colour tunability and transparency. p–n tandem DSSCs have garnered particular interest owing to their higher open-circuit voltage compared to single-junction DSSCs. However, the performance of such tandem devices remains limited by relatively low open-circuit voltage and short-circuit current density, primarily due to the scarcity of suitable p-type sensitizers. To address this challenge, we report a novel p–n tandem solar cell integrating a dye-sensitized TiO_2 photoanode with a perovskite-sensitized NiO photocathode, achieving a record power conversion efficiency of 4.02%. By optimizing the thickness of the TiO_2 layer, a maximum open-circuit voltage of 1060 mV and a peak short-circuit current density of 6.11 mA cm^{-2} were simultaneously attained.

Keywords: PN tandem solar cells; dye-sensitized TiO_2 photoanode; perovskite-sensitized NiO photocathode

1. Introduction

Dye-sensitized solar cells (DSCs) are attractive as next-generation solar cells because of many advantages, e.g., low cost and facile fabrication, earth-abundant raw materials, colourful and transparent [1–3]. The theoretic upper limit of photon-to-current conversion efficiency (PCE) of DSSC is 33% [4]. However, the reported highest efficiency of DSSC is only in the range of 12–15% [5–9]. One of the main limiting factors is due to the light absorption range of dyes covering only within 700–800 nm, which is much narrower than that of commercialized crystalline silicon-based solar cells and other kinds of inorganic thin film solar cells. PN tandem solar cells can not only widen the absorption spectrum but also avoid adverse interactions between two kind dyes positioned separately. However, several studies have been dedicated to PN tandem quantum dot-sensitized solar cells, but have not obtained competitive performance [10–12].

It is evident that the current reported performance of p–n tandem dye-sensitized solar cells (DSSCs) significantly lags behind that of conventional n-type DSSCs, primarily due to the limited efficiency of p-type DSSCs. With respect to the p-type semiconductor—exemplified by NiO—an ideal sensitizer must fulfill two key criteria. First, its highest occupied molecular orbital (HOMO) level should be lower in energy than the valence band of NiO (−5.1 eV versus vacuum), while its lowest unoccupied molecular orbital (LUMO)

level should be higher than the redox potential of the I_3^-/I^- couple (−4.85 eV versus vacuum). This energetic alignment ensures sufficient driving force for efficient hole injection into the valence band of NiO and simultaneous electron transfer to the electrolyte for the reduction of I_3^- to I^-. Second, the width of the absorption spectrum for the sensitizer is of great significance. The ideal sensitizer should possess broad spectral absorption across the solar spectrum to capture more photons to enable a higher short-circuit current density (*Jsc*).

It is obvious that the currently reported performance of pn tandem DSSCs is far behind that of conventional n-type DSSCs, which is limited by the poor performance of p-type DSSCs [13–16]. To date, numerous scientific researchers have dedicated significant efforts toward optimizing the performance of dye-sensitized solar cells (DSSCs). The PMI-6TTPA-TPA dye has attracted considerable attention due to its relatively broad absorption spectrum and high extinction coefficient [17,18]. P-type DSSCs based on this dye have achieved a power conversion efficiency (PCE) of 1.3%. To further enhance device performance, in 2015, Bach's group successfully introduced the tris(acetylacetonato)iron (III)/(II) redox couple ($[Fe(acac)_3]^0/^{1-}$) into p-type DSSCs, achieving an improved PCE of 2.51% [19]. Despite the passage of over a decade, the PCE of p-type DSSCs has remained largely stagnant at this level. The majority of reported devices exhibit a PCE below 1%, significantly lagging behind their n-type counterparts. This performance gap is primarily attributed to the lack of an efficient p-type sensitizer.

Organic–inorganic hybrid perovskites have attracted significant research interest due to their high extinction coefficient, bipolar charge transport characteristics, broad absorption spectrum, low material cost, and facile fabrication process. These advantageous properties have led to their widespread application in optoelectronic devices, particularly in solar cells and photodetectors [20–23]. Building upon these merits, our group previously reported an efficient $CH_3NH_3PbI_3$-sensitized p-type mesoporous NiO solar cell employing an iodine-based liquid electrolyte, achieving a high open-circuit voltage (*Voc*) of 205 mV and a remarkable short-circuit current density (*Jsc*) of 9.47 mA cm^{-2} [24]. In this work, we successfully designed a novel pn tandem dye-sensitized solar cell by integrating an organic dye (N719)-sensitized n-type TiO_2 photoanode and an organometal halide perovskite ($CH_3NH_3PbI_{3-x}Cl_x$)-sensitized p-type NiO photocathode, which share a common iodine-based liquid electrolyte to form a sandwich-structured device. By optimizing the thickness of the TiO_2 layer, a record power conversion efficiency of 4.02% was achieved, along with a *Voc* of 1060 mV, a *Jsc* of 6.11 mA cm^{-2}, and a fill factor (FF) of 0.62.

2. Experimental Section

2.1. Fabrication of the Perovskite-Sensitized NiO and Al_2O_3 Photocathode

All chemicals were of analytical grade and used as received unless otherwise specified. A compact NiO thin film was deposited on FTO glass (8 Ω sq^{-1}, Nippon Sheet Glass, Tokyo, Japan) via spray pyrolysis using a 0.2 mol L^{-1} solution of nickel acetylacetonate in acetonitrile at 500 °C [22]. Subsequently, mesoporous NiO and Al_2O_3 films were deposited onto the prepared NiO compact layer by screen printing, employing a paste consisting of commercially available NiO and Al_2O_3 nanoparticles (20 nm, Inframat, Manchester, CT, USA). The resulting film was then annealed at 450 °C for 30 min, followed by annealing at 550 °C for 15 min. A bright yellow $CH_3NH_3PbI_{3-x}Cl_x$ precursor solution was prepared by dissolving 1.224 g of $PbCl_2$ and 2.099 g of CH_3NH_3I in 5 mL of DMF and stirring the mixture at 50 °C for 2 h. The perovskite solution was then spin-coated onto the mesoporous NiO/Al_2O_3 film at 2000 rpm for 30 s under ambient conditions with controlled humidity (<30%), followed by thermal annealing at 100 °C for 90 min until a dark grey, uniform film formed.

https://doi.org/10.3390/mi17010099

2.2. Preparation of TiO_2 Photoanode Sensitized by N719 and Solar Cell

A dense TiO_2 layer was deposited on FTO glass (8 Ω sq^{-1}, Nippon Sheet Glass, Japan) following a previously reported method [9]. Briefly, clean FTO glass was placed on a hot plate maintained at 450 °C. A solution of 0.38 M titanium di-isopropoxide bis(acetylacetonate) (Sigma-Aldrich, St. Louis, MO, USA) in 2-propanol was atomized and sprayed onto the substrate surface, followed by annealing at 450 °C for 30 min. Subsequently, a mesoporous TiO_2 film was fabricated by screen-printing a TiO_2 paste onto the compact TiO_2 layer-coated FTO glass. The resulting film was then calcined in a stepwise manner: 375 °C for 15 min, 450 °C for 15 min, and 500 °C for 30 min. After cooling to 80 °C, the TiO_2 films were immersed in a 0.3 mM solution of N719 dye in a 1:1 (v/v) mixture of acetonitrile and tert-butyl alcohol and allowed to adsorb at room temperature for 20 h. The electrolyte, consisting of 0.5 M LiI, 0.25 M I_2, 0.3 M tert-butylpyridine, and 0.03 M urea in ethyl acetate, was introduced into the cell using the vacuum backfilling technique.

2.3. Characterizations

General material characterizations: The film thickness was measured using a profilometer (Dektak 150, Veeco Instruments Inc., Plainview, NY, USA). UV-vis-NIR spectra of the films were recorded with a Perkin-Elmer UV/Vis spectrophotometer (Lambda 950, PerkinElmer, Shelton, CT, USA). The crystalline phases were characterized by X-ray powder diffraction (XRD) using a PANalytical X'Pert (PANalytical, Almelo, The Netherlands) PRO diffractometer equipped with Cu Kα radiation.

Photovoltaic characterizations: A 450 W xenon arc lamp (Oriel, model 9119, NewPort, RI, USA) equipped with an AM 1.5G filter (Oriel, model 91192) was used to provide a simulated solar irradiance of 100 mW cm^{-2}. The current–voltage characteristics of the device were measured under these conditions by applying an external potential bias and recording the resulting photocurrent using a Keithley 2400 digital source meter (Keithley, Solon, OH, USA). To minimize light scattering, a 4 × 4 mm^2 aperture mask was placed on the solar cell active area. The same data acquisition system was employed to control the incident photon-to-current efficiency (IPCE) measurements. During IPCE measurements, a white light bias at 1% of standard sunlight intensity was applied to the sample along with an AC modulation signal (10 Hz).

3. Results and Discussion

The efficiency of the tandem cell (η = 4.02%) outperforms either of the half cells (3.24% for n-type half cell and 1.78% for p-type half cell). In comparison to the best pn tandem dye-sensitized solar cell reported in 2010 by Udo Bach, the J_{sc} of our tandem cell is much higher (6.11 mA cm^{-2} versus 2.40 mA cm^{-2}), which arises from the more efficient p-type perovskite sensitizer with a wider light absorption range. The overall efficiency is therefore improved by 110.48% (4.02% versus 1.91%). Such performance is superior to all of the previously reported PN tandem solar cells based on organic dyes and quantum dots (see Table 1). The primary reason for this can be attributed to the advantageous properties of perovskites: one is their broad absorption spectrum, and the other is their bipolar charge transport characteristics. Both of these properties contribute significantly to the performance of the fabricated pn tandem solar cell.

Figure 1 represents the structure of N719 (Figure 1a) and perovskite (Figure 1b) and a schematic configuration of the pn tandem solar cell with the approximate energy levels of each component. The potential electron transfer processes within the tandem cell are also depicted. The device comprises an N719 dye-sensitized n-type TiO_2 photoanode and an organometal halide perovskite ($CH_3NH_3PbI_{3-x}Cl_x$)-sensitized p-type NiO photocathode, arranged in a simple sandwich configuration with an intermediate electrolyte layer. Under

https://doi.org/10.3390/mi17010099

light illumination, the N719 dye sensitizer injects electrons into the conduction band of TiO_2 at the anode, while the $CH_3NH_3PbI_{3-x}Cl_x$ injects holes into the valence band of NiO at the cathode. The photo-oxidized N719 dye or reduced $CH_3NH_3PbI_{3-x}Cl_x$ sensitizer is then regenerated by a commonly used iodide/triiodide electrolyte. Because the two photoelectrodes are connected in series, the photovoltages of this tandem device are the sum of the corresponding p and n devices. Consequently, this tandem configuration achieves a significantly higher photovoltage and power conversion efficiency (PCE) compared to single-junction solar cells.

Table 1. Photoelectric properties of reported p-n tandem solar cells.

References	Cell Structure	*Voc* (mv)	*Jsc* (mA cm^{-2})	*PCE* (%)
[25]	P + N	732	2.26	0.39%
	P	83	0.269	/
	N	650	7.16	/
[26]	P + N (N side)	918	3.62	0.66%
	P + N (P side)	887	2.73	0.78%
	P	93	1.0	0.027%
	N	762	5.83	2.36%
[27]	P + N (N side)	910	0.97	0.55%
	P + N (P side)	880	0.53	0.37%
	P	350	1.66	0.2%
	N	660	1.64	0.61%
[18]	P + N (N side)	1079	2.4	1.91%
	P	186	4.64	0.3%
	N	905	2.74	1.79%
	P + N (P side)	958	4.07	2.42%
	P	227	3.87	0.3%
	N	799	11.80	5.88%

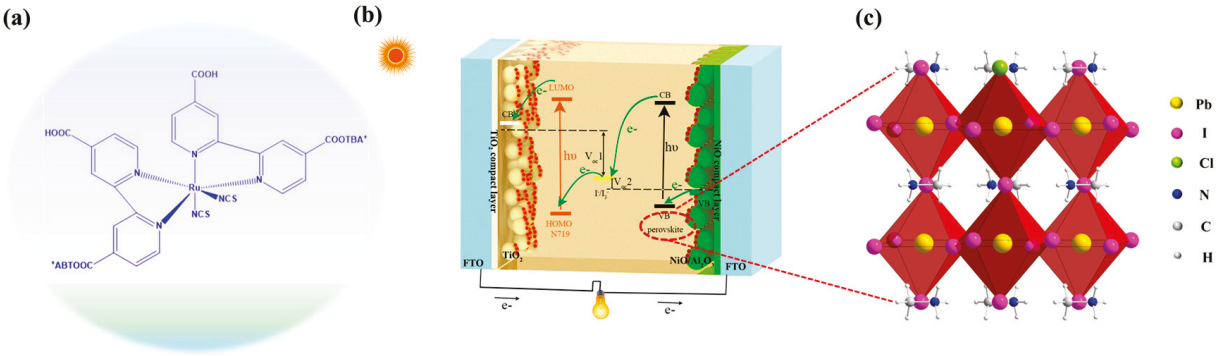


Figure 1. (**a**,**c**) The structures of N719 and perovskite. (**b**) Scheme representation of the tandem solar cell. The energy level (versus vacuum level, Vac) diagram of the component materials and a simple electron transfer processes are also shown.

The transmittance of the different films varies significantly, as shown in Figure 2a. Notably, the FTO glass/compact NiO/mesoporous Al_2O_3 structure exhibits higher transmittance compared to the FTO glass/compact NiO/mesoporous NiO structure. This difference can be attributed to the larger bandgap of Al_2O_3 relative to that of NiO, which enhances light penetration and consequently leads to a higher photocurrent in solar cells employing the FTO glass/compact NiO/mesoporous Al_2O_3 configuration as photocathodes.

https://doi.org/10.3390/mi17010099

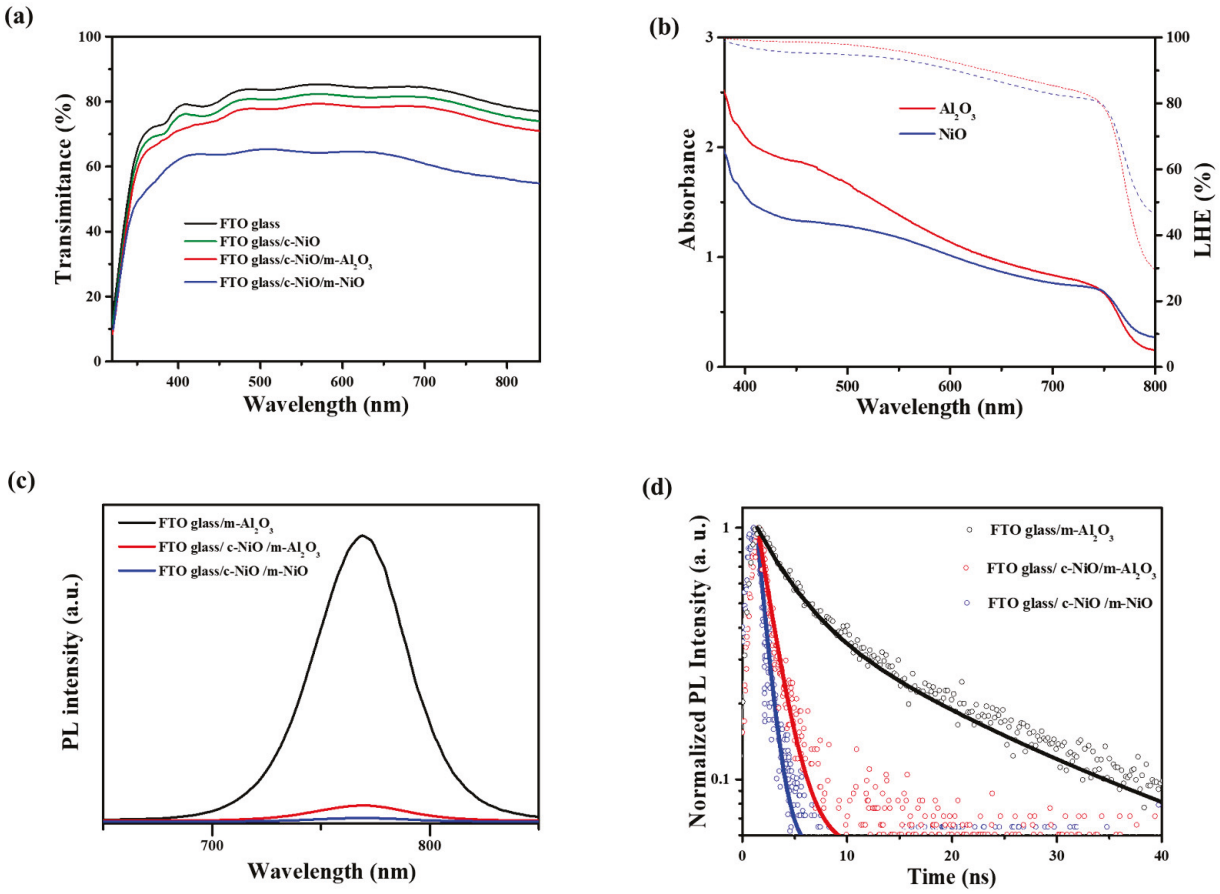


Figure 2. (**a**) Transmittance of FTO glass, FTO glass/c-NiO, FTO glass/c-NiO/m-Al_2O_3, and FTO glass/c-NiO/m-NiO. (**b**) Absorbance of pure NiO and Al_2O_3 films deposited with perovskite. (**c**,**d**) Steady-state and transient fluorescence spectroscopy of FTO glass/m-Al_2O_3, FTO glass/c-NiO/m-Al_2O_3, and FTO glass/c-NiO/m-NiO.

Furthermore, when perovskite is deposited on pure NiO and Al_2O_3 films, a distinct difference in absorbance is observed, as shown in Figure 2b. Compared with NiO films, Al_2O_3 films exhibit a higher extinction coefficient, which facilitates the capture of a greater number of photons and thereby contributes to a higher short-circuit current density in solar cell applications.

In addition, both the FTO glass/compact NiO (c-NiO)/mesoporous Al_2O_3 (m-Al_2O_3) and FTO glass/compact NiO/mesoporous NiO structures (m-NiO) were subjected to steady-state and time-resolved fluorescence measurements, as shown in Figure 2c,d. The results show that fluorescence quenching occurs rapidly in the FTO glass/compact NiO/mesoporous NiO structure, whereas the fluorescence lifetime is significantly longer in the FTO glass/compact NiO/mesoporous Al_2O_3 film. To accurately analyse the lifetime, we calculated the lifetimes for both samples. The carrier lifetimes are estimated to be approximately 7.8 and 3.6 ns for the FTO glass/c-NiO/m-Al_2O_3 and FTO glass/c-NiO/m-NiO, respectively. This indicates that porous NiO exhibits a stronger capability for capturing photogenerated carriers compared to porous Al_2O_3, thereby enabling more efficient hole extraction in the device and leading to a higher open-circuit voltage (Voc).

To analyse the morphology of NiO and confirm the adsorption of perovskite on its surface, scanning electron microscopy (SEM) and energy-dispersive X-ray spectroscopy (EDS) were performed on the FTO/NiO substrate after perovskite deposition, as displayed in Figure 3. The results reveal that the as-prepared porous NiO film exhibits uniform particle size. EDS mapping shows a homogeneous distribution of Pb, I, Cl, and C elements

https://doi.org/10.3390/mi17010099

across the surface, confirming the successful adsorption of perovskite onto the porous NiO layer.

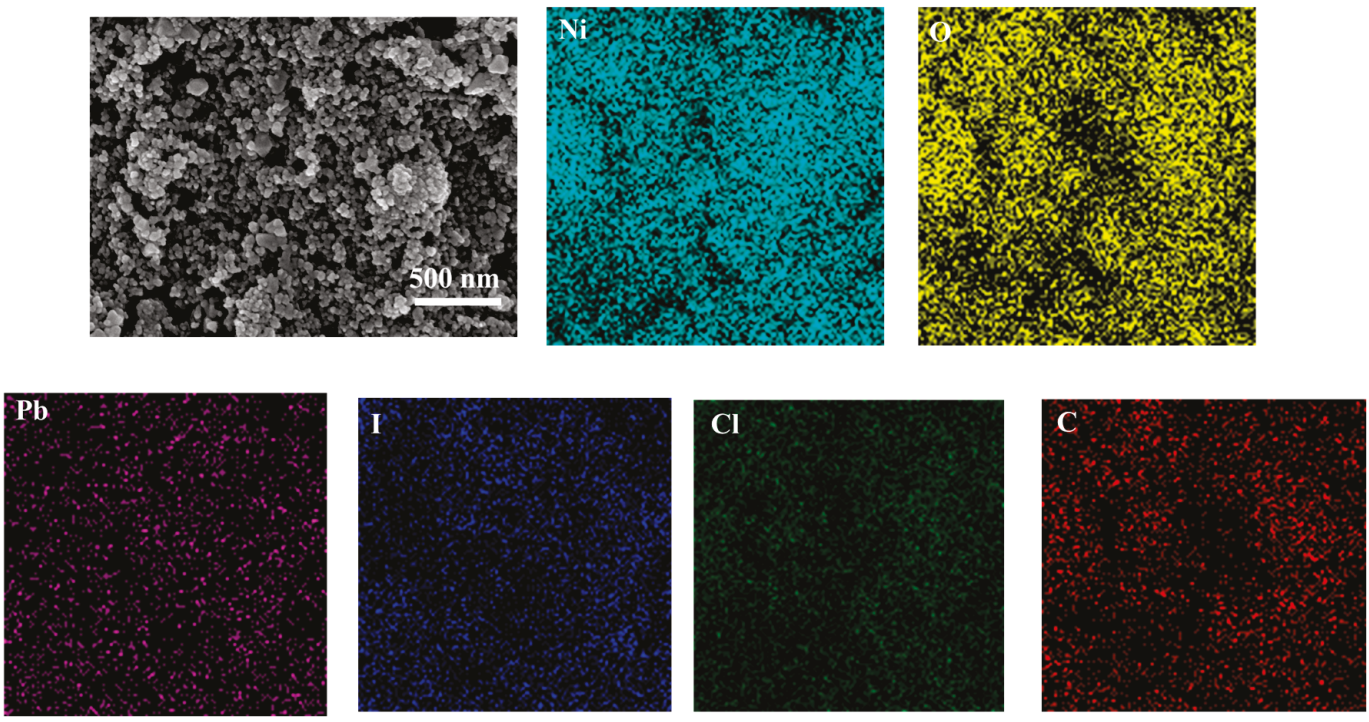


Figure 3. SEM of mesoporous NiO nanoparticles and EDS of Pb, I, Cl, and C elements.

To analyse the crystal structure of the perovskite, X-ray diffraction (XRD) measurements were conducted, as shown in Figure 4a. The annealed $MAPbI_{3-x}Cl_x$ film exhibits characteristic diffraction peaks at 2θ angles of 14.08°, 28.41°, 31.85°, 40.46°, and 43.16°, corresponding to the (110), (220), (310), (224), and (314) crystal planes of the tetragonal perovskite structure, respectively, which is consistent with the previously reported literature [28]. In addition, the peak located at 12.7 degrees is attributed to PbI_2 and is marked with a "#" symbol.To clarify the presence and chemical states of the elements in the prepared $MAPbI_{3-x}Cl_x$ film, X-ray photoelectron spectroscopy (XPS) was employed to analyse the elemental composition of the perovskite. As shown in Figure 4b, clear peaks corresponding to Pb, I, C, and N are observed. To detect the Cl element, high-resolution XPS spectra for Cl were acquired, as depicted in Figure 4c. The results confirm the presence of chlorine in the as-prepared perovskite film.

In order to fabricate a highly efficient pn tandem solar cell, we firstly have devoted effort to optimizing the performance of p- and n- single-junction solar cells. For the p part device, we have previously reported an efficient $CH_3NH_3PbI_3$-sensitized p-type mesoporous NiO solar cell based on iodine liquid electrolyte, with a high V_{oc} of 205 mv and a remarkable J_{sc} of 9.47 mA cm^{-2}. By simply replacing $CH_3NH_3PbI_3$ with a $CH_3NH_3PbI_{3-x}Cl_x$ sensitizer, the V_{oc} of the cell was further increased to 315 mV, and J_{sc} increased to 11.80 mA cm^{-2} (as shown Figure 5 and Table 2). It is particularly necessary to point out that both the V_{oc} and J_{sc} are the highest among the p-type DSCs or p-type QDSCs based on the iodide electrolyte. In addition, a perovskite-sensitized Al_2O_3-based solar cell was fabricated, which achieved a short-circuit current density of 14.95 mA cm^{-2}—significantly higher than that of the NiO-based device. This performance difference is primarily attributed to the intrinsic light absorption of NiO, which leads to parasitic absorption and consequently reduces the available photons for perovskite excitation, thereby lowering the short-circuit current density.

https://doi.org/10.3390/mi17010099

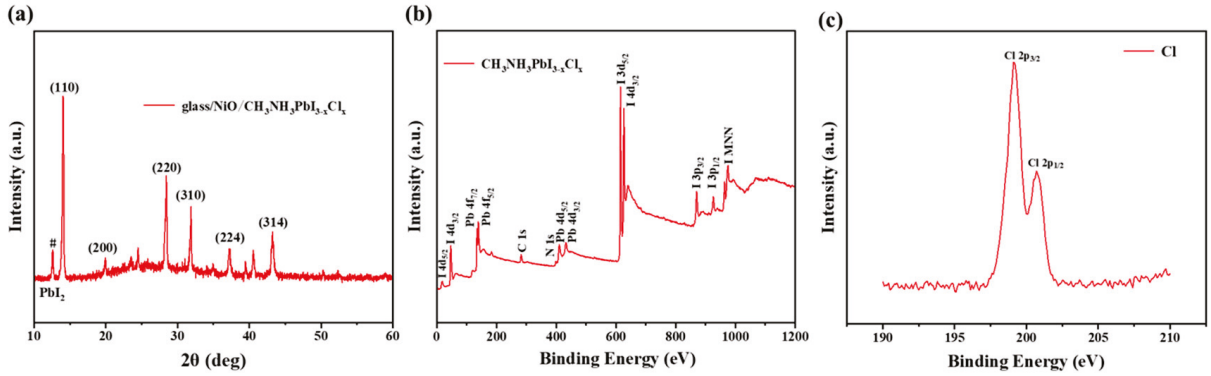


Figure 4. (**a**) XRD patterns and (**b**) XPS characterization of $CH_3NH_3PbI_{3-x}Cl_x$. (**c**) Cl 2p core-level XPS spectra of the perovskite films showing the characteristic doublet peaks of Cl 2p 3/2 and Cl 2p 1/2.

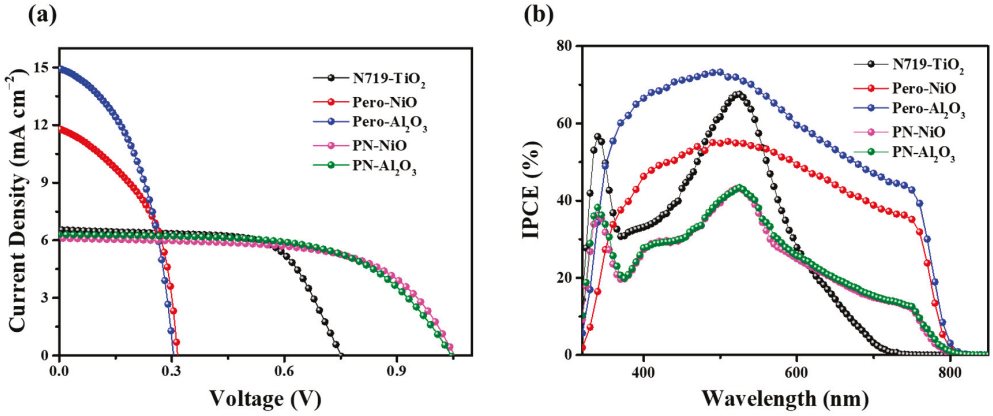


Figure 5. (**a**) Current–voltage characteristics and (**b**) incident photon-to-current conversion efficiency spectra of the $CH_3NH_3PbI_{3-x}Cl_x$/NiO-based p device (red), $CH_3NH_3PbI_{3-x}Cl_x$/NiO-based p device (blue), N719/TiO_2-based n device (black), the tandem pn device based on NiO (pink), and the tandem pn device based on NiO (green). A simulated AM1.5 light (100 mW cm^{-2}) was employed to illuminate from the photoanode side.

Table 2. Photovoltaic parameters for the pn-tandem solar cells as well as p-type solar cell and n-type DSSC.

Solar Cell Structure	V_{oc} (mv)	J_{sc} (mA cm^{-2})	*FF*	*PCE* (%)
p-type (NiO) solar cell	315	11.80	0.48	1.78
p-type (Al_2O_3) solar cell	304	14.95	0.46	2.09
n-type DSC	751	6.55	0.66	3.24
pn tandem solar cell (NiO)	1060	6.11	0.62	4.02
pn tandem solar cell (Al_2O_3)	1046	6.30	0.60	3.97

Tandem solar cells based on mesoporous Al_2O_3 and mesoporous NiO were fabricated, building upon the design principles of single-junction solar cells. Figure 5a shows the current voltage characteristics of a tandem cell illuminated through the photoanode. The resultant photovoltaic parameters are listed in Table 1. As clearly seen, the short-circuit current density (J_{sc} = 6.11 mA cm^{-2}) of the tandem cell based on mesoporous NiO nearly equals half of the p-type solar cell (J_{sc} = 14.95 mA cm^{-2}); the open-circuit voltage (V_{oc} = 1060 mV) nearly equals the sum of that of the n-type dye-sensitized half cell (751 mV) and p-type perovskite-sensitized half cell (315 mV); and the fill factor (FF = 0.62) is between that of the two half cells. The efficiency of the tandem cell (PCE = 4.02%) outperforms both of the half cells (3.24% for the n-type half cell and 1.78% for the p-type half cell). Although

https://doi.org/10.3390/mi17010099

the efficiency of the dye- and perovskite-based p–n tandem sensitized solar cells exceeds that of purely dye-sensitized p–n tandem solar cells, their performance still significantly lags behind that of solid-state perovskite tandem solar cells. The primary reason is that the liquid electrolyte is inefficient in extracting and transporting charge carriers. Moreover, the solvent in the liquid electrolyte can degrade the perovskite structure.

The stacked solar cells based on Al_2O_3 exhibit the same pattern, but the difference is that the open-circuit voltage of the Al_2O_3 stacked solar cells is lower than that of the NiO stacked solar cells, while the short-circuit current density is higher than that of the NiO-based stacked solar cells. The main reason for this is the parasitic light.

The incident photon-to-electron conversion efficiencies (IPCEs) of the devices were measured as shown in Figure 5b. The dye-sensitized solar cells exhibit two distinct absorption peaks at 340 nm and 532 nm, characteristic of the N719 dye. In contrast, perovskite-sensitized Al_2O_3 and NiO films show broad and intense absorption across the entire spectral range from 320 to 780 nm. Notably, the absorption intensity of the perovskite-sensitized Al_2O_3 device is higher than that of its NiO counterpart, suggesting a greater short-circuit current density, which is consistent with the current–voltage (J–V) measurements. For the tandem solar cells based on Al_2O_3 and NiO, respectively, their comparable absorption intensities indicate similar short-circuit current densities.

The stability of tandem solar cells based on NiO and Al_2O_3 was systematically investigated. The fabricated devices were stored in a closed container at room temperature (25 ± 5 °C) and humidity (RH 25% ± 5%) and monitored periodically, with performance measurements conducted approximately every 7 h. Both devices exhibited a slight increase in performance during the initial 40 h, followed by a rapid decline thereafter, as illustrated in Figure 6. By 100 h, the device performance had degraded to nearly zero. This pronounced degradation is primarily attributed to the use of polar organic solvents for electrolyte dissolution in this device architecture, which can readily interact with and destabilize the perovskite layer, leading to severe material decomposition and consequent performance loss.

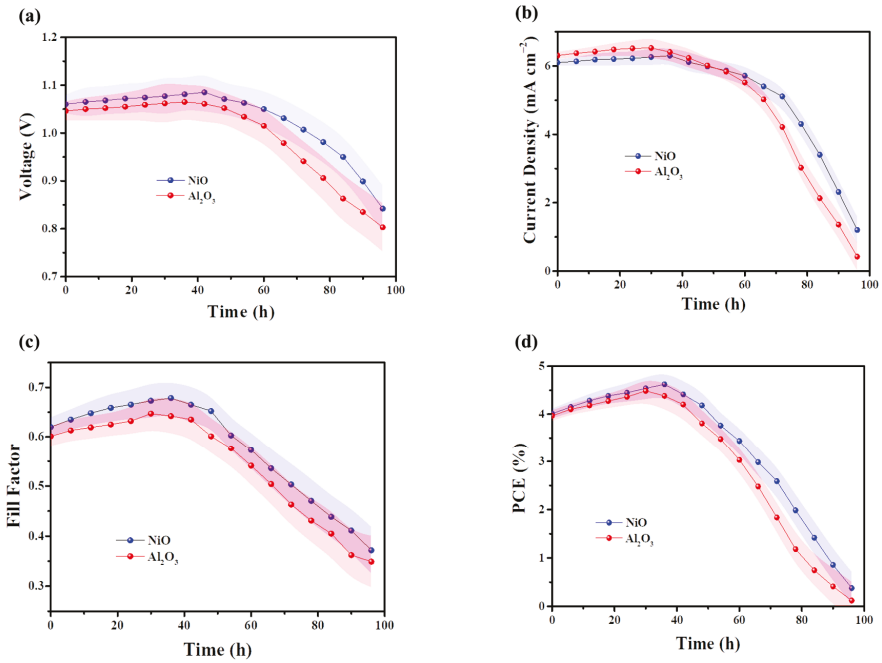


Figure 6. The stability of PN tandem solar cells based on NiO and Al_2O_3. (**a**) Voc, (**b**) Jsc, (**c**) Fill Factor, and (**d**) PCE. All of the fabricated devices were stored in a closed container at room temperature (25 ± 5 °C) and humidity (RH 25% ± 5%) and monitored periodically, with performance measurements conducted approximately every 7 h.

https://doi.org/10.3390/mi17010099

4. Conclusions

In conclusion, we have for the first time demonstrated a novel double junction solar cell by using dye-sensitized porous TiO_2 films as the photoanode and organometal halide perovskite ($CH_3NH_3PbI_{3-x}Cl_x$)-sensitized porous NiO films as the photocathode. The double junction cell achieved a photocurrent of 6.11 mA cm^{-2}, a photovoltage of 1060 mV, and a record efficiency of 4.02% at 1 sun light intensity. The utilization of a perovskite-sensitized p-type semiconductor layer as an alternative to noble Pt shows great potential to convert conventional single-junction solar cells into more efficient double junction solar ones with minor changes. Compared to organic dyes, perovskite materials are cost-effective, easy to prepare, and time-efficient. Moreover, they exhibit a high extinction coefficient, bipolar charge transport characteristics, and a broad absorption spectrum. When employed as sensitizers in pn tandem-sensitized solar cells, perovskites have the potential to exceed previously reported efficiency records, including improvements in the V_{oc}, J_{sc}, and FF parameters. Therefore, this work opens a new path of research on highly efficient tandem-sensitized solar cells for the future.

Author Contributions: Conceptualization, H.W.; methodology, H.W. and X.M.; validation, X.M.; investigation, H.W.; data curation, H.W. and W.T.; writing—original draft, H.W., W.T. and X.M.; writing—review & editing, H.W. and M.L.; funding acquisition, H.W. All authors have read and agreed to the published version of the manuscript.

Funding: This research was funded by the Central Universities (JZ2021HGQA0191), Anhui Natural Science Foundation (2408085QE147), and Transversal Corporate Fundation (W2025JSKF1361). And The APC was funded by Transversal Corporate Fundation (W2025JSKF1361).

Institutional Review Board Statement: Not applicable.

Informed Consent Statement: Not applicable.

Data Availability Statement: The original contributions presented in this study are included in the article. Further inquiries can be directed to the corresponding authors.

Conflicts of Interest: The authors declare no conflicts of interest.

References

1. Zhou, H.; Aftabuzzaman, M.; Masud; Kang, S.H. Key Materials and Fabrication Strategies for High-Performance Dye-Sensitized Solar Cells: Comprehensive Comparison and Perspective. *ACS Energy Lett.* **2025**, *10*, 881–895. [CrossRef]
2. Badawy, S.A.; Abdel-Latif, E.; Elmorsy, M.R. Tandem dye-sensitized solar cells achieve 12.89% efficiency using novel organic sensitizers. *Sci. Rep.* **2024**, *14*, 26072. [CrossRef]
3. Wu, W.; Li, Y.; Zhang, J.; Guo, X.; Wang, L.; Ågren, H. Theoretical modelling of metal-based and metal-free dye sensitizers for efficient dye-sensitized solar cells: A review. *Solar Energy* **2024**, *277*, 112748. [CrossRef]
4. McEvoy, A.J.; Nazeeruddin, M.K.; Rothenberger, G.; Grätzel, M. Development Status of Dye-Sensitized Nanocrystalline Photovoltaic Devices. *Electrochem. Electoch. Soc. Proc.* **2001**, *10*, 69–70.
5. Zhang, S.; Huang, F.; Guo, X.; Xiong, Y.; Huang, Y.; Ågren, H.; Wang, L.; Zhang, J. Boosting the Efficiency of Dye-Sensitized Solar Cells by a Multifunctional Composite Photoanode to 14.13%. *Angew. Chem. Int. Ed.* **2023**, *135*, e202302753. [CrossRef]
6. Masud; Kim, H.K. Redox Shuttle-Based Electrolytes for Dye-Sensitized Solar Cells: Comprehensive Guidance, Recent Progress, and Future Perspective. *Acs Omega* **2023**, *8*, 6139–6163. [CrossRef]
7. Yadav, I.S.; Misra, R. Design, synthesis and functionalization of BODIPY dyes: Applications in dye-sensitized solar cells (DSSCs) and photodynamic therapy (PDT). *J. Mater. Chem. C* **2023**, *11*, 8688–8723. [CrossRef]
8. Zhang, Y.; Higashino, T.; Imahori, H. Molecular designs, synthetic strategies, and properties for porphyrins as sensitizers in dye-sensitized solar cells. *J. Mater. Chem. A* **2023**, *11*, 12659. [CrossRef]
9. Sayah, D.; Ghaddar, T.H. Copper-Based Aqueous Dye-Sensitized Solar Cell: Seeking a Sustainable and Long-Term Stable Device. *ACS Sustain. Chem. Eng.* **2024**, *12*, 6424. [CrossRef]
10. Qian, J.; Jiang, K.-J.; Huang, J.-H.; Liu, Q.-S.; Yang, L.-M.; Song, Y. A Selenium-Based Cathode for a High-Voltage Tandem Photoelectrochemical Solar Cell. *Angew. Chem. Int. Ed.* **2012**, *51*, 10351–10354. [CrossRef]

https://doi.org/10.3390/mi17010099

11. Shalom, M.; Hod, I.; Tachan, Z.; Buhbut, S.; Tirosh, S.; Zaban, A. Quantum dot based anode and cathode for high voltage tandem photo-electrochemical solar cell. *Energy Environ. Sci.* **2011**, *4*, 1874–1878. [CrossRef]
12. Dai, P.-C.; Zhang, G.; Chen, Y.-C.; Jiang, H.-C.; Feng, Z.-Y.; Lin, Z.-J.; Zhan, J.-H. Porous copper zinc tin sulfide thin film as photocathode for double junction photoelectrochemical solar cells. *Chem. Commun.* **2012**, *48*, 3006–3008. [CrossRef]
13. Ge, F.; Xu, F.; Gong, K.; Liu, D.; Li, W.; Wang, L.; Zhou, X. Sensitizers designed toward efficient intramolecular charge separation for p-type dye-sensitized solar cells. Dyes and Pigments. *Dye. Pigment.* **2022**, *200*, 110127. [CrossRef]
14. Raut, P.; Kishnani, V.; Mondal, K.; Gupta, A.; Jana, S.C. A Review on Gel Polymer Electrolytes for Dye-Sensitized Solar Cells. *Micromachines* **2022**, *13*, 680. [CrossRef] [PubMed]
15. Kinoshita, T.; Fujisawa, J.; Nakazaki, J.; Uchida, S.; Kubo, T.; Segawa, H. Enhancement of Near-IR Photoelectric Conversion in Dye-Sensitized Solar Cells Using an Osmium Sensitizer with Strong Spin-Forbidden Transition. *J. Phys. Chem. Lett.* **2012**, *3*, 394–398. [CrossRef]
16. Murayama, M.; Mori, T. Dye-sensitized solar cell using novel tandem cell structure. *J. Phys. D Appl. Phys.* **2007**, *40*, 1664–1668. [CrossRef]
17. Powar, S.; Daeneke, T.; Ma, M.T.; Fu, D.; Duffy, N.W.; Gçtz, G.; Weidelener, M.; Mishra, A.; Bäuerle, P.; Spiccia, L.; et al. Highly Efficient p-Type Dye-Sensitized Solar Cells based on Tris(1,2-diaminoethane)Cobalt(II)/(III) Electrolytes. *Angew. Chem. Int. Ed.* **2013**, *52*, 602–605. [CrossRef]
18. Nattestad, A.; Mozer, A.J.; Fischer, M.K.; Cheng, Y.B.; Mishra, A.; Bauerle, P.; Bach, U. Highly efficient photocathodes for dye-sensitized tandem solar cells. *Nat. Mater.* **2010**, *9*, 31–35. [CrossRef]
19. Perera, I.R.; Daeneke, T.; Makuta, S.; Yu, Z.; Tachibana, Y.; Mishra, A.; Bäuerle, P.; Ohlin, C.; Bach, U. Application of the Tris(acetylacetonato)iron(III)/(II) Redox Couple in p-Type Dye-Sensitized Solar Cells. *Angew. Chem. Int. Ed.* **2015**, *54*, 3758–3762. [CrossRef]
20. Liu, S.; Li, J.; Xiao, W.; Chen, R.; Sun, Z.; Zhang, Y.; Lei, X.; Hu, S.; Kober-Czerny, M.; Wang, J.; et al. Buried interface molecular hybrid for inverted perovskite solar cells. *Nature* **2024**, *632*, 536–542. [CrossRef]
21. Tan, Q.; Li, Z.; Luo, G.; Zhang, X.; Che, B.; Chen, G.; Gao, H.; He, D.; Ma, G.; Wang, J.; et al. Inverted perovskite solar cells using dimethylacridine-based dopants. *Nature* **2023**, *620*, 545–551. [CrossRef]
22. Cao, Q.; Wang, T.; Pu, X.; He, X.; Xiao, M.; Chen, H.; Zhuang, L.; Wei, Q.; Loi, H.L.; Guo, P.; et al. Co-Self-Assembled Monolayers Modified NiOx for Stable Inverted Perovskite Solar Cells. *Adv. Mater.* **2024**, *36*, 2311970. [CrossRef]
23. Qu, G.; Cai, S.; Qiao, Y.; Wang, D.; Gong, S.; Khan, D.; Wang, Y.; Jiang, K.; Chen, Q.; Zhang, L.; et al. Conjugated linker-boosted self-assembled monolayer molecule for inverted solar cells. *Joule* **2024**, *8*, 1–12. [CrossRef]
24. Wang, H.; Zeng, X.W.; Huang, Z.F.; Zhang, W.J.; Qiao, X.F.; Hu, B.; Zou, X.P.; Wang, M.K.; Cheng, Y.-B.; Chen, W. Boosting the photocurrent density of p-type solar cells based on organometal halide perovskite-sensitized mesoporous NiO photocathodes. *Appl. Mater. Interfaces* **2014**, *6*, 12609. [CrossRef] [PubMed]
25. He, J.; Lindström, H.; Hagfeldt, A.; Lindquist, S.-E. Dye-sensitized nanostructured tandem cell-first demonstrated cell with a dye-sensitized photocathode. *Sol. Energy Mater. Sol. Cells* **2000**, *62*, 265–273. [CrossRef]
26. Nakasa, A.; Usami, H.; Sumikura, S.; Hasegawa, S.; Koyama, T.; Suzuki, E. A High Voltage Dye-sensitized Solar Cell using a Nanoporous NiO Photocathode. *Chem. Lett.* **2005**, *34*, 500–501. [CrossRef]
27. Gibson, E.A.; Smeigh, A.L.; Pleux, L.L.; Fortage, J.; Boschloo, G.; Blart, E.; Pellegrin, Y.; Odobel, F.; Hagfeldt, A.; Hammarström, L. A p-Type NiO-Based Dye-Sensitized Solar Cell with an Open-Circuit Voltage of 0.35 V. *Angew. Chem. Int. Ed.* **2009**, *121*, 4466–4469. [CrossRef]
28. Chen, J.; Xiong, Y.; Rong, Y.; Mei, A.; Sheng, Y.; Jiang, P.; Hu, Y.; Li, X.; Han, H. Solvent effect on the hole-conductor-free fully printable perovskite solar cells. *Nano Energy* **2016**, *27*, 130–137. [CrossRef]

Disclaimer/Publisher's Note: The statements, opinions and data contained in all publications are solely those of the individual author(s) and contributor(s) and not of MDPI and/or the editor(s). MDPI and/or the editor(s) disclaim responsibility for any injury to people or property resulting from any ideas, methods, instructions or products referred to in the content.

https://doi.org/10.3390/mi17010099

micromachines

MDPI

Article

O-Band 4 × 1 Combiner Based on Silicon MMI Cascaded Tree Configuration

Saveli Shaul Smolanski and Dror Malka *

Faculty of Engineering, Holon Institute of Technology (HIT), Holon 5810201, Israel
* Correspondence: drorm@hit.ac.il; Tel.: +972-3-502-6648

Abstract

High-speed silicon (Si) photonic transmitters operating in the O-band require higher on-chip optical power to support advanced modulation formats and ever-increasing line rates. A straightforward approach is to operate laser diodes at higher output power or employ more specialized sources, but this raises cost and exacerbates nonlinear effects such as self-phase modulation, two-photon absorption, and free-carrier generation in high-index-contrast Si waveguides. This paper proposes a low-cost 4 × 1 tree-cascade multimode interference (MMI) power combiner on a Si-on-insulator platform at 1310 nm wavelength that enables coherent power scaling while remaining fully compatible with standard commercial O-band lasers. The device employs adiabatic tapers and low-loss S-bends to ensure uniform field evolution, suppress local field enhancement, and mitigate nonlinear phase accumulation. The optimized layout occupies a compact footprint of 12 μm × 772 μm and achieves a simulated normalized power transmission of 0.975 with an insertion loss of 0.1 dB. Spectral analysis shows a 3 dB bandwidth of 15.8 nm around 1310 nm, across the O-band operating window. Thermal analysis shows that wavelength drift associated with ±50 °C temperature variation remains within the device bandwidth, ensuring stable operation under realistic laser self-heating and environmental changes. Owing to its broadband response, fabrication tolerance, and compatibility with off-the-shelf laser diodes, the proposed combiner is a promising building block for O-band transmitters and photonic neural-network architectures based on cascaded splitter and combiner meshes, while preserving linear transmission and enabling dense, large-scale photonic integration.

Keywords: multimode interference; optical power combiner; beam propagation method; O-band

1. Introduction

Optical power combiners are fundamental components in modern photonic integrated circuits, enabling compact, low-loss signal routing and power distribution for data communication and sensing systems [1–5]. In short-reach optical interconnects, particularly in the O-band around 1310 nm, the continuous drive toward higher line rates (800 Gb/s, 1.6 Tb/s, and beyond) has intensified the need for highly efficient on-chip power-combining schemes [6–8]. In such transmitters, modulators, passive routing, filtering elements, and packaging interfaces introduce several decibels of optical loss, thereby significantly tightening the link budget. As a result, higher optical power is required at the transmitter output than can typically be delivered by a single commercial O-band laser operated at standard drive conditions, which motivates the development of on-chip power-scaling techniques.

A straightforward approach is to drive laser diodes at higher output power or to employ specialized higher-power laser modules. However, these solutions increase system cost and reduce energy efficiency, and they may also exacerbate nonlinear effects such as self-phase modulation, two-photon absorption, and free-carrier generation in high-index-contrast silicon (Si) waveguides [9,10]. Under such conditions, these nonlinearities can degrade signal integrity and limit the linear dynamic range of advanced modulation formats. An alternative strategy is to coherently or quasi-coherently combine multiple moderate-power channels from standard commercial lasers using low-loss on-chip power combiners, thereby increasing the available optical power while preserving linearity and cost-effectiveness.

Among various combining mechanisms, multimode interference (MMI) couplers have emerged as reliable and fabrication-tolerant solutions due to their self-imaging property, simple geometry, and broadband operation [11,12]. MMI theory enables precise control of optical field replication inside a multimode region, supporting a wide range of power-splitting and power-combining configurations [13–15]. Continued development of MMI-based devices has led to implementations based on conventional Si waveguides, slot-waveguide structures, and hybrid material platforms [16–19]. These designs demonstrate stable performance, improved polarization tolerance, and enhanced modal control, thereby establishing MMIs as versatile building blocks for integrated photonics.

Material platforms play a critical role in determining the optical and thermal performance of MMI devices. Si, Si-nitride, Si-gallium nitride, and alumina have each been explored for wavelength-division multiplexing and power-combining applications, owing in particular to their low absorption in the O-band spectral range [20,21]. Slot-waveguide configurations, in which the optical field is strongly confined in a low-index region, can further enhance power efficiency and reduce device footprint [22]. Fabrication-tolerant layouts and hybrid dielectric structures improve the achievable insertion loss and bandwidth uniformity across the O-band [23–25]. Nevertheless, for multi-input combiners on high-index-contrast Si platforms, the strong field confinement that enables compactness may increase sensitivity to sidewall roughness, wavelength variation, and nonlinear effects at elevated optical intensities [26,27].

To alleviate these limitations, recent works have proposed cascaded and multi-stage MMI layouts, often based on slot-waveguide geometries, to distribute interference more evenly and suppress parasitic reflections [28]. Although slot-waveguide MMIs can offer strong field confinement, they typically require tighter lithographic control and more complex process steps. In contrast, the present work employs a buried Si waveguide MMI realized on a Si-on-insulator (SOI) platform, which is fully compatible with conventional complementary-metal-oxide-semiconductor (CMOS) fabrication flows and thereby simplifies practical implementation. The proposed tree-cascade 4×1 MMI power combiner is designed and numerically optimized for O-band operation, targeting low insertion loss, broad spectral robustness, and high fabrication tolerance.

By combining four moderate-power inputs from commercial O-band laser sources, the proposed architecture increases the available on-chip optical power without resorting to expensive high-power laser modules and may help reduce nonlinear penalties in the combining region. The design targets low insertion loss, broad spectral stability with a 3 dB bandwidth of 15.8 nm, and high fabrication and thermal tolerance, thereby providing a suitable solution for next-generation high-speed O-band transmitters. In addition, the compact 4×1 combiner can serve as a fundamental building block in photonic neural-network architectures that rely on cascaded networks of splitters, combiners, and active amplifying or weighting elements for implementing tunable synaptic weights and large-scale matrix operations [29].

https://doi.org/10.3390/mi17010031

2. Structural Design and Theoretical Analysis

The proposed 4 × 1 power combiner is implemented on a SOI platform, which provides high refractive-index contrast and enables strong optical confinement throughout the device. This material configuration supports compact routing and efficient control of modal evolution. Figure 1a illustrates the x-y cross-section of the proposed combiner. In this configuration, the high-index regions (shown in green) correspond to Si (n = 3.48) formed on a 220 nm-thick SOI platform marked as T_{Si}. The surrounding cladding (shown in white) is silicon dioxide (SiO_2) with a refractive index of 1.44.

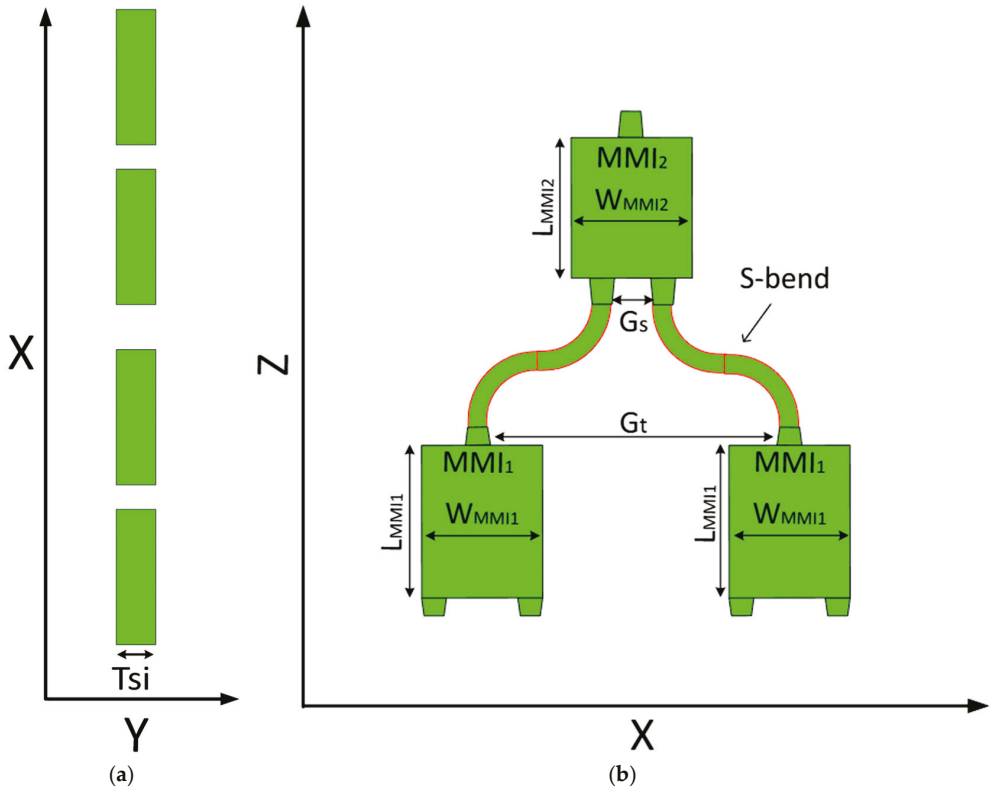


Figure 1. (**a**) Top-view (x–y) cross-section of the four Si input waveguides, embedded in a SiO_2 cladding. (**b**) Side-view (x–z) schematic of the tree-cascade MMI structure, including the tapered inputs, S-bend connections, and upper combining stage.

Figure 1b presents the x-z plane cross-section at Y = 0, showing the four input tapers, the two MMI_1 couplers, an output taper following each MMI_1, the pair of S-bend waveguides connecting MMI_1 to MMI_2, the two input tapers leading into MMI_2, the MMI_2 coupler, and the output taper. The input tapers in MMI_1 extend over an L_{taper} of 15 μm, and gradually expand from 0.5 μm to 0.8 μm, while the output transition has the same length and contracts from 0.8 μm back to 0.5 μm. A second taper length marked as L_{taper2} of 22.5 μm is also implemented with the same width transition for improved mode matching in the upper combining stage. The gap (G_t) between the output tapers of each MMI_1 is 7.2 μm.

Both MMI_1 constitute the first combining stage, merging the four input channels into two intermediate paths. These two paths are routed upward using S-bend waveguides with their widths matched to the 0.5 μm taper output. The S-bend length is 242.5 μm, while having an offset of 2.6 μm, and the center-to-center spacing (G_s) at the S-bend outputs is set to be 2 μm.

Finally, MMI_2 performs the final combining step, producing a single output channel at the top of the device. The overall device length is 772 μm.

https://doi.org/10.3390/mi17010031

The operation principle of the MMI device relies on the self-imaging effect, in which the input optical field is periodically reproduced along the propagation axis of the multimode region. The key parameters governing this effect are the effective width, beat length, and MMI length, given by the following equations:

The beat length of the MMI combiner is expressed as [30]:

$$L_\pi = \frac{4n_{eff}{W_e}^2}{3\lambda}, \tag{1}$$

where the operating wavelength is denoted by λ, the effective refractive index of the guided mode is represented by n_{eff}, and the effective width of the multimode interference region is denoted by W_e.

The effective width depends both on the physical width and the polarization state. For TE polarization, it is defined as [30]:

$$W_e = W_{MMI} + \frac{\lambda}{\pi}\left(\frac{n_{clad}}{\sqrt{{n_{eff}}^2 - {n_{clad}}^2}}\right), \tag{2}$$

where n_{clad} is the refractive index of the silica cladding.

The length of the MMI region that supports self-imaging is then given by [30]:

$$\mathrm{L_{MMI}} = \frac{3\mathrm{pL_\pi}}{4\mathrm{N}}, \tag{3}$$

where p is a positive integer, and N is the number of input sources. In this work, N = 2 for each individual MMI and p = 1 were selected to obtain a compact device length.

The optical bandwidth and fabrication tolerance of MMI couplers are known to depend strongly on these geometrical parameters, as small width or length variations can significantly alter the self-imaging condition.

The insertion loss (IL) of the combiner is described by:

$$\mathrm{IL[dB]} = -10\log_{10}\left(\frac{\mathrm{Pout}}{\mathrm{N\ Pin}}\right), \tag{4}$$

where $\mathrm{P_{out}}$ is the output optical power, and $\mathrm{P_{in}}$ is the power of a single input source (thus $\mathrm{N\ P_{in}}$ represents the total launched power for equal-amplitude inputs).

For simulation purposes, a multi-input excitation (N = 4) was applied in the beam propagation method (BPM) using its multi-objective optimization tool (MOST) analyses, while the full device operates as a 4×1 combiner under coherent illumination.

In addition to the parameters defining the MMI region, the performance of the combiner strongly depends on the geometry of the tapered transitions and S-bend sections. To reduce bending-related losses, the geometry of the S-bend sections was selected with particular care. Prior studies indicate that an offset of 5 μm is a suitable choice for Si waveguides [31]. For a given offset O and S-bend length L, the corresponding bend radius R can be obtained from the geometric relationship:

$$\mathrm{R} = \frac{\mathrm{L}^2 + \mathrm{O}^2}{4\mathrm{O}}, \tag{5}$$

In our design, substituting L and O into Equation (5) yields a bend radius of 5.65 mm. This relatively large radius is well above the typical minimum bend radius used in SOI waveguides and thus keeps bend-induced radiation loss in the S-bend sections negligible.

https://doi.org/10.3390/mi17010031

Unlike conventional MMI combiners, where inputs are symmetrically aligned, the proposed layout routes signals through curved geometries to support multi-layer interconnectivity. The tree-cascade MMI configuration further enhances robustness by enabling gradual mode evolution and reducing sensitivity to fabrication errors. These design features allow the combiner to serve as a high-efficiency component suitable for scalable photonic integration.

The analytical self-imaging relations provide an initial estimate for the MMI length under idealized assumptions. Because the proposed SOI layout includes access tapers and routing sections that affect the modal excitation and effective propagation constants, the final MMI dimensions were determined by full-device BPM optimization.

3. Simulation Results

Comprehensive numerical simulations were carried out using the BPM module in RSoft CAD (v2024.09) to validate the optical performance of the proposed 4 × 1 MMI power combiner. The analysis considers both the modal characteristics and the field propagation along the entire device, including the S-bend transitions, tapered input sections, and the tree-cascade MMI regions. The key design parameters, namely the S-bend geometry, MMI width, and MMI length, were systematically varied in order to maximize transmission efficiency and minimize IL over the O-band. The results presented in this section include the geometrical optimization of the MMI regions, optical field propagation maps, and the spectral response of the combiner.

To accurately model light propagation within the structure, the fundamental guided mode of the input buried Si waveguide was obtained using the Mode Solver in RSoft. The input waveguide consists of a Si core with dimensions of 500 nm (width) × 220 nm (thickness), embedded in a SiO_2 cladding. Figure 2a shows the transverse electric (TE) field component (E_x) of the fundamental TE_0 mode for the Si core, with an effective refractive index of 2.73. It can be seen that strong optical confinement is achieved within the Si core, with the field exhibiting evanescent decay into the surrounding cladding. This field distribution represents the steady-state modal solution of the Si core buried waveguide. The mode was normalized to unit power and exported as a field file for use as the input excitation in the subsequent BPM simulations. Figure 2b presents the optimization and tolerance analysis of the input Si waveguide as a function of width and silicon thickness. The optimal dimensions are 500 nm × 220 nm, where the normalized power reaches its maximum value. A robust tolerance window is observed around this point, where simultaneous deviations of approximately ±20 nm in both width and thickness maintain >90% of the normalized power. This indicates that the proposed design is relatively tolerant to realistic fabrication variations.

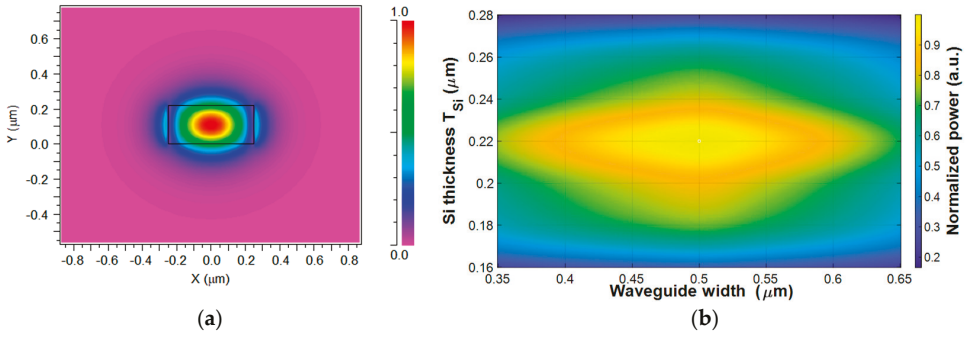


Figure 2. (**a**) Simulated fundamental mode profile in the Si core (x–y plane) for the nominal input waveguide geometry (500 nm × 220 nm). (**b**) Two-dimensional tolerance map of the normalized combined output power as a function of input waveguide width and T_{Si} around the nominal design point.

https://doi.org/10.3390/mi17010031

Figure 3a shows the transverse electric field distribution (E_x) of the fundamental TE_0 mode across the four input Si taper waveguides. The simulation exhibits four well-confined field regions, each localized within its corresponding Si core. The effective refractive index of the guided mode is calculated to be 2.73, thereby confirming single-mode operation in each input waveguide for the selected geometrical and material parameters. The strong light confinement within each Si core, together with the negligible field overlap between adjacent channels, indicates that inter-channel coupling and crosstalk at the input section are minimal. To further illustrate the mode uniformity, Figure 3b presents a one-dimensional line profile extracted along the central horizontal axis (Y = 0) of the same field map. The profile exhibits four distinct and symmetric intensity peaks associated with the four input waveguides. Each peak reaches a normalized amplitude close to 1, whereas the regions between neighboring peaks drop nearly to 0, forming two pairs of peaks separated by a low-intensity valley. This symmetry in the intensity distribution verifies that all four input channels are well balanced in optical power and that the simulated field distribution is spatially periodic and uniform across the input array.

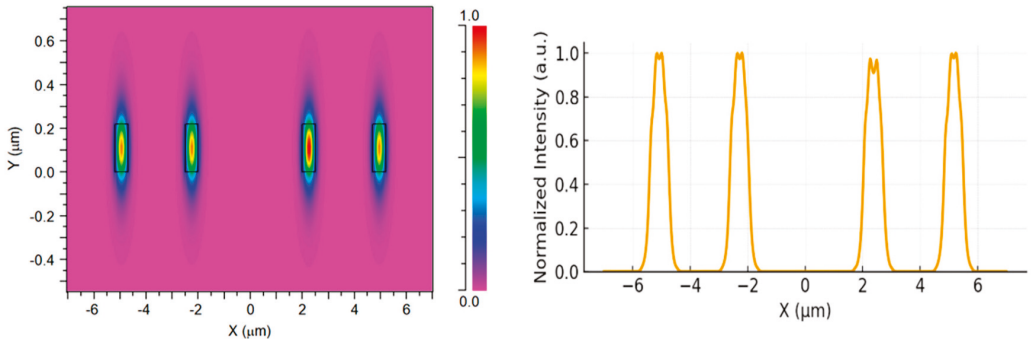


Figure 3. (**a**) TE_0 field distribution (x–y plane) of the four Si input taper waveguides at 1310 nm wavelength. (**b**) E_x intensity profile along the x-axis (Y = 0).

The balanced modal intensity is crucial for maintaining equal optical weighting when the fields propagate into the MMI region. Such uniform inputs guarantee that constructive and destructive interference in the MMI section will occur predictably, thereby ensuring high-efficiency optical power combination and minimal phase imbalance at the output.

To achieve high-efficiency optical power combining, the lengths and widths of both MMI sections were optimized using a parametric sweep with the MOST module in RSoft. The optimization was performed with BPM by launching the simulated fundamental TE mode at the inputs and modeling the complete cascaded structure (including access tapers and interconnecting S-bends). Therefore, the reported optimal MMI lengths correspond to the integrated device performance, rather than to an isolated, idealized slab-MMI estimate. The discrepancy from the analytical self-imaging length is expected because the analytical model relies on simplified assumptions (e.g., uniform multimode region and ideal excitation) and does not fully capture modal dispersion, effective-index variations, and transition-induced changes in modal excitation in high-index-contrast SOI implementations. The optimization process aimed to identify the structural dimensions that provide maximum output power and minimal IL within the O-band.

Figure 4a presents the normalized output power as a function of W_{MMI1}. The curve reaches its optimized value at 9 μm, where constructive interference between the guided modes is strongest. Importantly, the output remains above 80% of the peak across a tolerance window of ±0.15 μm, showing that the selected value lies at the center of a robust, fabrication-tolerant region.

https://doi.org/10.3390/mi17010031

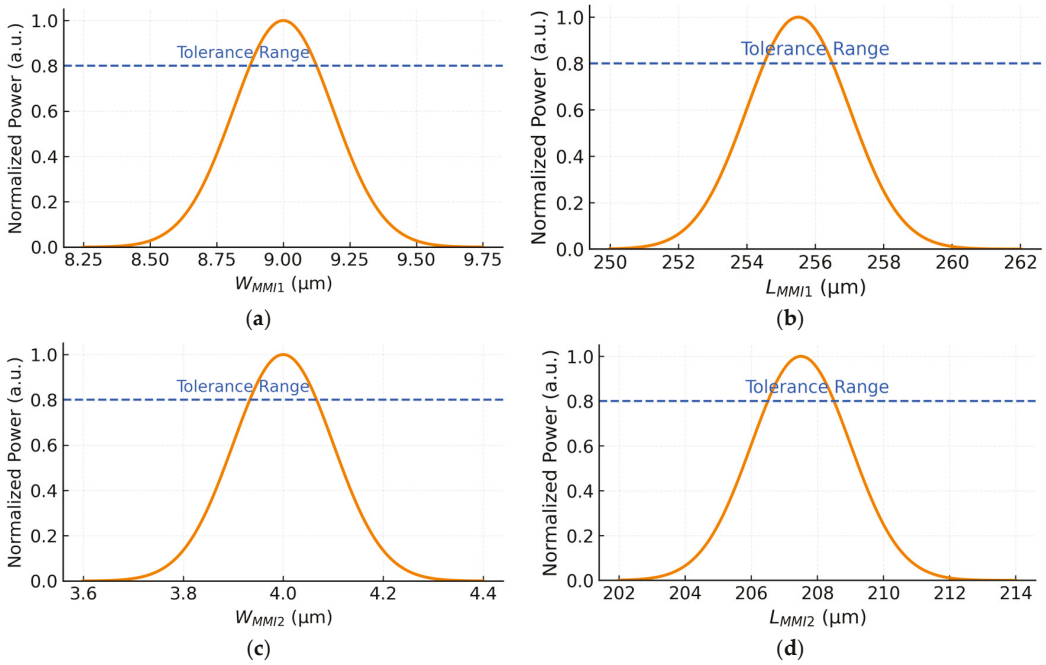


Figure 4. Normalized output power as a function of the MMI geometrical parameters. (**a**) W_{MMI1}. (**b**) L_{MMI1}. (**c**) W_{MMI2}. (**d**) L_{MMI2}.

Similarly, Figure 4b shows the length optimization of L_{MMI1}, with a simulated optimum of 255.5 μm. Using the analytical expressions for effective width (Equation (2)) and beat length (Equation (1)), MMI_1 yields an effective width of 9.25 μm, a beat length of 237.74 μm, and a calculated self-imaging length of roughly 267.45 μm from Equation (3). The difference between these analytical predictions and the simulated optimum follows the expected trend for SOI MMIs, where BPM optimization refines the idealized self-imaging estimate. The device maintains high performance within a tolerance of roughly ±6 μm, confirming that the chosen simulated length is stable under standard lithographic variations.

The MMI_2 stage, responsible for further field consolidation, was optimized in the same manner. As shown in Figure 4c, W_{MMI2} exhibits maximum transmission at 4 μm, with a tolerance band of ±0.1 μm. Despite its smaller geometry, the optimal point lies well inside the allowable tolerance range, preserving strong modal overlap and low IL.

Lastly, Figure 4d illustrates the optimization of L_{MMI2}. The optimal performance is obtained at 207.5 μm, again with a tolerance of ±6 μm. For reference, the analytical expressions for effective width and beat length (Equations (1) and (2)) yield an effective width of 4.25 μm and a beat length near 50.18 μm for this stage, and the corresponding self-imaging estimate from Equation (3) gives a calculated length of roughly 18.81 μm. As expected, these closed-form values differ from the BPM-optimized result, which accounts for full vectorial field evolution and taper-induced modal reshaping. The selected simulated value, therefore, ensures proper self-imaging and stable performance across typical dimensional variations, enabling reliable two-to-one combining into the output waveguide.

Overall, these results confirm that both MMI sections exhibit stable optical behavior over moderate fabrication variations. Maintaining normalized power above 0.8 across the tolerance ranges demonstrates that the device is highly robust and manufacturing-friendly for integration within photonic systems.

To support low-loss routing between the lower and upper combining stages, the interconnecting waveguides were implemented using smooth S-bend transitions. Their geometry was evaluated using the MOST optimization tool, and the resulting normalized transmission is presented in Figure 5. The simulated trend follows the expected behavior. Very short bends suffer from increased radiation loss, and as the length increases, the

https://doi.org/10.3390/mi17010031

transmission rises, reaching a maximum at an S-bend length of 242.5 μm. For longer bends, the transmitted power gradually decreases due to additional propagation loss. From this figure, the normalized power remains above 0.9 for S-bend lengths between approximately 200 μm and 280 μm, corresponding to a tolerance of about ±40 μm around the optimum value. This wide tolerance window indicates that the S-bend is highly robust to dimensional variations and can be reliably fabricated using standard CMOS-compatible processes.

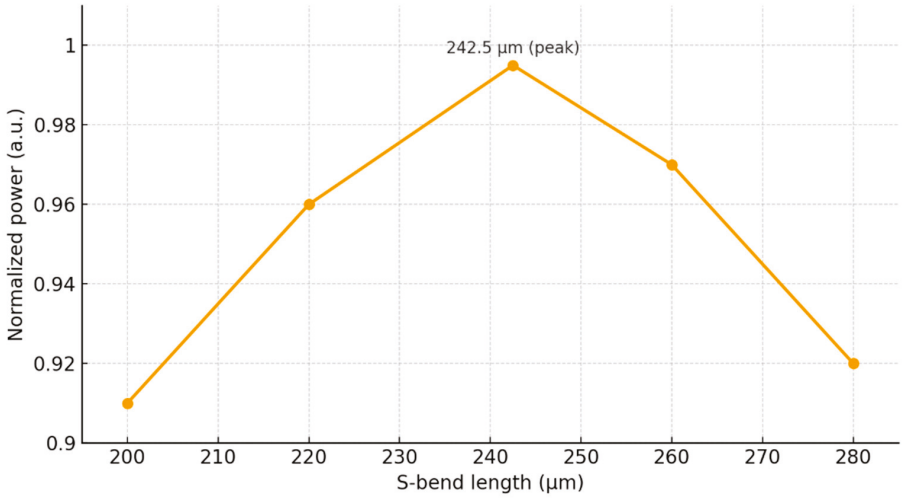


Figure 5. Normalized output power versus S-bend length.

Figure 6 shows the simulated optical field evolution in the designed 4 × 1 power combiner at 1310 nm under simultaneous excitation of all four input ports with equal amplitudes and in-phase operation (zero relative phase difference). The field evolution confirms stable confinement within the Si core across both MMI stages and along the interconnecting S-bend transitions. The optical energy follows the intended combining path without noticeable radiation into the silica cladding, indicating that the chosen geometry supports low-loss propagation. The output region exhibits the expected interference pattern associated with the final combining stage, with a well-defined mode emerging at the device exit. Overall, the field distribution demonstrates that the device maintains high transmission and robust modal behavior across the full 772 μm propagation length.

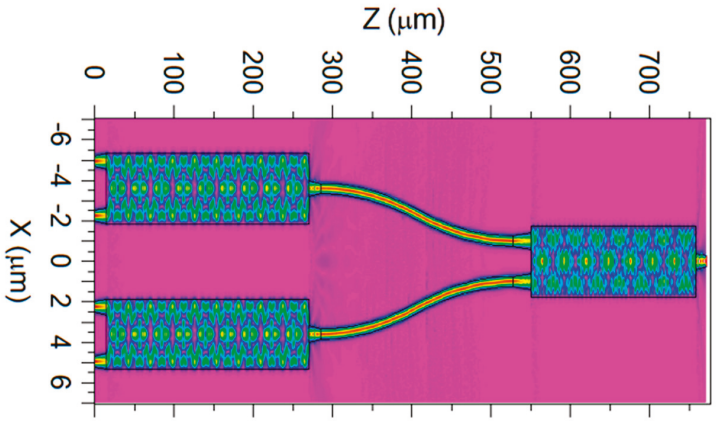


Figure 6. Simulated field propagation (x–z plane) of the optimized 4 × 1 power combiner.

The spectral response of the proposed combiner over the O-band (1260–1360 nm) was evaluated using BPM simulations, in which the fundamental mode at each wavelength was first obtained from the mode solver and then post-processed using a MATLAB (R2024a) script, as shown in Figure 7. The device exhibits high transmission at the operating

https://doi.org/10.3390/mi17010031

wavelength of 1310 nm. Applying the 3 dB criterion (normalized power of 0.5), the resulting optical bandwidth is 15.8 nm, extending from approximately 1301 nm to 1317 nm. These results demonstrate that the tree-cascade MMI combiner maintains high transmission efficiency within a 15.8 nm window around 1310 nm and can therefore operate effectively in the O-band region commonly employed in Si photonic communication systems.

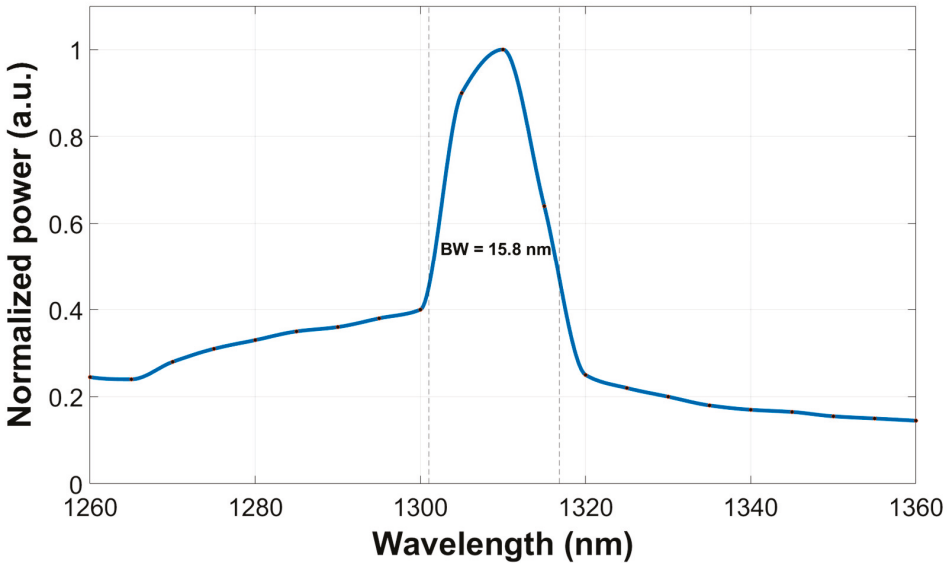


Figure 7. Spectral response of the combiner, showing peak transmission at 1310 nm and a well-defined 3 dB bandwidth across the O-band.

To assess thermal sensitivity, the thermo-optic coefficient of Si was taken into account, leading to an effective wavelength shift of approximately 0.1 nm/°C. A temperature excursion of 50 °C, therefore, produces a spectral shift of about ±5 nm around the nominal peak at 1310 nm. From a simulation perspective, the 3 dB bandwidth is mainly constrained by the wavelength dependence of the MMI mechanism, since deviations from the design wavelength introduce phase mismatch among the guided modes and degrade the self-imaging condition. From Figure 7, the normalized transmission at the shifted wavelengths (1305 nm and 1315 nm) remains between about 0.64 and 0.90, corresponding to a worst-case thermally induced excess loss of 1.9 dB with respect to the peak value. As shown in Figure 7, the device exhibits a 3 dB bandwidth of 15.8 nm, extending from approximately 1301 nm to 1317 nm, so this ±5 nm drift remains well within the high-efficiency operating window of the combiner. This bandwidth is primarily determined by the wavelength dependence of the MMI mechanism, as efficient power combining relies on maintaining the relative phase relationships among the guided modes within the multimode region. Deviations from the design wavelength lead to progressive phase mismatch, which degrades the self-imaging condition and defines the 3 dB operating window. Consequently, the output transmission and self-imaging behavior are only weakly affected by moderate temperature variations, indicating that the proposed design is thermally stable and suitable for reliable operation in dense Si photonic integration platforms.

A further consideration from a practical perspective is that the lasers may operate as mutually non-coherent sources. To quantify the associated performance penalty, simulations were performed in which independent phase offsets were applied to each of the four input sources. Figure 8 presents the normalized output power as a function of the relative (overall) phase mismatch among the four non-coherent inputs. The proposed combiner maintains high efficiency, achieving ≥90% combining efficiency for phase deviations between 0° and 8.49°. However, larger phase mismatches lead to a noticeable

https://doi.org/10.3390/mi17010031

reduction in combining performance; for example, at a 30° phase shift, the combining efficiency decreases to 65.1%. To mitigate this sensitivity, an active phase-control stage should be integrated at the input waveguide section to align the phases of the four sources. This functionality can be implemented using on-chip phase shifters, for instance, based on a doped Si rib waveguide heater [32], a titanium nitride (TiN) microheater [33], or a PIN-diode phase-shifting structure [34].

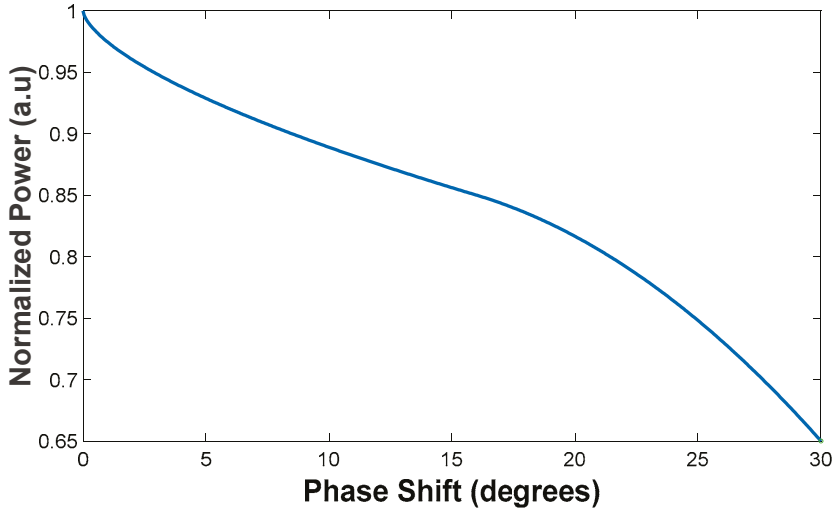


Figure 8. Normalized output power of the proposed combiner as a function of the relative phase shift between the non-coherent input sources.

To benchmark the proposed 4 × 1 combiner, a comparative study was carried out against previously reported MMI-based power combiners implemented on InP/InGaAsP and SOI platforms. The main design metrics, namely the footprint, number of input lasers, IL, and operating bandwidth, are summarized in Table 1. The comparison indicates that the proposed tree-cascade SOI combiner simultaneously achieves ultra-low IL and a compact layout while supporting four input lasers in the O-band.

Table 1. Comparison between the proposed power combiner and previously reported MMI-based designs.

MMI Power Combiner Type	Footprint (μm^2) (Width × Length)	Number of Lasers	IL (dB)	Bandwidth (nm)	Year
2-Stage combiner based on InP/InGaAsP [35]	5 × 1700	4	4.03	N/A	2013
MMI based on InP/InGaAsP waveguide [36]	6 × 1720	2	0.77	N/A	2015
MMI based on SOI strip waveguide [37]	5 × 142.186	2	2	N/A	2015
Tree-Cascade MMI 4 × 1 combiner (SOI)	12 × 772	4	0.1	15.8	In this work

In particular, the simulated IL is on the order of 0.1 dB, which is significantly lower than the multi-dB losses reported for earlier MMI combiners. Although the device footprint of 12 μm × 772 μm is only moderately larger in area than the most compact SOI structure reported for two inputs, the proposed combiner accommodates four inputs and substantially reduces the propagation length compared with other four-input designs. Moreover, it is the only device in the comparison for which a quantified 3 dB bandwidth

https://doi.org/10.3390/mi17010031

is provided. The measured bandwidth of 15.8 nm around 1310 nm shows that, despite the inherent wavelength sensitivity of the self-imaging mechanism, careful optimization of the MMI dimensions and S-bend transitions yields a broad operating window. This combination of ultra-low IL, compact footprint, and verified wide bandwidth makes the proposed combiner highly suitable for integration in dense silicon photonic circuits, where power efficiency and spectral robustness are critical. The insertion loss values reported in Table 1 are presented as representative values taken from the respective references, derived from either numerical simulations or experimental measurements, depending on the original work.

4. Conclusions

A 4 × 1 SOI power combiner based on a tree-cascade MMI architecture has been designed, optimized, and numerically evaluated for O-band operation at 1310 nm. The structure employs buried Si waveguides with adiabatic tapers and low-loss S-bend transitions in order to maintain controlled modal evolution and suppress radiation loss throughout the combining network. BPM simulations were used to determine the optimal geometrical parameters of the two MMI stages and the interconnecting S-bends, resulting in efficient self-imaging and a compact overall footprint of 12 μm × 772 μm.

At the nominal operating wavelength of 1310 nm, the device exhibits a normalized transmitted power of 0.975, which corresponds to an insertion loss of approximately 0.1 dB. Parametric optimization of the MMI widths and lengths shows that the normalized power remains above 0.8 within realistic width and length deviations, and the S-bend analysis indicates that normalized power above 0.9 is maintained for a wide range of bend lengths around the optimum value. These results confirm that the proposed geometry is highly tolerant to fabrication-induced dimensional variations and is compatible with standard CMOS processing.

The spectral response over the O-band was obtained by combining BPM simulations with a wavelength-by-wavelength mode solver and post-processing in MATLAB. Applying the 3 dB criterion with a normalized power level of 0.5, the combiner achieves a 3 dB bandwidth of 15.8 nm, extending from approximately 1301 nm to 1317 nm around the 1310 nm peak. This bandwidth is significant for a self-imaging-based device and demonstrates that careful optimization of the multimode region and taper transitions can overcome the intrinsic wavelength sensitivity of MMI structures. In addition, thermal analysis that incorporates the thermo-optic coefficient of silicon shows that a temperature variation of ±50 °C produces a wavelength shift of about ±5 nm, which remains well inside the obtained 3 dB bandwidth. The associated excess loss remains below 2 dB, indicating that the combiner maintains stable performance under realistic self-heating and environmental conditions.

A comparison with previously reported MMI-based power combiners implemented on InP/InGaAsP and SOI platforms shows that the proposed device combines several key advantages. It supports four input channels while achieving an IL that is significantly lower than the multi-dB values typically reported for similar functions. At the same time, the footprint is competitive with existing SOI implementations, and the required propagation length is notably shorter than that of other four-input designs. Furthermore, among the devices considered, the present work is the only one that reports a quantified 3 dB bandwidth, which provides a clear indication of the usable operating window for system-level design.

In summary, the 4 × 1 tree-cascade MMI combiner presented in this work offers ultra-low insertion loss, a compact footprint, wide optical bandwidth, and robust tolerance to both fabrication deviations and thermal drift. These characteristics make it a strong

https://doi.org/10.3390/mi17010031

candidate for integration in high-speed O-band transmitters, coherent power-combining front ends, and scalable silicon photonic circuits, including photonic neural network architectures that rely on cascaded meshes of splitters, combiners, and active weighting elements. Future work may address experimental realization, polarization-diverse operation, and extension of the architecture to larger input counts and other wavelength bands.

Author Contributions: Conceptualization, D.M.; Methodology, S.S.S. and D.M.; Software, S.S.S. and D.M.; Validation, S.S.S. and D.M.; Investigation, D.M.; Writing—original draft, S.S.S. and D.M.; Writing—review & editing, D.M.; Visualization, D.M.; Supervision, D.M. All authors have read and agreed to the published version of the manuscript.

Funding: This research received no external funding.

Data Availability Statement: The original contributions presented in this study are included in the article. Further inquiries can be directed to the corresponding author.

Conflicts of Interest: The authors declare no conflict of interest.

References

1. Wang, X.; Shu, Q.; Chu, Q.; Liu, C.; Yan, Y.; Wen, J.; Dong, K.; Tao, R.; Zhang, H.; Lin, H.; et al. Four-Channel Nanosecond Pulse Combination in the Non-Polarization-Maintaining Fiber System. *Photonics* **2025**, *12*, 363.
2. Liu, S.; Liu, B.; Lv, H.; Liang, Y.; Liu, F.; Wang, H.; Cong, Y.; Li, X.; Guo, Q. Design of a 1 × 3 Power Splitter Based on Multimode Interference in a Parabolic-Type Slot-Waveguide Structure. *Appl. Sci.* **2024**, *14*, 5829.
3. Li, C.; Zhou, Z.; Li, Y.; Liu, L. Multimode silicon photonics. *Nanophotonics* **2019**, *8*, 393–409.
4. Jang, H.-S.; Lee, D.; Heo, H.; Kim, Y.-S.; Lim, H.-T.; Jeon, S.-W.; Moon, S.; Kim, S.; Han, S.-W.; Jung, H. Aluminum nitride waveguide beam splitters for integrated photonics. *Photonics Res.* **2023**, *11*, 1196–1205.
5. Pugachov, Y.; Gulitski, M.; Malka, D. Photonic crystal flip-flops: Recent developments in all-optical memory components. *Materials* **2023**, *16*, 6467.
6. Bachmann, M.; Besse, P.A.; Melchior, H. General self-imaging properties in N×N multimode interference couplers including phase relations. *Appl. Opt.* **1994**, *33*, 3905–3911. [CrossRef]
7. Liu, F.; Lv, H.; Zhang, H.; Liu, S.; Liang, Y.; Wang, H.; Cong, Y.; Li, X.; Guo, Q. Design of polarization-independent 1 × 2 optical power splitter based on silicon nitride slot-waveguide structure. *Sci. Rep.* **2025**, *15*, 11404. [CrossRef]
8. Vázquez, C.; Fraile, F.J. Three-dimensional method for simulation of multimode interference couplers. *J. Light. Technol.* **1995**, *13*, 2296–2302. [CrossRef]
9. Rajarajan, M.; Rahman, B.M.A.; Wongcharoen, T.; Grattan, K.T.V. Accurate analysis of multimode interference devices with two-dimensional confinement. *J. Light. Technol.* **1996**, *14*, 2078–2084.
10. Katash, N.; Khateeb, S.; Malka, D. Combining four Gaussian lasers using silicon nitride MMI slot-waveguide structure. *Micromachines* **2022**, *13*, 1680. [CrossRef]
11. Doménech, J.D.; Fandiño, J.S.; Gargallo, B.; Muñoz, P. Arbitrary coupling ratio multimode interference couplers in silicon-on-insulator. *J. Light. Technol.* **2014**, *32*, 2536–2543. [CrossRef]
12. Mizera, T.; Gaso, P.; Pudis, D.; Ziman, M.; Kuzma, A.; Goraus, M. 3D Polymer-Based 1 × 4 MMI Splitter. *Nanomaterials* **2022**, *12*, 1749. [CrossRef]
13. Gao, Q.; Wang, X.; Huang, K.; Wei, J.; Huang, Y.; Zhang, Y.; Wang, R.; Yu, S. Four-channel silicon nitride wavelength beam combiners for multi-gas absorption spectroscopy. *Opt. Lett.* **2025**, *50*, 2469–2472. [CrossRef] [PubMed]
14. Zhao, Z.; Li, Z.; Niu, J.; Zhang, G.; Chen, H.; Fu, X.; Yang, L. Eight-Channel LAN WDM (De)Multiplexer Based on Cascaded Mach–Zehnder Interferometer on SOI for 400GbE. *Photonics* **2022**, *9*, 252. [CrossRef]
15. Hai, M.S.; Leinse, A.; Veenstra, T.; Liboiron-Ladouceur, O. A Thermally Tunable 1 × 4 Channel Wavelength Demultiplexer Designed on a Low-Loss Si_3N_4 Waveguide Platform. *Photonics* **2015**, *2*, 1065–1080. [CrossRef]
16. Fujisawa, T.; Koshiba, M. Theoretical investigation of ultrasmall polarization-insensitive multimode interference waveguide based on sandwiched structures. *IEEE Photonics Technol. Lett.* **2006**, *18*, 1246–1248. [CrossRef]
17. Mu, J.; Vázquez-Córdova, S.A.; Sefunc, M.A.; Yong, Y.S.; García-Blanco, S.M. A low-loss and broadband MMI-based multi/demultiplexer in Si_3N_4/SiO_2 technology. *J. Light. Technol.* **2016**, *34*, 3603–3609. [CrossRef]
18. Almeida, V.R.; Xu, Q.; Barrios, C.A.; Lipson, M. Guiding and confining light in void nanostructures. *Opt. Lett.* **2004**, *29*, 1209–1211. [CrossRef]
19. Brand, O.; Wolftson, B.; Malka, D. A compact polarization MMI combiner using silicon slot-waveguide structures. *Micromachines* **2023**, *14*, 1203. [CrossRef]

https://doi.org/10.3390/mi17010031

20. Jiao, S.; Qiu, J.; Zhao, G.; Wu, J. Photonic integrated coherent beam combiner based on MMI and the SPGD algorithm. *Appl. Opt.* **2024**, *63*, 2175–2179. [CrossRef]
21. Xu, Y.; Xiao, J.; Sun, X. Compact polarization beam splitter for silicon-based slot waveguides using an asymmetrical multimode waveguide. *J. Light. Technol.* **2014**, *32*, 4282–4288. [CrossRef]
22. Yin, M.; Yang, W.; Li, Y.; Wang, X.; Li, H. CMOS-compatible and fabrication-tolerant MMI-based polarization beam splitter. *Opt. Commun.* **2015**, *335*, 48–52. [CrossRef]
23. Felicetti, M.; Kojima, K.; Koike-Akino, T.; Wang, B.; Parsons, K.; Nishikawa, S.; Yagyu, E. MMI-based polarization beam splitter/combiner for InP photonic integrated circuits. In *Integrated Photonics Research, Silicon and Nanophotonics*; Optica Publishing Group: Washington, DC, USA, 2015.
24. Fang, Y.; Bao, C.; Wang, Z.; Liu, Y.; Zhang, L.; Huang, H.; Ren, Y.; Pan, Z.; Yue, Y. Polarization beam splitter based on Si_3N_4/SiO_2 horizontal slot waveguides for on-chip high-power applications. *Sensors* **2020**, *20*, 2862. [CrossRef]
25. Zhu, X.; La, X.; Li, H.; Zhou, D.; Lu, D.; Zhao, L.; Liang, S. MMI combiner integrated 4×50 Gb/s array of directly modulated 1.3 μm InGaAlAs/InP DFB laser array. *Opt. Express* **2025**, *33*, 1093–1103. [CrossRef]
26. Zhang, J.; Shi, X.; Zhang, Z.; Guo, K.; Yang, J. Ultra-compact, efficient, and high-polarization-extinction beam splitter. *Opt. Express* **2022**, *30*, 538–547.
27. Herrero-Bermello, A.; Luque-Gonzalez, J.M.; Velasco, A.V.; Ortega-Monux, A.; Cheben, P.; Halir, R. Design of a broadband polarization splitter based on anisotropy-engineered tilted subwavelength gratings. *IEEE Photonics J.* **2019**, *11*, 1–8. [CrossRef]
28. Menahem, J.; Malka, D. 1×4 wavelength demultiplexer C-band using cascaded multimode interference on SiN buried waveguide structure. *Materials* **2022**, *15*, 5067. [CrossRef]
29. Han, F.; He, Y.; Zhu, H.; Zhou, K. A Novel Catheter Shape-Sensing Method Based on Deep Learning with a Multi-Core Optical Fiber. *Sensors* **2023**, *23*, 7243. [CrossRef]
30. Besse, P.A.; Bachmann, M.; Melchior, H.; Soldano, L.B.; Smit, M.K. Optical Bandwidth and Fabrication Tolerances of Multimode Interference Couplers. *J. Light. Technol.* **1994**, *12*, 1001–1009. [CrossRef]
31. Zamhari, N.; Ehsan, A.A. Large cross-section rib silicon-on-insulator (SOI) S-bend waveguide. *Optik* **2017**, *130*, 1414–1420. [CrossRef]
32. Sitbon, E.; Ostrovsky, R.; Malka, D. Optimizations of thermo-optic phase shifter heaters using doped silicon heaters in rib waveguide structure. *Photonics Nanostruct. Fundam. Appl.* **2022**, *51*, 101052.
33. Krause, E.E.; Malka, D. Optimizations of Double Titanium Nitride Thermo-Optic Phase-Shifter Heaters Using SOI Technology. *Sensors* **2023**, *23*, 8587. [CrossRef]
34. Moshaev, V.; Leibin, Y.; Malka, D. Optimizations of Si PIN diode phase-shifter for controlling MZM quadrature bias point using SOI rib waveguide technology. *Opt. Laser Technol.* **2021**, *138*, 106844. [CrossRef]
35. Wang, B.; Kojima, K.; Koike-Akino, T.; Parsons, K.; Nishikawa, S.; Yagyu, E. A low-loss integrated beam combiner based on polarization multiplexing. In Proceedings of the Integrated Photonics Research, Silicon and Nano-Photonics (IPR), Rio Grande, PR, USA, 14–17 July 2013.
36. Kojima, K.; Koike-Akino, T. Novel multimode interference devices for wavelength beam splitting/combining. In Proceedings of the 2015 International Conference on Photonics in Switching (PS), Florence, Italy, 22–25 September 2015; pp. 34–36.
37. RayChaudhuri, K.; Henry, R. Design and analysis of generic optical power combiner for photonic integrated circuits. In Proceedings of the 2015 Workshop on Recent Advances in Photonics (WRAP 2015), Bangalore, India, 16–17 December 2015.

Disclaimer/Publisher's Note: The statements, opinions and data contained in all publications are solely those of the individual author(s) and contributor(s) and not of MDPI and/or the editor(s). MDPI and/or the editor(s) disclaim responsibility for any injury to people or property resulting from any ideas, methods, instructions or products referred to in the content.

https://doi.org/10.3390/mi17010031

micromachines

MDPI

Review

Plasmonics Meets Metasurfaces: A Vision for Next Generation Planar Optical Systems

Muhammad A. Butt

Institute of Microelectronics and Optoelectronics, Warsaw University of Technology, Koszykowa 75, 00-662 Warsaw, Poland; ali.butt@pw.edu.pl

Abstract

Plasmonics and metasurfaces (MSs) have emerged as two of the most influential platforms for manipulating light at the nanoscale, each offering complementary strengths that challenge the limits of conventional optical design. Plasmonics enables extreme subwavelength field confinement, ultrafast light–matter interaction, and strong optical nonlinearities, while MSs provide versatile and compact control over phase, amplitude, polarization, and dispersion through planar, nanostructured interfaces. Recent advances in materials, nanofabrication, and device engineering are increasingly enabling these technologies to be combined within unified planar and hybrid optical platforms. This review surveys the physical principles, material strategies, and device architectures that underpin plasmonic, MS, and hybrid plasmonic–dielectric systems, with an emphasis on interface-mediated optical functionality rather than long-range guided-wave propagation. Key developments in modulators, detectors, nanolasers, metalenses, beam steering devices, and programmable optical surfaces are discussed, highlighting how hybrid designs can leverage strong field localization alongside low-loss wavefront control. System-level challenges including optical loss, thermal management, dispersion engineering, and large-area fabrication are critically examined. Looking forward, plasmonic and MS technologies are poised to define a new generation of flat, multifunctional, and programmable optical systems. Applications spanning imaging, sensing, communications, augmented and virtual reality, and optical information processing illustrate the transformative potential of these platforms. By consolidating recent progress and outlining future directions, this review provides a coherent perspective on how plasmonics and MSs are reshaping the design space of next-generation planar optical hardware.

Keywords: plasmonics; metasurfaces; hybrid plasmonic system; modulators; nanolaser

1. Introduction

Modern optical systems are increasingly constrained by the size, complexity, and rigidity of conventional bulk components [1]. As emerging applications such as immersive displays [2,3], compact imaging [4,5], biomedical sensing [6,7], high-speed communication [8,9], and optical information processing [10] continue to expand, there is a growing demand for optical hardware that is thinner, lighter, faster, and more functionally versatile than traditional lens and waveguide-based architectures [11]. These demands have driven intense interest in planar and nanoscale approaches that enable optical functionality to be implemented directly at material interfaces rather than accumulated through long propagation paths [12,13].

Plasmonics [14,15] and metasurfaces (MSs) [16–19] have independently matured into powerful platforms for nanoscale light manipulation. Plasmonic structures exploit collective electron oscillations at metal–dielectric interfaces to confine optical fields far below the diffraction limit, enabling ultrafast light–matter interaction, strong optical nonlinearities, and extreme miniaturization of active devices [20,21]. MSs, in contrast, consist of planar arrays of subwavelength scatterers that enable precise control over optical phase, amplitude, polarization, and dispersion within layers only hundreds of nanometers thick [11,22]. Through appropriate design of their constituent meta-atoms, MSs can replace bulky refractive or diffractive elements with flat optical components capable of wavefront shaping, beam steering, holography, and imaging [23–28].

While plasmonics and MSs rely on distinct physical mechanisms, their functional roles are increasingly complementary. Plasmonic elements provide strong field localization and high-speed modulation over nanometer-scale interaction volumes, making them well-suited for modulators [24], detectors [25], nanolasers [29], and nonlinear optical elements [12]. MSs, on the other hand, excel at spatially distributed wavefront control and multifunctional optical processing, enabling complex transformations of optical fields in free space or in hybrid environments [26–28]. When combined within hybrid plasmonic–dielectric or plasmonic–MS architectures, these strengths can be leveraged simultaneously, allowing systems to achieve performance levels unattainable by either platform alone [30, 31].

Recent progress in materials science and nanofabrication has further accelerated this trend. Alternative plasmonic materials, including transparent conducting oxides, transition metal nitrides, and two-dimensional materials, offer improved tunability, reduced loss in selected spectral regimes, and compatibility with large-scale fabrication [21,32,33]. In parallel, advances in MS design methodologies and manufacturing techniques such as deep-ultraviolet lithography, nanoimprint lithography, and multilayer stacking are enabling large-area, high-yield production of complex planar optical components [34,35]. These developments have made it increasingly feasible to co-integrate plasmonic and MS functionalities within unified planar platforms.

This review surveys the fundamental principles, material platforms, and device-level implementations of plasmonic, MS, and hybrid plasmonic–dielectric systems, with a particular emphasis on interface-mediated optical functionality. Sections 2 and 3 revisit the physical foundations of plasmonics and MSs, highlighting design strategies and performance trade-offs relevant to planar and hybrid architectures. Subsequent sections examine representative devices and applications, including ultracompact modulators and detectors, metalenses, beam steering systems, programmable optical surfaces, and emerging optical information processing schemes. Key challenges related to optical loss, dispersion, thermal management, and large-area fabrication are critically discussed, followed by a forward-looking perspective on how plasmonics and MSs are shaping the future of flat, multifunctional, and programmable optical systems.

2. Rethinking Plasmonic Fundamentals for Planar and Interface-Engineered Optical Systems

Plasmonics is based on the excitation of surface plasmon polaritons and localized surface plasmon resonances at metal dielectric interfaces, enabling electromagnetic confinement far below the diffraction limit [36]. While the physical foundations of these modes are well-established, their relevance is increasingly defined by planar optical architectures in which functionality is concentrated at engineered interfaces rather than distributed along extended propagation paths. In this setting, plasmonic loss and limited propagation length

https://doi.org/10.3390/mi17010119

are no longer dominant constraints but are outweighed by the advantages of extreme field localization, ultrafast response, and strong light-matter interaction [37,38].

Surface plasmon polaritons originate from collective electron oscillations coupled to electromagnetic waves at metal dielectric boundaries and exhibit dispersion relations that deviate strongly from the free-space light line. This behavior enables precise control of modal confinement, group velocity, and the local density of optical states, allowing plasmonic structures to support slow light effects, enhanced spontaneous emission, and tailored mode coupling within compact footprints [39]. For planar systems that prioritize localized interaction and high functional density, these dispersion characteristics provide a powerful mechanism for engineering optical response at surfaces and interfaces rather than long-distance waveguides.

Localized surface plasmon resonances supported by metallic nanostructures such as nanorods, nanodisks, and bowtie antennas further expand the available design space by concentrating optical fields into nanoscale hotspots [40,41]. These localized fields enhance nonlinear optical processes, amplify Raman scattering, and strongly modify radiative emission pathways. Recent advances in inverse electromagnetic design allow systematic tailoring of resonance spectral position, symmetry, and near-field distribution, enabling efficient coupling to gain media, molecular emitters, and quantum systems [42,43]. As feature sizes and inter-element gaps approach the subnanometer regime, quantum mechanical effects such as electron tunneling and nonlocal response become increasingly significant, marking the onset of quantum plasmonic behavior [44,45].

Material selection remains a key factor in determining plasmonic performance and functionality [46,47]. Noble metals such as gold and silver continue to serve as reference materials, but are limited by interband absorption, chemical instability, and challenges in large-scale fabrication [48,49]. Transition metal nitrides, particularly titanium nitride, offer improved thermal stability and compatibility with complementary metal oxide semiconductor processes [50]. Aluminum enables plasmonic operation in the ultraviolet and visible spectral regions [51], while copper provides a cost-effective alternative when oxidation can be effectively managed [52]. Transparent conducting oxides, such as indium tin oxide, introduce epsilon near-zero regimes in which strong field enhancement and ultrafast tunability can be achieved [53]. Two-dimensional materials, including graphene, support highly confined and electrically tunable plasmons in the mid-infrared, enabling dynamically reconfigurable plasmonic responses at planar interfaces [54].

The functional role of plasmonic building blocks is also evolving. Plasmonic waveguides are increasingly valued not for long-distance transport but for maximizing interaction strength within minimal physical length [55]. Antennas are no longer passive scattering elements but multifunctional components capable of coupling, concentrating, modulating, and reradiating optical fields within engineered environments [56]. Resonant plasmonic structures provide sharp spectral selectivity and enhanced field confinement, enabling compact filtering, sensing, and switching functionalities. New coupling strategies between plasmonic elements and dielectric or MS-based structures enable controlled energy exchange across different confinement regimes without relying on extended propagation [36].

Together, these developments highlight a shift in how plasmonic physics is interpreted within modern optical systems. Rather than serving as a lossy alternative to conventional guiding, plasmonics is increasingly recognized as an enabling platform for interface-mediated optical functionality in planar and hybrid architectures. By localizing electromagnetic energy precisely where optical processing occurs at surfaces, boundaries, and engineered nanostructures, plasmonic modes provide a foundation for compact, ultrafast, and highly responsive optical components that naturally complement MSs and other planar photonic platforms [57].

https://doi.org/10.3390/mi17010119

3. MS Fundamentals Through a Forward-Looking Lens

MSs have redefined the concept of wavefront engineering by demonstrating that optical phase, amplitude, and polarization can be controlled within a planar layer of subwavelength scatterers [26,58]. Generalized Snell's law captures the essence of this approach by showing that abrupt phase shifts at an interface can redirect light in ways unattainable by conventional optics [59]. As MSs move from laboratory demonstrations to real integrated devices, the emphasis is shifting from simple beam steering toward complex, multifunctional responses that can operate across broad bandwidths and variable incident conditions [60].

The meta-atom is the primary building block of MSs [61]. Dielectric meta-atoms based on Mie resonances can produce strong electric and magnetic responses with minimal absorption loss [62]. This dual response allows designers to achieve full two pi phase control while maintaining high transmission efficiency. Metallic meta-atoms, while more lossy, continue to be valuable for achieving polarization rotation, broadband absorption, and tunable behavior [28]. The future of MS engineering likely lies in hybrid meta-atoms that combine the strengths of dielectric confinement and plasmonic field intensification. Such structures can open new parameter spaces for multifunctional devices that simultaneously control polarization, spectral response, and wavefront curvature [30,63,64].

Functional control in MSs is becoming increasingly versatile. Phase modulation alone can produce lenses, beam deflectors, and holograms, but amplitude modulation allows the creation of spatial filters, structured illumination systems, and complex imaging platforms [65–67]. Polarization control enables devices that convert linear to circular polarization or tailor polarization singularities [68]. Dispersion engineering allows MSs to achieve achromatic focusing, multi-wavelength functionality, and group delay control. As MSs continue to evolve, these functional mechanisms will merge, resulting in optical interfaces that act as integrated field processors capable of performing spatial, spectral, and polarization-based transformations simultaneously.

The future of MSs depends critically on fabrication technologies. Electron beam lithography has facilitated the exploration of novel designs, but it cannot support commercialization due to low throughput [69]. Wang et al. demonstrated a broadband, polarization-insensitive TiO_2 achromatic metalens for near-infrared biological imaging [70]. The device relied on a scalable process that produces high-aspect-ratio nanopillars, ~1.5 μm tall with nearly vertical sidewalls, enabling the required group-delay control for operation across 650–1000 nm. Within this band, the metalens achieved 77–88.5% efficiency and operates with a numerical aperture of 0.24–0.1. The fabrication steps are outlined in Figure 1a. A 1500 nm TiO_2 layer was deposited by electron-beam evaporation, patterned using PMMA A2 and electron-beam lithography, and transferred into a Cr hard mask via lift-off. Reactive ion etching defined the nanopillars, and the final TiO_2 structures emerged after Cr removal. Top-view SEM images in Figure 1b,c show 4725 nanopillars with four cross-section types, closely matching the intended design. The tilt-view SEM in Figure 1d confirms ~89°–90° sidewalls and aspect ratios up to ~37.5. Optical characterization is presented in Figure 1e,f. As shown in Figure 1e, all wavelengths from 650 to 1000 nm focus at ~60 μm, matching the designed focal length and NA = 0.24. Figure 1f depicts circular, diffraction-limited focal spots across the band, with Strehl ratios > 0.81 and FWHM deviations < 9%. These results confirm that the fabricated nanopillar array accurately delivers the phase and group-delay profiles required for broadband achromatic performance.

https://doi.org/10.3390/mi17010119

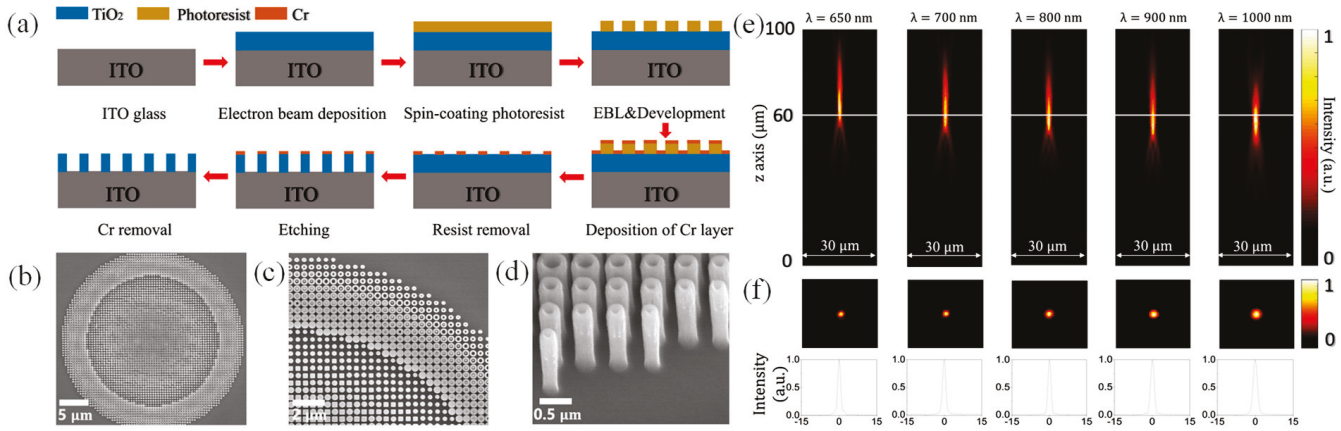


Figure 1. (**a**) Schematic of the fabrication process, showing the highly directional etching used to form the TiO_2 nanostructures. (**b**,**c**) Top-view SEM images of the achromatic metalens at different magnifications, where four distinct nanopillar geometries are visible. (**d**) Tilt-view SEM image highlighting the structural quality of the fabricated metalens. (**e**,**f**) Measured focal-spot intensity profiles in the x–z and x–y planes at multiple wavelengths; the lower panels show the corresponding radial intensity distributions (solid lines) with fitted curves (dashed lines) [70].

Nanoimprint lithography presents a path toward scalable manufacturing, while deep ultraviolet lithography may eventually enable MS fabrication in standard semiconductor foundries [71]. Recently, Hutterhofer et al. introduced a scalable imprint-lithography method for fabricating semiconductor photoelectrodes and applied it to amorphous gallium phosphide (a-GaP) [72]. By combining anapole modes with MS lattice resonances, broadband absorption enhancement was achieved. The process offered high throughput and low cost while preserving the engineered photonic response. As shown in Figure 2a, the resist-coated sample was imprinted with the inverted stamp, forming a ~180 nm-thick polymer mask that can be used directly for etching, reducing processing steps. Residual polymer was removed with acetone and isopropanol. Figure 2b–d shows the unit-cell design and SEM images confirming uniform nanostructuring, with only minor radius variations originating from the stamp. The final MS electrode and a planar a-GaP film are shown in Figure 2d. After etching, the exposed ITO around the edges functions as the back contact for both electrodes [72]. Photoelectrochemical measurements under sunlight and hydrogen-evolution conditions showed a 5.7-fold photocurrent increase over a planar film, supported by optical characterization and numerical modeling of both individual nanodisks and the full MS [72].

Additional techniques such as atomic layer deposition and multilayer stacking may allow MSs to expand into three-dimensional architectures, offering enhanced control over optical dispersion and modal composition [73]. Overcoming fabrication challenges will determine whether MSs can transition from specialized components to ubiquitous optical elements in commercial systems. A comparison of plasmonic, MS, and hybrid approaches is presented in Table 1, emphasizing their operational principles and the performance attributes that define their application potential.

https://doi.org/10.3390/mi17010119

Table 1. Key Characteristics of Plasmonics, MSs, and Hybrid Photonic Platforms.

Dimension	Plasmonics	Metasurfaces (MSs)	Hybrid Plasmonic–MS/Plasmonic–Dielectric Systems
Core Physical Strength	Extreme subwavelength confinement; ultrafast electron–mediated response; strong nonlinearities [74–77].	Complete phase, amplitude, and polarization control at planar interfaces; broadband functionality improving [78,79].	Combines strong confinement (plasmonics) with low-loss routing and wavefront control (dielectric/MS) [30,80–82].
Key Advantages	Enables nanometer-scale modulators, detectors, and quantum-scale hotspots; supports ENZ-based ultrafast switching [24,25,83].	Enables flat optics, ultrathin lenses, programmable apertures; supports multifunctionality and complex wavefront shaping [11,13,84,85].	Achieves high modulation efficiency with reduced loss; allows highly integrated and programmable photonics; enables compact optical processors [63,86,87].
Main Limitations (Current)	Ohmic (absorption) loss; short propagation lengths; heat generation; material stability constraints [88].	Fabrication scalability; limited broadband achromaticity; need for multi-layer integration for complex functions [89,90].	Coupling mismatch between dielectric and plasmonic modes; thermal management; fabrication tolerance demands [55,91,92].
Materials Outlook	Alternatives to Au/Ag: TiN (CMOS-compatible), Al (UV), Cu (low-cost), ITO (ENZ), graphene (tunable mid-IR) [50,93].	High-index dielectrics (Si, TiO_2); hybrid designs combining metallic and dielectric scatterers; phase-change materials for reconfigurability [11,18,28,62].	ITO + Si, graphene + ITO, plasmonic inserts in Si waveguides; meta-waveguides with engineered dispersion and polarization control [94,95].
Device-Level Examples	Plasmonic modulators, nanolasers, hotspots for sensing, ultrathin detectors [96,97].	Metalenses, holographic processors, beam steering devices, MS-based neural networks [98,99].	Hybrid ENZ modulators, MS-enabled compact waveguides, reconfigurable intelligent photonic surfaces [100,101].
Performance Frontier	Femtosecond-scale modulation; deep subwavelength mode confinement; intense local fields for nonlinear processes [102].	System-level optical functionality: multi-frequency control, phase–amplitude–polarization multiplexing; flat optical architectures for cameras and LiDAR [103,104].	Best-of-both-worlds: high speed + low footprint + programmable wavefront control; pathways toward optical computing [105].
Scalability Outlook	Requires new plasmonic materials with lower loss and CMOS compatibility [106].	Moving toward mass production via nanoimprint, DUV lithography; multi-layer stacking likely [34,107].	Depends on seamless integration in Si photonics; improved thermal handling and coupling engineering [108].
Role in Future Optical Computing	Provides nonlinear activation, ultrafast switching, and strong light–matter interaction for deep photonic neural networks [57,109].	Provides spatial transformations and diffractive computing layers (e.g., MS neural networks) [110,111].	Forms complete photonic compute stacks: MS front-end for linear ops + plasmonic activation layers [112].
Role in Imaging and Sensing	Raman enhancement, nanoscale detectors, localized field hotspots [113,114].	Metalenses, reconfigurable holography, spectral filters and absorbers [115–117].	On-chip structured illumination, MS-controlled plasmonic sensors, integrated spectrometers [118,119].
Role in AR/VR and Compact Optics	Enhances sensing elements (photodetectors, modulators) [120,121].	Enables ultrathin imaging stacks, folded metalenses, beam combiners for headsets [11,122].	Compact, integrated emitter–MS–detector stacks for next-gen wearable optics [123].
Application Sectors Poised for Disruption	High-speed interconnects, ultrafast computing nodes, quantum sources [124,125].	Consumer imaging, LiDAR, 3D sensing, AR/VR displays, optical encryption [123,126,127].	Full-stack systems: flat cameras, photonic processors, adaptive optical networks [128].

https://doi.org/10.3390/mi17010119

Table 1. *Cont.*

Dimension	Plasmonics	Metasurfaces (MSs)	Hybrid Plasmonic–MS/Plasmonic–Dielectric Systems
Future Research Priorities	Low-loss materials, thermal management, quantum-plasmonic integration [46,129].	Broadband achromatic operation, dynamic tunability, large-area manufacturing [130–132].	Thermal engineering, mode-matching strategies, foundry-compatible fabrication [133].
Long-Term Vision	Plasmonics: acts as nanoscale "processing nodes" embedded in larger photonic circuits [134].	MSs: universal optical interfaces providing programmable wavefront control [135].	Hybrid platforms: planar, scalable, computationally aware optical systems defining the next photonic paradigm [136,137].

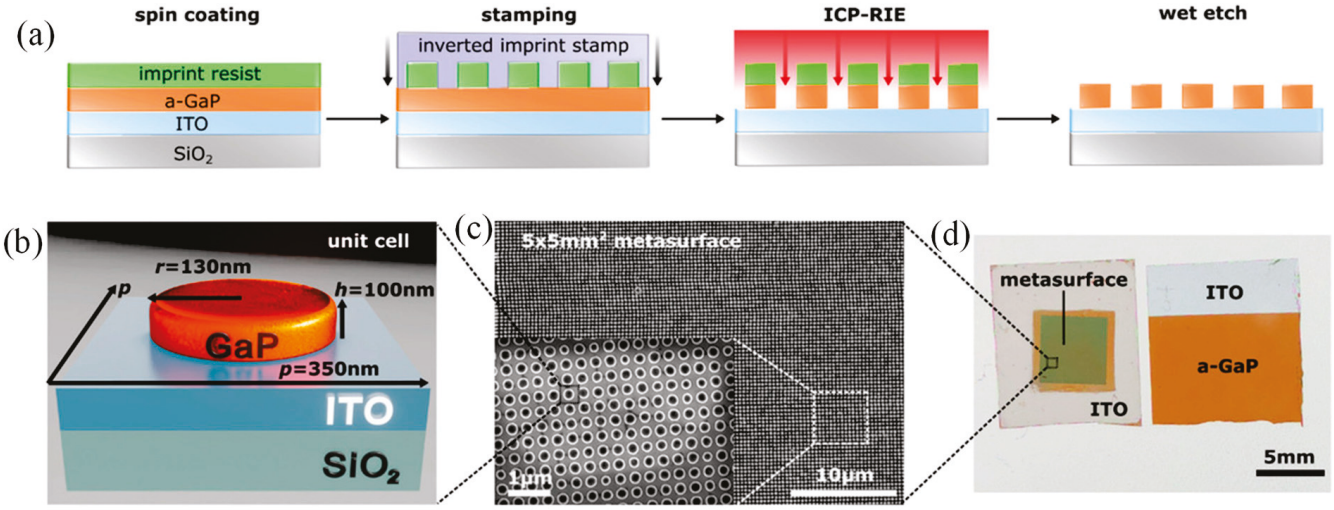


Figure 2. (**a**) Workflow for fabricating the a-GaP MS using nanoimprint lithography, where the patterned polymer layer serves as the etching mask, (**b**) Illustration of the individual MS unit cell, (**c**) SEM micrographs at multiple magnifications showing the large-area nanostructure, (**d**) Photograph comparing two photoelectrodes: one incorporating the imprinted MS (left) and the other consisting of a uniform 100 nm thick a-GaP film, each deposited on a 100 nm thick ITO layer [72].

4. Plasmonic Devices as Drivers of Extreme Performance

Plasmonic devices excel where high field intensity and ultrafast response are essential. Plasmonic modulators demonstrate this potential by achieving significant refractive index changes over extremely small interaction lengths [138]. Transparent conducting oxides in the epsilon near-zero regime support strong index modulation with minimal voltage, enabling modulators that operate at terahertz speeds and potentially even support femtosecond-scale switching [33]. As data rates continue to rise, such modulators could form key building blocks for next-generation on-chip interconnects and optical logic circuits. Coherent optical communication enables the highest data throughput and spectral efficiency, making it well-suited to meet rapidly growing bandwidth demands. It relies on in-phase/quadrature (IQ) electro-optic modulators that encode information in both the amplitude and phase of light. For large-scale integration, these modulators must combine energy efficiency with a compact footprint.

Heni et al. reported ultracompact silicon-based IQ modulators with an active region of 4 × 25 µm × 3 µm, operable with sub-1 V drivers [139]. The plasmonic–organic hybrid IQ modulators consist of two imbalanced high-speed plasmonic Mach–Zehnder modulators (MZMs) integrated into a silicon photonic Mach–Zehnder interferometer (MZI), as shown in Figure 3a. The phase shift between the I and Q arms was controlled either

https://doi.org/10.3390/mi17010119

by a thermo-optic phase shifter or by wavelength tuning enabled by the MZI imbalance. DC biases independently set the operating points of the two MZMs. Each MZM contained a 15 or 20 µm plasmonic slot waveguide with a 130 nm slot width (Figure 3b). The metal–insulator–metal (MIM) slot was filled with the organic electro-optic (OEO) composite HD-BB-OH/YLD124. In the active region, the electrical RF field and the optical mode were both tightly confined to the slot and exhibited nearly complete spatial overlap (Figure 3c,d). They achieved exceptionally low electrical energy consumption: 0.07 fJ bit^{-1} at 50 Gbit s^{-1}, 0.3 fJ bit^{-1} at 200 Gbit s^{-1}, and 2 fJ bit^{-1} at 400 Gbit s^{-1}. These performance metrics highlight the potential of such devices for both long-haul and short-reach coherent communication systems.

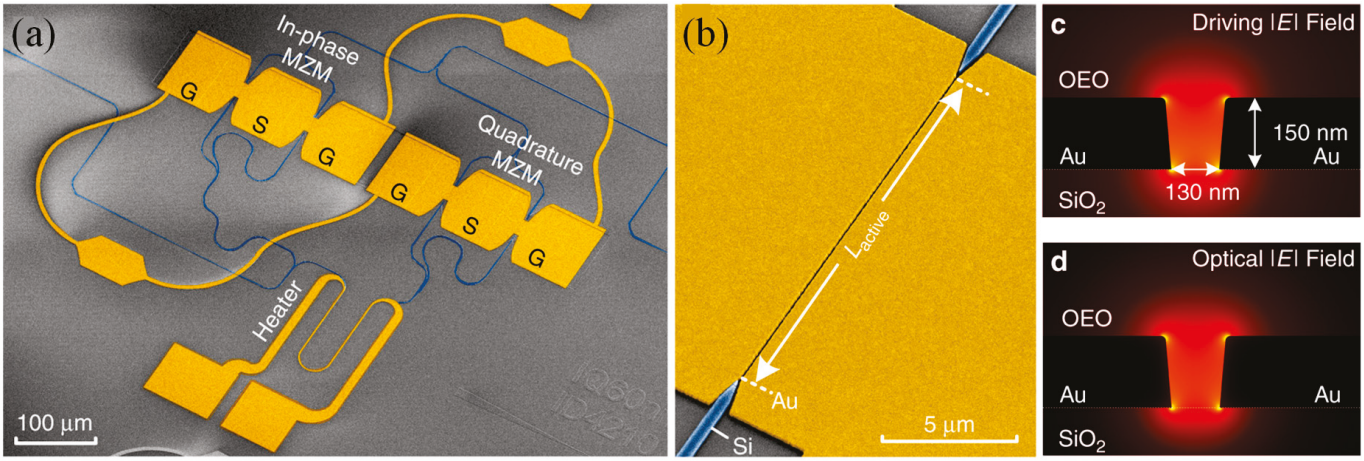


Figure 3. Plasmonic IQ modulators with attojoule-per-bit energy consumption: (**a**) Colorized SEM image of a plasmonic IQ modulator on a silicon platform, incorporating two Mach–Zehnder modulators (MZMs), (**b**) Close-up of the active plasmonic slot waveguide. Light from the silicon waveguide is coupled into the gold slot waveguide via tapered mode converters. The slot is filled with an organic electro-optic material, (**c**,**d**) Cross sections of the plasmonic slot waveguide showing simulated c electrical driving field and d optical field distributions [139].

Photodetectors that incorporate plasmonic structures utilize localized resonances to concentrate optical energy into the semiconductor region or generate hot electrons that contribute directly to photocurrent [140,141]. These mechanisms can extend detection bandwidth, enhance responsivity, and reduce detector volume. Plasmonic detectors could be integrated into multispectral imaging systems, biosensing platforms, and hyperspectral cameras, especially when combined with MSs that provide spectral filtering or beam shaping [4,142]. Oshita et al. presented a plasmonic photodetector that reconfigures its spectral responsivity through electromechanical deformation rather than electrical bias control [143]. The photodetector consisted of an n-type silicon cantilever with a plasmonic gold diffraction grating on its surface and a nearby electrode (Figure 4a). Applying a voltage between the electrode and the cantilever generates an electrostatic force that drives the cantilever into resonance (Figure 4b), thereby changing the incident angle θ and reconfiguring the plasmonic resonance. Dual zigzag support structures reduce stiffness and increase the angular scanning amplitude.

When light of an appropriate wavelength strikes the grating at the resonant angle, surface plasmon resonance (SPR) enhances absorption. The absorbed energy excites electrons in the gold, enabling them to overcome the Schottky barrier at the Au/n-Si interface. These electrons are collected as a photocurrent I(t) between the gold anode and aluminum cathode. Because the incident angle is periodically modulated, the detector's spectral response is scanned in time. However, capacitive coupling between the cantilever and the electrode (Figure 4c) introduces a displacement current D(t), which appears as a periodic

https://doi.org/10.3390/mi17010119

background signal due to repeated charging and discharging of the capacitor. This approach produced clear peak shifts across 1250–1310 nm. To highlight potential applications, near-infrared spectroscopy was also demonstrated using the device. Because the structure enables sub-bandgap detection in silicon via a Schottky junction, this photodetector is a promising candidate for compact near-infrared spectrometers integrated into industrial silicon imaging systems [143].

Plasmonic nanolasers offer a route to coherent light generation at scales far smaller than traditional optical cavities [144,145]. By confining electromagnetic fields within volumes comparable to the cubic wavelength in matter or even smaller, nanolasers can interact strongly with emitters and achieve threshold reductions [146]. Their small footprint makes them compatible with dense photonic integration and suggests they may become key components of optical interconnect networks or photonic neural architectures [29]. Extraordinary optical transmission (EOT) in metal nanohole arrays (NHAs) and Tamm plasmon (TP) states have been studied since their discoveries in 1998 and 2007, respectively. Both phenomena underpin a wide range of plasmonic devices, including absorbers, lasers, and narrowband filters. Although the influence of hole size and geometry on EOT has been well documented, the corresponding effects on TP structures incorporating metal NHAs remain less explored—particularly the role of controlled randomness in the hole arrangement.

Shahid et al. systematically varied both the hole size and spatial distribution in metal NHAs and examined the resulting changes in EOT and Tamm resonances [147]. Three configurations were investigated: a bare NHA, a passive TP cavity, and a TP laser. The device structures and excitation direction are shown in Figure 4d–h. Figure 4d,e illustrate the Tamm plasmon (TP) cavity, which consists of a 100 nm-thick perforated Au film on top of a PU layer. The hole-array configurations in Figure 4f–h are applied to the Au layer of the TP cavity shown in Figure 4e. When the PU layer was doped with IR-140 dye molecules, the passive TP structure became an active Tamm plasmon laser (TPL). The characteristics of the Au nanohole array (NHA) were controlled by adjusting the hole arrangement, the unit-cell length (Λ), and the hole size (d_h). Figure 4f–h present the three NHA configurations investigated. The first is a simple periodic square array with period Λ. The second, shown in Figure 4g, is a multilattice (ML) arrangement composed of two concentric square arrays with periods Λ_1 and Λ_2. The third configuration, shown in Figure 4h, consists of nanoholes placed randomly within each repeating unit cell. As periodicity increases, multiple Tamm resonances emerge; however, these resonances disappear once the array transitions to a pseudo-periodic random configuration, defined as holes placed randomly within a repeating square unit cell. The appearance of multiple resonances was attributed to dispersion-line folding in periodically patterned TP cavities. Dispersion calculations further clarify the origin and behavior of these resonance features in both transmission and lasing emission spectra [147].

Plasmonic waveguides, although limited by propagation loss, remain valuable for routing optical energy within extremely compact regions [77,92]. Hybrid waveguides that combine dielectric and plasmonic confinement can balance loss and confinement to achieve functional pathways for dense circuit architectures [81,148]. As the need for optical interconnect density increases, plasmonic waveguides may provide the only viable solution for submicron-scale wiring.

https://doi.org/10.3390/mi17010119

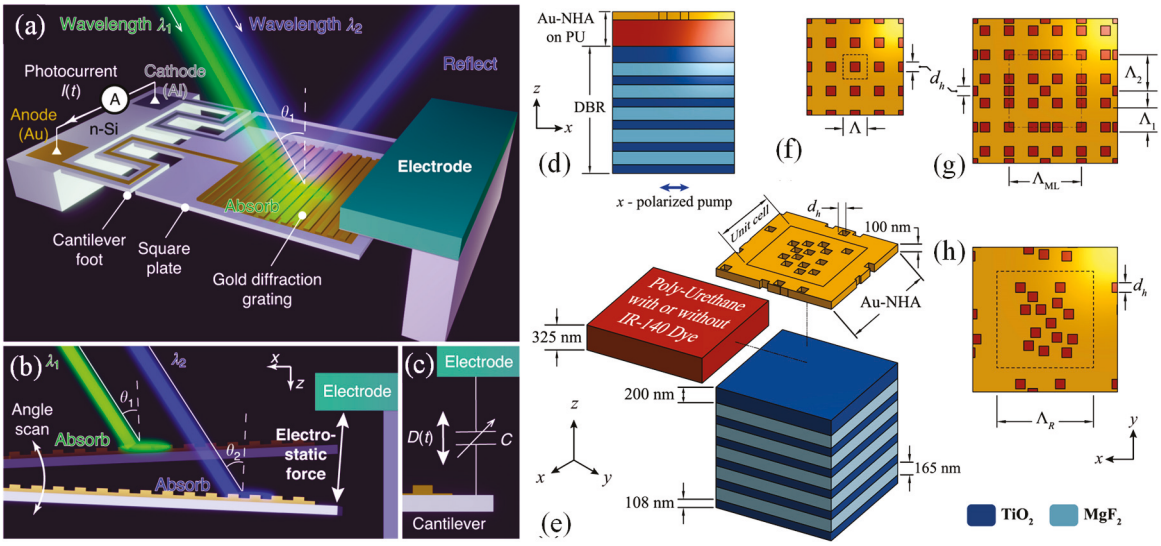


Figure 4. Principle of the electromechanically reconfigurable plasmonic photodetector, (**a**) Schematic of the device featuring a plasmonic structure with a gold diffraction grating, (**b**) Electromechanical angular scanning enabling wavelength-dependent photodetection, (**c**) Capacitive coupling between the fixed electrode and the cantilever, generating a periodic displacement current [143], (**d**) Schematic of the Tamm plasmon (TP) device comprising a Au nanohole array (Au-NHA) on a polyurethane (PU) layer placed atop a DBR, illuminated from below along the + z direction, (**e**) Exploded view with key structural parameters. The PU layer can be either undoped—serving as a passive resonant cavity—or doped with IR-140 dye to form a Tamm plasmonic laser (TPL), (**f**–**h**) Top-view illustrations of three NHA configurations and their corresponding unit-cell lengths: (**f**) a regular NHA with period Λ, (**g**) a multilattice (ML) NHA with additional periods Λ_1 and Λ_2, and (**h**) a unit cell containing randomly distributed holes. All Au-NHA holes are square with a side length [147].

5. MS Photonic Devices as System-Level Disruptors

MS devices have advanced beyond individual optical components and are now poised to reshape entire systems [115,126,135]. Beam steering MSs, for example, can replace bulky mechanical systems in LiDAR by imposing electronically controlled phase gradients. This approach allows rapid scanning speeds, reduced power consumption, and compact form factors suitable for consumer electronics and autonomous navigation systems [149]. Metalenses illustrate the transformative potential of MSs by collapsing the complexity of traditional lens systems into thin, planar layers [11]. These lenses can be engineered for specific spectral bands, for broad achromatic operation, or for insensitivity to polarization. As computational imaging techniques mature, metalenses may be integrated with algorithms to produce imaging systems that achieve superior performance with minimal hardware [115].

Recently, Ullah et al. demonstrated an all-dielectric coding MS that advances the understanding of spin-dependent light–matter interactions and enables spin-switchable wavefront manipulation [150]. Their design, composed of Si nanobricks arranged in a square lattice, exploits tailored coding patterns to simultaneously modulate the geometric and propagation phases at 780 nm. This capability allows efficient spin-dependent wavefront control, enabling functionalities such as generating optical vortex beams with various orbital angular momentum (OAM) states and performing beam-shaping operations that split and steer the incident beam at prescribed angles. Figure 5 presents the schematic configuration of the proposed 2-bit/1-bit spin-selective coding MS. When circularly polarized (CP) light with handedness $\pm\sigma$ is incident normally, the MS directs the output into the cross-polarized channel, generating either an OAM-carrying structured beam or a split beam depending on the input spin state. Under right-handed circular polarization

https://doi.org/10.3390/mi17010119

(RCP, +σ), the MS functions as a vortex-beam generator, producing distinct OAM modes. In contrast, left-handed circular polarization (LCP, −σ) induces controlled beam splitting at a designed angle. These functionalities arise from the precise engineering of the coding patterns and the hybrid 2-bit/1-bit encoding, which enables flexible and independent manipulation of the transmitted wavefronts. Convolution-based operations further enhance the versatility of the MS, supporting more complex and multichannel optical manipulations. Collectively, this strategy provides a simple yet powerful framework for developing high-capacity encrypted communications, quantum information systems, and advanced non-invasive imaging technologies [150].

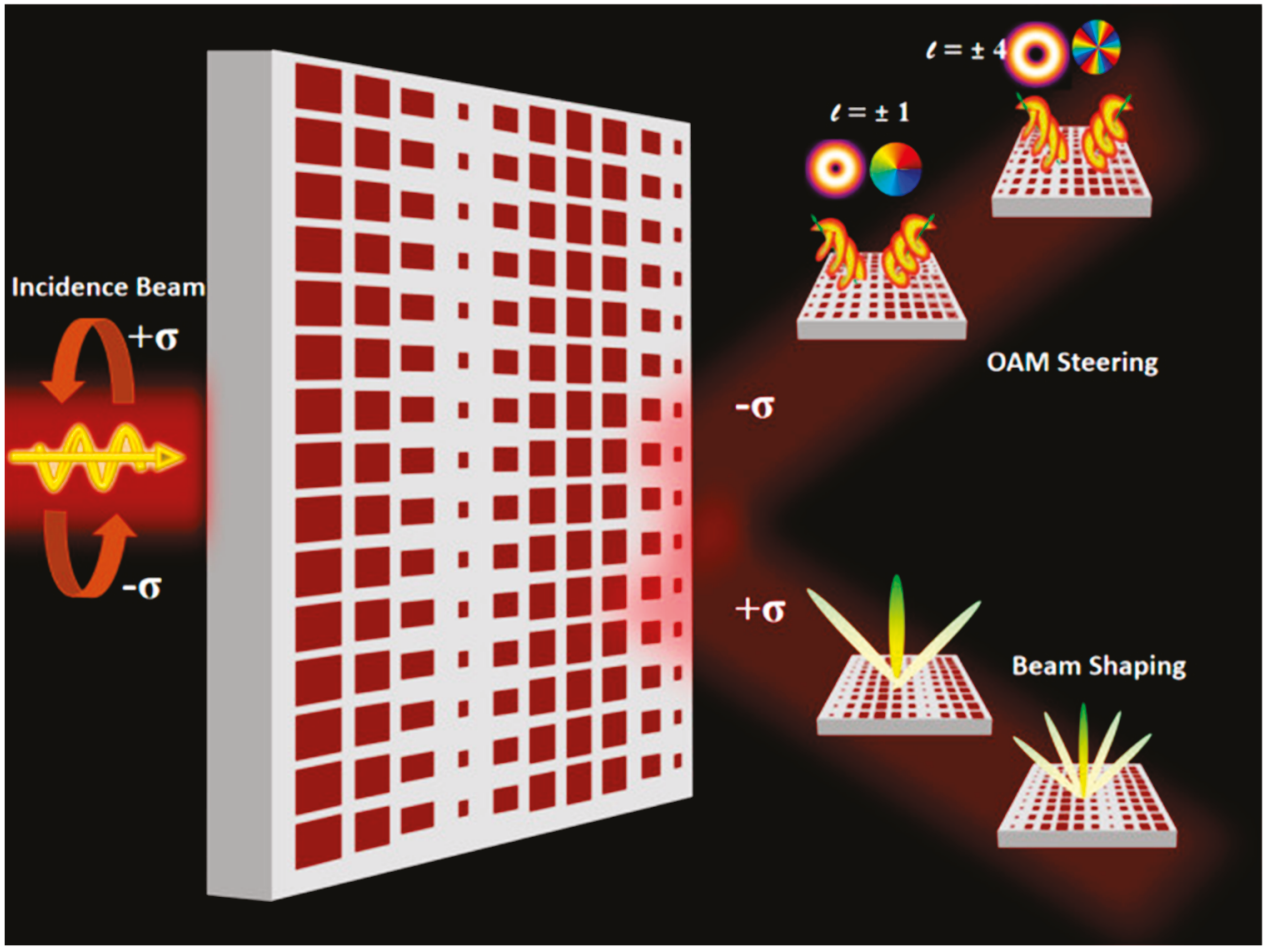


Figure 5. Schematic illustration of the various spin-switchable functionalities enabled in the proposed design by altering the handedness of the incident light [150].

Holographic MSs extend this concept by offering complete control over the structure of optical wavefronts [151,152]. They can generate three-dimensional holograms, encode spatial information into beams, or perform optical transformations that mimic the functions of neural networks. Such holographic processors could one day serve as analog accelerators for machine learning workloads [153]. Hu et al. presented a 3D-integrated MS device that stacked a hologram MS with a monolithic Fabry–Pérot cavity color-filter microarray, enabling simultaneous low-crosstalk, polarization-independent, high-efficiency full-color holography and color microprinting [154]. This dual-function platform offers a new route for applications such as data storage, security encoding, color display technologies, and information processing. The 3D integration strategy can be further expanded by incorporating additional functional MS layers, such as polarizers or metalenses to create multifunctional flat optical systems. Figure 6a shows the 3D-integrated MS, consisting

https://doi.org/10.3390/mi17010119

of a stepwise MDMFP color-filter array and a hologram MS. The metal–dielectric–metal Fabry–Pérot filters, formed by varying the dielectric thickness, provide high transmission, a wide color gamut, and narrow linewidths, superior to plasmonic color filters [154].

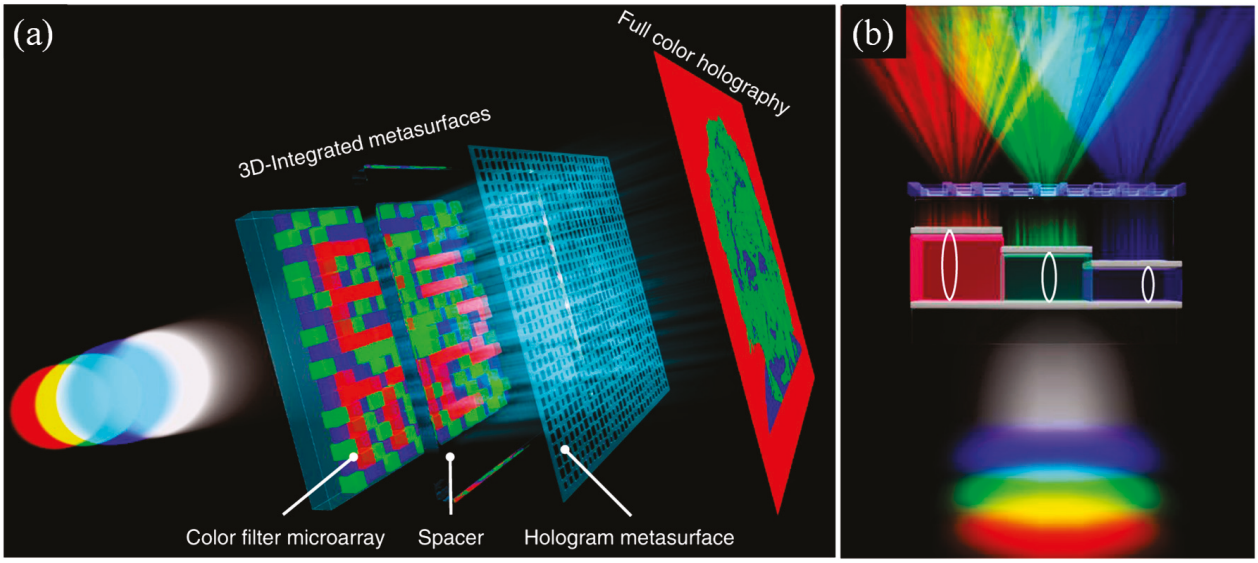


Figure 6. 3D-Integrated MSs for Full-Color Holography: (**a**) The exploded diagram shows the device architecture. A color-filter microarray forms a visible microprint under white-light illumination, while the underlying MS encodes holographic phase information. When illuminated with red, green, and blue lasers, the structure produces three independent far-field holograms that can be combined to form a full-color image, (**b**) The front view shows three micro-units composed of metal–dielectric–metal Fabry–Pérot cavity filters. Each filter transmits only the laser wavelength closest to its resonance, directing the selected light to the hologram MS and generating three separate monochromatic greyscale holograms [154].

The hologram MS, made of isotropic dielectric nanostructures, imparts the required phase profile for high-quality far-field holography. As illustrated in Figure 6b, under RGB laser illumination, each wavelength passes only through the filter whose resonance closely matches it, then reaches the hologram layer to form three independent monochromatic greyscale holograms. Combining these channels yields a full-color hologram. The device simultaneously encodes holographic information and color microprint patterns within the arranged filter array. This 3D integration offers several advantages over wavelength-multiplexed plasmonic and PB-phase MS holography: (i) higher transmission and diffraction efficiency due to FP cavity filters and dielectric nanostructures; (ii) reduced inter-channel crosstalk from the narrow FP resonances; (iii) polarization-independent operation; and (iv) straightforward fabrication using standard EBL and metal deposition without pattern-transfer steps [154].

Reconfigurable MSs represent one of the most exciting directions for future research [11,116,117]. By incorporating materials such as phase change alloys, liquid crystals, graphene, or mechanical actuation layers, MSs can dynamically alter their optical response [155–157]. These platforms can tailor electromagnetic wave propagation through a wide range of tuning mechanisms that modify their effective optical, electrical, or geometric properties (Figure 7). Electrical tuning uses components including varactors, PIN diodes, and graphene gating to adjust the response by altering circuit parameters or carrier density [158]. Thermal tuning, enabled by phase-change materials such as VO_2 or GST and by thermo-optic effects, modulates the refractive index through controlled heating [159]. Optical tuning relies on photoexcitation or nonlinear optical processes to modify carrier concentration or refractive index using incident light [160,161]. Mechanical tuning, imple-

https://doi.org/10.3390/mi17010119

mented with MEMS actuators or flexible substrates, directly alters the physical geometry of the meta-atoms [162]. Additional mechanisms such as electro-optic tuning, which exploits the Pockels or Kerr effects, and magneto-optic tuning, which uses magnetic bias in ferrites, provide high-speed or nonreciprocal control [163]. Collectively, these mechanisms offer powerful and versatile pathways for achieving dynamic beam steering, tunable absorption, reconfigurable holography, and adaptive wavefront engineering.

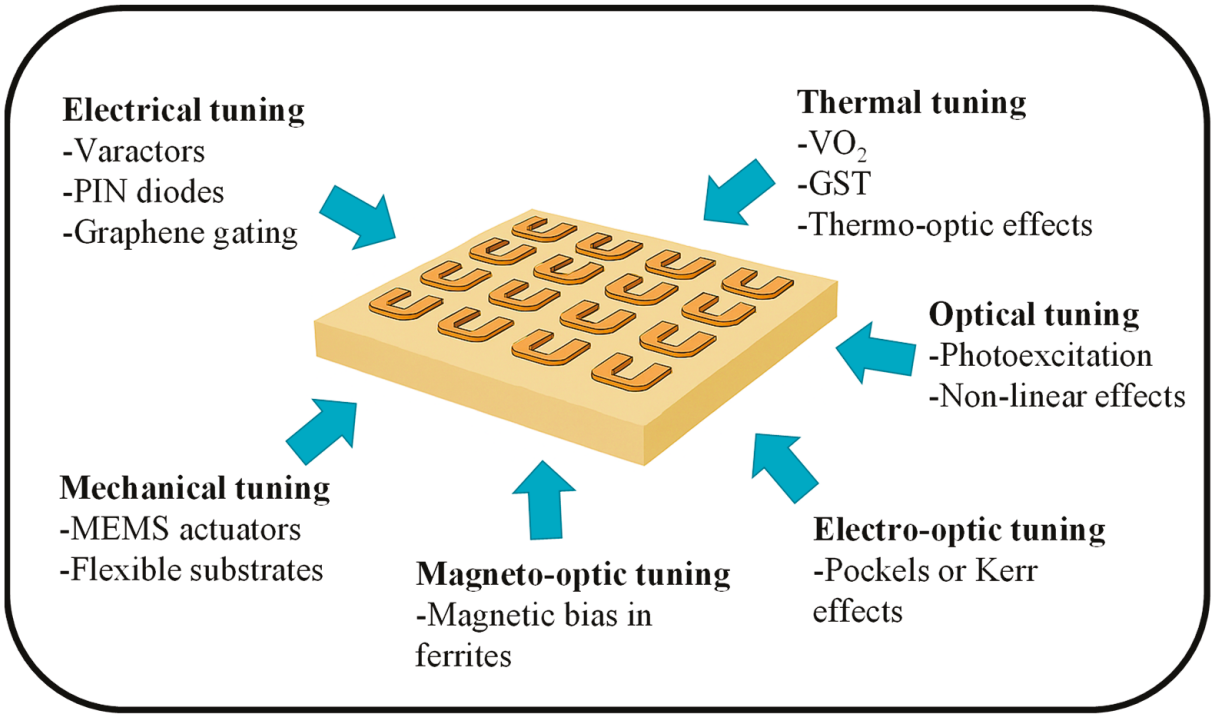


Figure 7. Tuning mechanisms for reconfigurable MSs.

6. Hybrid Plasmonic and Photonic Architectures for Planar Optical Systems

Hybrid photonic plasmonic systems provide an effective pathway for combining the complementary strengths of dielectric photonics, plasmonics, and MSs within planar optical platforms. Dielectric components offer low-loss signal distribution and stable optical functionality, while plasmonic elements enable extreme field confinement, ultrafast response, and enhanced light-matter interaction within deeply subwavelength regions [55,80,164,165]. By incorporating plasmonic functionality only where strong interaction is required, hybrid systems achieve high performance without the efficiency penalties associated with fully plasmonic architectures.

Hybrid modulators serve as a representative example of this approach. In such devices, localized plasmonic regions are incorporated within otherwise dielectric guiding structures, enabling large modulation efficiency over short interaction lengths [166,167]. Kieninger et al. demonstrated long-term thermally stable silicon organic hybrid modulators that satisfy Telcordia high temperature storage requirements [168]. These results highlight the suitability of hybrid architectures for practical and reliable optical systems. The silicon organic hybrid Mach-Zehnder modulator shown in Figure 8 illustrates the operating principles of this approach. Figure 8a presents the top view of the device, showing the Mach Zehnder interferometer geometry with multimode interference couplers for optical splitting and recombination, along with the ground signal ground transmission line used for electrical driving. Figure 8b depicts the cross section of each interferometer arm, where a silicon slot waveguide filled with an electro-optic polymer concentrates the radio frequency

https://doi.org/10.3390/mi17010119

electric field within a nanoscale region. This configuration enables strong overlaps between the electrical and optical fields, resulting in efficient phase modulation while maintaining low loss dielectric propagation. Figure 8c shows the high-speed transmission configuration used to evaluate device performance, illustrating how the modulated optical signal is generated, amplified, and detected. Figure 8d presents representative eye diagrams at forty gigabits per second after extended thermal storage, demonstrating stable high speed operation and confirming the robustness of the hybrid design [168].

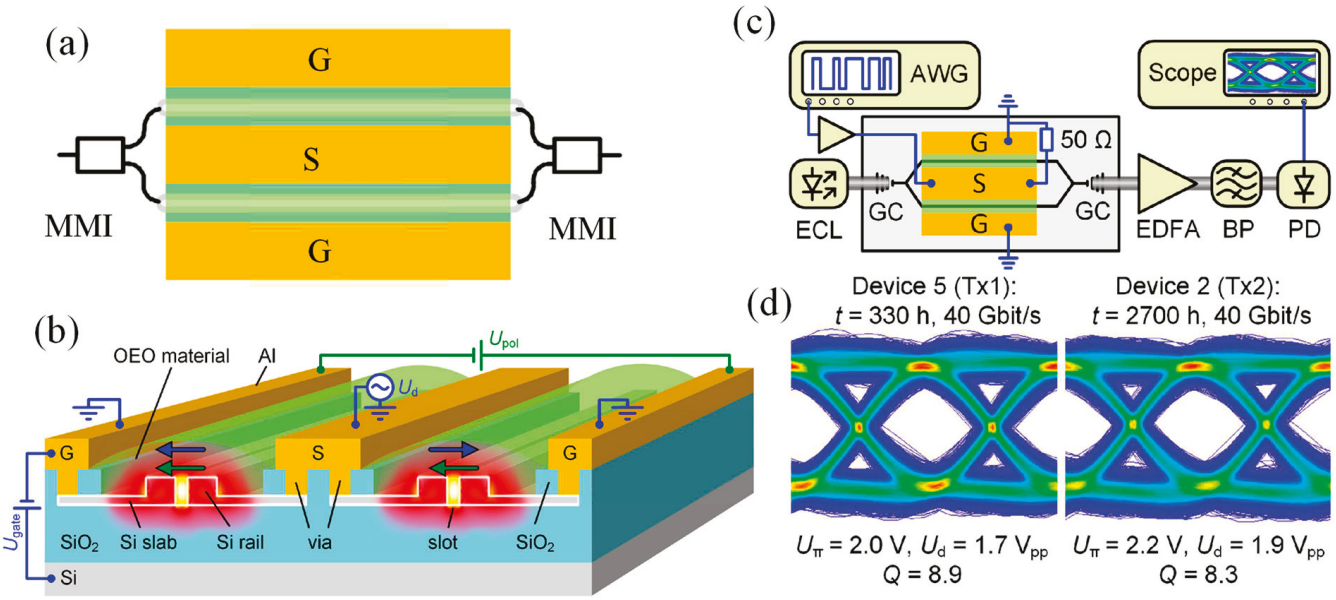


Figure 8. SOH modulator concept. (**a**) Top view of the SOH MZM with GSG transmission line and MMI couplers, (**b**) Perspective view showing the Si slot waveguides, EO-filled slot, poling process, and push–pull operation, (**c**) Setup for generating and detecting 40-Gbit/s signals using the SOH modulator, (**d**) 40-Gbit/s eye diagrams for devices after 330 h and 2700 h of high-temperature storage, showing ~10% drive-voltage increase for the aged device [168].

Hybridization also extends naturally to MS-based platforms, where plasmonic and active material responses can be combined at the meta-atom level. Figure 9 illustrates a terahertz hybrid MS that integrates multiple control mechanisms within each meta-atom [169]. Figure 9a shows the unit cell architecture, in which phase change material and semiconductor components are co-located to enable electrically and optically driven modulation. Figure 9b illustrates the simulated or measured electromagnetic response of the MS under different external stimuli, demonstrating independent tuning channels. Figure 9c presents system-level functionality in the form of switching or logic operations enabled by multi-field control. This example highlights how hybrid MSs move beyond passive wavefront shaping to support programmable and multifunctional optical behavior [169].

Efficient coupling between dielectric and plasmonic regions remains a central challenge due to mismatched modal profiles and dispersion characteristics [55,80]. Design strategies such as tapered transitions, slot-based confinement, and impedance-matching structures enable controlled energy transfer over short distances, allowing plasmonic regions to function as localized processing nodes embedded within larger planar optical systems.

Despite their advantages, hybrid photonic plasmonic systems face challenges related to optical loss, thermal management, and fabrication tolerance [165]. Heat generated by plasmonic elements can influence nearby dielectric or MS structures, while nanoscale fabrication variations can affect coupling efficiency and device reproducibility. Continued

https://doi.org/10.3390/mi17010119

advances in alternative plasmonic materials, thermal engineering, and scalable nanofabrication techniques are therefore essential.

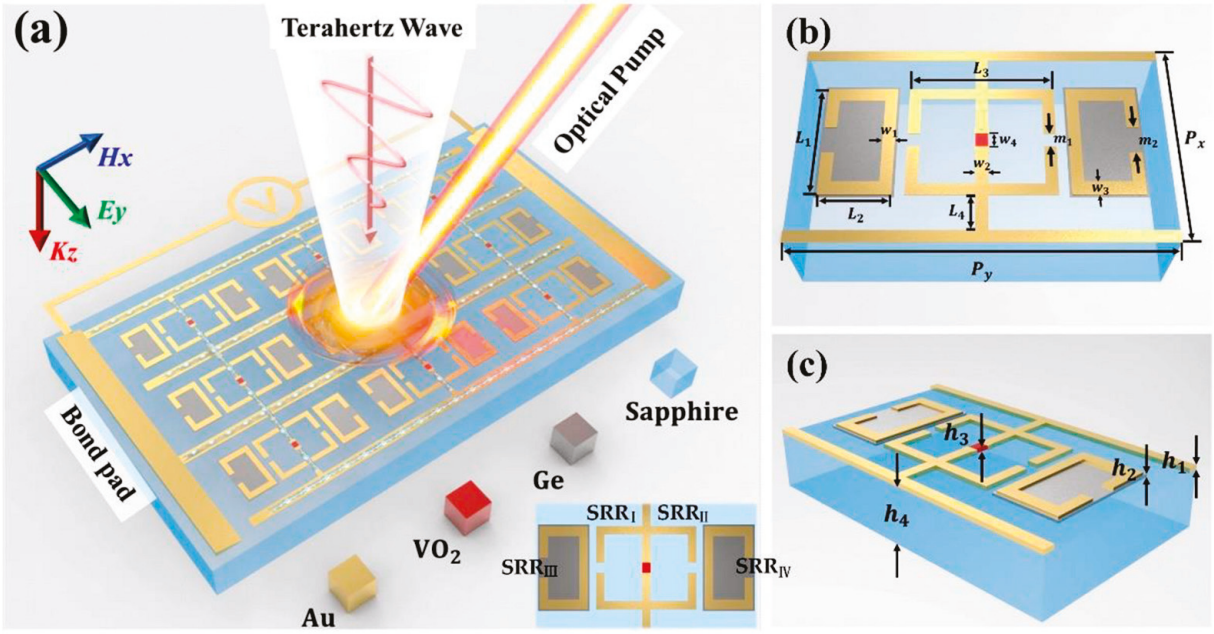


Figure 9. Schematic design and operating mechanism of the proposed hybrid MS. (**a**) Conceptual illustration of the MS, where the phase-change material VO_2 is electrically driven, and the semiconductor Ge is modulated by optical pumping. (**b**,**c**) Geometric configuration and detailed dimensional parameters of the unit cell [169].

From a system perspective, hybrid platforms enable simultaneous optimization of footprint, efficiency, speed, and functionality. Compared to purely dielectric devices, hybrid systems offer enhanced modulation efficiency and access to ultrafast and nonlinear optical responses [101,170]. Compared to fully plasmonic implementations, they provide improved stability and reduced loss. As a result, hybrid photonic plasmonic architectures represent a practical pathway toward compact, multifunctional, and programmable planar optical systems that bridge nanoscale physics and real-world applications [5,64,171–173].

7. Applications and Emerging Technologies That Will Drive Adoption

The convergence of plasmonics and MSs aligns closely with several emerging technological trends [174]. Optical computing stands at the forefront, requiring high-speed operations and parallel processing capabilities [175,176]. MS-based optical neural networks can process information at the speed of light by performing matrix multiplications in free space, while plasmonic nonlinearities may offer the necessary activation functions for all optical deep learning systems [175].

Augmented reality (AR) and virtual reality (VR) demand compact, lightweight, and high-performance optical systems [5]. MSs can produce thin lens stacks, holographic combiners, and tunable beam shaping devices that are essential for next generation wearable displays. Integrating plasmonic sensors into these systems could provide simultaneous health monitoring or environmental sensing [177]. Contact lenses play a central role in vision correction and are increasingly regarded as a promising platform for AR displays through the incorporation of electronic and optical functionalities. MSs provide rich optical control within an ultrathin footprint, making them attractive for compact imaging and display applications. Despite this potential, integrating MSs into contact lenses remains difficult due to the limited biocompatibility of conventional imprinting materials and structural deformation arising from swelling and contraction on hydrated surfaces.

https://doi.org/10.3390/mi17010119

Ko et al. presented a biocompatible transfer strategy that employs hyaluronic acid (HA) as a soft mold to realize MS integration on contact lenses and enable holographic light projection [178]. A high-efficiency metahologram was achieved using all-metallic three-dimensional meta-atoms with rectangular anisotropy and a reflective metallic backplane. Figure 10 illustrates the schematic of an MS-integrated contact lens. In the reflection mode, the MS-engineered wavefront propagates into the far field, where it reconstructs the target holographic image. The phase-only computer-generated hologram (CGH) was obtained using the Gerchberg–Saxton (GS) algorithm based on iterative Fourier transforms. To efficiently realize the retrieved phase profile, the MS consists of uniformly sized meta-atoms with spatially varying in-plane rotation angles, enabling phase control through the Pancharatnam–Berry (PB) mechanism. By leveraging the PB phase, the reflected wavefront acquires a spatially tailored phase distribution while maintaining a nearly uniform amplitude. To suppress wrinkling and maintain structural integrity during transfer onto soft, wettable lenses, a corrugated metallic layer on the HA mold was reinforced with a SiO_2 capping layer. This biocompatible transfer approach opens a pathway for embedding diverse optical elements, including holograms, lenses, and gratings onto contact lenses, advancing AR displays and human–computer interaction technologies [178].

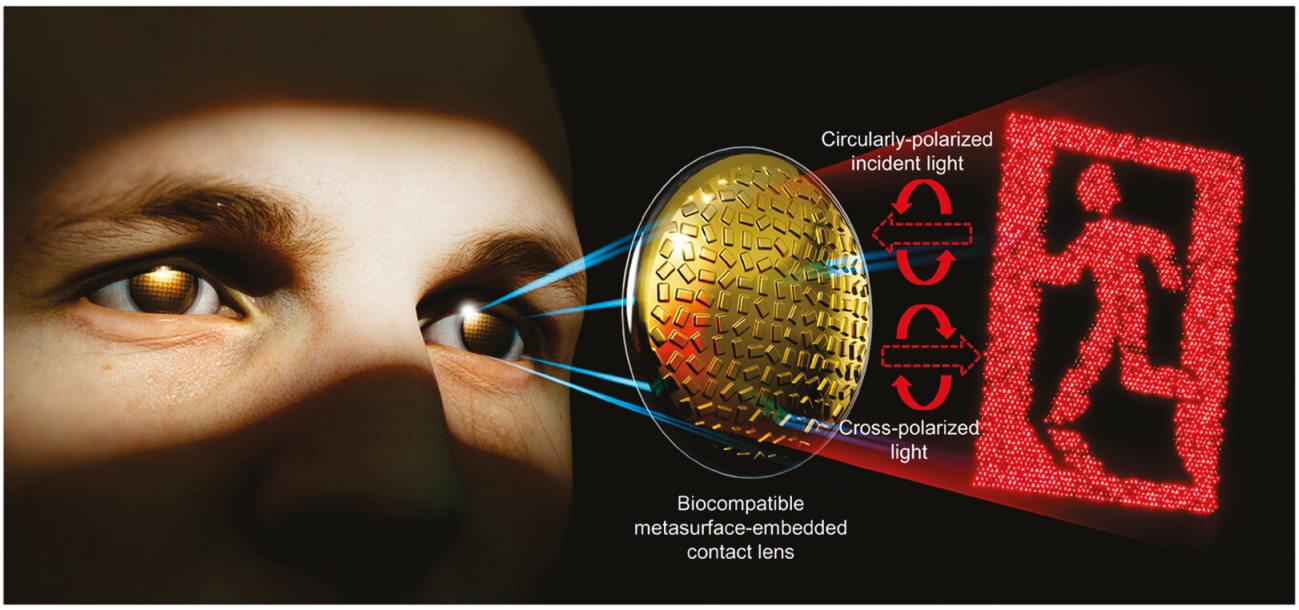


Figure 10. Schematic illustration of an MS-integrated contact lens for holographic light projection. Upon illumination with circularly polarized light, the all-metallic MS reflects and reconstructs the designed holographic image [178].

Sensing and spectroscopy represent another major application space [171–173]. Plasmonic hotspots greatly enhance Raman scattering, enabling the detection of molecular signatures at extremely low concentrations. MS-based absorbers and filters allow for compact spectrometers that operate across visible, infrared, and terahertz bands. These platforms can support portable diagnostic devices, environmental sensors, and chemical analysis systems [179]. Bound states in the continuum (BICs) are nonradiative optical modes with strong field confinement and growing relevance in nanophotonics. They are commonly classified as symmetry-protected or accidental BICs, depending on the radiation suppression mechanism. While symmetry-protected BICs are typically controlled by a single structural parameter, accidental BICs rely on complex mode coupling, making their design and application more challenging. Li et al. developed an accidental BIC MS based on periodic H-shaped Si_3N_4 nanopillars and evaluated its refractive index sensing performance through both wavelength shift and intensity modulation [180]. The sensor

https://doi.org/10.3390/mi17010119

demonstrated high sensitivity, achieving 501 nm/RIU in wavelength-based detection and 9.35×10^4 counts/RIU in intensity-based detection, and shows strong potential for biodetection applications. These results provide new insights into mode coupling in BIC systems and introduce an effective dual-channel approach for high-sensitivity optical sensing [180].

Optical biosensors enable quantitative analysis and molecular structural identification, yet conventional refractive-index-based methods often lack the sensitivity needed to detect low-molecular-weight analytes. Although non-optical platforms such as field-effect transistors offer higher sensitivity, they do not provide molecular fingerprinting capabilities. To address these limitations, Zhu et al. developed mid-infrared biosensors based on optical conductivity, enabling sensitive and quantitative detection of small molecules while enhancing their spectroscopic signatures [173]. These sensors employed a hybrid MS composed of monolayer graphene integrated with metallic nanoantennas, combining plasmonic, electronic, and spectroscopic functionalities. Molecular adsorption induces carrier doping in graphene, which can be optically detected with high sensitivity. Because the resulting resonance shifts are directly linked to graphene carrier density, the platform enables reliable quantification of molecular interactions and is insensitive to carrier mobility degradation. Figure 11 shows the structure and optical response of the hybrid MS.

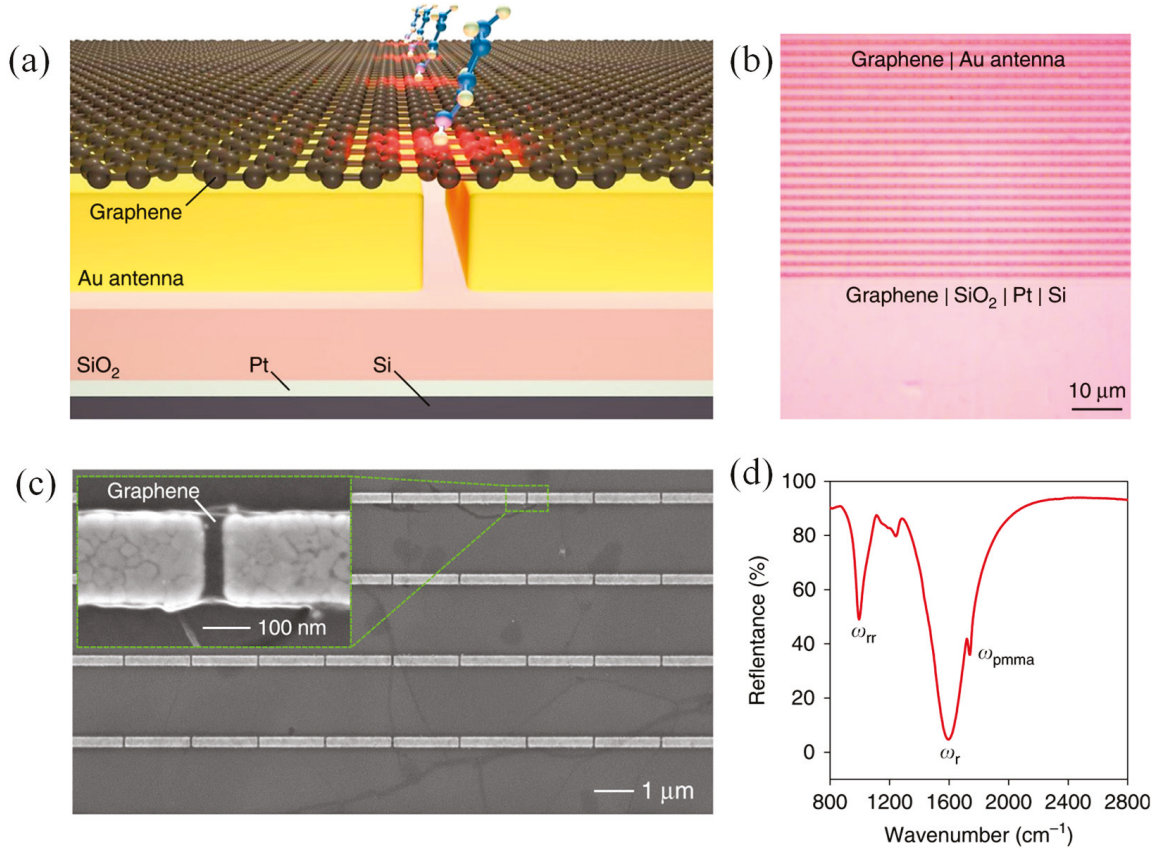


Figure 11. (**a**) Schematic illustration of the graphene–metal MS, where small analyte molecules are adsorbed onto suspended monolayer graphene. (**b**) Optical microscopy image of a fabricated device, confirming the uniform and continuous coverage of graphene across a large area. (**c**) SEM image of graphene-coated nanorod antennas; the inset highlights a single antenna gap bridged by suspended graphene. (**d**) Measured reflectance spectrum showing the dominant plasmonic resonance (ω_r) around 1500 cm^{-1}, a secondary resonance dip (ω_{rr}) near 1000 cm^{-1}, and the PMMA absorption feature (ω_PMMA) at approximately 1700 cm^{-1} [173].

As illustrated in Figure 11a, the device consisted of a periodic array of Au nanorod antennas coated with monolayer graphene and separated from a Pt back reflector by a

https://doi.org/10.3390/mi17010119

SiO_2 spacer, forming an optical cavity. The optical micrograph in Figure 11b confirms uniform graphene coverage over a large area, while the SEM image in Figure 11c reveals graphene conformally covering the nanorods and remaining suspended across 30 nm gaps, as highlighted in the inset. The reflectance spectrum in Figure 11d exhibits two mid-infrared resonance features arising from plasmon–phonon coupling: a primary plasmonic resonance near 1500 cm^{-1} (ω_r) and a secondary dip around 1000 cm^{-1} (ω_{rr}), along with a PMMA-related absorption peak near 1700 cm^{-1}. In addition, the MS supported surface-enhanced infrared spectroscopy, allowing detection of sub-nanometer molecular monolayers and affinity-based glucose sensing down to 200 pM, as well as enhanced infrared fingerprinting of trace biomolecules and polymers [173].

Communications technology continues to push for higher bandwidth and lower latency [181]. MS-based wavelength management and plasmonic high-speed modulators can significantly enhance the performance of optical interconnects [182,183]. Liu et al. presented a hybrid optical modulator formed by integrating a graphene sheet with a dielectric MS that supports a pronounced toroidal resonance [184]. The MS was composed of a pair of mirror-imaged, asymmetric silicon split-ring resonators capable of sustaining a strong toroidal dipole mode characterized by an ultra-narrow spectral linewidth (~0.77 nm), a high-quality factor (~1702), and nearly complete resonance contrast. Numerical simulations revealed that incorporating graphene enables effective control of the resonance transmission by tuning its Fermi level. A maximum modulation depth of approximately 78% was obtained, demonstrating the strong modulation capability of the proposed structure. In addition, the influence of resonator asymmetry on the toroidal response was systematically analyzed, along with the dependence of modulation efficiency on graphene parameters. These findings highlight the potential of the graphene–dielectric MS platform for applications in optical modulation, filtering, and biochemical sensing [184].

Furthermore, Zeng et al. exploited the synergistic integration of graphene with engineered MSs to realize a free-space mid-infrared modulator that operates at gigahertz frequencies, requires low driving voltages, and functions at room temperature [185]. By further patterning the hybrid graphene–MS structure into addressable pixels, a prototype spatial light modulator capable of high-frame-rate single-pixel imaging was demonstrated, offering performance improvements by several orders of magnitude compared with traditional liquid-crystal or micromirror-based devices. These results paved the way for advanced infrared wavefront manipulation, where rapid temporal and spatial modulation is essential for next-generation photonic technologies [185]. Figure 12 illustrates the operation and imaging performance of the hybrid graphene–MS spatial light modulator (SLM). The fabricated prototype consists of a 6×6 array of electrically isolated functional pixels, as shown in Figure 12a,b. Each pixel can be independently switched between an "ON" and "OFF" state by applying gate voltages of +7 V and -3 V, respectively, enabling programmable spatial modulation of mid-infrared light.

The device functionality was first characterized through raster scanning of individual pixels. As shown in the insets of Figure 12c, predefined mask patterns forming the letters "CINT" were clearly resolved by sequentially activating one pixel at a time while keeping all others in the OFF state. These measurements, performed at a wavelength of 8.3 μm, demonstrated accurate spatial encoding by the MS SLM. When the pixels corresponding to each mask are switched ON simultaneously, the reflected signal exhibits distinct real-time variations as different masks are applied, as indicated by the red trace in Figure 12c. The single-pixel imaging capability of the SLM was demonstrated using the experimental configuration shown schematically in Figure 12d. Reconstructed images of a cross-shaped object at different wavelengths are presented in Figure 12e, confirming broadband imaging functionality. Higher image contrast was observed at wavelengths

https://doi.org/10.3390/mi17010119

of 7 μm and 8.5 μm, whereas reduced contrast appeared at 5.5 μm and 9.5 μm, reflecting the wavelength-dependent modulation efficiency of the device. Together, Figure 12a–e validate the feasibility of the hybrid graphene–MS SLM for high-speed, programmable mid-infrared imaging applications [185].

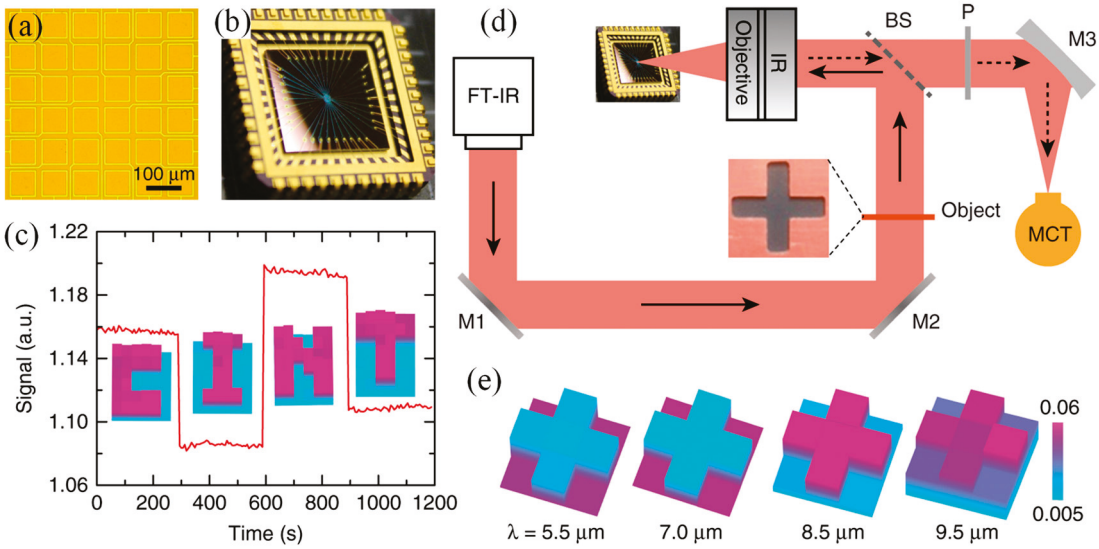


Figure 12. Hybrid graphene–MS spatial light modulator and single-pixel imaging demonstration. (**a**) Optical micrograph of the active region, showing a 6 × 6 array of independently addressable functional pixels, (**b**) Photograph of the fabricated device after wire bonding to a chip carrier, (**c**) Measured spatial reflection patterns forming the word "CINT" at a wavelength of 8.3 μm, obtained by selectively applying gate voltages of −3 V (OFF) and +7 V (ON) to individual pixels. The insets show the corresponding mask patterns acquired by raster scanning, where only one pixel is switched ON at a time while all others remain OFF (purple denotes the ON state). Variations in the applied SLM patterns lead to distinct changes in the detected single-pixel signal intensity, (**d**) Schematic of the single-pixel imaging setup incorporating the hybrid graphene–MS SLM, including flat mirrors (M1, M2), a beam splitter (BS), a polarizer (P), a parabolic mirror (M3), and a mercury–cadmium–telluride (MCT) single-pixel detector, (**e**) Reconstructed images of a cross-shaped target obtained using a raster-scan measurement matrix at wavelengths of 5.5 μm, 7 μm, 8.5 μm, and 9.5 μm, demonstrating broadband imaging capability [185].

8. Core Challenges Driving the Research Strategy

Although the future appears promising, several grand challenges stand between current technologies and large-scale deployment. As summarized in Figure 13, advancing MS and plasmonic platforms toward scalable, high-performance operation requires addressing four primary hurdles: (i) intrinsic material losses that limit efficiency in plasmonic systems, (ii) chromatic dispersion that constrains broadband and achromatic functionality, (iii) fabrication scalability necessary for wafer-level patterning with nanoscale precision, and (iv) thermal reliability issues arising from optical field–induced heating and repeated phase-change cycling.

From a manufacturing perspective, scalable preparation technologies capable of balancing nanoscale accuracy with high throughput are rapidly emerging [186]. Deep ultraviolet lithography, particularly 193 nm immersion processes, offers excellent critical dimension control, overlay accuracy, and compatibility with CMOS foundries, making it well-suited for wafer-scale MS and plasmonic device fabrication [187,188]. Nanoimprint lithography provides a complementary approach, enabling cost-effective, high-throughput replication of dense nanostructures over large areas and has already been adopted for commercial metalens production [189,190]. Hybrid fabrication strategies that combine optical lithography for alignment-sensitive layers with nanoimprint techniques for large-area patterning

https://doi.org/10.3390/mi17010119

further enhance manufacturability, suggesting a realistic pathway toward mass production of plasmonic and MS-based optical systems [35,191].



Figure 13. Key Technical Challenges Limiting Scalable MS and Plasmonic Technologies.

Loss in plasmonic materials remains a fundamental issue, particularly for applications requiring high efficiency [32,192]. Advances in material synthesis, epitaxy, and hybrid mode engineering may mitigate these losses, but completely overcoming them remains difficult [193]. MSs face their own limitations in chromatic dispersion, which restricts broadband functionality and achromatic imaging performance [194]. Scalability of fabrication is another major barrier. To integrate MSs into consumer electronics or large area optical systems, manufacturing processes must transition toward wafer-scale patterning without sacrificing nanoscale precision [195,196]. Furthermore, thermal reliability presents concerns for both plasmonic and phase change-based MSs, as repeated cycling or sustained field intensity can degrade material performance [197,198]. These challenges reflect not only technological hurdles but also opportunities for interdisciplinary innovation. The combined expertise of materials scientists, nanofabrication engineers, optical physicists, and computational designers will be essential for shaping the next generation of integrated optical systems.

Beyond the challenges discussed above, several open issues remain insufficiently explored at a fundamental and system level. In particular, the long-term stability, aging behavior, and failure mechanisms of densely integrated plasmonic and MS structures under realistic electrical, thermal, and optical operating conditions are not yet well understood. Equally important is the absence of unified system-level design methodologies that explicitly account for cross-domain interactions among optics, electronics, thermal transport, and control circuitry. Finally, there is a growing need for predictive multiscale modeling frameworks that can bridge nanoscale electromagnetic response with macroscopic system performance, reliability, and manufacturability. Addressing these issues will be critical for the transition from proof-of-concept demonstrations to robust, scalable photonic technologies.

An additional challenge that becomes increasingly critical at the system level is balancing peak device performance with power consumption and thermal management [199]. While plasmonic and MS devices often demonstrate record speed, compactness, or field confinement, practical deployment requires optimization of energy-per-operation rather than isolated performance metrics [200]. In many cases, reduced device length, lower

https://doi.org/10.3390/mi17010119

capacitance, and strong light–matter interaction enable overall energy efficiency despite intrinsic optical loss. Hybrid architectures that localize high-speed or high-field functionality to specific regions, while relying on low-loss dielectric routing elsewhere, provide a practical pathway for managing thermal load [201,202]. As a result, performance, power dissipation, and thermal stability must be treated as coupled design variables in future integrated photonic systems rather than optimized independently.

9. Future Vision: Roadmap for Next-Generation Plasmonic and MS Photonics

The future of planar optical systems is increasingly shaped by concrete experimental demonstrations that translate plasmonic and MS concepts from theoretical constructs into functional devices and system-level components [123]. A growing body of work reveals a clear trajectory toward optical platforms that are flat by design, programmable in functionality, and tightly coupled to electronic drivers and computational frameworks, signaling a fundamental shift in how optical hardware is conceived and implemented [203,204]. Rather than relying on bulk components or extended propagation paths, future optical systems emphasize interface-engineered functionality, where light manipulation occurs within subwavelength regions and planar layers.

Metalens-based imaging platforms provide one of the most visible indicators of this transition. Commercial demonstrations have shown that a single MS lens can replace complex stacks of refractive elements in compact sensing modules, while remaining compatible with semiconductor manufacturing and delivering performance suitable for depth sensing and biometric applications [205]. Academic and industrial efforts have further extended this concept to compact infrared imaging systems for extended reality headsets and multi-wavelength metalenses for aerial and mobile cameras [122]. These developments outline a realistic pathway toward optical stacks for cameras, microscopes, and head-mounted displays that achieve high performance within thicknesses of only hundreds of nanometers to a few micrometers.

A similar evolution is occurring in beam steering and ranging technologies. MS-based beam steering using liquid crystal loading and high-index nanoantenna arrays has demonstrated solid-state operation without mechanical motion and with angular coverage sufficient for automotive lidar [149]. Emerging commercial platforms further validate this approach by introducing programmable MS chips capable of large-angle beam steering controlled entirely through software, already integrated into three-dimensional ranging modules [206]. These results suggest that future depth sensing, free space communication, and adaptive illumination systems will increasingly rely on flat programmable apertures rather than mechanically scanned optics or phased arrays.

Intelligent photonic surfaces represent another major pillar of the roadmap. Diffractive and MS-based optical neural networks have demonstrated that passive planar layers can perform classification and inference tasks directly in the optical domain [207]. Subsequent implementations using MSs with tailored phase profiles have enabled image recognition, digit classification, and multiplexed optical processing in both near-field and far-field configurations, including architectures that exploit geometric phase control and polarization multiplexing [208]. More recent proposals extend this concept toward all optical convolutional neural networks in which MSs implement convolutional operations and diffractive layers act as optical decoders, pointing toward physically implemented machine learning systems that operate at the speed of light [209]. These advances illustrate how MSs can evolve from static optical components into adaptive information processing layers co-designed with electronic learning and control algorithms.

https://doi.org/10.3390/mi17010119

On the plasmonic side, hybrid photonic plasmonic devices provide a complementary pathway toward ultrafast and energy-efficient active functionality at deeply subwavelength scales. Hybrid modulators incorporating transparent conducting oxides operating in the epsilon near zero regime have demonstrated micrometer-scale footprints, femtojoule per bit energy consumption, and multi-gigahertz modulation bandwidths [210]. Related architectures that integrate indium tin oxide or similar materials within slot waveguides or asymmetric coupling structures further enhance light-matter interaction while maintaining manageable insertion loss [93]. Proposals combining transparent conducting oxides with graphene indicate that two-dimensional materials will play an increasingly important role in future active devices by enabling stronger tunability and reduced driving voltages [211]. Collectively, these results support a vision in which plasmonic elements function as localized switching and modulation nodes embedded within broader planar optical systems rather than as standalone guiding platforms.

Reconfigurable MSs form an additional cornerstone of the roadmap. Platforms based on phase change materials, mechanical actuation, and electro-optical tuning enable dynamic control over phase, amplitude, and beam direction [212]. Low-loss phase change materials such as antimony selenide have enabled rewritable on-chip MSs with strong refractive index contrast and nonvolatile operation in technologically relevant spectral bands [213,214]. Mechanically tunable and liquid crystal-based MSs have demonstrated real-time beam steering and adaptive wavefront control, directly addressing the needs of lidar, adaptive optics, and dynamic imaging systems [215,216]. As these technologies mature, intelligent photonic surfaces capable of real-time optimization through sensor feedback and machine learning based controllers become increasingly feasible.

Taken together, these developments outline a coherent roadmap for next-generation planar photonics. Continued progress in low-loss plasmonic materials and optimized hybrid geometries is required to push modulators and switches into regimes where they outperform purely dielectric devices in both energy efficiency and footprint [136,217]. MSs must advance toward broadband and multifunctional operation, as demonstrated by multicolor metalenses and folded MS imaging systems that already show compact and high-quality performance in proof-of-concept devices [218]. Three-dimensional meta-optical architectures that combine multiple planar layers or folded optical paths will be essential for realizing complete imaging and spectroscopic systems within millimeter or submillimeter thicknesses. At the same time, compatibility with standard semiconductor fabrication processes remains a key enabler for large-scale deployment, as evidenced by commercial efforts in flat optics and foundry-compatible MS platforms targeting mass production [205]. These trends support a future in which hybrid plasmonic and MS photonics provides a unified design framework for planar, programmable, and computationally aware optical systems [172].

To synthesize these directions at the system level, Figure 14 presents a consolidated roadmap linking plasmonic, MS, and hybrid planar platforms to emerging application domains. As illustrated, MS-based imaging, sensing, and beam steering technologies are positioned for near term commercialization due to their reliance on predominantly passive functionality and strong compatibility with wafer-scale manufacturing [219–221]. In contrast, optical computing and highly reconfigurable photonic processors offer substantial long-term impact but face higher barriers related to system integration, programmability, power consumption, and thermal management [111,222]. This progression suggests a staged development pathway in which passive and quasi-static planar optics mature first, followed by increasingly complex active and computational photonic systems.

https://doi.org/10.3390/mi17010119

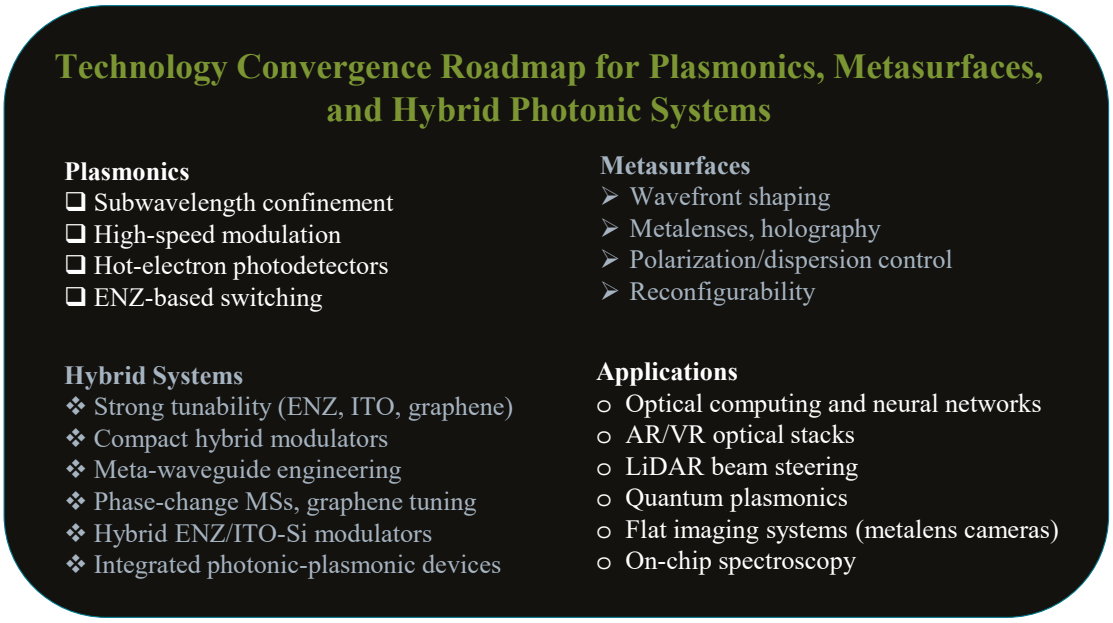


Figure 14. Roadmap illustrating the functional domains of plasmonics, MSs, and hybrid photonic systems, and their connection to emerging optical applications.

10. Concluding Remarks

The convergence of plasmonics and MSs marks a pivotal moment in the evolution of planar and interface-engineered photonic systems, reshaping long-standing assumptions about how optical hardware should be designed, fabricated, and optimized. Throughout this review, it has become evident that plasmonics provides unmatched field confinement, ultrafast light matter interaction, and the ability to engineer strong optical nonlinearities within deeply subwavelength volumes. At the same time, MSs introduce unprecedented control over phase, amplitude, polarization, and dispersion within planar interfaces measured in only hundreds of nanometers. When these two domains are considered jointly rather than independently, a new design space emerges in which optical functionalities traditionally requiring bulky components or long propagation lengths can be realized within compact, reconfigurable, and computationally aware architectures.

Central to this vision is the recognition that future photonic platforms will depend critically on interface-mediated control rather than bulk material propagation. Plasmonics enables modulators, detectors, and nanoscale resonant elements that operate at terahertz or even femtosecond speeds, while MSs offer versatile wavefront shaping, multiplexed information channels, and the ability to embed computational transformations directly into optical layers. Emerging hybrid systems demonstrate that these strengths are complementary rather than competitive. By combining plasmonic field enhancement with the low-loss routing and broadband manipulation offered by dielectric MSs, hybrid devices can surpass the performance of either platform alone. This synergy is already evident in applications ranging from ultracompact electro-optic modulators to multifunctional metalenses, coding MSs, and three-dimensional integrated optical processors.

Despite these opportunities, several challenges remain foundational to future progress. Loss in plasmonic materials continues to constrain efficiency for many applications. Broadband achromatic behavior in MSs is limited by dispersion, and large-area nanofabrication still requires breakthroughs in throughput, cost, and reproducibility. Thermal reliability, particularly in devices that rely on high field intensities or phase change materials, must also be addressed. These challenges are not barriers but catalysts for interdisciplinary innovation. Advances in alternative plasmonic materials such as transition metal nitrides

https://doi.org/10.3390/mi17010119

and transparent conducting oxides, along with scalable fabrication strategies such as nanoimprint lithography, deep ultraviolet patterning, and multilayer stacking, are already beginning to close these gaps.

Looking ahead, the technological trajectory outlined in this review suggests a clear roadmap. Hybrid plasmonic and MS architectures are likely to form the backbone of next-generation planar optical systems that are flatter, faster, more energy efficient, and inherently programmable. MS-based beam steering, full color holography, reconfigurable optical interfaces, and metalens-based imaging stacks are rapidly transitioning from academic demonstrations to industrial adoption. Plasmonic modulators and detectors are poised to reshape high-speed communication and optical information processing. Diffractive and MS-based neural networks point toward optical processors that merge physical wave propagation with artificial intelligence. Together, these developments indicate that future planar photonic platforms will be characterized by compact footprints, multifunctional operation, and deep coupling with electronic and computational systems.

In essence, plasmonics and MSs are no longer parallel research directions but complementary pillars of a unified planar photonics paradigm. Their combination enables devices that process, sense, modulate, and compute optical information with efficiencies and form factors unattainable in traditional bulk or waveguide-dominated architectures. As materials continue to evolve and fabrication techniques mature, plasmonic and MS-based technologies will play a defining role in next-generation optical hardware, influencing fields as diverse as optical computing, augmented and virtual reality, quantum technologies, sensing, spectroscopy, and telecommunications. The vision that emerges is one of truly planar and programmable photonic systems capable of transforming both fundamental research and applied technological landscapes.

Funding: This research received no external funding.

Data Availability Statement: No new data were created or analyzed in this study.

Acknowledgments: The author acknowledges the constant support of Warsaw University of Technology in the completion of this work.

Conflicts of Interest: The author declares no conflicts of interest.

References

1. Picot-Clémente, J. Innovations and Challenges in Modern Optical Design. *PhotonicsViews* **2024**, *21*, 22–26. [CrossRef]
2. Park, J.; Kang, H.; Huh, C.; Lee, M.J. Do Immersive Displays Influence Exhibition Attendees' Satisfaction?: A Stimulus-Organism-Response Approach. *Sustainability* **2022**, *14*, 6344. [CrossRef]
3. Klatt, S.; Smeeton, N.J. Immersive Screens Change Attention Width but Not Perception or Decision-Making Performance in Natural and Basic Tasks. *Appl. Ergon.* **2020**, *82*, 102961. [CrossRef] [PubMed]
4. Mukhtar, S.; Arbabi, A.; Viegas, J. Compact Spectral Imaging: A Review of Miniaturized and Integrated Systems. *Laser Photonics Rev.* **2025**, *19*, e01042. [CrossRef]
5. Chen, Q.; Zhou, J.; Pian, S.; Xu, J.; Li, X.; Li, B.; Lu, C.; Wang, Z.; Jiang, Q.; Qin, S.; et al. Hybrid Meta-Optics Enabled Compact Augmented Reality Display with Computational Image Reinforcement. *ACS Photonics* **2024**, *11*, 3794–3803. [CrossRef]
6. Xin, Y.; Pandraud, G.; Otten, L.; Zhang, Y.; French, P. Surface Functionalization of SU-8 Vertical Waveguide for Biomedical Sensing: Bacteria Diagnosis. *Proceedings* **2018**, *2*, 1081. [CrossRef]
7. Akkaş, T.; Reshadsedghi, M.; Şen, M.; Kılıç, V.; Horzum, N. The Role of Artificial Intelligence in Advancing Biosensor Technology: Past, Present, and Future Perspectives. *Adv. Mater.* **2025**, *37*, 2504796. [CrossRef]
8. Sozos, K.; Bogris, A.; Bienstman, P.; Sarantoglou, G.; Deligiannidis, S.; Mesaritakis, C. High-Speed Photonic Neuromorphic Computing Using Recurrent Optical Spectrum Slicing Neural Networks. *Commun. Eng.* **2022**, *1*, 24. [CrossRef]
9. Zhang, Y.; Shen, W.; Wu, S.; Tang, W.; Shu, Y.; Ma, K.; Zhang, B.; Zhou, P.; Wang, S. High-Speed Transition-Metal Dichalcogenides Based Schottky Photodiodes for Visible and Infrared Light Communication. *ACS Nano* **2022**, *16*, 19187–19198. [CrossRef]

https://doi.org/10.3390/mi17010119

10. Efron, U. Spatial Light Modulators for Optical Computing and Information Processing. In Proceedings of the Twenty-Second Annual Hawaii International Conference on System Sciences, Kailua-Kona, HI, USA, 3–6 January 1989; Volume 1: Architecture Track, pp. 416–423.
11. Khonina, S.N.; Butt, M.A.; Kazanskiy, N.L. A Review on Reconfigurable Metalenses Revolutionizing Flat Optics. *Adv. Opt. Mater.* **2024**, *12*, 2302794. [CrossRef]
12. de Ceglia, D.; Alù, A.; Neshev, D.N.; Angelis, C.D. Analog Image Processing with Nonlinear Nonlocal Flat Optics. *Opt. Mater. Express* **2024**, *14*, 92–100. [CrossRef]
13. Yu, N.; Capasso, F. Flat Optics with Designer Metasurfaces. *Nat. Mater.* **2014**, *13*, 139–150. [CrossRef]
14. Odom, T.W.; Schatz, G.C. Introduction to Plasmonics. *Chem. Rev.* **2011**, *111*, 3667–3668. [CrossRef] [PubMed]
15. Wang, Z.; Chen, C.; Wu, K.; Chong, H.; Ye, H. Transparent Conductive Oxides and Their Applications in Near Infrared Plasmonics. *Phys. Status Solidi A* **2019**, *216*, 1700794. [CrossRef]
16. Iwanaga, M.; Hu, Q.; Tang, Y. Metasurface Biosensors: Status and Prospects. *Appl. Phys. Rev.* **2025**, *12*, 021305. [CrossRef]
17. Agrahari, R.; Dwivedi, S.; Jain, P.K.; Mahto, M. High Sensitive Metasurface Absorber for Refractive Index Sensing. *IEEE Trans. Nanotechnol.* **2023**, *22*, 328–335. [CrossRef]
18. Butt, M.A.; Khonina, S.N.; Kazanskiy, N.L.; Piramidowicz, R. Hybrid Metasurface Perfect Absorbers for Temperature and Biosensing Applications. *Opt. Mater.* **2022**, *123*, 111906. [CrossRef]
19. Chen, Z.; Liu, M.; Cheng, S.; Wang, J.; Yi, Y.; Li, B.; Tang, C.; Gao, F. Bilayer Graphene Metasurface with Dynamically Reconfigurable Terahertz Perfect Absorption. *Curr. Appl. Phys.* **2025**, *80*, 282–290. [CrossRef]
20. Herkert, E.K.; Garcia-Parajo, M.F. Harnessing the Power of Plasmonics for in Vitro and in Vivo Biosensing. *ACS Photonics* **2025**, *12*, 1259–1275. [CrossRef]
21. Guler, U.; Shalaev, V.M.; Boltasseva, A. Nanoparticle Plasmonics: Going Practical with Transition Metal Nitrides. *Mater. Today* **2015**, *18*, 227–237. [CrossRef]
22. Kazanskiy, N.L.; Khonina, S.N.; Butt, M.A. Recent Development in Metasurfaces: A Focus on Sensing Applications. *Nanomaterials* **2023**, *13*, 118. [CrossRef] [PubMed]
23. Chen, S.; Jonsson, M.P. Dynamic Conducting Polymer Plasmonics and Metasurfaces. *ACS Photonics* **2023**, *10*, 571–581. [CrossRef]
24. Hou, A.; Wang, Y.; Geng, F.; Zhang, Y.; Huang, C.; Zhou, L. Plasmonic Modulators Based on Enhanced Interaction between Graphene and Localized Transverse-Electric Plasmonic Mode. *Opt. Express* **2024**, *32*, 40730–40740. [CrossRef]
25. Nordin, L.; Petluru, P.; Kamboj, A.; Muhowski, A.J.; Wasserman, D. Ultra-Thin Plasmonic Detectors. *Optica* **2021**, *8*, 1545–1551. [CrossRef]
26. Cai, C.; Li, Y.; Li, M.; Qin, Y.; Zhou, Y. Phase and Amplitude Simultaneously Coding Metasurface with Multi-Frequency and Multifunctional Electromagnetic Modulations. *Sci. Rep.* **2024**, *14*, 20904. [CrossRef]
27. Wang, S.; Deng, Z.-L.; Wang, Y.; Zhou, Q.; Wang, X.; Cao, Y.; Guan, B.-O.; Xiao, S.; Li, X. Arbitrary Polarization Conversion Dichroism Metasurfaces for All-in-One Full Poincaré Sphere Polarizers. *Light Sci. Appl.* **2021**, *10*, 24. [CrossRef]
28. Butt, M.A. A Perspective on Plasmonic Metasurfaces: Unlocking New Horizons for Sensing Applications. *Nanotechnology* **2025**, *36*, 182501. [CrossRef] [PubMed]
29. Deng, H.; Lippi, G.L.; Mørk, J.; Wiersig, J.; Reitzenstein, S. Physics and Applications of High-β Micro- and Nanolasers. *Adv. Opt. Mater.* **2021**, *9*, 2100415. [CrossRef]
30. Abdollahramezani, S.; Hemmatyar, O.; Taghinejad, M.; Taghinejad, H.; Kiarashinejad, Y.; Zandehshahvar, M.; Fan, T.; Deshmukh, S.; Eftekhar, A.A.; Cai, W.; et al. Dynamic Hybrid Metasurfaces. *Nano Lett.* **2021**, *21*, 1238–1245. [CrossRef]
31. Rifat, A.A.; Rahmani, M.; Xu, L.; Miroshnichenko, A.E. Hybrid Metasurface Based Tunable Near-Perfect Absorber and Plasmonic Sensor. *Materials* **2018**, *11*, 1091. [CrossRef]
32. Hopper, E.R.; Boukouvala, C.; Asselin, J.; Biggins, J.S.; Ringe, E. Opportunities and Challenges for Alternative Nanoplasmonic Metals: Magnesium and Beyond. *J. Phys. Chem. C* **2022**, *126*, 10630–10643. [CrossRef]
33. Babicheva, V.E.; Boltasseva, A.; Lavrinenko, A.V. Transparent Conducting Oxides for Electro-Optical Plasmonic Modulators. *Nanophotonics* **2015**, *4*, 165–185. [CrossRef]
34. Dirdal, C.A.; Jensen, G.U.; Angelskår, H.; Thrane, P.C.V.; Gjessing, J.; Ordnung, D.A. Towards High-Throughput Large-Area Metalens Fabrication Using UV-Nanoimprint Lithography and Bosch Deep Reactive Ion Etching. *Opt. Express* **2020**, *28*, 15542–15561. [CrossRef]
35. Basu, P.; Verma, J.; Abhinav, V.; Ratnesh, R.K.; Singla, Y.K.; Kumar, V. Advancements in Lithography Techniques and Emerging Molecular Strategies for Nanostructure Fabrication. *Int. J. Mol. Sci.* **2025**, *26*, 3027. [CrossRef] [PubMed]
36. Khonina, S.N.; Kazanskiy, N.L.; Butt, M.A.; Kaźmierczak, A.; Piramidowicz, R. Plasmonic Sensor Based on Metal-Insulator-Metal Waveguide Square Ring Cavity Filled with Functional Material for the Detection of CO_2 Gas. *Opt. Express* **2021**, *29*, 16584–16594. [CrossRef]
37. Johns, P.; Beane, G.; Yu, K.; Hartland, G.V. Dynamics of Surface Plasmon Polaritons in Metal Nanowires. *J. Phys. Chem. C* **2017**, *121*, 5445–5459. [CrossRef]

https://doi.org/10.3390/mi17010119

38. Gao, L.; Huo, Y.; Zang, K.; Paik, S.; Chen, Y.; Harris, J.S.; Zhou, Z. On-Chip Plasmonic Waveguide Optical Waveplate. *Sci. Rep.* **2015**, *5*, 15794. [CrossRef]
39. Yu, H.; Peng, Y.; Yang, Y.; Li, Z.-Y. Plasmon-Enhanced Light–Matter Interactions and Applications. *npj Comput. Mater.* **2019**, *5*, 45. [CrossRef]
40. Luther, J.M.; Jain, P.K.; Ewers, T.; Alivisatos, A.P. Localized Surface Plasmon Resonances Arising from Free Carriers in Doped Quantum Dots. *Nat. Mater.* **2011**, *10*, 361–366. [CrossRef]
41. Mayer, K.M.; Hafner, J.H. Localized Surface Plasmon Resonance Sensors. *Chem. Rev.* **2011**, *111*, 3828–3857. [CrossRef]
42. Li, Z.; Pestourie, R.; Lin, Z.; Johnson, S.G.; Capasso, F. Empowering Metasurfaces with Inverse Design: Principles and Applications. *ACS Photonics* **2022**, *9*, 2178–2192. [CrossRef]
43. Tutgun, M.; Yılmaz, D.; Yeltik, A.; Turduev, M.; Kurt, H. Inverse Design of All-Dielectric Parallel-Plane Mirror Optical Resonator. *Photonics Nanostruct. Fundam. Appl.* **2020**, *40*, 100787. [CrossRef]
44. Scholl, J.A.; García-Etxarri, A.; Koh, A.L.; Dionne, J.A. Observation of Quantum Tunneling between Two Plasmonic Nanoparticles. *Nano Lett.* **2013**, *13*, 564–569. [CrossRef]
45. Barbiellini, B.; Das, S.; Renugopalakrishnan, V.; Somasundaran, P. Electromagnetic Field in Hybrid Quantum Plasmonic-Photonic Systems. *Condens. Matter* **2018**, *3*, 10. [CrossRef]
46. Boriskina, S.V.; Ghasemi, H.; Chen, G. Plasmonic Materials for Energy: From Physics to Applications. *Mater. Today* **2013**, *16*, 375–386. [CrossRef]
47. Negm, A.; Howlader, M.M.R.; Belyakov, I.; Bakr, M.; Ali, S.; Irannejad, M.; Yavuz, M. Materials Perspectives of Integrated Plasmonic Biosensors. *Materials* **2022**, *15*, 7289. [CrossRef] [PubMed]
48. Todorov, R.; Hristova-Vasileva, T.; Katrova, V.; Atanasova, A. Silver and Gold Containing Compounds of P-Block Elements As Perspective Materials for UV Plasmonics. *ACS Omega* **2023**, *8*, 14321–14341. [CrossRef]
49. Baburin, A.S.; Merzlikin, A.M.; Baryshev, A.V.; Ryzhikov, I.A.; Panfilov, Y.V.; Rodionov, I.A. Silver-Based Plasmonics: Golden Material Platform and Application Challenges [Invited]. *Opt. Mater. Express* **2019**, *9*, 611–642. [CrossRef]
50. Han, W.; Reiter, S.; Schlipf, J.; Mai, C.; Spirito, D.; Jose, J.; Wenger, C.; Fischer, I.A. Strongly Enhanced Sensitivities of CMOS Compatible Plasmonic Titanium Nitride Nanohole Arrays for Refractive Index Sensing under Oblique Incidence. *Opt. Express* **2023**, *31*, 17389–17407. [CrossRef]
51. Gillibert, R.; Colas, F.; Yasukuni, R.; Picardi, G.; de la Chapelle, M.L. Plasmonic Properties of Aluminum Nanocylinders in the Visible Range. *J. Phys. Chem. C* **2017**, *121*, 2402–2409. [CrossRef]
52. Kim, D.; Bang, J.; Won, P.; Kim, Y.; Jung, J.; Lee, J.; Kwon, J.; Lee, H.; Hong, S.; Jeon, N.L.; et al. Biocompatible Cost-Effective Electrophysiological Monitoring with Oxidation-Free Cu–Au Core–Shell Nanowire. *Adv. Mater. Technol.* **2020**, *5*, 2000661. [CrossRef]
53. Jaffray, W.; Saha, S.; Shalaev, V.M.; Boltasseva, A.; Ferrera, M. Transparent Conducting Oxides: From All-Dielectric Plasmonics to a New Paradigm in Integrated Photonics. *Adv. Opt. Photon.* **2022**, *14*, 148–208. [CrossRef]
54. Butt, M.A. Graphene in Photonic Sensing: From Fundamentals to Cutting-Edge Applications. *Fundam. Res.* **2025**, *in press*. [CrossRef]
55. Magno, G.; Yam, V.; Dagens, B. Integration of Plasmonic Structures in Photonic Waveguides Enables Novel Electromagnetic Functionalities in Photonic Circuits. *Appl. Sci.* **2023**, *13*, 12551. [CrossRef]
56. Dregely, D.; Lindfors, K.; Dorfmüller, J.; Hentschel, M.; Becker, M.; Wrachtrup, J.; Lippitz, M.; Vogelgesang, R.; Giessen, H. Plasmonic Antennas, Positioning, and Coupling of Individual Quantum Systems. *Phys. Status Solidi B* **2012**, *249*, 666–677. [CrossRef]
57. Butt, M.A.; Janaszek, B.; Piramidowicz, R. Lighting the Way Forward: The Bright Future of Photonic Integrated Circuits. *Sens. Int.* **2025**, *6*, 100326. [CrossRef]
58. Martínez-Llinàs, J.; Henry, C.; Andrén, D.; Verre, R.; Käll, M.; Tassin, P. A Gaussian Reflective Metasurface for Advanced Wavefront Manipulation. *Opt. Express* **2019**, *27*, 21069–21082. [CrossRef]
59. Chen, H.-T.; Taylor, A.J.; Yu, N. A Review of Metasurfaces: Physics and Applications. *Rep. Prog. Phys.* **2016**, *79*, 076401. [CrossRef]
60. Kumar, K.; Vidal, B.; Garcia-Meca, C. Metasurface Based on Phase Change Materials for Electrically Reconfigurable THz Beam Steering in Copolarized Transmission Mode. *Sci. Rep.* **2025**, *15*, 40666. [CrossRef]
61. Meinzer, N.; Barnes, W.L.; Hooper, I.R. Plasmonic Meta-Atoms and Metasurfaces. *Nat. Photonics* **2014**, *8*, 889–898. [CrossRef]
62. Arbabi, A.; Horie, Y.; Bagheri, M.; Faraon, A. Dielectric Metasurfaces for Complete Control of Phase and Polarization with Subwavelength Spatial Resolution and High Transmission. *Nat. Nanotechnol.* **2015**, *10*, 937–943. [CrossRef]
63. Qin, F.; Ding, L.; Zhang, L.; Monticone, F.; Chum, C.C.; Deng, J.; Mei, S.; Li, Y.; Teng, J.; Hong, M.; et al. Hybrid Bilayer Plasmonic Metasurface Efficiently Manipulates Visible Light. *Sci. Adv.* **2016**, *2*, e1501168. [CrossRef] [PubMed]
64. Feng, J.; Wu, L.-S.; Mao, J.-F. Switchable Broadband/Narrowband Absorber Based on a Hybrid Metasurface of Graphene and Metal Structures. *Opt. Express* **2023**, *31*, 12220–12231. [CrossRef] [PubMed]

https://doi.org/10.3390/mi17010119

65. Hu, D.; Zheng, J.; Liao, E.; Syu, T.; Du, A. Modulating Both Amplitude and Phase in a Single-Spatial Light Modulator (SLM). In Proceedings of the Practical Holography XXXVI: Displays, Materials, and Applications, San Francisco, CA, USA, 22–27 January 2022; SPIE: Bellingham, WA, USA, 2022; Volume 12026, pp. 51–64.
66. Rolland, J.P.; Davies, M.A.; Suleski, T.J.; Evans, C.; Bauer, A.; Lambropoulos, J.C.; Falaggis, K. Freeform Optics for Imaging. *Optica* **2021**, *8*, 161–176. [CrossRef]
67. Yang, Y.; Forbes, A.; Cao, L. A Review of Liquid Crystal Spatial Light Modulators: Devices and Applications. *Opto-Electron. Sci.* **2023**, *2*, 230026–230029. [CrossRef]
68. Zhou, J.; Ma, H.; Zhang, S.; Yuan, W.; Min, C.; Yuan, X.; Zhang, Y. Controllable Split Polarization Singularities for Ultra-Precise Displacement Sensing. *Photon. Res.* **2024**, *12*, 1478–1484. [CrossRef]
69. Khonina, S.N.; Kazanskiy, N.L.; Butt, M.A. Exploring Diffractive Optical Elements and Their Potential in Free Space Optics and Imaging—A Comprehensive Review. *Laser Photonics Rev.* **2024**, *18*, 2400377. [CrossRef]
70. Wang, Y.; Chen, Q.; Yang, W.; Ji, Z.; Jin, L.; Ma, X.; Song, Q.; Boltasseva, A.; Han, J.; Shalaev, V.M.; et al. High-Efficiency Broadband Achromatic Metalens for near-IR Biological Imaging Window. *Nat. Commun.* **2021**, *12*, 5560. [CrossRef]
71. Wu, D.; Rajput, N.S.; Luo, X. Nanoimprint Lithography—The Past, the Present and the Future. *Curr. Nanosci.* **2016**, *12*, 712–724. [CrossRef]
72. Hüttenhofer, L.; Golibrzuch, M.; Bienek, O.; Wendisch, F.J.; Lin, R.; Becherer, M.; Sharp, I.D.; Maier, S.A.; Cortés, E. Metasurface Photoelectrodes for Enhanced Solar Fuel Generation. *Adv. Energy Mater.* **2021**, *11*, 2102877. [CrossRef]
73. Saleem, M.R.; Ali, R.; Khan, M.B.; Honkanen, S.; Turunen, J. Impact of Atomic Layer Deposition to Nanophotonic Structures and Devices. *Front. Mater.* **2014**, *1*, 18. [CrossRef]
74. Guchhait, S.; Chatterjee, S.; Chakravarty, T.; Ghosh, N. A Metal-Insulator-Metal Waveguide-Based Plasmonic Refractive Index Sensor for the Detection of Nanoplastics in Water. *Sci. Rep.* **2024**, *14*, 21495. [CrossRef]
75. Wu, Q.; Zhang, Y.; Qu, D.; Li, C. MIM Waveguide System with Independently Tunable Double Resonances and Its Application for Two-Parameter Detection. *Appl. Opt.* **2022**, *61*, 7409–7414. [CrossRef]
76. Butt, M.A.; Kazanskiy, N.L.; Khonina, S.N. Metal-Insulator-Metal Waveguide Plasmonic Sensor System for Refractive Index Sensing Applications. *Adv. Photonics Res.* **2023**, *4*, 2300079. [CrossRef]
77. Butt, M.A. Plasmonic Sensors Based on a Metal–Insulator–Metal Waveguide—What Do We Know So Far? *Sensors* **2024**, *24*, 7158. [CrossRef] [PubMed]
78. Wang, H.L.; Zhang, Y.K.; Zhang, T.Y.; Ma, H.F.; Cui, T.J. Broadband and Programmable Amplitude-Phase-Joint-Coding Information Metasurface. *ACS Appl. Mater. Interfaces* **2022**, *14*, 29431–29440. [CrossRef] [PubMed]
79. Wang, Q.; Zhang, X.; Xu, Y.; Gu, J.; Li, Y.; Tian, Z.; Singh, R.; Zhang, S.; Han, J.; Zhang, W. Broadband Metasurface Holograms: Toward Complete Phase and Amplitude Engineering. *Sci. Rep.* **2016**, *6*, 32867. [CrossRef] [PubMed]
80. Briggs, R.M.; Grandidier, J.; Burgos, S.P.; Feigenbaum, E.; Atwater, H.A. Efficient Coupling between Dielectric-Loaded Plasmonic and Silicon Photonic Waveguides. *Nano Lett.* **2010**, *10*, 4851–4857. [CrossRef]
81. Oulton, R.F.; Sorger, V.J.; Genov, D.A.; Pile, D.F.P.; Zhang, X. A Hybrid Plasmonic Waveguide for Subwavelength Confinement and Long-Range Propagation. *Nat. Photonics* **2008**, *2*, 496–500. [CrossRef]
82. García García, B.; Fernández-Manteca, M.G.; Zografopoulos, D.C.; Gómez-Galdós, C.; Ocampo-Sosa, A.A.; Rodríguez-Cobo, L.; Algorri, J.F.; Cobo, A. Plasmonic and Dielectric Metasurfaces for Enhanced Spectroscopic Techniques. *Biosensors* **2025**, *15*, 401. [CrossRef]
83. Dhama, R.; Panahpour, A.; Pihlava, T.; Ghindani, D.; Caglayan, H. All-Optical Switching Based on Plasmon-Induced Enhancement of Index of Refraction. *Nat. Commun.* **2022**, *13*, 3114. [CrossRef]
84. Dainese, P.; Chen, W.T.; Fan, J.; Lu, Y.-J.; Capasso, F. Flat Optics: Feature Issue Introduction. *Opt. Express* **2024**, *32*, 22563–22565. [CrossRef] [PubMed]
85. Chen, W.T.; Zhu, A.Y.; Capasso, F. Flat Optics with Dispersion-Engineered Metasurfaces. *Nat. Rev. Mater.* **2020**, *5*, 604–620. [CrossRef]
86. Soliman, A.; Williams, C.; Wilkinson, T.D. High Transmission Efficiency Hybrid Metal-Dielectric Metasurfaces for Mid-Infrared Spectroscopy. *Nanomaterials* **2025**, *15*, 1456. [CrossRef]
87. Liang, Y.; Lin, H.; Lin, S.; Wu, J.; Li, W.; Meng, F.; Yang, Y.; Huang, X.; Jia, B.; Kivshar, Y. Hybrid Anisotropic Plasmonic Metasurfaces with Multiple Resonances of Focused Light Beams. *Nano Lett.* **2021**, *21*, 8917–8923. [CrossRef]
88. Boriskina, S.V.; Cooper, T.A.; Zeng, L.; Ni, G.; Tong, J.K.; Tsurimaki, Y.; Huang, Y.; Meroueh, L.; Mahan, G.; Chen, G. Losses in Plasmonics: From Mitigating Energy Dissipation to Embracing Loss-Enabled Functionalities. *Adv. Opt. Photon.* **2017**, *9*, 775–827. [CrossRef]
89. He, F.; Fuentes-Domínguez, R.; Cousins, R.; Mellor, C.J.; Rocha, A.D.; Adams, Z.; Barton, J.K.; Gordon, G.S.D. Scalable Fabrication of Single- and Multi-Layer Planar Lenses on Fiber Imaging Probes. *APL Photonics* **2025**, *10*, 056114. [CrossRef]
90. Cao, J.; Salhi, S.; Peltier, J.; Coudevylle, J.-R.; Edmond, S.; Villebasse, C.; Herth, E.; Vivien, L.; Alonso-Ramos, C.; Melati, D. Single-Layer Silicon Metalens for Broadband Achromatic Focusing and Wide Field of View. *Sci. Rep.* **2025**, *15*, 43343. [CrossRef]

https://doi.org/10.3390/mi17010119

91. Coello, V.; Abdulkareem, M.A.; Garcia-Ortiz, C.E.; Sosa-Sánchez, C.T.; Téllez-Limón, R.; Peña-Gomar, M. Plasmonic Coupled Modes in a Metal–Dielectric Periodic Nanostructure. *Micromachines* **2023**, *14*, 1713. [CrossRef]
92. Butt, M.A.; Piramidowicz, R. Orthogonal Mode Couplers for Plasmonic Chip Based on Metal–Insulator–Metal Waveguide for Temperature Sensing Application. *Sci. Rep.* **2024**, *14*, 3474. [CrossRef]
93. Abbaszadeh-Azar, O.; Abedi, K. Design of a Low Power Silicon-Plasmonic Hybrid Electro-Optic Modulator Relied on ITO. *Opt. Mater.* **2022**, *125*, 112081. [CrossRef]
94. Neira, A.D.; Wurtz, G.A.; Zayats, A.V. Superluminal and Stopped Light Due to Mode Coupling in Confined Hyperbolic Metamaterial Waveguides. *Sci. Rep.* **2015**, *5*, 17678. [CrossRef] [PubMed]
95. Qin, X.; Sun, W.; Zhou, Z.; Fu, P.; Li, H.; Li, Y. Waveguide Effective Plasmonics with Structure Dispersion. *Nanophotonics* **2022**, *11*, 1659–1676. [CrossRef]
96. Duan, Q.; Liu, Y.; Chang, S.; Chen, H.; Chen, J. Surface Plasmonic Sensors: Sensing Mechanism and Recent Applications. *Sensors* **2021**, *21*, 5262. [CrossRef]
97. Nocerino, V.; Miranda, B.; Tramontano, C.; Chianese, G.; Dardano, P.; Rea, I.; De Stefano, L. Plasmonic Nanosensors: Design, Fabrication, and Applications in Biomedicine. *Chemosensors* **2022**, *10*, 150. [CrossRef]
98. Kazanskiy, N.L.; Khonina, S.N.; Oseledets, I.V.; Nikonorov, A.V.; Butt, M.A. Revolutionary Integration of Artificial Intelligence with Meta-Optics-Focus on Metalenses for Imaging. *Technologies* **2024**, *12*, 143. [CrossRef]
99. Badloe, T.; Seong, J.; Rho, J. Trichannel Spin-Selective Metalenses. *Nano Lett.* **2023**, *23*, 6958–6965. [CrossRef] [PubMed]
100. Jiang, L.; Hu, Q.; Feng, Y. Reconfigurable High-Efficiency Power Dividers Using Waveguide Epsilon-Near-Zero Media for On-Demand Splitting. *Photonics* **2025**, *12*, 897. [CrossRef]
101. Alfaraj, N.; Helmy, A.S. Silicon-Integrated Next-Generation Plasmonic Devices for Energy-Efficient Semiconductor Applications. *Adv. Mater. Technol.* **2025**, *10*, e00389. [CrossRef]
102. Oulton, R.F.; Sorger, V.J.; Zentgraf, T.; Ma, R.-M.; Gladden, C.; Dai, L.; Bartal, G.; Zhang, X. Plasmon Lasers at Deep Subwavelength Scale. *Nature* **2009**, *461*, 629–632. [CrossRef]
103. Khan, H.Z.; Zafar, J.; Jabbar, A.; Kazim, J.u.R.; Rehman, M.U.; Imran, M.A.; Abbasi, Q.H. Advancements in Metasurfaces for Polarization Control: A Comprehensive Survey. *Next Res.* **2025**, *2*, 100407. [CrossRef]
104. Schulz, S.A.; Oulton, R.; Kenney, M.; Alù, A.; Staude, I.; Bashiri, A.; Fedorova, Z.; Kolkowski, R.; Koenderink, A.F.; Xiao, X.; et al. Roadmap on Photonic Metasurfaces. *Appl. Phys. Lett.* **2024**, *124*, 260701. [CrossRef]
105. Meng, Y.; Chen, Y.; Lu, L.; Ding, Y.; Cusano, A.; Fan, J.A.; Hu, Q.; Wang, K.; Xie, Z.; Liu, Z.; et al. Optical Meta-Waveguides for Integrated Photonics and Beyond. *Light Sci. Appl.* **2021**, *10*, 235. [CrossRef]
106. Zia, R.; Schuller, J.A.; Chandran, A.; Brongersma, M.L. Plasmonics: The next Chip-Scale Technology. *Mater. Today* **2006**, *9*, 20–27. [CrossRef]
107. Alnakhli, Z.; Liu, Z.; AlQatari, F.; Cao, H.; Li, X. UV-Assisted Nanoimprint Lithography: The Impact of the Loading Effect in Silicon on Nanoscale Patterns of Metalens. *Nanoscale Adv.* **2024**, *6*, 2954–2967. [CrossRef]
108. Margalit, N.; Xiang, C.; Bowers, S.M.; Bjorlin, A.; Blum, R.; Bowers, J.E. Perspective on the Future of Silicon Photonics and Electronics. *Appl. Phys. Lett.* **2021**, *118*, 220501. [CrossRef]
109. Chen, C.; Yang, Z.; Wang, T.; Wang, Y.; Gao, K.; Wu, J.; Wang, J.; Qiu, J.; Tan, D. Ultra-Broadband All-Optical Nonlinear Activation Function Enabled by MoTe2/Optical Waveguide Integrated Devices. *Nat. Commun.* **2024**, *15*, 9047. [CrossRef] [PubMed]
110. Sakib Rahman, M.S.; Ozcan, A. Integration of Programmable Diffraction with Digital Neural Networks. *ACS Photonics* **2024**, *11*, 2906–2922. [CrossRef]
111. Hu, J.; Mengu, D.; Tzarouchis, D.C.; Edwards, B.; Engheta, N.; Ozcan, A. Diffractive Optical Computing in Free Space. *Nat. Commun.* **2024**, *15*, 1525. [CrossRef]
112. de Abajo, F.J.G.; Basov, D.N.; Koppens, F.H.L.; Orsini, L.; Ceccanti, M.; Castilla, S.; Cavicchi, L.; Polini, M.; Gonçalves, P.A.D.; Costa, A.T.; et al. Roadmap for Photonics with 2D Materials. *ACS Photonics* **2025**, *12*, 3961–4095. [CrossRef]
113. Yang, Q.; Wu, Y.; Chen, J.; Lu, M.; Wang, X.; Zhang, Z.; Xiong, H.; Choo, J.; Chen, L. Plasmonic Nanomaterial-Enhanced Fluorescence and Raman Sensors: Multifunctional Platforms and Applications. *Coord. Chem. Rev.* **2024**, *507*, 215768. [CrossRef]
114. Hossain, M.K. Detection of Surface Enhanced Raman Scattering Active Hotspot Using near Field Scanning Optical Microscopy. *Sci. Rep.* **2024**, *14*, 10559. [CrossRef]
115. Hu, Z.; Gu, M.; Tian, Y.; Li, C.; Zhu, M.; Zhou, H.; Fang, B.; Hong, Z.; Jing, X. Review for Optical Metalens Based on Metasurfaces: Fabrication and Applications. *Microsyst. Nanoeng.* **2025**, *11*, 189. [CrossRef] [PubMed]
116. Pan, X.; Cai, Z.; Chen, Z.; Ding, Y.; Zheng, Z.; Ding, F. Recent Progress in Mechanically Reconfigurable Metasurfaces. *APL Photonics* **2025**, *10*, 080901. [CrossRef]
117. Karim, M.E.; Choudhury, S.M. Reconfigurable Broadband Metasurface with Switchable Functionalities in the Visible Range. *Opt. Mater. Express* **2023**, *13*, 1409–1423. [CrossRef]
118. Cetin, A.E.; Coskun, A.F.; Galarreta, B.C.; Huang, M.; Herman, D.; Ozcan, A.; Altug, H. Handheld High-Throughput Plasmonic Biosensor Using Computational on-Chip Imaging. *Light Sci. Appl.* **2014**, *3*, e122. [CrossRef]

https://doi.org/10.3390/mi17010119

119. Tua, D.; Liu, R.; Yang, W.; Zhou, L.; Song, H.; Ying, L.; Gan, Q. Imaging-Based Intelligent Spectrometer on a Plasmonic Rainbow Chip. *Nat. Commun.* **2023**, *14*, 1902. [CrossRef]
120. Xiong, J.; Hsiang, E.-L.; He, Z.; Zhan, T.; Wu, S.-T. Augmented Reality and Virtual Reality Displays: Emerging Technologies and Future Perspectives. *Light Sci. Appl.* **2021**, *10*, 216. [CrossRef]
121. Choi, M.-H.; Han, W.; Min, K.; Min, D.; Han, G.; Shin, K.-S.; Kim, M.; Park, J.-H. Recent Applications of Optical Elements in Augmented and Virtual Reality Displays: A Review. *ACS Appl. Opt. Mater.* **2024**, *2*, 1247–1268. [CrossRef]
122. Yun, J.-G.; Kang, H.; Lee, K.; Jeong, Y.; Lee, E.; Kim, J.; Choi, M.; Koo, B.; Kim, D.; Choi, J.; et al. Compact Eye Camera with Two-Third Wavelength Phase-Delay Metalens. *Nat. Commun.* **2025**, *16*, 7299. [CrossRef]
123. Yang, Y.; Seong, J.; Choi, M.; Park, J.; Kim, G.; Kim, H.; Jeong, J.; Jung, C.; Kim, J.; Jeon, G.; et al. Integrated Metasurfaces for Re-Envisioning a near-Future Disruptive Optical Platform. *Light Sci. Appl.* **2023**, *12*, 152. [CrossRef]
124. Xu, D.; Xiong, X.; Wu, L.; Ren, X.-F.; Png, C.E.; Guo, G.-C.; Gong, Q.; Xiao, Y.-F. Quantum Plasmonics: New Opportunity in Fundamental and Applied Photonics. *Adv. Opt. Photon.* **2018**, *10*, 703–756. [CrossRef]
125. Li, N.; Liu, K.; Sorger, V.J.; Sadana, D.K. Monolithic III–V on Silicon Plasmonic Nanolaser Structure for Optical Interconnects. *Sci. Rep.* **2015**, *5*, 14067. [CrossRef]
126. Wu, C.; Huang, X.; Ji, Y.; Cheng, T.; Wang, J.; Chi, N.; Yu, S.; Chang-Hasnain, C.J. Addressable Structured Light System Using Metasurface Optics and an Individually Addressable VCSEL Array. *Photon. Res.* **2024**, *12*, 1129–1137. [CrossRef]
127. Lee, J.; Kim, S.-J. Meta-Optics for Optical Engineering of Next-Generation AR/VR Near-Eye Displays. *Micromachines* **2025**, *16*, 1026. [CrossRef] [PubMed]
128. Montes McNeil, A.; Li, Y.; Zhang, A.; Moebius, M.; Liu, Y. Fundamentals and Recent Developments of Free-Space Optical Neural Networks. *J. Appl. Phys.* **2024**, *136*, 030701. [CrossRef]
129. Bouillard, J.-S.G.; Dickson, W.; O'Connor, D.P.; Wurtz, G.A.; Zayats, A.V. Low-Temperature Plasmonics of Metallic Nanostructures. *Nano Lett.* **2012**, *12*, 1561–1565. [CrossRef]
130. Yu, F.; Zhao, Z.; Chen, J.; Wang, J.; Jin, R.; Chen, J.; Wang, J.; Li, G.; Chen, X.; Lu, W. Reconfigurable Metasurface with Tunable and Achromatic Beam Deflections. *Opt. Mater. Express* **2022**, *12*, 49–58. [CrossRef]
131. Chen, W.T.; Zhu, A.Y.; Sisler, J.; Huang, Y.-W.; Yousef, K.M.A.; Lee, E.; Qiu, C.-W.; Capasso, F. Broadband Achromatic Metasurface-Refractive Optics. *Nano Lett.* **2018**, *18*, 7801–7808. [CrossRef]
132. Liu, R.; Li, L.; Zhou, J. The Principle and Application of Achromatic Metalens. *Micromachines* **2025**, *16*, 660. [CrossRef]
133. Chen, A.; Zhang, M.; Crowley, D.; Gangi, N.; Begović, A.; Huang, Z.R. Silicon Photonics Foundry Fabricated, Slow-Light Enhanced, Low Power Thermal Phase Shifter. *J. Appl. Phys.* **2024**, *136*, 163101. [CrossRef]
134. Becher, C.; Gao, W.; Kar, S.; Marciniak, C.D.; Monz, T.; Bartholomew, J.G.; Goldner, P.; Loh, H.; Marcellina, E.; Goh, K.E.J.; et al. 2023 Roadmap for Materials for Quantum Technologies. *Mater. Quantum. Technol.* **2023**, *3*, 012501. [CrossRef]
135. Elsawy, M.; Kyrou, C.; Mikheeva, E.; Colom, R.; Duboz, J.-Y.; Kamali, K.Z.; Lanteri, S.; Neshev, D.; Genevet, P. Universal Active Metasurfaces for Ultimate Wavefront Molding by Manipulating the Reflection Singularities. *Laser Photonics Rev.* **2023**, *17*, 2200880. [CrossRef]
136. Nakajima, M.; Tanaka, K.; Inoue, K.; Nakajima, K.; Hashimoto, T. Densely Parallelized Photonic Tensor Processor on Hybrid Waveguide/Free-Space-Optics. In Proceedings of the 2023 International Conference on Photonics in Switching and Computing (PSC), Mantova, Italy, 26–29 September 2023; pp. 1–3.
137. Gupta, S.; Xavier, J. Neuromorphic Photonic On-Chip Computing. *Chips* **2025**, *4*, 34. [CrossRef]
138. Cai, W.; White, J.S.; Brongersma, M.L. Compact, High-Speed and Power-Efficient Electrooptic Plasmonic Modulators. *Nano Lett.* **2009**, *9*, 4403–4411. [CrossRef] [PubMed]
139. Heni, W.; Fedoryshyn, Y.; Baeuerle, B.; Josten, A.; Hoessbacher, C.B.; Messner, A.; Haffner, C.; Watanabe, T.; Salamin, Y.; Koch, U.; et al. Plasmonic IQ Modulators with Attojoule per Bit Electrical Energy Consumption. *Nat. Commun.* **2019**, *10*, 1694. [CrossRef]
140. Huang, J.-A.; Luo, L.-B. Low-Dimensional Plasmonic Photodetectors: Recent Progress and Future Opportunities. *Adv. Opt. Mater.* **2018**, *6*, 1701282. [CrossRef]
141. Kim, H.; Lee, J.; Lee, C.B.; Lee, Y.H. Recent Progress of Plasmonic Perovskite Photodetectors. *Inorganics* **2025**, *13*, 351. [CrossRef]
142. Duempelmann, L.; Gallinet, B.; Novotny, L. Multispectral Imaging with Tunable Plasmonic Filters. *ACS Photonics* **2017**, *4*, 236–241. [CrossRef]
143. Oshita, M.; Saito, S.; Kan, T. Electromechanically Reconfigurable Plasmonic Photodetector with a Distinct Shift in Resonant Wavelength. *Microsyst. Nanoeng.* **2023**, *9*, 26. [CrossRef]
144. Wang, D.; Wang, W.; Knudson, M.P.; Schatz, G.C.; Odom, T.W. Structural Engineering in Plasmon Nanolasers. *Chem. Rev.* **2018**, *118*, 2865–2881. [CrossRef]
145. Yang, A.; Odom, T.W. Breakthroughs in Photonics 2014: Advances in Plasmonic Nanolasers. *IEEE Photonics J.* **2015**, *7*, 1–6. [CrossRef]
146. Wang, D.; Yang, A. Miniaturized Optics from Structured Nanoscale Cavities. *Prog. Quantum Electron.* **2024**, *94*, 100507. [CrossRef]

https://doi.org/10.3390/mi17010119

147. Shahid, S.; Anisuzzaman Talukder, M. Beyond Periodicity: Tailoring Tamm Resonances in Plasmonic Nanohole Arrays for Multimodal Lasing. *New J. Phys.* **2025**, *27*, 013014. [CrossRef]
148. Butt, M.A. Racetrack Ring Resonator-Based on Hybrid Plasmonic Waveguide for Refractive Index Sensing. *Micromachines* **2024**, *15*, 610. [CrossRef]
149. Gorkunov, M.V.; Geivandov, A.R.; Mamonova, A.V.; Simdyankin, I.V.; Kasyanova, I.V.; Ezhov, A.A.; Artemov, V.V. Non-Mechanical Multiplexed Beam-Steering Elements Based on Double-Sided Liquid Crystal Metasurfaces. *Photonics* **2022**, *9*, 986. [CrossRef]
150. Ullah, N.; Khalid, A.U.R.; Iqbal, S.; Imran, M.; Khan, M.I.; Laxmi, V.; Tian, Y.; Tian, X. All-Dielectric Coding Metasurface Designs for Spin-Selective Beam Shaping and Multichannel Optical Vortex Beam Manipulation. *Results Phys.* **2025**, *73*, 108265. [CrossRef]
151. Zhu, R.; Wang, J.; Fu, X.; Liu, X.; Liu, T.; Chu, Z.; Han, Y.; Qiu, T.; Sui, S.; Qu, S.; et al. Deep-Learning-Empowered Holographic Metasurface with Simultaneously Customized Phase and Amplitude. *ACS Appl. Mater. Interfaces* **2022**, *14*, 48303–48310. [CrossRef]
152. Zou, Y.; Jin, H.; Zhu, R.; Zhang, T. Metasurface Holography with Multiplexing and Reconfigurability. *Nanomaterials* **2024**, *14*, 66. [CrossRef]
153. Jiang, Q.; Jin, G.; Cao, L. When Metasurface Meets Hologram: Principle and Advances. *Adv. Opt. Photon.* **2019**, *11*, 518–576. [CrossRef]
154. Hu, Y.; Luo, X.; Chen, Y.; Liu, Q.; Li, X.; Wang, Y.; Liu, N.; Duan, H. 3D-Integrated Metasurfaces for Full-Colour Holography. *Light Sci. Appl.* **2019**, *8*, 86. [CrossRef]
155. Jiang, K.; Feng, H.; Gu, M.; Jing, X.; Li, C. Research Progress on Tunable Absorbers for Various Wavelengths Based on Metasurfaces. *Photonics* **2025**, *12*, 968. [CrossRef]
156. Pillai, V.V.; Ramasubramanian, B.; Sequerth, O.; Pilla, S.; Wang, T.; Mohanty, A.K.; Govindaraj, P.; Alhassan, S.M.; Salim, N.; Kingshott, P.; et al. Nanomaterial Advanced Smart Coatings: Emerging Trends Shaping the Future. *Appl. Mater. Today* **2025**, *42*, 102574. [CrossRef]
157. Said, Z.; Pandey, A.K.; Tiwari, A.K.; Kalidasan, B.; Jamil, F.; Thakur, A.K.; Tyagi, V.V.; Sarı, A.; Ali, H.M. Nano-Enhanced Phase Change Materials: Fundamentals and Applications. *Prog. Energy Combust. Sci.* **2024**, *104*, 101162. [CrossRef]
158. Chang, X.; Pivnenko, M.; Shrestha, P.; Wu, W.; Zhang, W.; Chu, D. Electrically Tuned Active Metasurface towards Metasurface-Integrated Liquid Crystal on Silicon (Meta-LCoS) Devices. *Opt. Express* **2023**, *31*, 5378–5387. [CrossRef] [PubMed]
159. Zhang, S.; Wang, Q.; Zeng, R.; Chang, C.; Zhang, D.; Zhuang, S. Thermal Tuning Nanoprinting Based on Liquid Crystal Tunable Dual-Layered Metasurfaces for Optical Information Encryption. *Opt. Express* **2024**, *32*, 4639–4649. [CrossRef] [PubMed]
160. Makarov, S.V.; Zalogina, A.S.; Tajik, M.; Zuev, D.A.; Rybin, M.V.; Kuchmizhak, A.A.; Juodkazis, S.; Kivshar, Y. Light-Induced Tuning and Reconfiguration of Nanophotonic Structures. *Laser Photonics Rev.* **2017**, *11*, 1700108. [CrossRef]
161. Ko, J.H.; Yoo, Y.J.; Lee, Y.; Jeong, H.-H.; Song, Y.M. A Review of Tunable Photonics: Optically Active Materials and Applications from Visible to Terahertz. *iScience* **2022**, *25*, 104727. [CrossRef]
162. He, S.; Yang, H.; Jiang, Y.; Deng, W.; Zhu, W. Recent Advances in MEMS Metasurfaces and Their Applications on Tunable Lens. *Micromachines* **2019**, *10*, 505. [CrossRef]
163. Weigand, H.; Vogler-Neuling, V.V.; Escalé, M.R.; Pohl, D.; Richter, F.U.; Karvounis, A.; Timpu, F.; Grange, R. Enhanced Electro-Optic Modulation in Resonant Metasurfaces of Lithium Niobate. *ACS Photonics* **2021**, *8*, 3004–3009. [CrossRef]
164. Khodadadi, M.; Nozhat, N.; Nasari, H. A Comprehensive Review on Hybrid Plasmonic Waveguides: Structures, Applications, Challenges, and Future Perspectives. *Nanotechnol. Rev.* **2025**, *14*, 20240137. [CrossRef]
165. Sharma, T.; Zhang, Z.; Wang, J.; Cheng, Z.; Yu, K. Past, Present, and Future of Hybrid Plasmonic Waveguides for Photonics Integrated Circuits. *Nanotechnol. Precis. Eng.* **2024**, *7*, 045001. [CrossRef]
166. Lu, G.-W.; Hong, J.; Qiu, F.; Spring, A.M.; Kashino, T.; Oshima, J.; Ozawa, M.; Nawata, H.; Yokoyama, S. High-Temperature-Resistant Silicon-Polymer Hybrid Modulator Operating at up to 200 Gbit S^{-1} for Energy-Efficient Datacentres and Harsh-Environment Applications. *Nat. Commun.* **2020**, *11*, 4224. [CrossRef] [PubMed]
167. Xu, H.; Elder, D.L.; Johnson, L.E.; de Coene, Y.; Heni, W.; Moor, D.; Hammond, S.R.; O'Malley, K.M.; Clays, K.; Leuthold, J.; et al. Ultrahigh Performance Cross-Linkable Organic Electro-Optic Material for Hybrid Modulators. *Chem. Mater.* **2025**, *37*. [CrossRef]
168. Kieninger, C.; Kutuvantavida, Y.; Miura, H.; Kemal, J.N.; Zwickel, H.; Qiu, F.; Lauermann, M.; Freude, W.; Randel, S.; Yokoyama, S.; et al. Demonstration of Long-Term Thermally Stable Silicon-Organic Hybrid Modulators at 85 °C. *Opt. Express* **2018**, *26*, 27955–27964. [CrossRef]
169. Zhao, X.; Jiao, Y.; Liang, J.; Lou, J.; Zhang, J.; Lv, J.; Du, X.; Shen, L.; Zheng, B.; Cai, T. Multifield-Controlled Terahertz Hybrid Metasurface for Switches and Logic Operations. *Nanomaterials* **2022**, *12*, 3765. [CrossRef]
170. Wang, Y.; Yu, J.; Mao, Y.-F.; Chen, J.; Wang, S.; Chen, H.-Z.; Zhang, Y.; Wang, S.-Y.; Chen, X.; Li, T.; et al. Stable, High-Performance Sodium-Based Plasmonic Devices in the near Infrared. *Nature* **2020**, *581*, 401–405. [CrossRef]
171. Sun, K.; Li, J.; Ge, L.; Zhong, K.; Wang, Y.; Xu, D.; Yang, X.; Fu, W.; Yao, J. Graphene-Enhanced Hybrid Terahertz Metasurface Sensor for Ultrasensitive Nortriptyline Sensing and Detection. *Opt. Express* **2022**, *30*, 35749–35758. [CrossRef]

https://doi.org/10.3390/mi17010119

172. Butt, M.A. Ultra-Sensitive Refractive Index Sensing Enabled by High-Q Hybrid Plasmonic Metasurface Absorbers. *Opt. Laser Technol.* **2025**, *192*, 113743. [CrossRef]
173. Zhu, Y.; Li, Z.; Hao, Z.; DiMarco, C.; Maturavongsadit, P.; Hao, Y.; Lu, M.; Stein, A.; Wang, Q.; Hone, J.; et al. Optical Conductivity-Based Ultrasensitive Mid-Infrared Biosensing on a Hybrid Metasurface. *Light Sci. Appl.* **2018**, *7*, 67. [CrossRef]
174. Zhao, P.; Lü, C.; Sun, S.; Wu, F. Plasmon–Exciton Strong Coupling in Low-Dimensional Materials: From Fundamentals to Hybrid Nanophotonic Platforms. *Nanomaterials* **2025**, *15*, 1463. [CrossRef]
175. Wang, M.; Wang, J.; Zhang, C.; Zhang, Q.; Liu, Y.; Xia, H.; Chen, B.; Yu, Z.; Wang, C.; Zhou, Z.; et al. Self-Tunable Metasurface Photoelectric Hybrid Neural Network. *Laser Photonics Rev.* **2025**, e02006. [CrossRef]
176. Isnard, E.; Héron, S.; Lanteri, S.; Elsawy, M. Hybrid Model to Simulate Optical Systems Combining Metasurfaces and Classical Refractive Elements. *Opt. Express* **2025**, *33*, 52600–52613. [CrossRef]
177. Aththanayake, A.; Lininger, A.; Strangi, C.; Griswold, M.A.; Strangi, G. Tunable Holographic Metasurfaces for Augmented and Virtual Reality. *Nanophotonics* **2025**, *14*, 3813–3823. [CrossRef]
178. Ko, J.; Kim, G.; Kim, I.; Hwang, S.H.; Jeon, S.; Ahn, J.; Jeong, Y.; Ha, J.-H.; Heo, H.; Jeong, J.-H.; et al. Metasurface-Embedded Contact Lenses for Holographic Light Projection. *Adv. Sci.* **2024**, *11*, 2407045. [CrossRef]
179. Luo, M.; Zhou, Y.; Zhao, X.; Guo, Z.; Li, Y.; Wang, Q.; Liu, J.; Luo, W.; Shi, Y.; Liu, A.Q.; et al. High-Sensitivity Optical Sensors Empowered by Quasi-Bound States in the Continuum in a Hybrid Metal–Dielectric Metasurface. *ACS Nano* **2024**, *18*, 6477–6486. [CrossRef]
180. Li, H.; Shi, Z.; Zhang, H.; Qiu, S.; Zhou, Z.-K. Hybrid Metasurface Based on Si3N4 Nanopillar for Optical Sensing with Dual Channels. *ACS Appl. Nano Mater.* **2025**, *8*, 2965–2973. [CrossRef]
181. Soma, G.; Ariu, K.; Karakida, S.; Tsubai, Y.; Tanemura, T. Subvolt High-Speed Free-Space Modulator with Electro-Optic Metasurface. *Nat. Nanotechnol.* **2025**, *20*, 1625–1632. [CrossRef] [PubMed]
182. Wang, C.; Xu, H.-X.; Liu, T.; Zhang, F. Hybrid-Phase Assisted Amplitude and Phase Control Using Full-Space Metasurface. *Adv. Opt. Mater.* **2024**, *12*, 2302153. [CrossRef]
183. Luo, W.; Abbasi, S.A.; Li, X.; Ho, H.-P.; Yuan, W. Dynamic Tunable and Switchable Broadband Near-Infrared Absorption Modulator Based on Graphene-Hybrid Metasurface. *Opt. Laser Technol.* **2025**, *180*, 111460. [CrossRef]
184. Liu, G.-D.; Zhai, X.; Xia, S.-X.; Lin, Q.; Zhao, C.-J.; Wang, L.-L. Toroidal Resonance Based Optical Modulator Employing Hybrid Graphene-Dielectric Metasurface. *Opt. Express* **2017**, *25*, 26045–26054. [CrossRef]
185. Zeng, B.; Huang, Z.; Singh, A.; Yao, Y.; Azad, A.K.; Mohite, A.D.; Taylor, A.J.; Smith, D.R.; Chen, H.-T. Hybrid Graphene Metasurfaces for High-Speed Mid-Infrared Light Modulation and Single-Pixel Imaging. *Light Sci. Appl.* **2018**, *7*, 51. [CrossRef]
186. Khonina, S.N.; Kazanskiy, N.L.; Butt, M.A. Grayscale Lithography and a Brief Introduction to Other Widely Used Lithographic Methods: A State-of-the-Art Review. *Micromachines* **2024**, *15*, 1321. [CrossRef]
187. Holmes, S.J.; Mitchell, P.H.; Hakey, M.C. Manufacturing with DUV Lithography. *IBM J. Res. Dev.* **1997**, *41*, 7–19. [CrossRef]
188. Totzeck, M.; Ulrich, W.; Göhnermeier, A.; Kaiser, W. Pushing Deep Ultraviolet Lithography to Its Limits. *Nat. Photonics* **2007**, *1*, 629–631. [CrossRef]
189. Einck, V.J.; Torfeh, M.; McClung, A.; Jung, D.E.; Mansouree, M.; Arbabi, A.; Watkins, J.J. Scalable Nanoimprint Lithography Process for Manufacturing Visible Metasurfaces Composed of High Aspect Ratio TiO2 Meta-Atoms. *ACS Photonics* **2021**, *8*, 2400–2409. [CrossRef]
190. Kim, W.; Yoon, G.; Kim, J.; Jeong, H.; Kim, Y.; Choi, H.; Badloe, T.; Rho, J.; Lee, H. Thermally-Curable Nanocomposite Printing for the Scalable Manufacturing of Dielectric Metasurfaces. *Microsyst. Nanoeng.* **2022**, *8*, 73. [CrossRef]
191. Li, J.; Wang, S.; Li, X. Cross-Scale Structures Fabrication via Hybrid Lithography for Nanolevel Positioning. *Microsyst. Nanoeng.* **2025**, *11*, 163. [CrossRef]
192. Khurgin, J.B.; Boltasseva, A. Reflecting upon the Losses in Plasmonics and Metamaterials. *MRS Bull.* **2012**, *37*, 768–779. [CrossRef]
193. Chou Chau, Y.-F. Nanophotonic Materials and Devices: Recent Advances and Emerging Applications. *Micromachines* **2025**, *16*, 933. [CrossRef]
194. Wu, P.; Li, X.; Xing, Y.; Wang, J.; Zheng, W.; Wang, Z.; Ma, Y. Broadband Achromatic Hybrid Metalens Module with 100° Field of View for Visible Imaging. *Sensors* **2025**, *25*, 3202. [CrossRef] [PubMed]
195. Cho, J.H.; Cayll, D.; Behera, D.; Cullinan, M. Towards Repeatable, Scalable Graphene Integrated Micro-Nano Electromechanical Systems (MEMS/NEMS). *Micromachines* **2022**, *13*, 27. [CrossRef] [PubMed]
196. Seong, J.; Jeon, Y.; Yang, Y.; Badloe, T.; Rho, J. Cost-Effective and Environmentally Friendly Mass Manufacturing of Optical Metasurfaces Towards Practical Applications and Commercialization. *Int. J. Precis. Eng. Manuf.-Green Tech.* **2024**, *11*, 685–706. [CrossRef]
197. Morciano, M.; Fasano, M.; Chiavazzo, E.; Mongibello, L. Trending Applications of Phase Change Materials in Sustainable Thermal Engineering: An up-to-Date Review. *Energy Convers. Manag. X* **2025**, *25*, 100862. [CrossRef]
198. Islam, A.; Pandey, A.K.; Palam, K.D.P.; Bhutto, Y.A.; Saidur, R. Thermal Performance and Shape Stability Evaluation of Boron Nitride and Expanded Graphite Synergy in Beeswax-Based Composite Phase Change Material. *Energy Storage* **2025**, *7*, e70255. [CrossRef]

https://doi.org/10.3390/mi17010119

199. Miller, D.A.B. Attojoule Optoelectronics for Low-Energy Information Processing and Communications. *J. Light. Technol.* **2017**, *35*, 346–396. [CrossRef]
200. Dionne, J.A.; Sweatlock, L.A.; Atwater, H.A.; Polman, A. Plasmon Slot Waveguides: Towards Chip-Scale Propagation with Subwavelength-Scale Localization. *Phys. Rev. B* **2006**, *73*, 035407. [CrossRef]
201. Zhang, B.; Bian, Y.; Ren, L.; Guo, F.; Tang, S.-Y.; Mao, Z.; Liu, X.; Sun, J.; Gong, J.; Guo, X.; et al. Hybrid Dielectric-Loaded Nanoridge Plasmonic Waveguide for Low-Loss Light Transmission at the Subwavelength Scale. *Sci. Rep.* **2017**, *7*, 40479. [CrossRef] [PubMed]
202. Hassan, H.M.I.; Areed, N.F.F.; El-Mikati, H.A.; Hameed, M.F.O.; Obayya, S.S.A. Low Loss Hybrid Plasmonic Photonic Crystal Waveguide for Optical Communication Applications. *Opt. Quant. Electron.* **2022**, *54*, 431. [CrossRef]
203. Khonina, S.N.; Savelyev, D.A.; Degtyarev, S.A.; Azizian-Kalandaragh, Y. Metalens for Creation of the Longitudinally Polarized Photonic Needle. *J. Phys. Conf. Ser.* **2019**, *1368*, 022008. [CrossRef]
204. Kazanskiy, N.L.; Khonina, S.N.; Butt, M.A. Transforming High-Resolution Imaging: A Comprehensive Review of Advances in Metasurfaces and Metalenses. *Mater. Today Phys.* **2025**, *50*, 101628. [CrossRef]
205. Home Page—Metalenz. 2022. Available online: https://metalenz.com/ (accessed on 9 December 2025).
206. Home Page—Lumotive. Available online: https://lumotive.com/ (accessed on 9 December 2025).
207. Lin, X.; Rivenson, Y.; Yardimci, N.T.; Veli, M.; Luo, Y.; Jarrahi, M.; Ozcan, A. All-Optical Machine Learning Using Diffractive Deep Neural Networks. *Science* **2018**, *361*, 1004–1008. [CrossRef]
208. Cheng, K.; Deng, C.; Ye, F.; Li, H.; Shen, F.; Fan, Y.; Gong, Y. Metasurface-Based Image Classification Using Diffractive Deep Neural Network. *Nanomaterials* **2024**, *14*, 1812. [CrossRef]
209. Liang, Z.; Xiang, C.; Xiao, S.; Qiu, J.; Li, J.; Liu, Q.; Zou, C.; Liu, T. Metasurface-Based All-Optical Diffractive Convolutional Neural Networks. *arXiv* **2025**, arXiv:2512.05558.
210. Zhou, B.; Li, E.; Bo, Y.; Wang, A.X. High-Speed Plasmonic-Silicon Modulator Driven by Epsilon-Near-Zero Conductive Oxide. *J. Light. Technol.* **2020**, *38*, 3338–3345. [CrossRef]
211. Das, H.R.; Mondal, H. Plasmonic Integrated Electro-Absorption Modulator on an SiO_2 Platform for Advanced Photonic Systems. *Appl. Opt.* **2025**, *64*, 7262–7270. [CrossRef] [PubMed]
212. Cotrufo, M.; Sulejman, S.B.; Wesemann, L.; Rahman, M.A.; Bhaskaran, M.; Roberts, A.; Alù, A. Reconfigurable Image Processing Metasurfaces with Phase-Change Materials. *Nat. Commun.* **2024**, *15*, 4483. [CrossRef] [PubMed]
213. Gu, T.; Kim, H.J.; Rivero-Baleine, C.; Hu, J. Reconfigurable Metasurfaces towards Commercial Success. *Nat. Photon.* **2023**, *17*, 48–58. [CrossRef]
214. Zarei, S. Programmable Diffractive Deep Neural Networks Enabled by Integrated Rewritable Metasurfaces. *Sci. Rep.* **2025**, *15*, 35624. [CrossRef]
215. Zhang, W.; Pivnenko, M.; Chu, D. Fast-Speed Electrically Tunable Liquid Crystal Metasurface for 2π Phase Modulation at Normal and Oblique Angles of Incidence. *Opt. Express* **2025**, *33*, 8911–8923. [CrossRef]
216. Herle, D.; Kiselev, A.; Villanueva, L.G.; Martin, O.J.F.; Quack, N. Broadband Mechanically Tunable Metasurface Reflectivity Modulator in the Visible Spectrum. *ACS Photonics* **2023**, *10*, 1882–1889. [CrossRef] [PubMed]
217. Boes, A.; Strain, M.; Chang, L.; Nader, N. Hybrid and Heterogeneous Integration in Photonics: From Physics to Device Applications. *Appl. Phys. Lett.* **2025**, *127*, 130401. [CrossRef]
218. Kim, Y.; Choi, T.; Lee, G.-Y.; Kim, C.; Bang, J.; Jang, J.; Jeong, Y.; Lee, B. Metasurface Folded Lens System for Ultrathin Cameras. *Sci. Adv.* **2024**, *10*, eadr2319. [CrossRef]
219. Lin, Q.; Fang, S.; Yu, Y.; Xi, Z.; Shao, L.; Li, B.; Li, M. Optical Multi-Beam Steering and Communication Using Integrated Acousto-Optics Arrays. *Nat. Commun.* **2025**, *16*, 4501. [CrossRef]
220. Wang, J.; Song, R.; Li, X.; Yue, W.; Cai, Y.; Wang, S.; Yu, M. Beam Steering Technology of Optical Phased Array Based on Silicon Photonic Integrated Chip. *Micromachines* **2024**, *15*, 322. [CrossRef]
221. Takashima, Y. Beam and Image Steering by MEMS Array for AR and Lidar Applications. In Proceedings of the 2022 International Symposium on Imaging, Sensing, and Optical Memory (ISOM) and the 13th International Conference on Optics-Photonics Design and Fabrication (ODF), Sapporo, Japan, 31 August–5 September 2022; Paper IWPK_OWP_03. Optica Publishing Group: Washington, DC, USA, 2022.
222. Chen, R.T. Silicon Photonics for Optical Computing, Interconnects and Sensing. In Proceedings of the 2017 22nd Microoptics Conference (MOC), Tokyo, Japan, 19–22 November 2017; pp. 74–75.

Disclaimer/Publisher's Note: The statements, opinions and data contained in all publications are solely those of the individual author(s) and contributor(s) and not of MDPI and/or the editor(s). MDPI and/or the editor(s) disclaim responsibility for any injury to people or property resulting from any ideas, methods, instructions or products referred to in the content.

https://doi.org/10.3390/mi17010119

MDPI AG
Grosspeteranlage 5
4052 Basel
Switzerland
Tel.: +41 61 683 77 34

Micromachines Editorial Office
E-mail: micromachines@mdpi.com
www.mdpi.com/journal/micromachines



Disclaimer/Publisher's Note: The title and front matter of this reprint are at the discretion of the Guest Editor. The publisher is not responsible for their content or any associated concerns. The statements, opinions and data contained in all individual articles are solely those of the individual Editor and contributors and not of MDPI. MDPI disclaims responsibility for any injury to people or property resulting from any ideas, methods, instructions or products referred to in the content.





Academic Open
Access Publishing

mdpi.com

ISBN 978-3-7258-8748-4